

Mitochondrial Ca²⁺ uptake in Inflammation and Innate Immunity

Philip V. Seegren

Eldersburg, MD

M.S. Biotechnology, Johns Hopkins University

B.S. Biotechnology, James Madison University

A Dissertation presented to the Graduate Faculty of the University of Virginia in
Candidacy for the Degree of Doctor of Philosophy

Department of Pharmacology

University of Virginia

December 2022

Bimal N. Desai, Ph.D.

Kevin R. Lynch, Ph.D.

Doug Bayliss, Ph.D.

Sarah Ewald, Ph.D.

Hervé Agaisse, Ph.D.

Michelle Bland, Ph.D.

Abstract

The innate immune system surveys peripheral tissue and provides the first line of defense against invading pathogens. Macrophages are the commanders of this innate immunity, transforming the diversity of environmental signals into functional host defense and tissue homeostasis. As we age, this chain of command breaks down. We experience a progressive loss of physiological integrity resulting in impaired immunologic functions and susceptibility to infection and disease. Within macrophage, mitochondria provide the cellular energy needed for this lifelong battle. Mitochondria are uniquely adept to rapidly respond to changes in tissue environment. The movement of Ca^{2+} across the mitochondrial membrane is a strike of lightning to the heart of this metabolic machine. Here we show that: (1) mitochondrial Ca^{2+} uptake buffers the cytosol from deviant inflammatory outputs and (2) mitochondrial Ca^{2+} shifts the metabolic tone of macrophages to fuel the machineries of pathogen destruction. These roles have a significant impact on aging physiology with implications for age-related diseases. In essence, the Mitochondrial Calcium Uniporter provides a spark in innate immunity previously unknown.

Acknowledgements

There are many people I would like to thank for their help along the way. First and foremost, I thank my parents for their constant optimism in the face of adversity and unwavering support of my career. My mother, Karen Seegren, you have been an unwavering force in my life and always make yourself available for me in times of need. From driving me to college tours when I was young to answering the phone anytime now, I know that you will always be there. You have endless optimism and faith in me that I will continue to cherish as I progress through life. My father, Paul Seegren, you are the most light-hearted and kind man I have ever met. You have overcome so much adversity in your life and never once let these trials impact your love and support of me. One of my favorite stories from my younger years is the one that set me on this path. In traditional fashion, I was slow to respond to a call for applications to a new undergraduate research program at James Madison University. The day before my application was due, you drove to FedEx and overnighted it so it would arrive on time. This application was accepted, and I began my journey as a scientist and gained invaluable experiences that paved the way to where I am today. Thank you both.

To my brothers, Paul and Chris, I could not have asked for two better brothers. I am so proud of how we have all turned out and can't wait to see how we progress with our careers and life. Paul, over the past few years your dad-mode has kicked in and you have turned into the sappy one. You are a great support line that I know I will have for the rest of my life. Chris, you continue to be the wild one, but I couldn't be prouder of you as an individual. Your determination and drive to succeed will carry you through life. You both are so caring and supportive, and I know that both of you will continue to be the foundation of my support system in life.

I would like to thank Dr. Louise Temple my first scientific mentor at James Madison University. It was just over 10 years ago now that I first joined your lab at JMU. At the time, I had a very rudimentary understanding of what being a scientist entailed. I think back on my time in your lab often as one of my fondest memories of JMU. It is your unwavering support and enthusiasm towards developing young scientists that got me to where I am today. I'm not sure I would be here if it were not for your guidance and belief in me during my time at JMU. You provided a letter of recommendation for my application to Advanced Biosciences Laboratory (ABL) which was the primary reason I was hired, and again provided your support for me applying to UVA. I couldn't be more grateful for everything you've done to help over these years and wanted you to know the integral part you played in getting me to where I am today.

I would like to thank Dr. Anthony Cristillo and Dr. Cecilia Huaman for your support at ABL. This was my first experience as a full-time researcher and your mentorship and support molded me into the scientist I am today. I learned many of the techniques I applied during graduate school with you and developed a nose for technical rigor under your guidance. You both supported me in my application to a master's program at Johns Hopkins University and were instrumental in my acceptance. You went above and beyond the duties of your position at ABL to allow me to work on independent research that culminated in a publication with my name on it. This support is undoubtedly the reason I was accepted at UVA for my graduate training. Thank you for being the kind of mentor to young scientist we should all strive to become.

Now to Charlottesville. Charlottesville will forever be my home away from home and I couldn't image spending these last 6 years anywhere else. I'm so grateful for the faculty, staff, and students that build this great community of scientists. Thank you to the new friends I have made here and the mentors who have shaped my career. Thank you to my committee members, Drs. Sarah

Ewald, Kevin Lynch, Doug Bayliss, Michelle Bland, and Hervé Agaisse for your guidance and support over these years. You have guided my project from each of your fields and pushed me to be the best scientist I can be. You taught me to think critically about my work and uphold the highest rigor in my scientific research. You each have impacted my life greatly and I am beyond appreciative for all your support.

I want to thank all the members of the Desai Lab over these past six years. Your friendship and support have helped me tremendously over these years. The environment we have created here is one of nurturing support and critical evaluation that is indispensable for a young scientist. I am so proud and thankful of all the collaborations, scientific exchanges, and general comradery we have developed over these years. I can honestly say that you are all some of my closest friends and I look forward to seeing our careers. Thank you, Mike Schappe, for your wisdom and optimism when it comes to any form of adversity. I was always amazed by your ability to get along with anyone you meet. You are professional, kind, and supportive of your peers. I am glad that we have remained close after your departure from lab and look forward to your continued support as a colleague in the future. Thank you, Marta Stremaska, I can honestly say that you became one of my closest friends during my time at UVA. I never had a sister growing up, but I imagine that if I did, she would be just like you. In lab, you were a source of friendship and reason. Your critical evaluation of me, both professionally and personally, has helped me become the person and scientist I am today. I hope we will remain friends and colleagues in the future and appreciate all you've done for me over the years. Thank you, Catherine Doyle, for your honesty and determination. When I think of my time in lab, I can honestly say I believe you will be one of the most successful members of the Desai lab in the future. You have a knack for hard work and continually impress me with your scientific drive. I have appreciated your sincerity and honesty and am so glad we have become closer friends over the years. Hopefully, we will both be able to

play golf again in the future as professors/ doctors but only on the most expensive courses. Thank you, Greg Busey, as the newest graduate student in the lab your quickly became a great friend. You have a positivity that is infectious, and I hope that some of this will rub off on me as I continue my career. I will look back on your “fix-it” mentality and appreciate the time we spent together in lab. To Joel Kennedy and Eric Stipes, thank you for all the help you’ve provided in lab. It truly makes lab a more enjoyable experience when we have a support team like you. To all my undergrads: Dana, Rachel, Logan, and Priya – I couldn’t have asked for more determined students to work with over the years. Each of you has contributed to the success of these projects and made my time in the Desai lab easier. I wish you all the best and know each of you will be successful in your future endeavors.

Captain of the Desai Lab, Dr. Bimal N. Desai, I am beyond grateful for your support and mentorship throughout my graduate career. One of the biggest concerns as a new graduate student is the choice of mentor. As I reflect on this decision, I could not be better-off with my choice to join the Desai Lab. You’ve maintained an open door throughout my career and have been open and available for any hurdle in my life, both professionally and personally. You have given me invaluable wisdom from choosing a career path to managing the financial hardships of beginning a scientific career. You are direct but kind and have an intuition that I hope to gain as a scientist. You’ve taught me to look at the bigger picture and directed me towards meaningful and important questions that hopefully will lay the foundation for future scientists. Thank you for your letters of support and constant editing of my work (although some “Bimal-isms” occasionally needed to be removed). You have been a wonderful mentor and colleague and I hope to stay in touch and know that you will be available as a source of guidance throughout my career.

Lastly, to my fiancé, Taylor – It's funny to look back on our old slack messages for buffer formulas or reagents in the fridge knowing where we are today. From Softball teammates to lab partners, to spending time together late night while you were bartending, to amateur animal rescuers, to animal parents, and now fiancé you have been my greatest source of support and companionship through these years. You have been there through the toughest times and the best of times in grad school (of which there are many). Throughout all this, you have been my rock and a beacon of light to come home to every day. I truly do not know how I managed before I met you. I know you will continue to support me through my life and will push me to be the best in all that I do. Your family-orientated, caring, and determined nature are a constant source of strength in my life. I am so proud of the success you have had and will continue to have as you progress in your career. You are the smartest person I know and continue to amaze me each day. I would not be the scientist I am today if it weren't for you and everything you do for me. I love you more than anything and am so glad I get to share these accomplishments with you.

I cannot express my fortune and gratitude to all those who have paved the way for my success in graduate school. I can only hope to take these meaningful relationships and experiences and use them to shape myself into the best scientist and person I can be. Thank you all so much.

Table of Contents

Abstract.....	2
Acknowledgements.....	3
List of Figures	15
List of Tables.....	17
List of Abbreviations	18
Chapter One: Mitochondrial Ca ²⁺ Signaling: discovery to physiological importance.....	20
Discovery of mitochondrial Ca ²⁺ uptake	20
General principles of Ca ²⁺ Signaling.....	22
Ca ²⁺ binding motifs.....	22
Ca ²⁺ movement across a membrane converts transient electrical signals into long-lasting biological processes.....	23
The role of mCa ²⁺ uptake on mitochondrial metabolism.....	25
FAD-glycerol phosphate dehydrogenase.....	25
Pyruvate dehydrogenase phosphatase	26
Figure 1: Historical data on mitochondrial Ca ²⁺ uptake	28
Oxoglutarate dehydrogenase (α-ketoglutarate dehydrogenase).....	29
NAD-isocitrate dehydrogenase	29
Mitochondrial RHO GTPase (MIRO).....	29
Figure 2: The roles of mitochondrial Ca ²⁺	32
New horizons for mCa ²⁺ uptake.....	33
The Mitochondrial Calcium Uniporter Complex.....	34
MCU	34
MICU1, MICU2, and MICU3.....	36
EMRE.....	37
MCUb	37
Figure 3: Characterization and Identification of MCU	39
A new era for mitochondrial Ca ²⁺ studies.....	40
Focus: MCU in innate immunity.....	43
Mitochondria are central to innate immunity	43
MCU as a central regulator of innate immunity.....	45

Chapter Two: Reduced Mitochondrial Calcium Uptake in Macrophages is a Major Driver of Age-related Inflammation.....	46
Authors:.....	46
Affiliations:	46
Note	46
Graphical Abstract.....	47
Abstract.....	48
Introduction.....	49
Results	51
Gene expression analysis of human blood reveals clear signs of chronic age-associated low-grade inflammation.....	51
Figure 4: Gene expression analysis of human blood reveals clear signs of chronic age-associated inflammation.	54
In human blood, expression of genes involved in mitochondrial Ca ²⁺ uptake correlates inversely with age	56
Figure 5: In human blood, expression of genes involved in mitochondrial Ca ²⁺ uptake correlates inversely with age.....	59
Figure 6: Age related changes in <i>Mcu</i> expression across GTEx tissue and patient death parameters.....	61
Macrophage derived from older mice exhibit a marked reduction in mitochondrial Ca ²⁺ uptake.	62
Figure 7: Aged macrophages exhibit reduction in mCa ²⁺ uptake and signs of cellular senescence.	66
Figure 8: Expression profiling of MCU complex in aged macrophages and further characterization of mitochondrial defects.	70
Increased cytosolic Ca ²⁺ oscillations in zymosan-stimulated macrophages derived from old mice.	71
<i>Mcu</i> ^{-/-} BMDMs derived from young (<25-wk) mice recapitulate the amplified cytosolic Ca ²⁺ signals seen in BMDMs derived from old wt mice.	72
Figure 9: Characterization of mitochondria in aged macrophages and cytosolic Ca ²⁺ dynamics in <i>Mcu</i> ^{-/-} macrophages.....	75
BMDMs-O and <i>Mcu</i> ^{-/-} macrophages show signatures of senescence.	77
Hyper-inflammatory responses in both <i>wt</i> BMDMs-O and <i>Mcu</i> ^{-/-} BMDMs-Y.	77
Figure 10: Both <i>wt</i> BMDMs-O and <i>Mcu</i> ^{-/-} BMDMs-Y exhibit a hyper-inflammatory response to fungal stimulation.	81

Figure 11: NFκB translocation in response to <i>C. albicans</i> and M1 vs M2 immune-profiling of <i>Mcu</i> ^{-/-} macrophages.....	83
Increased cytosolic Ca ²⁺ is the driver of hyperinflammation in <i>Mcu</i> ^{-/-} macrophages.	84
Figure 12: Enhanced cytosolic Ca ²⁺ drives hyper inflammatory phenotype in <i>Mcu</i> ^{-/-} macrophages.....	87
<i>Mcu</i> ^{-/-} BMDMs also show increased pyroptosis and secretion of IL-1β after NLRP3 inflammasome activation.	88
Figure 13: <i>Mcu</i> ^{-/-} BMDMs-Y show increased pyroptosis and secretion of IL-1β after NLRP3 inflammasome activation.....	91
Figure 14: A model of Zymosan-Induced Peritonitis in <i>Mcu(M)</i> ^{-/-} mice.	93
Diminished mCa ²⁺ -uptake increases inflammatory outputs in presence and absence of inflammatory stimuli.	94
Figure 15: Bulk RNA-seq on <i>Mcu</i> ^{-/-} BMDMs-Y reveals hyper-inflammatory phenotype in response to fungal pathogens and under baseline conditions.	97
Figure 16: Analysis of Ca ²⁺ -sensitive inflammatory gene profiles point to a key role for RelA family of transcription factors.	99
Analysis of Ca ²⁺ -sensitive inflammatory gene expression points to a key role for RelA family of transcription factors.	100
siRNA mediated <i>Mcu</i> knockdown in human blood born macrophages increases their inflammatory output.	100
Figure 17: <i>Mcu</i> knockdown in human-monocyte derived macrophages recapitulates mouse phenotype.....	103
Figure 18: Validation of <i>Mcu</i> knockdown in HMDMs.....	105
Discussion	106
Acknowledgements.....	111
Author Contributions	111
Declaration of Interests	111
Resource Availability	112
Lead Contact.....	112
Materials Availability	112
Experimental Model and Subject Details.....	113
Mouse Strains.....	113
Cell culture.....	113
Methods	114

GTEX and differential gene expression analysis.....	114
Mitochondrial Ca ²⁺ uptake in permeabilized macrophages.....	114
Cytosolic Ca ²⁺ -imaging using ratiometric Fura-2	114
CALIMA analysis	115
Bulk RNAseq analysis	115
Binding Analysis for Regulation of Transcription (BART).....	116
Immunoblotting	116
Nuclear and cytoplasmic fractions.....	117
qPCR.....	117
Primers for qPCR.....	118
Immunofluorescence	119
MitoGenie	120
LDH assay.....	120
IL-1 β ELISA.....	120
Zymosan-Induced Peritonitis.....	121
Differentiation of Human Monocyte Derived Macrophages (HMDMs)	121
Quantification and Statistical Analysis	123
Statistics.....	123
Chapter Three: Mitochondrial Ca ²⁺ -signaling is an Electrometabolic Switch to Fuel Phagosome Killing	124
Authors:.....	124
Affiliations:	124
Note	124
Graphic Abstract.....	125
Highlights.....	126
Abstract.....	127
Introduction.....	128
Results	130
MCU has a crucial function in cell autonomous killing of fungal pathogens.	130
Figure 19: MCU has a crucial function in cell autonomous killing of fungal pathogens.....	133
Figure 20: Characterization of Mcu ^{-/-} macrophages at baseline.....	136

<i>Mcu(M)</i> ^{-/-} mice are highly susceptible to disseminated candidiasis	137
Figure 21: <i>Mcu(M)</i> ^{-/-} mice are highly susceptible to disseminated candidiasis.....	139
Fungal pathogens trigger store operated Ca^{2+} entry, the phase 1 of mitochondrial Ca^{2+} signaling.	141
Figure 22: Fungal pathogens trigger store operated Ca^{2+} entry, the phase 1 of mitochondrial Ca^{2+} signaling.	143
Rapid elevations in mitochondrial Ca^{2+} (phase 2) are detected immediately after the recognition of <i>C. albicans</i>	144
Figure 23: Rapid elevations in mitochondrial Ca^{2+} (phase 2) are detected after fungal recognition.....	147
Figure 24: RAW3mt validation and analysis of PPMiCa responses	149
Mitochondrial Ca^{2+} signaling controls phagosomal ROS production.....	150
Figure 25: Mitochondrial Ca^{2+} signaling controls phagosomal ROS production.....	153
Figure 26: Gating strategy for flow cytometry.....	155
Figure 27: Mitochondrial ROS and validation of phagosomal ROS by flow cytometry.....	157
<i>Mcu</i> ^{-/-} macrophages are unable to meet the NADPH demand of phagosomal killing.	158
<i>Mcu</i> ^{-/-} macrophages exhibit an abnormal immunometabolic shift in response to fungal pathogens.	159
Figure 28: <i>Mcu</i> ^{-/-} macrophages exhibit an abnormal immunometabolic shift in response to fungal pathogens.....	161
Figure 29: NADPH/NADP ⁺ biochemical analysis and seahorse quantification	163
Metabolomic analysis of <i>Mcu</i> ^{-/-} macrophages responding to zymosan.	164
Dysregulated TCA cycle underlies defective killing by <i>Mcu</i> ^{-/-} macrophages.	164
Mitochondrial Ca^{2+} triggers dephosphorylation and activation of pyruvate dehydrogenase.....	165
Figure 30: Dysregulated TCA cycle underlies defective killing by <i>Mcu</i> ^{-/-} macrophages	168
Figure 31: Metabolomic analysis of glycolysis and pentose phosphate pathway.....	171
Figure 32: Metabolomic analysis of TCA cycle and quantification of pPDH immunofluorescence.....	173

Discussion	174
Acknowledgements.....	177
Author Contributions	177
Declaration of Interests	177
Resource Availability	178
Lead Contact:.....	178
Materials Availability	178
Data and Code Availability.....	178
Experimental Model and Subject Details.....	179
Mouse Strains.....	179
Cell lines and cell culture	179
Methods.....	180
Ca ²⁺ channel siRNA screen.....	180
<i>In vivo</i> (mouse) disseminated candidiasis model.....	181
Isolation of mitochondria	181
Killing assays	181
<i>In vitro</i> mitochondrial Ca ²⁺ uptake assay.....	182
Preparation of fungal aqueous extracts.....	182
LDH release assay.....	182
Generation of RAW3mt stable cell line.....	183
Live cell mitochondrial Ca ²⁺ imaging during zymosan phagocytosis.....	183
Transmission Electron Microscopy (TEM)	183
Cytosolic Ca ²⁺ imaging using ratiometric Fura-2.....	184
ATP measurements	184
Flow cytometry.....	184
Mitochondrial ROS measurements	185
Fluorescence Lifetime Imaging (FLIM) microscopy.....	185
Seahorse assays.....	186
Immunofluorescence	186
Metabolomics.....	187
Key Resources Table	188
Table 3: Key Resources Table Cell Reports Paper.....	188
Quantification and Statistical Analysis.....	191

Statistics.....	191
Chapter Four: Discussion and Future Directions	192
Aging and mCa ²⁺ uptake.....	192
Figure 33: Inflammaging	195
Figure 34: Immunophenotyping young vs old, Mcu ^{-/-} vs wt.....	197
Relationship between SOCE and mCa ²⁺ uptake	198
Transcriptional regulation of <i>Mcu</i>	199
Figure 35: Mcu expression in response to zymosan	200
Cellular Aging.....	201
Figure 36: Aging Macrophages from Tabula Muris Senis	202
Phagocytosis requires a rapid switch in metabolism.....	203
Metabolic requirements for pathogen killing	203
Summary	204
Figure 37: Metabolic regulation of pathogen killing	207
References	208

List of Figures

Figure 1: Historical data on mitochondrial Ca ²⁺ uptake	27
Figure 2: The roles of mitochondrial Ca ²⁺	31
Figure 3: Characterization and Identification of MCU	38
Figure 4: Gene expression analysis of human blood reveals clear signs of chronic age-associated inflammation.	53
Figure 5: In human blood, expression of genes involved in mitochondrial Ca ²⁺ uptake correlates inversely with age.....	58
Figure 6: Age related changes in Mcu expression across GTEx tissue and patient death parameters.	60
Figure 7: Aged macrophages exhibit reduction in mCa ²⁺ uptake and signs of cellular senescence.	65
Figure 8: Expression profiling of MCU complex in aged macrophages and further characterization of mitochondrial defects.....	69
Figure 9: Characterization of mitochondria in aged macrophages and cytosolic Ca ²⁺ dynamics in Mcu ^{-/-} macrophages.	74
Figure 10: Both wt BMDMs-O and Mcu ^{-/-} BMDMs-Y exhibit a hyper-inflammatory response to fungal stimulation.	80
Figure 11: NFκB translocation in response to <i>C. albicans</i> and M1 vs M2 immune-profiling of Mcu ^{-/-} macrophages.	82
Figure 12: Enhanced cytosolic Ca ²⁺ drives hyper inflammatory phenotype in Mcu ^{-/-} macrophages.....	86
Figure 13: Mcu ^{-/-} BMDMs-Y show increased pyroptosis and secretion of IL-1β after NLRP3 inflammasome activation.	90
Figure 14: A model of Zymosan-Induced Peritonitis in Mcu(M) ^{-/-} mice.	92
Figure 15: Bulk RNA-seq on Mcu ^{-/-} BMDMs-Y reveals hyper-inflammatory phenotype in response to fungal pathogens and under baseline conditions.	96
Figure 16: Analysis of Ca ²⁺ -sensitive inflammatory gene profiles point to a key role for RelA family of transcription factors.	98

Figure 17: Mcu knockdown in human-monocyte derived macrophages recapitulates mouse phenotype.....	102
Figure 18: Validation of Mcu knockdown in HMDMs.....	104
Figure 19: MCU has a crucial function in cell autonomous killing of fungal pathogens.....	132
Figure 20: Characterization of Mcu ^{-/-} macrophages at baseline.....	135
Figure 21: Mcu(M) ^{-/-} mice are highly susceptible to disseminated candidiasis.	138
Figure 22: Fungal pathogens trigger store operated Ca ²⁺ entry, the phase 1 of mitochondrial Ca ²⁺ signaling.....	142
Figure 23: Rapid elevations in mitochondrial Ca ²⁺ (phase 2) are detected after fungal recognition.....	146
Figure 24: RAW3mt validation and analysis of PPMiCa responses	148
Figure 25: Mitochondrial Ca ²⁺ signaling controls phagosomal ROS production	152
Figure 26: Gating strategy for flow cytometry.....	154
Figure 27: Mitochondrial ROS and validation of phagosomal ROS by flow cytometry	156
Figure 28: Mcu ^{-/-} macrophages exhibit an abnormal immunometabolic shift in response to fungal pathogens.....	160
Figure 29: NADPH/NADP ⁺ biochemical analysis and seahorse quantification.	162
Figure 30: Dysregulated TCA cycle underlies defective killing by Mcu ^{-/-} macrophages	167
Figure 31: Metabolomic analysis of glycolysis and pentose phosphate pathway	170
Figure 32: Metabolomic analysis of TCA cycle and quantification of pPDH immunofluorescence.....	172
Figure 33: Inflammaging	195
Figure 34: Immunophenotyping young vs old, Mcu ^{-/-} vs wt.....	196
Figure 35: Mcu expression in response to zymosan	200
Figure 36: Aging Macrophages from Tabula Muris Senis	202
Figure 37: Metabolic regulation of pathogen killing	206

List of Tables

Table 1: Animal models for uniporter proteins.	41
Table 2: Human disease associations of MCU components	42
Table 3: Key Resources Table Cell Reports Paper	188

List of Abbreviations

ADP Adenosine triphosphate	GPDH Glyceraldehyde-3-phosphate dehydrogenase
ATP Adenosine diphosphate	GSDMD Gasdermin D
BMDMs Bone-marrow derived macrophages	GTE _x Genotype-Tissue Expression Project
CASP1 Caspase 1	HMDMs Human Monocyte Derived Macrophages
CoA Coenzyme A	HIF-1 α Hypoxia inducible factor-1 alpha
CX3CR1 C-X3-C Motif Chemokine Receptor 1	IFN γ Interferon Gamma
DAMP Damage-associated molecular pattern	IL-1 β Interleukin-1 beta
ETC Electron Transport Chain	IL-6 Interleukin-6
EDTA Ethylenediaminetetraacetic acid	IRG1 Immunoresponsive gene-1
EGTA Ethylene glycol-bis(2-aminoethylether)- N,N,N',N'-tetraacetic acid	LPS Lipopolysaccharide
ELISA Enzyme-linked immunosorbent assay	mCa ²⁺ Mitochondrial Ca ²⁺
EMRE Essential MCU regulator	MCU Mitochondrial Calcium Uniporter
ER Endoplasmic Reticulum	MCUb Mitochondrial Calcium Uniporter Subunit beta
FAD Flavin adenine dinucleotide	MICU1 Mitochondrial Calcium Uptake 1
MICU1 Mitochondrial Calcium Uptake 1	MICU2 Mitochondrial Calcium Uptake 2
MIRO Mitochondrial rho GTPase	SDH Succinate Dehydrogenase

NO
Nitric Oxide

NAD⁺/ NADH
Nicotinamide adenine dinucleotide

NADP⁺/ NADPH
Nicotinamide adenine dinucleotide phosphate

NF κ B
Nuclear factor kappa B

NFAT
Nuclear factor of activated T-cells

OCR
Oxygen Consumption Rate

OGDH
Oxoglutarate dehydrogenase

ORAI
Calcium-release activated calcium modulator

OxPAPC
Oxidized PAPC

PAMPs
Pathogen-associated molecular patterns

PDH
Pyruvate Dehydrogenase

PDP
Pyruvate Dehydrogenase phosphatase

qPCR
Quantitative Polymerase Chain Reaction

ROS
Reactive Oxygen Species

SOCE
Store-operated Calcium Entry

TCA
The tricarboxylic acid cycle

TNF α
Tumor necrosis factor alpha

Chapter One: Mitochondrial Ca^{2+} Signaling: discovery to physiological importance.

I will start this thesis with a historical perspective on the field of mitochondrial Ca^{2+} (mCa^{2+}) uptake and signaling. It is best to know where we came from to better appreciate where we are today. This chapter benefitted from several insightful reviews by Ernesto Carafoli on the history of mCa^{2+} uptake¹⁻³. Opportunistically, these stories end just before the beginning of my own. Shortly after his last review, the labs of Drs. Vamsi Mootha and Rosario Rizzuto independently discovered the molecular identity of the mitochondrial calcium uniporter (MCU), the ion channel that mediates mCa^{2+} uptake, marking a new molecular era in mCa^{2+} research^{4,5}. In this chapter, I reflect on these historical discoveries and discuss new advances made possible by the identification of MCU and its regulatory subunits. Today, mCa^{2+} is a rapidly growing field with hundreds of publications each year (**Figure 1A**) but it is clear we are still at the beginning of our understanding of this fundamental biological process and its functions in cell biology and its physiological manifestations.

Discovery of mitochondrial Ca^{2+} uptake

The discovery of mCa^{2+} uptake is attributed to Vasington, Murphy⁶, DeLuca and Engstrom⁷, who showed that isolated mitochondria take up Ca^{2+} through an energy-dependent process. The important take away from these seminal papers was that mitochondria could only take up Ca^{2+} under aerobic conditions and at above ambient temperature ($\sim 30^\circ\text{C}$ is required) (**Figure 1B**). It's quite astonishing how accurate these early experiments were in capturing mitochondrial Ca^{2+} uptake. The key to the assay is its ingredients: (1) Succinate is a necessary substrate for aerobic metabolism (with the addition of malate and glutamate being optional), (2) intracellular salts and (3) inorganic phosphate is all that is required for healthy mitochondria to take up Ca^{2+} .

Follow up studies on the relationship between mCa²⁺ uptake and the electron transport chain were pioneered by Albert L. Lehninger at Johns Hopkins University in the 1960s and early 70s. Lehninger is best known for his co-discovery of mitochondria being the site of oxidative phosphorylation and his publication of *Principles of Biochemistry*, a textbook that is still widely used in introductory biochemistry courses. His contributions to our understanding of mitochondrial Ca²⁺ uptake include: (1) the stoichiometry of Ca²⁺ and inorganic phosphate accumulation in mitochondria⁸, and (2) the observation that ATP can support mCa²⁺ uptake in the absence of ETC activity^{9,10}. These studies demonstrated that mCa²⁺ uptake is accompanied by an uptake of inorganic phosphate into the mitochondrial matrix, resulting in the accumulation of the insoluble precipitate Ca²⁺:phosphate⁸. The quick chelation of Ca²⁺ within the matrix by inorganic phosphate is essential for robust and continued mCa²⁺ uptake¹¹. This process ensures that minimal depolarization occurs in response to mCa²⁺ uptake and the driving force for Ca²⁺ influx into the matrix is maintained. Secondly, not all components of the ETC are required for mCa²⁺ uptake and under physiological conditions (i.e. in the presence of ATP), some ETC components are dispensable for the uptake of mCa²⁺^{9,10}. Lehninger's biochemical analysis of mCa²⁺ uptake led to the hypothesis that a mitochondrial Ca²⁺ uniporter (MCU) is responsible for the rapid influx of Ca²⁺ into the mitochondrial matrix, but its molecular identity remained a tantalizing enigma for many decades, frustrating many decades of determined attempts by my predecessors.

Despite numerous and highly credible studies demonstrating *in vitro* mCa²⁺ uptake, the field entered a relatively dark period of extreme skepticism and disbelief. The most detrimental observation was that cytosolic Ca²⁺ seemed to oscillate in the nM range, and numerous labs reported a half-maximal rate (K_m) for mCa²⁺ uptake in the μ M range. Simply put, it appeared that cytosolic Ca²⁺ was never or rarely high enough to enable mCa²⁺ uptake. We now understand that cytosolic [Ca²⁺] can be significantly high in certain microdomains and this is

enough to trigger the opening of MCU through the activity of its regulatory subunits MICU1 and MICU2, whose EF-hands have a K_d for Ca^{2+} binding at $\sim 500\text{nM}$ ¹². However, these molecular mechanisms would not be discovered until after 2010 and during the 1970s-1990s, studies on mCa^{2+} uptake and signaling fell out of favor and the field was often derided for being a laboratory artifact. At best, it was thought that mCa^{2+} uptake played a relatively minor role in the regulation of TCA cycle dehydrogenases and its regulation of cytosolic Ca^{2+} was limited to extreme pathological conditions where cell membrane had lost its integrity and cytosolic $[\text{Ca}^{2+}]$ has reached catastrophic levels – a desperate last gasp of a dying cell to survive a little longer.

General principles of Ca^{2+} Signaling

Before we go further into mitochondrial Ca^{2+} signaling, this section will briefly review fundamental principles of Ca^{2+} signaling. These principles of Ca^{2+} signaling are reviewed in more detail in this review by David Clapham¹³.

Ca^{2+} binding motifs

Endowed with two positive charges, Ca^{2+} binding can alter protein structure and this rapid change in its conformation can yield new functions – the protein is then said to be activated by Ca^{2+} . This is best exemplified by common Ca^{2+} -binding domains such as EF-hands and C2 domains.

The working of EF-hands is structurally similar to how Ca^{2+} -chelating molecules such as EDTA and EGTA “cage” Ca^{2+} . Although chelation is more simply understood as the compartmentalization or sequestration of the metal ions, in the case of EF hands, it results in a dramatic change in its conformation, with functional consequences. EF hands cage Ca^{2+} through the interaction of negatively charged amino acids (usually glutamate) located within a helix-turn-helix motif of the EF-hand.

C2 domains are approximately 130 residues and found in many mammalian proteins. C2 domains have substantial variation between proteins

and not all bind Ca^{2+} ¹⁴. The most well-known Ca^{2+} binding C2 domains are found in Protein Kinase C (PKCs) family of kinases. The Ca^{2+} -binding C2 domains have variable loops that contain amino acid sequences capable of binding to Ca^{2+} and most domains bind multiple Ca^{2+} ions. In general, when Ca^{2+} is bound to the C2 domain of a target protein, the protein displays a higher affinity for the negatively charged phospholipids in the plasma membrane. Essentially, Ca^{2+} binding to C2 domains triggers a switch in the localization of the protein from the cytosol to the plasma membrane. This is true for PKC, and another example of this is the C2 domain of 5-lipoxygenase, which preferentially binds phosphatidyl choline (PC) on the plasma membrane following Ca^{2+} -binding¹⁵.

While EF-hands and C2 domains are two well established Ca^{2+} -binding motifs, there are hundreds of other proteins that are activated by Ca^{2+} , without containing clearly recognizable Ca^{2+} -binding domains. A primary example of this phenomenon is the transcription factor NF κ B. It has long been known that Ca^{2+} regulates the subcellular localization of NF κ B^{16,17}, however NF κ B and its known regulators have no reported Ca^{2+} -binding motifs. In this example, it is exciting that the precise mechanism of Ca^{2+} -mediated NF κ B regulation is yet to be discovered. The regulation of NF κ B will be discussed in greater detail in Chapter 3 and is highly relevant for this thesis.

Ca²⁺ movement across a membrane converts transient electrical signals into long-lasting biological processes

Biological membranes store electrical energy across their surfaces. This electrical energy is defined by difference in the ionic composition (Ca^{2+} , K^+ , Na^+ , Mg^{2+} , Cl^- , etc.) of the extracellular and intracellular compartments. The electrical voltage across a membrane, the Membrane potential (V_m), emerges from the combination of chemical and ionic gradients. Cells use this charge difference across the membrane (voltage) to generate rapid electrical signals – this is done predominantly through the precise location and gating of ion channels. The movement of specific ions across a membrane is determined by the membrane

potential and its permeability (channel opening). The resting membrane potential for a typical plasma membrane range from -50 mV to -70 mV (negatively charged on the cytosolic side). The orientation of this charge gradient determines which direction the ion will move when a channel is open. This means that positively charged ions in the extracellular space (i.e., Ca^{2+}) will move down their electrical gradient into the cytosol. Furthermore, the chemical gradient (difference in concentration) for Ca^{2+} is maintained at a ~20,000-fold difference (outside ~2 mM Ca^{2+} to inside ~100 nM Ca^{2+}). The combined electrochemical gradient for Ca^{2+} produces an awesome driving force for the entry of Ca^{2+} into the cytosol – poised constantly for instantaneous signaling by gating a Ca^{2+} -permeable ion channel. This apparently infinite reservoir of information transfer is paid for in advance. Electrochemical gradients of key ions are maintained in large part by the constant activity of ATP-consuming pumps. Cells invest a large portion of their energy to fuel these pumps – estimated to be around 60% for excitable cells such as neurons and muscle, and 40% for non-excitable cells. How metabolic processes are coordinated with electrical activity is still not understood in terms of concrete molecular mechanisms but a crucial role for mitochondria has been conjectured.

The above outlined concepts also apply to the mitochondrial inner membrane (MIM). The mitochondrial outer membrane (MOM) is highly porous to ions and is completely depolarized. The resting membrane potential of the mitochondrial inner membrane is determined by the activity of the electron transport chain (**Figure 1C**). Protons (H^+) are pumped into the intermembrane space by the activity of ETC complexes I, III, and IV. This activity is coupled to the oxidation of NADH and FADH_2 , and the movement of electrons across the inner mitochondrial membrane. The concentration gradient of H^+ across the inner membrane results in a resting membrane potential of -180 mV (negative on the side of the matrix). This gradient creates an enormous driving force for cytosolic Ca^{2+} ions (remember that MOM is porous) to move into the mitochondrial matrix.

The electrical field strength across the MIM amounts to ~30 million V/m, which is comparable to the electrical field generated during a bolt of a lightning¹⁸.

The role of mCa²⁺ uptake on mitochondrial metabolism

FAD-glycerol phosphate dehydrogenase

In our journey, we are now in the 1970s through 1990s and despite a general disbelief in the physiological conditions required for mCa²⁺ uptake, several labs continued to study the role of Ca²⁺ on mitochondrial metabolism. One of the first enzymes shown to be regulated by μM levels of Ca²⁺ was the FAD-glycerol phosphate dehydrogenase now known as the glycerol-3-phosphate dehydrogenase (GPDH)¹⁹. In this study, it was shown that the divalent chelator EDTA lowered the activity (K_m) for glycerol phosphate and the IC₅₀ for Ca²⁺ inhibition was ~100nM. GPDH has both a mitochondrial (GPDH-m) and a cytosolic (GPDH-c) isoform. Together, they work in a shuttle where GPDH-c oxidizes NADH to NAD⁺ in the conversion of dihydroxyacetone phosphate to glycerol 3-phosphate (G3P). In turn, GPDH-m reduces FAD to FADH₂ by converting G3P back to dihydroxyacetone. Together, these reactions play an important role in the redox balance of cells. The GPDH shuttle regenerates NAD⁺ in the cytosol. These initial studies were performed on isolated mitochondria suggesting the GPDH-m is the target of Ca²⁺ regulation. Importantly, direct binding of Ca²⁺ to GPDH-m has been demonstrated *in vitro*²⁰. An important distinction in GPDH from the other molecules listed below is the location of its Ca²⁺-binding motif. GPDH-m resides in the MIM, and its EF-hands are located in the intermembrane space. Thus, we would hypothesize GPDH-m is primarily regulated by increased cytosolic Ca²⁺ and the buffering of Ca²⁺ by mitochondria would in fact dampen this activation.

Pyruvate dehydrogenase phosphatase

Pyruvate dehydrogenase (PDH) bridges the glycolytic pathway to the TCA cycle by converting pyruvate into acetyl-CoA within the mitochondrial matrix. This is a terminal transition and is considered an endpoint for pyruvate metabolism. This fate decision for pyruvate is tightly regulated on a cellular and physiological level²¹. In the 1980s, McCormack and Denton identified the effects of mCa^{2+} on pyruvate dehydrogenase in isolated mitochondria²²⁻²⁶. They showed that in mitochondria isolated from several tissues (heart, liver, fat cells, brain and kidneys), PDH activity is enhanced in the presence of Ca^{2+} and in most systems the K_m for Ca^{2+} was $\sim 1 \mu M$ ($1 \mu M Ca^{2+}$ increased PDH activity to $\frac{1}{2}$ its maximal rate) (Figure 1D). Similar kinetics were seen for oxoglutarate dehydrogenase (OGDH) (Figure 1D). It took until 2004 for the mechanism of this regulation to be revealed²⁷.

The regulation of PDH by mCa^{2+} is mediated by the pyruvate dehydrogenase phosphatase (PDP). PDH is regulated by concentrations of its input and output products Acetyl-CoA/CoA and NADH/NAD⁺, as well as the reversible phosphorylation of three sites on the E1 subunit²⁸. PDP in mammals is found in two isoforms PDP1 and PDP2. PDP1 and PDP2 dephosphorylate the E1 subunit of PDH resulting in increased PDH activity²⁹. Ca^{2+} binding assays showed that the $K_{0.5}$ for PDP1 is $\sim 1 \mu M$, which correlates with the observations for PDH from the 1980s²⁷. Structural analysis of PDP1 predicts that Ca^{2+} binds to the L2 domain of PDP1 in a region with structural homology to troponin C³⁰. This sequence contains a putative EF-hand for Ca^{2+} binding but structural analysis of PDP1 in the presence of Ca^{2+} has not yet confirmed these observations. PDP2 has a similar domain but key changes in the amino acid sequence make it Ca^{2+} insensitive. The differential expression of PDP1 and PDP2 across many tissues suggests a unique role for Ca^{2+} regulation of PDH activity in a tissue/cell specific context. PDP1 is the most well studied of Ca^{2+} regulated enzymes due to its role in regulating pyruvate metabolism. Our studies build upon these observations by showing a salient role for mCa^{2+} on PDH activity in macrophages (Chapter 3).

Figure 1: Historical data on mitochondrial Ca^{2+} uptake

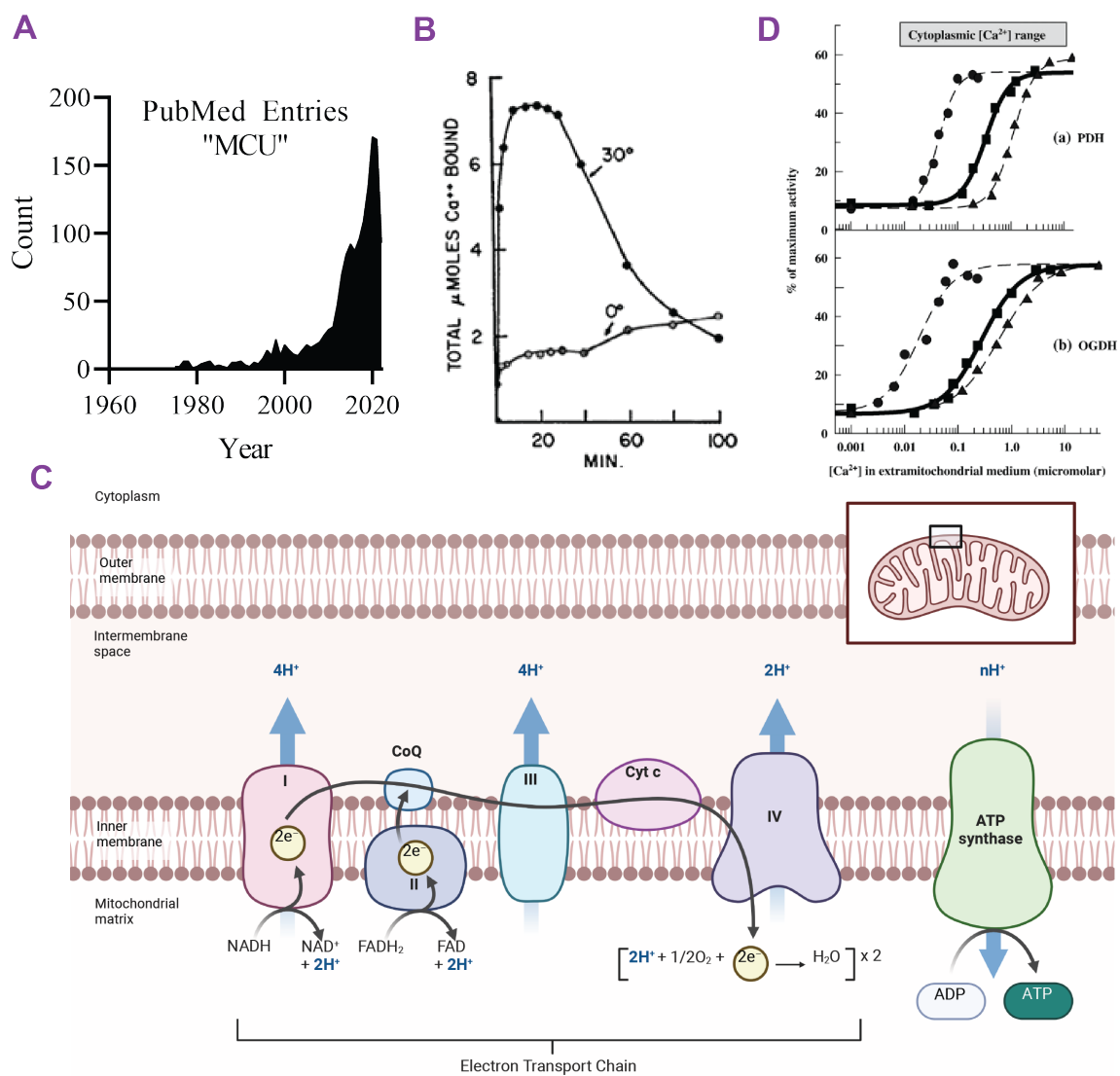


Figure 1: Historical data on mitochondrial Ca²⁺ uptake

A. Number of PubMed entries plotted by year.

B. Figure was taken from Vasington and Murphy, 1962⁶. Uptake of Ca²⁺ by isolated rat kidney mitochondria. Mitochondria were isolated by a conventional cell fractionation procedure. The reaction medium (isotonic NaCl, pH 7.0) contained a respiratory substrate (succinate), ATP, Mg²⁺, and 2.5 mM radioactive Ca²⁺. At the end of the incubation mitochondria were sedimented by centrifugation, and radioactivity was measured in a Geiger counter.

C. Figure was taken from Denton, McCormack, and Edgell, 1980²². Sensitivity of the pyruvate dehydrogenase system and oxoglutarate dehydrogenase in coupled rat heart mitochondria to changes in extramitochondrial calcium ion concentration. (a) Pyruvate dehydrogenase (PDH) activity: mitochondria were incubated in medium containing phosphate, oxoglutarate and malate plus CaEGTA buffers to give required extramitochondrial calcium ion concentration and in the presence of (●), no additions; (•), 15 mM NaCl and 0.5 mM Mg₂Cl; (▲) uncoupler FCCP plus ATP. (b) Oxoglutarate dehydrogenase (OGDH) activity: mitochondria were incubated in the same conditions as (a), but 2 mM ADP was added and the initial concentration of oxoglutarate was 0.5 mM; no ATP was added with uncoupler ATP.

D. Schematic of the electron transport chain created in Biorender.

Oxoglutarate dehydrogenase (α -ketoglutarate dehydrogenase)

OGDH has similar structural features to PDH with three main subunits (E1, E2, and E3). OGDH catalyzes the reaction between α -ketoglutarate, NAD⁺, and CoA into Succinyl-CoA and NADH. The regulation of OGDH by mCa²⁺ was shown again by McCormack and Denton in 1979 from isolated pig-heart mitochondria³¹ (**Figure 1D**). The key difference between OGDH and PDH is that Ca²⁺ is thought to directly bind to OGDH increasing its activity³². However, the binding site for Ca²⁺ on OGDH is poorly understood and no putative Ca²⁺ binding domains have been identified. Current hypotheses suggest that Ca²⁺ regulates the enzyme by binding directly to the E2 subunit of OGDH.

NAD-isocitrate dehydrogenase

NAD-isocitrate dehydrogenase (IDH) is another TCA cycle enzyme regulated by Ca²⁺. As with OGDH and PDH, the regulation of IDH was first reported by McCormack and Denton in isolated mitochondria³³. Like OGDH, Ca²⁺ is thought to bind directly to IDH, increasing enzyme activity, but no binding sites have been identified. An interesting difference in the regulation of IDH is the requirement of ADP or ATP for Ca²⁺ sensitivity³⁴. Of the three Ca²⁺ sensitive dehydrogenases, IDH shows the least sensitivity with a $K_{0.5}$ for Ca²⁺ at ~ 5 μ M, depending on the ATP/ADP ratio. Interestingly, IDH and OGDH have been shown to be Ca²⁺ sensitive in vertebrate systems only, suggesting an evolutionary dichotomy from yeast, plants and insects.

Mitochondrial RHO GTPase (MIRO)¹

The most recent addition to Ca²⁺ regulated proteins on the mitochondrion is the atypical RHO GTPase, MIRO. MIRO has two isoforms MIRO1 and MIRO2 which are anchored to the mitochondrial outer membrane by their c-terminal transmembrane segment^{35,36}. MIRO1 has two functional EF-hands that bind Ca²⁺

¹ MIRO is not known to be regulated by mCa²⁺ uptake but is important to discuss due to its role in mitochondrial physiology and its regulation by cytosolic Ca²⁺

to regulate its activity. MIRO1 functions in the microtubule and actomyosin-mediated movement of mitochondria. In this regard, MIRO1 acts as a tether that binds mitochondria to Myosin proteins on microtubules. When cytosolic Ca^{2+} is elevated, the EF-hands of MIRO bind Ca^{2+} and dissociate from the microtubules resulting in mitochondrial arrest. The precise mechanism of arrest is not understood but point mutations in MIRO1 (E208K and E328K) that disrupt the Ca^{2+} binding motif result in Ca^{2+} -insensitive movement of mitochondria along microtubules³⁷. An overview of all the Ca^{2+} -sensitive enzymes discussed in this section can be found in [Figure 2](#).

Figure 2: The roles of mitochondrial Ca^{2+}

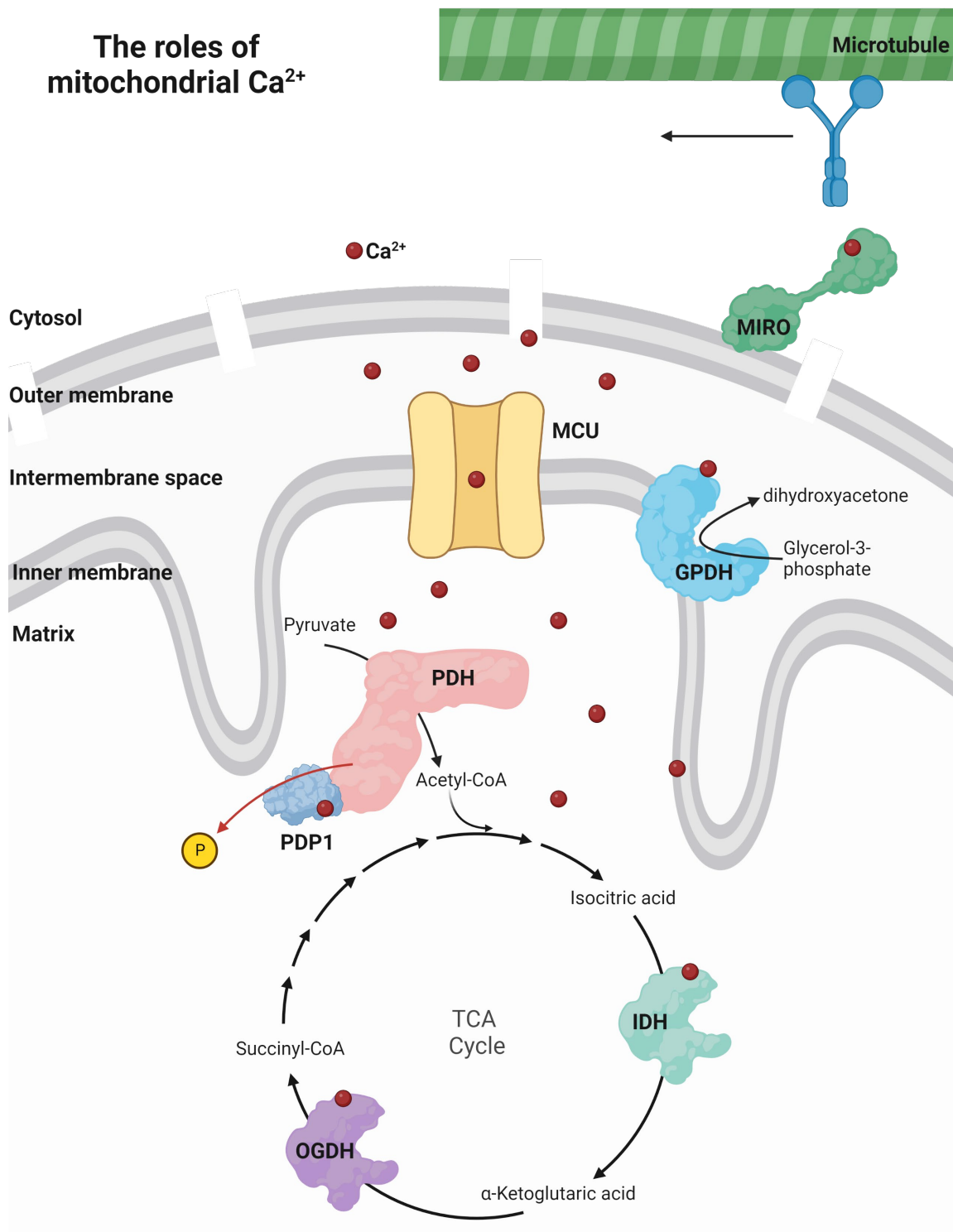


Figure 2: The roles of mitochondrial Ca^{2+}

A. Schematic of known mCa^{2+} sensitive proteins. Ca^{2+} ions are shown as red circles.

New horizons for mCa²⁺ uptake

From the discovery of mCa²⁺ uptake in the 1960s to the identification of Ca²⁺ sensitive proteins from the 1970s to early 2000s the identity of the mitochondrial calcium uniporter remained a mystery. Nevertheless, by early 2000s, mCa²⁺ quickly came back to the forefront of mitochondrial research with a particular emphasis on the identification of MCU and physiological conditions that resulted in mCa²⁺ uptake.

The first breakthrough was in 1992 when Rosario Rizzuto and Tullio Pozzan showed for the first time, that nM concentrations of cytosolic Ca²⁺ did not necessarily reflect the concentrations observed at the mitochondrial membranes³⁸. They coined the term “Ca²⁺-hotspots or Ca²⁺-microdomains,” as regions of Ca²⁺ within the cytosol where Ca²⁺ concentrations reached the levels required for mCa²⁺ uptake. While this term is debated today, the observation that the endoplasmic reticulum plays an important role in Ca²⁺ transfer to the mitochondria remains relevant today. In essence, they proposed that Ca²⁺ concentrations >1μM are present at mitochondria-ER contact sites (MERCs), enabling mCa²⁺ uptake in mitochondria that are juxtaposed with the ER. This discovery was made possible using the mitochondria-targeted aequorin which can report mCa²⁺ in live cells. In the same vein, modern studies utilize fluorescent mitochondria-targeted genetically encoded Ca²⁺ indicators (mGECI) and we used such a sensor for our studies (Chapter 3).

Another exciting breakthrough prior to the discovery of MCU was the biophysical analysis of mitoplasts by mitochondrial-patch clamp performed by Yuriy Kirichok in the lab of David Clapham in 2004³⁹. Until this point, it was debated whether MCU was a channel or a transporter and many related aspects of its activity such as ion selectivity and conductance were at best conjectural. This study established that MCU was an ion channel with a high selectivity and affinity (<2nM) for Ca²⁺. They demonstrated that MCU has an inwardly rectifying current (I_{MiCa}) that increases with Ca²⁺ concentrations in the bath, which for mitoplast recordings corresponds to cytosol (Figure 3A)³⁹. I_{MiCa} is ruthenium red

inhibitable with a current density of $\sim 55 \text{ pA pF}^{-1}$ at $100 \text{ }\mu\text{M}$ external Ca^{2+} . I_{MiCa} is highly selective for Ca^{2+} and the removal of Na^{+} from the extracellular bath had no effect on I_{MiCa} current in the presence of Ca^{2+} . However, MCU conducts related non-physiological divalents – with a relative selectivity sequence: $\text{Ca}^{2+} \approx \text{Sr}^{2+} \gg \text{Mn}^{2+} \approx \text{Ba}^{2+}$. Interestingly, no conductance of Mg^{2+} is observed (**Figure 3B**)³⁹. The characterization of I_{MiCa} by mitoplast electrophysiology remains the gold standard for studying the regulation of MCU today. However, this technique is extremely difficult to establish and even today, only a few labs across the world are capable of measuring I_{MiCa} from isolated mitoplasts.

The Mitochondrial Calcium Uniporter Complex

MCU

In 2011, Rosario Rizzuto and Vamsi Mootha co-discovered the molecular identity of MCU as a novel transmembrane protein, CCDC109A^{4,5}. This discovery was made possible by the identification of MICU1 by Vamsi Mootha in the previous year¹². Through a comparative proteomics analysis, MICU1 was shown to be an EF-hand containing protein required for mCa^{2+} uptake. With the identification of MICU1, Mootha et al performed a whole-genome phylogenetic profiling, genome-wide RNA co-expression and organelle-wide co-expression analysis to predict proteins functionally related to MICU1. Using this comparative genomic analysis, MCU was identified as a 40-kDa protein located within the mitochondrial inner membrane (**Figure 3C**). MCU has two coiled-coil domains and two transmembrane domains connected by a short loop. MCU subunits have been shown to oligomerize in the inner mitochondrial membrane to form the Ca^{2+} conduction channel. Human MCU has a conserved DIME motif (Asp-Ile-Met-Glu) at amino acid positions 261-264 which forms the channel entrance.

MCU resides in an oligomeric complex with the regulatory subunits MICU1, MICU2, MICU3, EMRE, and MCUB. EMRE with MCU are the minimal subunits necessary for mCa^{2+} uptake⁴⁰. MICU1^{12,41}, MICU2⁴²⁻⁴⁴, and MICU3^{42,45} are regulatory subunits that are involved in Ca^{2+} -dependent gating of MCU⁴⁶.

MICU1 and MICU2 are ubiquitously expressed whereas MICU3 is thought to be tissue-specific with the highest expression occurring in the brain. MCUB is a dominant negative subunit of MCU that impairs the ability of the MCU complex to promote mCa^{2+} uptake⁴⁷. The structure of human MCU was recently published and found to be a tetrameric holocomplex^{48,49}. Four MCU subunits with four EMRE constitute a functional channel associated with MICU1 and MICU2 in the intermembrane space (**Figure 3D**).

Orthologs of MCU can be found in metazoans and plants while fungi and protozoans lack evidence for mCa^{2+} uptake. The observation that cells can survive without MCU suggests that mitochondrial Ca^{2+} uptake is not a requirement for mitochondrial function or integrity. This raises the possibility that MCU plays a more adaptive role in mitochondrial physiology. In fact, our studies would argue that at least in macrophages, loss of MCU at baseline has little or no effect on mitochondrial physiology. Instead, MCU functions become more relevant when cells are responding to specific stimuli or insult – an adaptive role for some but not all cellular functions. In support of this idea, whole mitoplast patch clamp of mitochondria isolated from different tissues in mice display a wide range of I_{MiCa} current densities⁵⁰. In addition to a wide variance in MCU current densities, transcriptional analysis of the MCU complex components show considerable heterogeneity across tissues and cell-types. With such large differences in MCU activities, we speculate that MCU functions may be especially salient in some tissues. This may reveal a potential pharmacological means to manipulate specific physiological functions or interdict some pathologies.

Whole body knockout mice for *Mcu* (*Mcu*^{-/-}) were created by the Finkel lab in 2013⁵¹. *Mcu* deletion on a C57 background results in embryonic lethality. The heterozygous *Mcu*^{+/-} mice present mild phenotypes including a decrease in lean body mass, increased circulating HDL, increased fasting glucose, and increased total body fat. To generate homozygous *Mcu*^{-/-} mice, C57 heterozygotes were outbred onto a CD1 background. Surprisingly, some *Mcu*^{-/-} mice on this mixed

background were viable but born at non-Mendelian ratios⁵². Surprisingly, the surviving mice had normal basal metabolism with modest alterations in PDH activity within skeletal muscle. Together, this data suggests that despite the fact that MCU is highly conserved⁵³, *Mcu* deletion is well tolerated (or at least compensated) in the mixed background. It is now becoming increasingly clear that a major role for mitochondrial Ca^{2+} -signaling is tied to adaptive responses, which are masked in the unchallenging conditions of a mouse vivarium.

MICU1, MICU2, and MICU3

MICU1, MICU2, and MICU3 are homologs of the MICU family proteins with molecular weights between 45-55kDA. MICU1 and MICU2 were originally described as “gatekeepers” of the channel, blocking Ca^{2+} uptake at lower concentrations of cytosolic Ca^{2+} ^{43,54}. These initial studies suggested that MICU1 required cytosolic Ca^{2+} concentrations greater than ~500nM to allow MCU channel opening. However, recently this has been challenged by whole mitoplast patch clamp experiments. This new evidence suggests that MICU1 and MICU2 do not function as “gatekeepers,” but instead act to potentiate channel opening in the presence and absence of Ca^{2+} ⁴⁶. While precise mechanisms are still in dispute, it is universally accepted that MICU1-3 are important regulator of MCU.

The importance of MICU1 regulation of MCU was recently shown in a cohort of children with loss of function mutations in MICU1. These patients presented with proximal skeletal weakness, learning difficulty, and movement disorder⁵⁵. These human mutations recapitulate phenotypes observed in *Micu1*^{-/-} mice. Like *Mcu*^{-/-} mice, MICU1 mice are only semi-viable as homozygotes. Homozygotes who survive present with impaired locomotor behavior, decreased activity, and abnormal gait. Together, this data suggests that regulation of MCU is important for muscular function at baseline. In the case of MICU1 deletion, these symptoms are mediated by an increase in mitochondrial Ca^{2+} load and reduced cytoplasmic Ca^{2+} transience⁵⁵.

EMRE

EMRE is encoded by the gene *SMDT1* in the human genome. EMRE is a small ~10 kDa protein with a single transmembrane domain that is essential for channel activity in vertebrates⁴⁰. EMRE interacts with MCU through its transmembrane helices. Cells lacking EMRE have significantly impaired mCa²⁺ uptake and decreased MCU channel activity^{56,57}.

Like MICU1 and MCU, whole body knockout of EMRE results in premature lethality. *Smdt1*^{+/-} mice present with neurological pathologies including tremors, decreased locomotor activity and unresponsiveness to tactile stimulation.

MCUb

MCUb is a ~33kDa protein that shares ~50% identity with MCU. The key difference in MCUb is a modified amino acid sequence within the DIME motif located in the Ca²⁺ binding domain of MCU⁴⁷. MCU and MCUb have distinct transcriptional patterns across mammalian tissues which are thought to contribute to heterogeneity (~3:1, heart or lung to ~40:1, skeletal muscle) in mCa²⁺ uptake capacity⁵⁰. MCUb is the only complex component without embryonic lethality and in general, whole body knockout mice present with very mild phenotypes.

Figure 3: Characterization and Identification of MCU

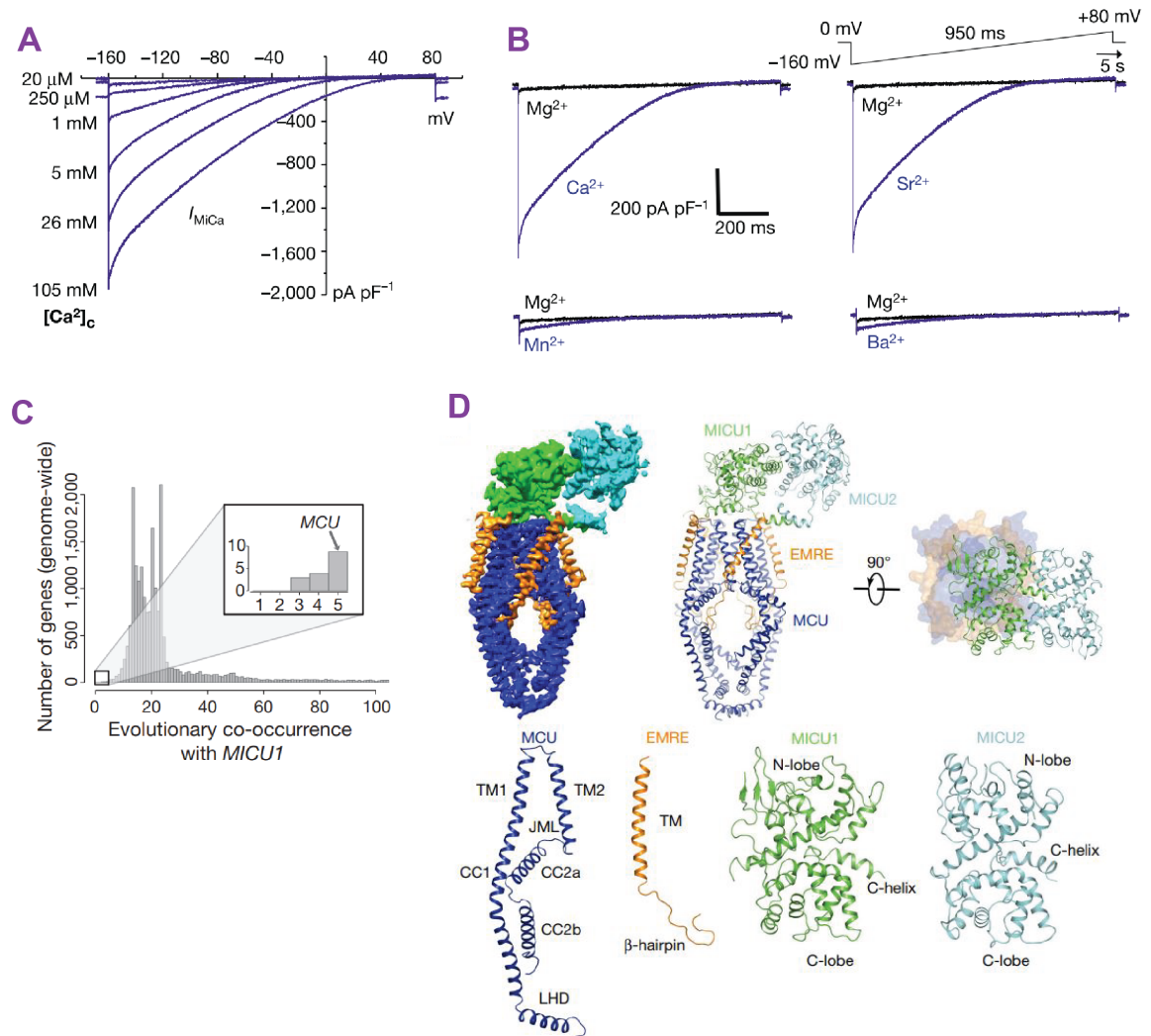


Figure 3: Characterization and Identification of MCU

A. Figure was taken from Kirichok, Krapivinsky and Clapham 2004³⁹. I_{MiCa} elicited by voltage ramps. Negative current flows from the cytoplasmic face of the inner mitochondrial membrane (bath) to the interior of the mitoplast. Bath = 0 mV. Inside mitoplast (pipette), Cs-gluconate solution; bath, HEPES-Tris solution.

B. Figure was taken from Kirichok, Krapivinsky and Clapham 2004³⁹. I_{MiCa} in 5 mM Ca^{2+} , Sr^{2+} , Mn^{2+} , Ba^{2+} (blue traces) or Mg^{2+} (black traces). Recordings are from the same mitoplast in HEPES-Tris-based solution, washed between applications with 1 mM EGTA/EDTA solution. Pipettes contained Na-gluconate solution.

C. Figure was taken from Baughman et al, 2011⁴. Phylogenetic RNA co-expression profile neighbors. Hamming distances between phylogenetic profiles were computed genome-wide for all 20,000 mammalian genes across 500 fully sequenced organisms. Genes co-expressed with *MICU1* were computed genome-wide by Pearson correlation using a mouse atlas of 81 tissues. Protein expression correlation with *MICU1* was analyzed for all mitochondrial proteins across 14 mouse tissues.

D. Figure was taken from Fan et al, 2020⁴⁸. Architecture of the uniporter. The cryo-EM map (left) and ribbon representation (middle) are viewed from the membrane. On the right, the uniporter (with MCU–EMRE shown as a surface representation and *MICU1*–*MICU2* as a ribbon) is viewed from the top. Lower structures show domain organization of MCU, EMRE, *MICU1* and *MICU2*. LHD, linker helix domain.

A new era for mitochondrial Ca^{2+} studies

Prior to the discovery of MCU, groups hypothesized physiological roles for MCU in a multitude of pathologies. These hypotheses have since been put to the test through genetic manipulation of *Mcu* and its regulatory subunits. For brevity, the major findings related to systems outside the immune system are summarized in **Table 1**. Additionally, human diseases linked to *MCU* genetics are summarized in **Table 2** (Garbincius and Elrod, 2022)⁵⁸.

Table 1: Animal models for uniporter proteins.

Reference	Model	Phenotype reported
Pan et al ⁵¹	<i>Mcu</i> gene trap mouse (<i>Mcu</i> -null)	Impaired PDH activity in skeletal muscle. No protection from cardiac I/R injury.
Holmstrom et al ⁵⁹	<i>Mcu</i> gene trap mouse (<i>Mcu</i> -null)	Normal Cardiac function at baseline and no change in models of pressure overload.
Luongo et al ⁶⁰ and Kwong et al ⁶¹	<i>Mcu</i> ^{fl/fl} – Cardiomyocyte Cre	Protection from I/R injury and impaired response to β -adrenergic stimulation.
Mammucari et al ⁶²	8-wk AAV-mediated MCU knockdown in skeletal muscle	Decreased fiber size and attenuated PGC-1 α 4 and IGF1-Akt/PKB signaling in skeletal muscle.
Kwong et al ⁶³	<i>Mcu</i> ^{fl/fl} – Skeletal muscle Cre	Impaired TCA cycle metabolism associated with impaired exercise physiology.
Flicker et al ⁶⁴	<i>Mcu</i> ^{fl/fl} – Brown adipose Cre	Little to no effect in cold tolerance, diet-induced obesity or cold responses.
Drago and Davis ⁶⁵	Drosophila RNAi-silencing of <i>MCU</i>	Developmental lethality and defects in adult memory.
Tufi et al ⁶⁶	<i>Mcu</i> deletion in whole drosophila	Impaired lifespan and oxygen consumption.
Liu et al ⁶⁷	Constitutive deletion of <i>Emre</i> (<i>Emre</i> -null)	Born at non-Mendelian ratios and are smaller in size. No protection from I/R injury.
Antony et al ⁶⁸	Constitutive deletion of <i>Micu1</i> (<i>Micu1</i> -null)	Perinatal lethality with signs of impaired neuronal development. Some defects in respiration.
Debattisti et al ⁶⁹	<i>Micu1</i> ^{fl/fl} – Skeletal muscle Cre	Muscle weakness and wasting.
Bick et al ⁷⁰	Constitutive deletion of <i>Micu2</i> (<i>Micu2</i> -null)	Little baseline phenotype. Cardiac phenotypes.
Puente et al ⁷¹	Constitutive deletion of <i>Micu3</i> (<i>Micu3</i> -null)	Protection from isoproterenol induced overload.
Huo et al ⁷²	Constitutive deletion of <i>McuB</i> (<i>McuB</i> -null)	No observed phenotype in cardiac function.

Table 2: Human disease associations of MCU components

Reference	Genetic Defect	Phenotype reported
Logan et al ⁵⁵	LoF <i>MICU1</i>	Proximal myopathy, learning defects, and progressive extrapyramidal movement disorder
Lewis-Smith et al ⁷³	Homozygous, 2755-bp deletion in <i>MICU1</i>	Childhood lethargy, fatigue, and muscle weakness
O'Grady et al ⁷⁴	LoF <i>MICU1</i>	Congenital muscular dystrophy
Musa et al ⁷⁵	Homozygous c.553C>T (p.Q185*) in <i>MICU1</i> (predict LoF)	Muscle weakness, fatigue; some cases with learning disability, nystagmus, and cataracts
Mojbafan et al ⁷⁶	C1295delA mutation in <i>MICU1</i> – frameshift mutation	Myopathy with extrapyramidal signs
Wilton et al ⁷⁷	c.161 + 1G>A (splice mutation) and c.386G>C (missense mutation) in <i>MICU1</i>	Myopathy with extrapyramidal signs with acute encephalopathy and abnormalities in brain development.
Shamseldin et al ⁷⁸	Homozygous c.42G>A:P.W14* mutation in <i>MICU2</i> (early stop mutation)	Severe cognitive impairment with associated neurodevelopmental disorder.

Focus: MCU in innate immunity

The field of mCa²⁺ was revolutionized by the identification of MCU and its regulatory subunits. The main conclusion from early studies was that whole body deletion of MCU was insufficient in the identification of specific roles for mCa²⁺ uptake. The modest phenotypes displayed by global deletion of MCU is most likely confounded by compensatory processes during embryogenesis. When I started this thesis, conditional deletion of *Mcu* using tissue specific Cre recombinases was in still in its infancy. Early studies using siRNA knockdown of *Mcu* were beginning to reveal a role for MCU in the immune system but were not definitive. As a lab with expertise in ion channel biophysics and innate immunity, we were perfectly suited to examine the role of MCU in innate immunity and provide clarity on this topic. By studying the impact of *Mcu* deletion in various functions of macrophages, we were able to firmly establish that MCU is not required for house-keeping functions but there is a salient role for mitochondrial Ca²⁺ uptake in very specific aspects of innate immunity and inflammation. The responsive nature of mCa²⁺ makes MCU an ideal target for rapid regulation of biological processes related to mitochondrial physiology. We focused our studies on innate immunity due to the salience of MCU in immunological responses. The innate immune system is mobile, responsive, adaptive, and ubiquitous throughout the body. It is the perfect environment to reveal unique roles for mCa²⁺ across many organ systems. Furthermore, “mitochondrial immunity” and immunometabolism are at the forefront of innate immune responses, the connections seem obvious in hindsight, but when I was starting my research project, there were considerable uncertainties and my project was deemed risky, or even futile, by a certain resistance in the research community that mitochondrial Ca²⁺ uptake was not essential for cellular physiology.

Mitochondria are central to innate immunity

Mitochondria are not simply the powerhouse of the cell. Mitochondria serve as a signaling hub for cellular metabolism, transcription, and immune

signaling. As of now it has been shown that: (1) TCA cycle intermediates are involved in processes of inflammation, (2) mitochondrial DNA promotes gene transcription through the activation of transcription factors and (3) the mitochondrial membrane serves as a platform for innate immune receptors responding to pathogen components. These multifaceted roles of mitochondria have revealed that mitochondria are at the heart of the cell-intrinsic defense mechanisms.

Mitochondrial metabolites in innate immunity

Succinate accumulates in inflammatory macrophages, and it can be oxidized by succinate dehydrogenase (SDH), otherwise known as complex II of the ETC. Succinate oxidation by SDH is thought to be a major contributor to the generation of mitochondrial reactive oxygen species (ROS). In immune cells, this process has been shown to activate the transcription factor HIF-1 α driving transcription on IL-1 β ⁷⁹. What is often overlooked from this analysis is the time course of IL-1 β activation. In fact, this supposedly seminal discovery that succinate promotes IL-1 β transcription through the activation of HIF-1 α was observed after 48 hours of LPS stimulation (Figure 1 from Mills et al.)⁷⁹. While this may be important for low-grade chronic inflammation, the feeble rate of this transcriptional response does not explain the rapid inflammatory response required to defend against pathogens.

Citrate is emerging as a very important metabolite for innate immunity. Citrate synthase converts Acetyl-CoA (generated by PDH) into citrate. Citrate is a versatile metabolite with multiple end points. It can: (1) stay in the TCA cycle and facilitate ATP generation through the ETC, (2) become a building block for fatty acid synthesis, or (3) be shunted into amino acid pathways for the generation of nitric oxide (NO) and ROS. All three of these possibilities have important functions in innate immune response. It is hypothesized that as a major precursor for fatty acid synthesis, citrate is essential for membrane biogenesis and antigen presentation in dendritic cells⁸⁰. In macrophages, it has been shown to promote the production of NO, ROS and prostaglandins during lipopolysaccharide (LPS)

stimulation^{81,82}. Most recently, it has been implicated in bacterial killing through its conversion to itaconate by the interferon responsive gene 1 (IRG1)⁸³⁻⁸⁵. However, as we saw with succinate, these conclusions overlook many important details. The consensus model is that in response to LPS, the mitochondrial citrate carrier (CIC) is upregulated by NFκB transcription, incorporated into mitochondria and used to shunt citrate for immunological purposes^{81,82}. Again, the time it would take for this process to mount an effective immune response is not especially inspiring. These significant shortcomings in the prevailing model inspired us to re-evaluate how mitochondria might serve a more immediate immunometabolic function in cell-intrinsic immunity. We reasoned simply that a rapid flux of Ca^{2+} into the mitochondria during pathogen recognition could shift the gears of metabolic machinery to fight the infection more efficiently. As is often the case, we stumbled on findings that not only substantiated this simple concept but flung open doors to an entirely new facet of immunometabolism.

MCU as a central regulator of innate immunity

As we have discussed, mCa^{2+} uptake and MCU are important regulators of TCA cycle metabolism. With the growing focus on TCA cycle metabolites in innate immune response, it seemed likely that mCa^{2+} uptake could provide an essential signal for mitochondria during host defense. This was the framework of our initial foray into MCU and innate immunity.

Chapter Two: Reduced Mitochondrial Calcium Uptake in Macrophages is a Major Driver of Age-related Inflammation

Authors:

Philip V. Seegren^{1, 2}, Logan R. Harper¹, Taylor K. Downs^{1, 2}, Xiao-Yu Zhao^{2, 3}, Shivapriya B. Viswanathan¹, Marta E. Stremaska^{2, 3}, Rachel J. Olson¹, Joel Kennedy¹, Sarah E. Ewald^{2, 3}, Pankaj Kumar^{4, 6}, Bimal N. Desai^{1, 2, 5*}

Affiliations:

¹Pharmacology Department, University of Virginia School of Medicine, Pinn Hall, 1340 Jefferson Park Avenue, Charlottesville, VA 22908

²Carter Immunology Center, University of Virginia School of Medicine, 345 Crispell Dr. MR-6, Charlottesville, VA 22908

³Microbiology, Immunology, and Cancer Biology Department, University of Virginia School of Medicine, Pinn Hall, 1340 Jefferson Park Avenue, Charlottesville, VA 22908

⁴Biochemistry and Molecular Genetics Department, University of Virginia School of Medicine, Pinn Hall, 1340 Jefferson Park Avenue, Charlottesville, VA 22908

⁵University of Virginia Cardiovascular Research Center, 415 Lane Rd, Charlottesville, VA 22908

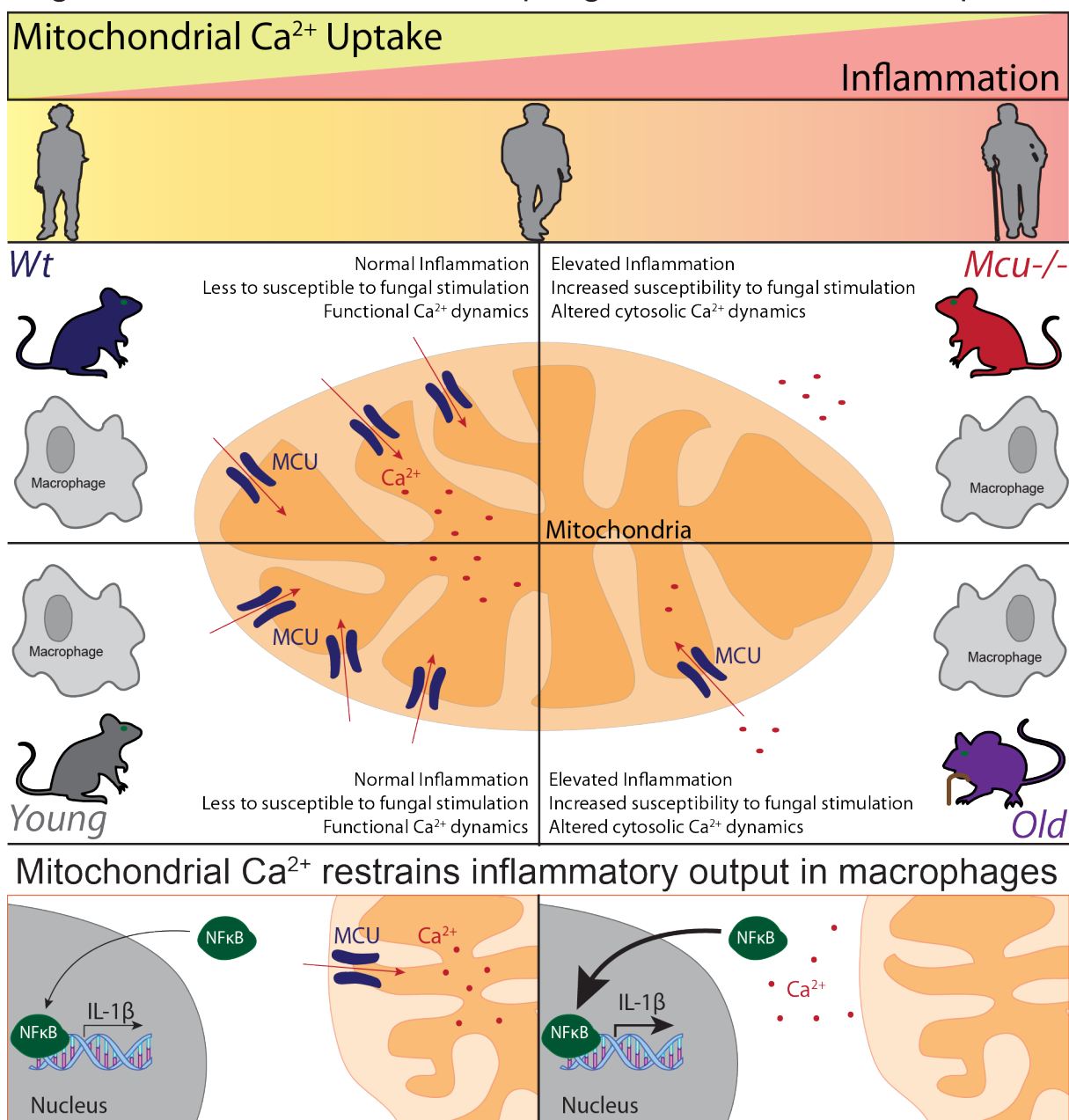
⁶University of Virginia, Bioinformatics Core, 1312A Pinn Hall, 1340 Jefferson Park Avenue, Charlottesville, VA 22908

*Correspondence and Lead Contact: bdesai@virginia.edu

Note

The contents of this chapter appear as submitted to Nature Aging. 2022.

Graphical Abstract

Age-related decrease in macrophage mitochondrial Ca^{2+} uptake

Abstract

Chronic low-grade inflammation is a hallmark of aging, but its etiology is not well understood⁸⁶⁻⁹¹. Mitochondrial dysfunction has been linked to both cellular senescence and age-related inflammation or *inflammaging* but fundamental mechanisms underlying these links are unclear^{92,93}. We analyzed age-related gene expression in different human tissues and discovered that in blood, the mRNA expression of Mitochondrial Calcium Uniporter (*MCU*) and its regulatory subunit *MICU1* correlated inversely with age. MCU is the pore-forming subunit of a Ca^{2+} -selective ion channel complex residing in the mitochondrial inner membrane and is the main conduit for Ca^{2+} -influx into the mitochondrial matrix^{4,5,39,40,94-96}. Based on these findings we tested the simple hypothesis that mitochondrial Ca^{2+} uptake capacity of macrophages decreases with age, and this is an important driver of chronic low-grade inflammation. We found a significant reduction in the mitochondrial Ca^{2+} -uptake capacity of macrophages derived from aged (80-90 weeks) mice. These macrophages display amplified cytosolic Ca^{2+} elevations and increased inflammatory output. To test the salience of mitochondrial calcium uptake in this process, we deleted *Mcu* selectively in macrophages. The *Mcu*^{-/-} macrophages of young mice (<25 weeks) express more inflammatory genes at baseline and show a hyper-inflammatory response when stimulated. Reduced mitochondrial Ca^{2+} disrupts cytosolic Ca^{2+} dynamics and potentiates downstream NF κ B activation, which is central to inflammation⁹⁷⁻¹⁰⁰. The regulation of inflammatory response by mitochondrial Ca^{2+} uptake is also seen readily in human macrophages. Our findings pinpoint the MCU complex as a keystone molecular apparatus that links age-related changes in mitochondrial physiology to macrophage-mediated inflammation. Resident macrophages are intrinsic to every organ system and the steady erosion of their mitochondrial Ca^{2+} -uptake capacity may play a germinal or exacerbating role in many age-related neurodegenerative, cardiometabolic, renal and musculoskeletal diseases that afflict us.

Introduction

The ever-increasing burden of age-related diseases is a challenge to public health systems around the world. Aging is a highly complex multifactorial process that can be best understood by identifying the key drivers and defining their molecular mechanisms in terms of simple clear concepts. Inflammation is widely recognized as a key driver of aging. A low-grade, chronic inflammatory state promotes aging-associated tissue damage and hence this process is referred to as *inflammaging*^{86-91,101,102}. The etiology of inflammaging is not well understood but it is thought that a steady accumulation of sterile and non-sterile stimuli increases the baseline inflammatory output by immune cells, as evident from higher cytokine levels and other inflammatory markers in the blood of aged humans¹⁰³⁻¹⁰⁶. The inflammatory stimuli can originate from multiple sources: pathogens, resident microbiomes, tissue damage associated inflammatory signals, and even spontaneous production of inflammatory molecules by senescent cells¹⁰⁷⁻¹⁰⁹. Myeloid cells of the immune system, such as macrophages and neutrophils, are central players in inflammation and tissue homeostasis. Macrophages reside in every organ system and act as sentinel cells monitoring their environment for infection or injury^{89,110,111}. Through numerous receptors, macrophages can detect a wide spectrum of pathogen-associated molecular patterns (PAMPs) or tissue damage-associated molecular patterns (DAMPs). After detecting such alarming signals, they secrete a wide range of inflammatory mediators to initiate or amplify tissue inflammation.

The inflammatory gene expression in macrophages is a highly regulated process with multiple checkpoints. Dysregulation in this process can have a profound effect on the inflammatory tone of the overall physiology. NFκB, a family of dimeric transcription factors, have an evolutionarily conserved and central role in inflammatory gene expression^{98,100}. NFκB is activated by numerous upstream receptors and orchestrates the gene expression of a large subset of inflammatory genes. Many studies have pointed to the salience of NFκB to inflammaging¹¹²⁻¹¹⁵. Notably, analysis of age-related changes in gene

expression in human and mouse tissues identified the NF κ B pathway as the most strongly associated transcriptional pathway to aging¹¹². The secretion of high levels of pro-inflammatory cytokines in two different mouse models of accelerated aging was also found to be dependent on abnormal NF κ B activation¹¹⁴. These studies suggest that a lowered threshold of NF κ B activation underlies inflammaging, but how this transpires is not understood. Many positive and negative signaling elements control the post-translational modifications and nuclear translocation of NF κ B⁹⁸. Among these regulatory checkpoints, the nuclear translocation and transcriptional activity of NF κ B is also controlled by cytosolic Ca²⁺-signaling^{16,17}. The amplitude, frequency, and duration of cytosolic Ca²⁺ oscillations have a profound impact on NF κ B-mediated gene transcription.

Ca²⁺ is a ubiquitous and essential second messenger in cell biology¹³. Cells expend a significant amount of energy to maintain a ~20,000-fold gradient between the extracellular and intracellular Ca²⁺ concentrations. At resting membrane potential, the enormous driving force for the influx of Ca²⁺ into the cytosol can be harnessed for rapid signaling in less than a second. Elevations in cytosolic Ca²⁺ trigger an influx of Ca²⁺ into the mitochondrial matrix through the Mitochondrial Calcium Uniporter (MCU), a Ca²⁺-selective ion channel that resides in the mitochondrial inner membrane (MIM)^{4,5,39,94}. The mitochondrial outer membrane (MOM) is porous to ions, but the inner membrane has a resting membrane potential between -160 mV and -200 mV, relative to the cytosol^{39,116}. MICU1^{12,41} and MICU2⁴², the EF-hand containing, Ca²⁺-sensitive regulatory subunits of MCU, interact directly with MCU in the intermembrane space. Structural studies support the view that MCU-MICU1-MICU2 interactions are configured to have a switch-like sensitivity to [Ca²⁺], enabling rapid mitochondrial Ca²⁺ (mCa²⁺) uptake when cytosolic [Ca²⁺] increases beyond the resting range ~10-100 nM^{48,49,117,118}. Since mitochondrial matrix contains many metabolic enzymes that are Ca²⁺-regulated, the mCa²⁺-signaling within the matrix has a profound effect on mitochondrial physiology and metabolism^{95,119,120}. The cells of the vertebrate immune system use Ca²⁺-signaling for an immediate-early

response to antigenic and inflammatory stimuli – cytosolic Ca^{2+} elevations regulate the activation of both the innate and adaptive immune cells¹²¹. Recently, we revealed that mCa^{2+} -signaling functions as an electrometabolic switch to fuel macrophage-mediated phagosomal killing¹²². The process involves a fast two-step Ca^{2+} -relay to meet the bioenergetic demands of phagosomal killing. Upon detection of a fungal pathogen, macrophages elevate cytosolic Ca^{2+} (phase 1) and this triggers a rapid influx of Ca^{2+} into the mitochondria (phase 2). mCa^{2+} is emerging as a central node for innate immunity and inflammatory responses. Recent reports have supported a role for MCU and mCa^{2+} in macrophage polarization^{123,124}, host defense^{122,125} and tissue homeostasis¹²⁶⁻¹²⁸. Here we report a surprising discovery that mitochondrial Ca^{2+} -uptake capacity of macrophages decreases progressively with age, and this is a major driver of inflammaging. The reduction in mCa^{2+} -uptake increases the frequency and amplitude of cytosolic Ca^{2+} -oscillations in macrophages. This greatly promotes NF κ B-mediated inflammatory response and renders the macrophages prone to chronic low-grade inflammatory output at baseline and hyper-inflammatory when stimulated.

Results

Gene expression analysis of human blood reveals clear signs of chronic age-associated low-grade inflammation.

To gain insights into inflammaging, we mined the publicly available Genotype-Tissue Expression (GTEx) database (gtexportal.org)¹²⁹ for tissue-specific gene expression across five different human age groups (**Figure 4a**). Since mature Red Blood Cells (RBCs) are anucleated and do not contain any appreciable amounts of mRNA, RNAseq of whole blood is a reasonable surrogate of combined gene expression in the white blood cells and platelets. Expression profile data were obtained for different tissues, binned into age groups and then subjected to differential gene expression analysis using DESeq2 R package. Principle Component Analysis (PCA) plots, from the five different age

groups, revealed clear age-associated clustering (**Figure 4b**). The variance in overall gene expression was greatest when we compared the youngest population (age 20-29) with the oldest population (age 60-69) (**Figure 4c**), but the least when we compared the second-oldest population (age 50-59) to the oldest (age 60-69) (**Figure 5a**). Although unsurprising, these data nicely confirm that gene expression in the blood changes significantly with age. To derive further insights and to distill testable hypotheses for the etiology of inflammaging, we focused our analysis on differences between the youngest (age 20-29) and oldest (age 60-69) samples. GSEA hallmark and GO pathway analyses of differentially expressed genes showed that the genes associated with inflammatory responses were upregulated in the older population (**Figure 4d**, **Figure 5b**). Additionally, we observed a significant decrease in the gene expression related to oxidative phosphorylation, a mitochondrial process, in the older populations. Enrichment scores and gene ranks of inflammatory genes (**Figure 4e – Figure 4g**) and oxidative phosphorylation associated genes (**Figure 4h**) suggest a significant dysregulation in these pathways in the aged population. As shown in the heat map (**Figure 4i**), genes associated with TNF α -NF κ B pathway are upregulated in the blood cells of older humans. Overall, these gene expression analyses show clear signs of age-associated chronic low-grade inflammation in the whole blood of human samples.

Figure 4: Gene expression analysis of human blood reveals clear signs of chronic age-associated inflammation.

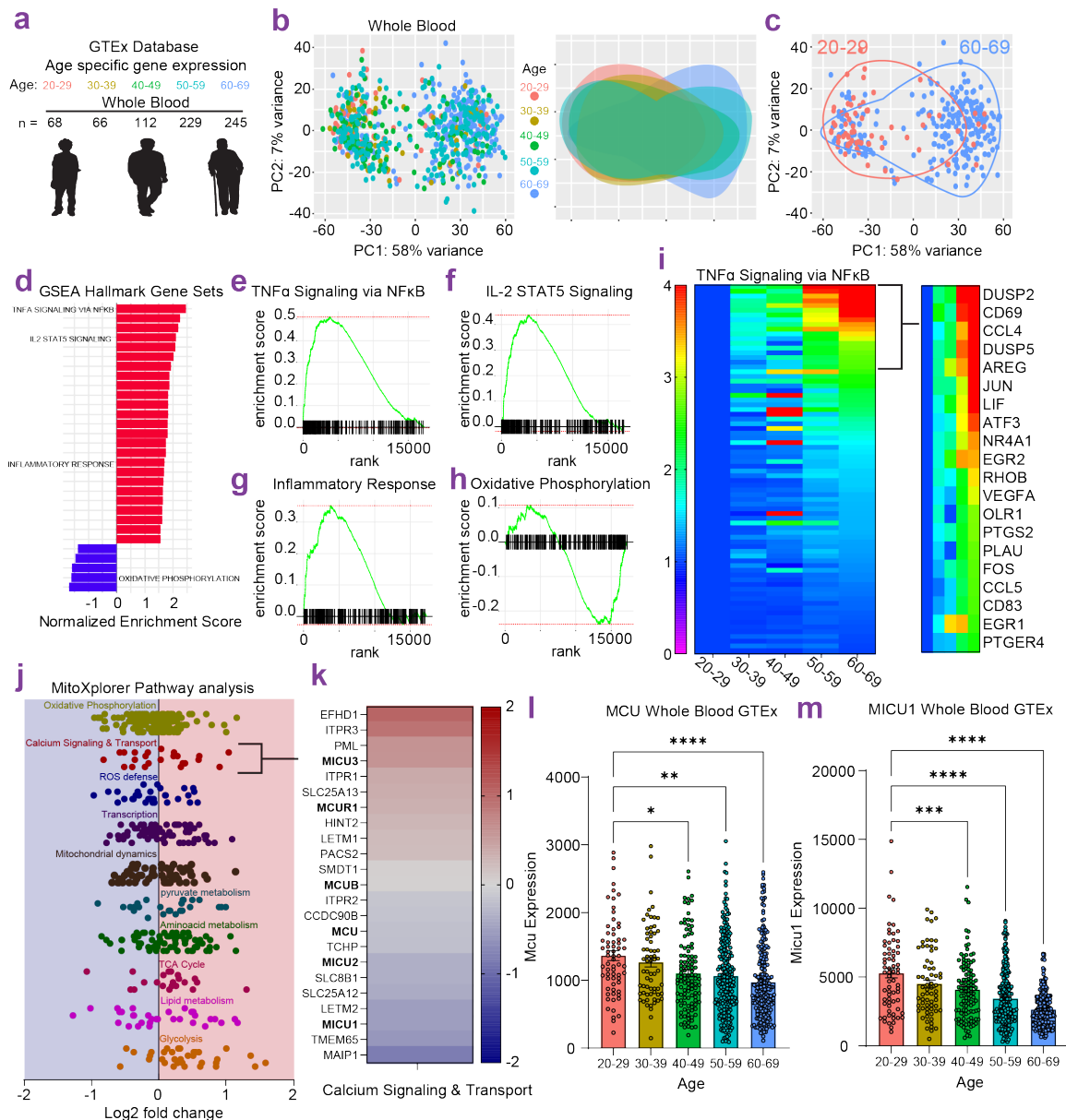


Figure 4: Gene expression analysis of human blood reveals clear signs of chronic age-associated inflammation.

- a. GTEx database mined for tissue-specific gene expression across five indicated age groups – note the color coding for the age groups.
- b. Principal Component Analysis of whole blood gene expression from every sample, color-coded according to the age groups. *Right panel* shows the same data by overlaying the color-coded clusters from each age group. Note the variance in gene-expression from different age groups.
- c. The PCA plots from panel b were used to show only samples from the youngest and oldest age groups analyzed.
- d. GSEA hallmark gene set enrichment analysis based on differential gene expression between the oldest (60-69) and youngest (20-29) data sets. Pathways are ranked by *p-value* and plotted on x-axis by the normalized enrichment scores (NES).
- e. Gene set enrichment analysis of GSEA hallmark pathway, TNF α Signaling via NF κ B, based on differential gene expression of oldest (60-69y) versus youngest (20-29y) GTEx samples. Enrichment scores (ES) are plotted on y-axis and genes ranked in the ordered dataset are plotted in x-axis.
- f. Gene set enrichment analysis of IL2-STAT5 GSEA hallmark pathway
- g. Gene set enrichment analysis of Inflammatory Response GSEA hallmark pathway
- h. Gene set enrichment analysis of Oxidative Phosphorylation GSEA hallmark pathway
- i. Heat map of expression levels of genes associated with TNF α -NF κ B pathway. Expression values were calculated as a fold change from the 20-29 age group.
- j. MitoXplorer Pathway analysis based on DSeq2 analysis of oldest (60-69y) versus youngest (20-29y) GTEx samples.
- k. Individual genes in the Calcium Signaling & Transport pathway identified from MitoXplorer Pathway Analysis based on DSeq2 analysis of oldest (60-69y) vs

youngest (20-29y) GTEx samples. Fold change was determined as a relative change in 60-69y compared to 20-29y GTEX samples.

l. *MCU* gene counts for each sample in GTEx database sorted by age.

m. *MICU1* gene counts for each sample in GTEx database sorted by age.

In human blood, expression of genes involved in mitochondrial Ca^{2+} uptake correlates inversely with age

Both inflammation and mitochondrial dysfunction are hallmarks of aging⁸⁸ and we wondered if there was a relationship pertinent to inflammaging. For the analysis of age-related changes in mitochondrial function, we used MitoXplorer, an analysis and visualization tool specialized for genes associated with mitochondrial functions (Mito-genes)¹³⁰. In accord with previous observations, we saw significant age-related changes in the expression of Mito-genes (**Figure 5c – Figure 5f**). We noted a decrease in the Mito-genes associated with oxidative phosphorylation, calcium signaling and ROS production (**Figure 4j**). The Mito-genes associated with mitochondrial transcription, mitochondrial dynamics, pyruvate metabolism, amino acid metabolism and lipid metabolism were not different. The TCA cycle and glycolysis genes were expressed at higher levels in the aged population. Since Ca^{2+} -signaling has a direct impact on inflammatory signaling in immune cells, we took a deeper look at these genes and were struck by the decreased expression *MCU*, *MICU1* and *MICU2* (**Figure 4k**). Moreover, the decrease in *MCU* and *MICU1* expression was strongly associated with age, decreasing progressively as humans age (**Figure 4l – Figure 4m**). These observations suggested an age-associated dysregulation in mCa^{2+} uptake in the blood-borne immune cells. Interestingly, this transcriptional dysregulation of *Mcu* and its subunits was only observed in *Mcu*, *Micu1*, *Micu2*, and *Emre* while the dominant negative regulation *McuB* showed no significant change with age (**Figure 4l – Figure 4m, Figure 5g**). We wondered if such age-related decrease in *MCU* is found in all human tissues. We checked the *MCU* gene expression in different tissues in the age-stratified GTEx data we had mined and found that the age-associated decrease was only seen in a few tissues – heart, whole blood, and cerebellum (**Figure 6a**). A vast majority of tissues did not show decreased *MCU* expression and some tissues. Skeletal muscle, adipose tissue and thyroid showed the opposite trend – the *MCU* expression in these tissues increased with age. Patients' death parameters are reported in the GTEx database on a Hardy-

Scale. To ensure the observed dysregulation of Mcu cannot be attributed to a specific method of death we assessed Mcu expression across the reported Hardy-Scale and saw no discernable trends in Mcu expression (**Figure 6b**). Furthermore, when we control for the most abundant death parameter (death 0, ventilator death), we still observed an age-dependent decrease in Mcu derived from the whole-blood of these patients (**Figure 6c**). Together, these results show that mitochondrial Ca^{2+} -uptake capacity changes with age in many tissues and likely contributes to age-related changes in the physiology of these tissues. But from the standpoint of age-associated inflammation, the analyses put a spotlight on the key finding that in the blood, expression of *MCU* and *MICU1* decreased progressively with age. We developed this novel insight to investigate the role of mitochondrial Ca^{2+} uptake in age-related inflammation.

Figure 5: In human blood, expression of genes involved in mitochondrial Ca^{2+} uptake correlates inversely with age.

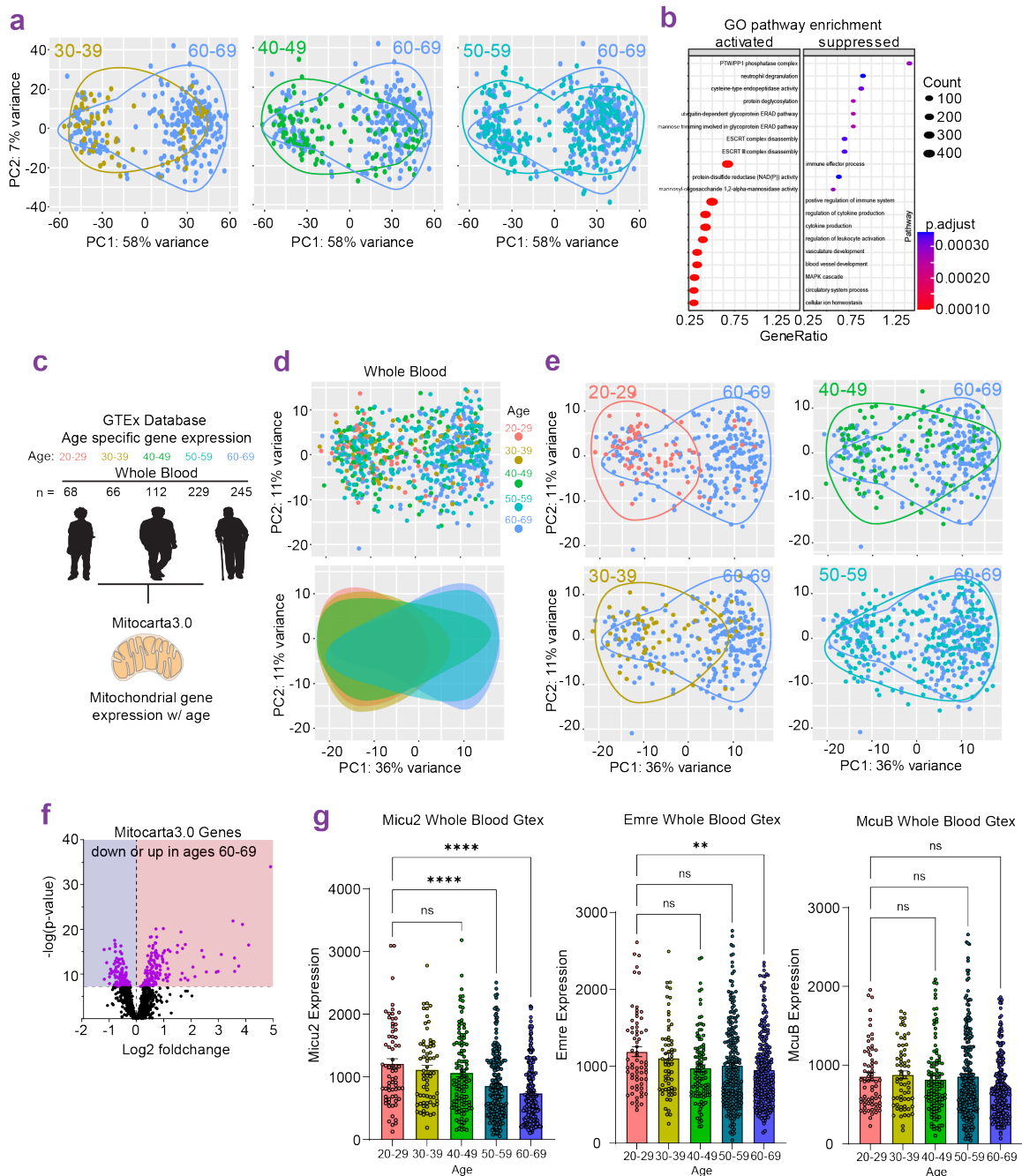


Figure 5: In human blood, expression of genes involved in mitochondrial Ca^{2+} uptake correlates inversely with age.

- a.** Variance in gene expression in whole blood of different age groups based on Principal Component analysis on GTEx samples.
- b.** GO pathway enrichment analysis based on DSeq2 from GTEx samples. Differential gene expression is plotted for ages 60-69 vs 20-29.
- c.** Pipeline used for the analysis of genes encoding for mitochondria-localized proteins (Mito-genes).
- d.** Principal component analysis on Mito-genes from GTEx samples. Variance in gene expression is shown for individual age groups.
- e.** Variance in gene expression shown for age 20-29 vs 60-69, 30-39 vs 60-69, 40-49 vs 60-69, and 50-59 vs 60-69.
- f.** Volcano plot of Mito-genes expression levels in old (60-69y) vs young (20-29y) samples.
- g.** *MICU2*, *EMRE*, and *MCUB* gene reads for each sample in GTEx database sorted by age.

Figure 6: Age related changes in Mcu expression across GTEx tissue and patient death parameters.

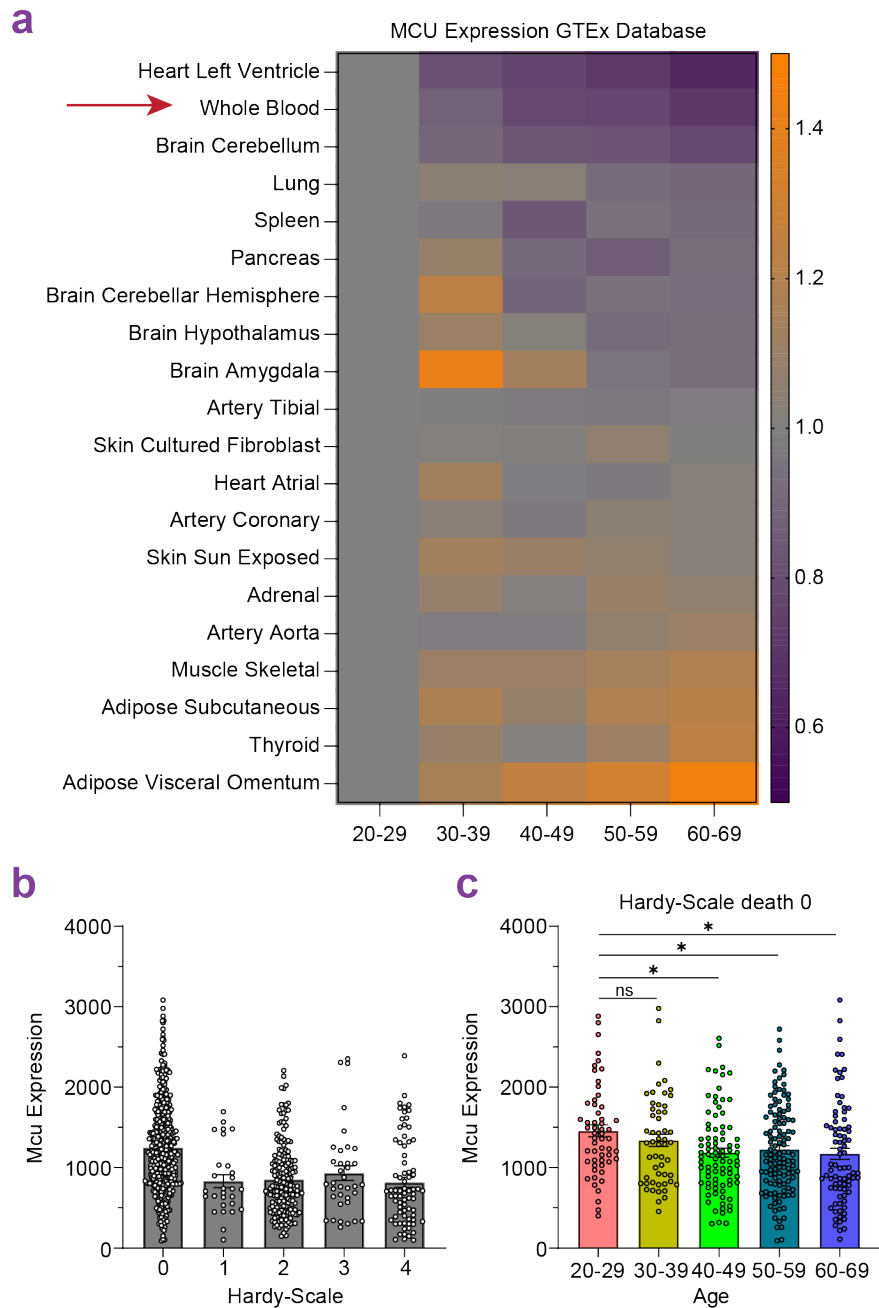


Figure 6: Age related changes in *Mcu* expression across GTEx tissue and patient death parameters.

- a.** Heat map for fold change gene reads of *MCU* across different tissues.
- b.** *MCU* gene reads for each sample in GTEx database sorted by 4-point Hardy-Scale.
- c.** *MCU* gene reads for each sample in GTEx database sorted by age for all death circumstance 0 on 4-point Hardy-Scale.

Macrophage derived from older mice exhibit a marked reduction in mitochondrial Ca²⁺ uptake.

The most abundant cell types in the human blood are myeloid cells – composed mainly of neutrophils and monocytes. Both these cells are short-lived in the blood but play a crucial role in inflammation. We reasoned that monocytes are more important for chronic-low grade inflammation because they can differentiate into macrophages and dendritic cells, and thereby sustain low-grade inflammation and inflammatory cascades over a relatively long period of time. Furthermore, all tissues and organs contain specialized resident-macrophages which are central to local inflammation and homeostasis. We also knew that mitochondrial Ca²⁺-uptake plays an important role in macrophage-mediated phagocytosis¹²², but we were extremely surprised to find that *MCU* expression decreases in immune cells with age. Considering all these aspects, we focused our investigative spotlight on how mCa²⁺ signaling might affect macrophage-mediated inflammation. First, we confirmed that age-associated decrease in *Mcu* expression was recapitulated in murine macrophages (**Figure 7a**). Importantly, this expression deficit results in decreased observable Mcu protein in murine macrophages as well (**Figure 8a**). We wondered if this transcriptional defect was a result of macrophage differentiation *ex vivo* or intrinsic to immune cells found within older mice. To test this, we measured *Mcu* and its regulatory subunits expression in undifferentiated bone-marrow cells (BMCs), peripheral blood mononuclear cells (PBMCs) and bone marrow derived macrophages (BMDMs) isolated from young (15-25-weeks) and old (80-90-weeks) mice (**Figure 8b**). PBMCs only showed a modest reduction in *Mcu* and *McuB* and may suggest lymphoid cells (the predominate cell type in murine PBMCs) do not harbor this aging defect (**Figure 8b**). Decreased *Mcu* expression was the most consistently observed defect as measure by two different primer sets targeting the *Mcu* mRNA sequence in BMCs and BMDMs, suggesting the decrease in *Mcu* expression is intrinsic to macrophage progenitors prior to their differentiation (**Figure 8b**). While the defect in BMCs suggests further studies to reveal a role of

Mcu in myeloid progenitors we focused our analysis on macrophages because mouse bone marrow derived macrophages (BMDMs) are the mainstay primary cells to study fundamental aspects of macrophage biology. Following transcriptional and protein analysis, we tested the most obvious hypothesis that macrophages exhibit an age-dependent decrease in their mitochondrial Ca^{2+} (mCa^{2+}) uptake. The basic technical design of this relatively uncommon assay is to add Ca^{2+} to permeabilized macrophages, and as the mitochondria take up the added Ca^{2+} , its loss from the bath solution is reported by the reduction in the fluorescence of calcium green-5N (CG-5N), a small molecule Ca^{2+} -indicator in the bath solution. When Ca^{2+} is first added to the solution containing permeabilized macrophages, we see a sharp increase in the CG-5N fluorescence and then it decays according to the rate at which Ca^{2+} is taken up by the mitochondria (and lost from the bath). We show that BMDMs from the young mice (BMDMS-Y) exhibit robust mCa^{2+} -uptake, but this process is significantly impaired in the BMDMs derived from the old mice (BMDMS-O). The representative traces are shown (**Figure 7b**) and a quantification of the percentage of the added Ca^{2+} taken up by the mitochondria is shown in **Figure 7c**. The addition of the mitochondrial uncoupler FCCP stops the Ca^{2+} uptake and even reverses it (**Figure 7b**), indicating that the mCa^{2+} uptake is driven by the membrane potential of the mitochondrial inner membrane. Similarly, Ruthenium Red (10 μM), a known blocker of MCU^{39,116}, abrogates mCa^{2+} uptake, showing that the process is largely dependent on MCU. This age-associated reduction in mCa^{2+} uptake was found in both females and males (**Figure 7d**). Interestingly, in the BMDMS-O we observed an additional impairment in Ca^{2+} retention as indicated by the release of Ca^{2+} from the mitochondria prior to the addition of FCCP. Using the same assay, we tested the retention capacity by performing a Ca^{2+} pulse assay. In this experiment we pulse a much lower dose of Ca^{2+} (1 μM , compared to 15 μM previously) and test the capacity of *Mcu* to continually buffer Ca^{2+} . In these experiments BMDMS-O were capable of mCa^{2+} uptake for the first two pulses but began to lag behind BMDMS-Y after the third pulse (**Figure 8c**).

With the lower concentration of Ca^{2+} pulses the BMDMS-O didn't show the impaired Ca^{2+} retention suggesting this is a secondary defect observed with higher concentration Ca^{2+} pulse. To assess additional defects in mitochondrial function of BMDMS-O we measured mitochondrial membrane potential (MMP) with TMRM and observed a modest impairment of MMP in BMDMS-O at baseline and following zymosan stimulation (**Figure 8d**). Furthermore, we carried out confocal microscopy of BMDMs stained for TOM20 and then applied an automated image processing software to quantify mitochondrial numbers and morphology across dozens of confocal images¹³¹. Comparing hundreds of BMDMs-Y and BMDMs-O in this manner, we found a modest reduction in mitochondrial numbers and no significant differences in mitochondrial area, roundness, and branches (**Figure 9a – Figure 9e**). These results argue that the age-related reduction in mCa^{2+} -uptake is a result of factors other than mitochondrial numbers and morphology and is more likely tied to the stoichiometric changes in the composition of the MCU complex itself.

Figure 7: Aged macrophages exhibit reduction in mCa²⁺ uptake and signs of cellular senescence.

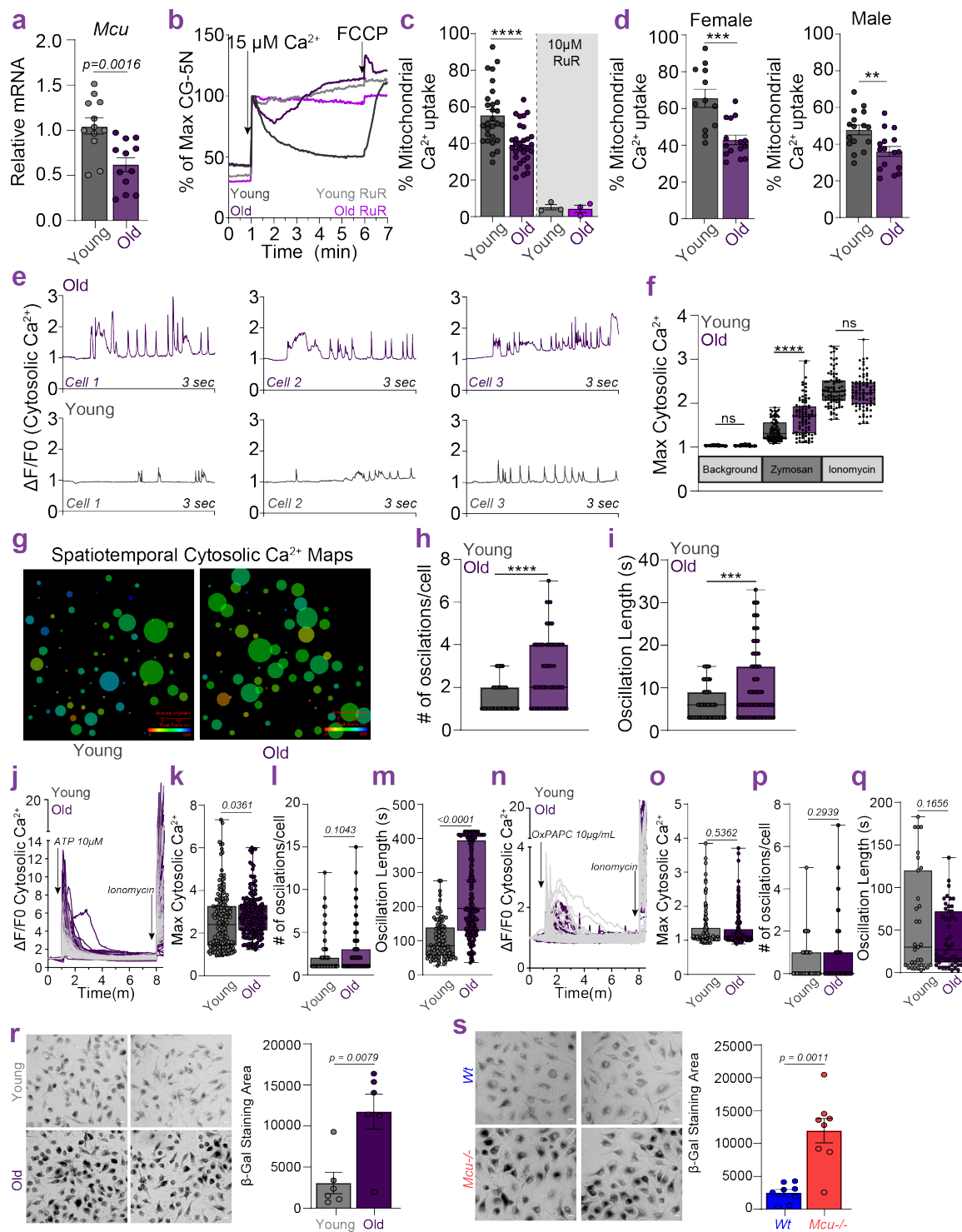


Figure 7: Aged macrophages exhibit reduction in mCa²⁺ uptake and signs of cellular senescence.

a. *Mcu* expression in BMDMs derived from *young* (n = 12 mice) and *old* (n = 12 mice) mice. Error bars reflect SEM; $p=0.0016$ according to Welch's t test, two-tailed.

b. Representative traces of Mitochondrial Ca²⁺ uptake measured in permeabilized BMDMs generated from young (<25 weeks) and old (80 – 90 weeks) mice.

c. Quantification of Mitochondrial Ca²⁺ uptake shown in panel b. Error bars reflect SEM; p -values($p<0.0001$ (****), $p\leq 0.001$ (***), $p\leq 0.01$ (**), $p\leq 0.05$ (*)) were calculated using Ordinary one-way ANOVA.

d. Mitochondrial Ca²⁺ uptake data shown in panel c – segregated by sex.

e. Representative cytosolic Ca²⁺ Oscillations in BMDMs derived from *young* and *old* mice using the ratiometric Ca²⁺ indicator FURA2-AM. Oscillations were recorded after the addition of zymosan.

f. Maximum cytosolic Ca²⁺ levels in individual cells, as reflected by max $\Delta F/F_0$ during zymosan stimulation. Box and whiskey plot represents the min to max values for each data set. Box represents 75th and 25th percentile. Line is at the median; $p<0.0001$ according to one-way ANOVA.

g. Spatiotemporal Ca²⁺ dynamics (from panel f) depicted by maps generated using CALIMA software. Circle size indicates number of Ca²⁺ spikes per given location. Circle color represents the time at which the first Ca²⁺ spike occurred.

h. Number of oscillations in individual cells. Box and whiskey plots represent the min to max values for each data set. Line is at the median; $p<0.0001$ according to Welch's t test, two-tailed.

i. Oscillation length determined for individual cells. Box and whiskeys represent the min to max values for each data set. Line is at the median; $p<0.0001$ according to Welch's t test, two-tailed.

- j.** Cytosolic Ca^{2+} Oscillations in BMDMs derived from *young* and *old* mice using the ratiometric Ca^{2+} indicator FURA2-AM. Cells were stimulated with ATP (10 μM) at 1 minute and Ionomycin (5 μM) was added at the end of the experiment.
- k.** Maximum cytosolic Ca^{2+} levels in individual cells, as reflected by max $\Delta\text{F}/\text{F0}$ during ATP (10 μM) stimulation. Box and whiskey plot represents the min to max values for each data set. Box represents 75th and 25th percentile. Line is at the median; *p-value* according to Welch's t test, two-tailed.
- l.** Number of oscillations in individual cells. Box and whiskey plots represent the min to max values for each data set. Line is at the median; *p-value* according to Welch's t test, two-tailed.
- m.** Oscillation length determined for individual cells. Box and whiskeys represent the min to max values for each data set. Line is at the median; *p*<0.0001 according to Welch's t test, two-tailed.
- n.** Cytosolic Ca^{2+} Oscillations in BMDMs derived from *young* and *old* mice using the ratiometric Ca^{2+} indicator FURA2-AM. Cells were stimulated with OxPAPC (10 $\mu\text{g}/\text{mL}$) at 1 minute and Ionomycin (5 μM) was added at the end of the experiment.
- o.** Maximum cytosolic Ca^{2+} levels in individual cells, as reflected by max $\Delta\text{F}/\text{F0}$ during ATP (10 μM) stimulation. Box and whiskey plot represents the min to max values for each data set. Box represents 75th and 25th percentile. Line is at the median; *p-value* according to Welch's t test, two-tailed.
- p.** Number of oscillations in individual cells. Box and whiskey plots represent the min to max values for each data set. Line is at the median; *p-value* according to Welch's t test, two-tailed.
- q.** Oscillation length determined for individual cells. Box and whiskeys represent the min to max values for each data set. Line is at the median; *p*<0.0001 according to Welch's t test, two-tailed.
- r.** Representative images of *young* and *old* BMDMs stained for senescence associated β -galactosidase (SA- β -gal) activity with X-gal. Bar graph is

quantification of SA- β -gal activity (staining area) in *young* and *old* BMDMs. Error bars reflect SEM; *p-values* were calculated using Welch's t test, two-tailed.

s. same as above for of *wt* and *Mcu*^{-/-} BMDMs.

Figure 8: Expression profiling of MCU complex in aged macrophages and further characterization of mitochondrial defects.

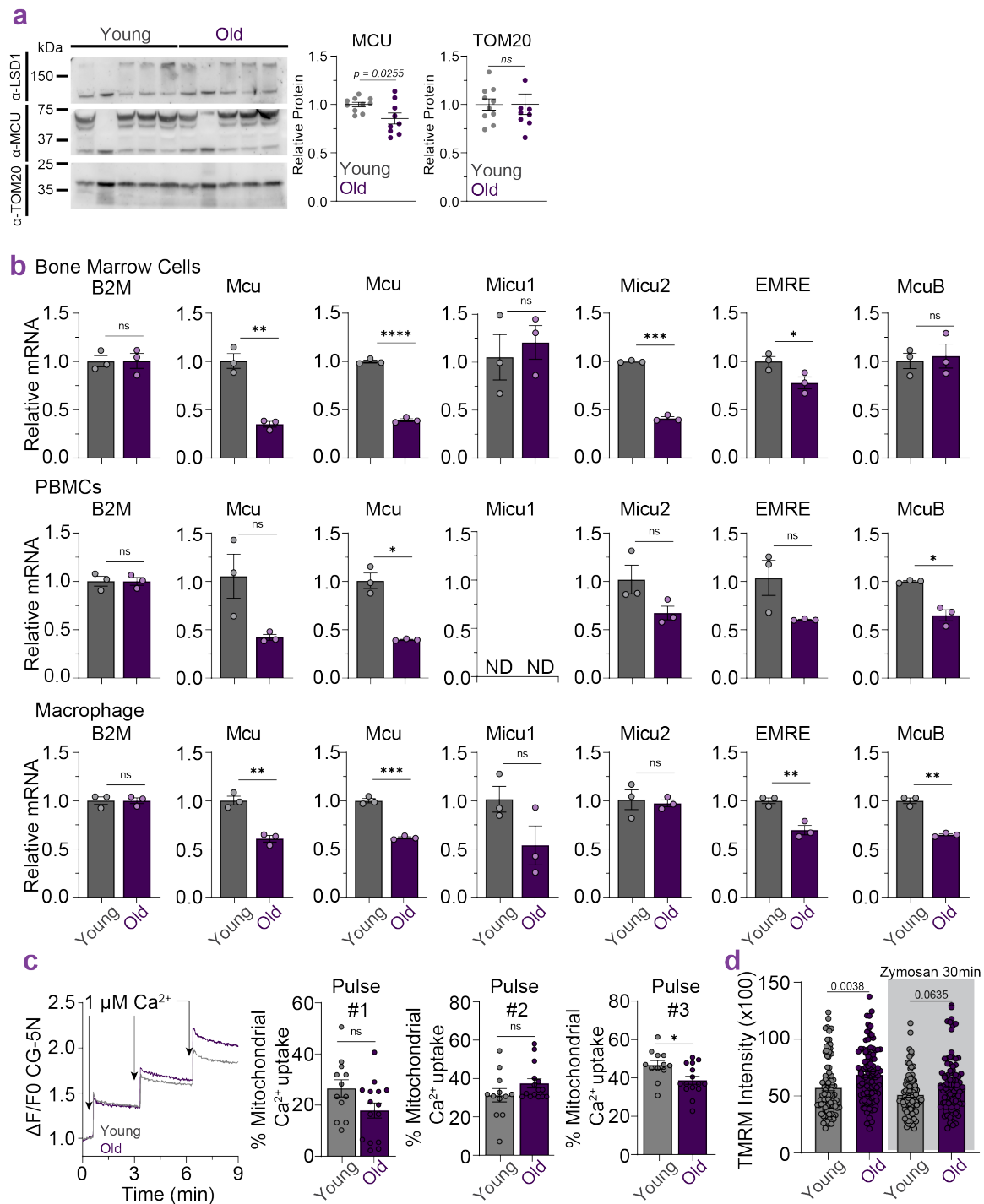


Figure 8: Expression profiling of MCU complex in aged macrophages and further characterization of mitochondrial defects.

- a.** Western blot analysis of *MCU* protein from *young* and *old* BMDMs. Quantification of MCU and TOM20 relative to loading control LSD1 shown on right. Error bars reflect SEM; *p-value* determined by Welch's t test, two-tailed.
- b.** Quantitative-PCR of *Mcu* and its regulatory subunits. Relative mRNA was quantified from undifferentiated bone-marrow cells, peripheral blood mononuclear cells (PBMCs) and bone-marrow derived macrophages (BMDMs) in *young* and *old* mice.
- c.** Pulsed mitochondrial Ca^{2+} uptake was measured in permeabilized BMDMs from *young* and *old* mice. Quantification of percent mitochondrial Ca^{2+} uptake was measured from 3 consecutive 1 μM Ca^{2+} pulses.
- d.** Mitochondrial membrane potential measured by TMRM intensity. Baseline intensity was recorded for individual cells and again following 30 minutes of zymosan stimulation. Error bars reflect SEM; *p-value* determined by one-way ANOVA.

Increased cytosolic Ca²⁺ oscillations in zymosan-stimulated macrophages derived from old mice.

We hypothesized that a reduction in mCa²⁺ uptake would disrupt cytosolic Ca²⁺ (cCa²⁺) signaling which is crucial for inflammatory signaling. We reasoned this may be possible in myeloid cells due to similar reports for mCa²⁺ uptake in lymphoid cells¹³². We challenged BMDMs derived from young and old mice with zymosan, a fungal glucan wherein the glucose monomers are polymerized through β -1,3 glycosidic bonds. Zymosan is a potent stimulator of both TLR2 and Dectin-1 (CLEC7A) receptors on myeloid cells. The downstream activation of PLC γ elicits a robust Store-operated Ca²⁺ entry (SOCE) which involves an initial release of ER-resident Ca²⁺ stores, followed by more sustained entry of extracellular Ca²⁺ through the ORAI channels. Inflammatory gene expression mediated by multiple transcription factors, especially NF κ B, is highly sensitive to cytosolic Ca²⁺ oscillations^{16,17}. In response to zymosan, the amplitudes of the cCa²⁺ oscillations in BMDMs-O were significantly elevated compared to BMDMs-Y (**Figure 7e**, **Figure 9f**). A comparison of the maximum Ca²⁺ elevations achieved in each cell also showed that the BMDMs-O achieved significantly higher amplitudes (**Figure 7f**). In these experiments, ionomycin, a Ca²⁺ ionophore, is added last as a positive control demonstrating that both cell populations were loaded equivalently with the Ca²⁺ dye (FURA-2AM) and were thus capable of reporting higher and equivalent levels of Ca²⁺. Although amplitudes are easily observed in the overlaid traces of cCa²⁺ shown in **Figure 9f**, the spatial distribution of these oscillations across the imaging field (containing many cells) is lost and individual cells are shown in **Figure 7e**. For a deeper analysis, we used CALIMA, an image analysis software specially designed to measure spatiotemporal aspects of Ca²⁺ oscillations¹³³. The spatial distribution of Ca²⁺ oscillations in representative image fields is shown (**Figure 7g**) with the origin of each circle at the cellular location and the diameter proportional to the number of spikes originating from that location. The color spectrum of the circles denotes the time at which that location first reported a

spike. For instance, in each field, the location of the reddish-brown circle reported a Ca^{2+} spike earlier than the circles colored green and so on. These spatial maps clearly show that BMDMs-O exhibit significantly higher number of Ca^{2+} oscillations per cell and they also start spiking sooner than BMDMs-Y. These are quantified (Figure 7h), and the difference in oscillatory lengths are also shown (Figure 7i). These data establish that Ca^{2+} -elevations are amplified in the macrophages derived from older mice during inflammatory signaling. We focused our analysis on Ca^{2+} dynamics in response to fungal pathogens as this is highly relevant to chronic low-grade inflammation attributed to dysregulated microbiome and “leaky gut” observed in older populations¹³⁴. However, we were curious if this may also pertain to other mechanisms of chronic low-grade inflammation. Two additional sources of low-grade inflammation in older populations are ATP release from dying cells and oxidative stress. We subjected BMDMs-O to our comprehensive cCa^{2+} analysis in response to ATP (Figure 7j – Figure 7m) and Oxidized PAPC (OxPAPC) (Figure 7n – Figure 7q). BMDMs-O showed dysregulated cCa^{2+} responses in repose to ATP similar to those observed by zymosan suggesting the shared a similar axis (store-operated Ca^{2+} entry) for Ca^{2+} entry and were thus impaired similarly in response to decreased Mcu activity. In the case of OxPAPC the upstream Ca^{2+} signaling, in terms of Ca^{2+} activated channels are less understood and perhaps is unaffected by mCa^{2+} buffering. This analysis revealed an interesting dichotomy in the regulation of cCa^{2+} by loss of mCa^{2+} uptake that will need to be further explored.

***Mcu*^{-/-} BMDMs derived from young (<25-wk) mice recapitulate the amplified cytosolic Ca^{2+} signals seen in BMDMs derived from old wt mice.**

To firmly establish that this effect on cytosolic Ca^{2+} -signaling is because of reduced mitochondrial Ca^{2+} -uptake, we show that the effect can be robustly recapitulated in BMDMs derived from young mice (age range: 15-25 weeks) by simply deleting *Mcu*. As shown (Figure 9a) *Mcu*^{-/-} BMDMs, derived from *Mcu^{fl}(Cx3cr1-cre)* mice¹²² show a robust amplification of cytosolic Ca^{2+} -

oscillations in response to zymosan. The maximum Ca^{2+} levels achieved by individual cells are shown in **Figure 9b**. Appropriate controls for long term Ca^{2+} imaging is shown in **Figure 9c – Figure 9e**. The spatiotemporal analysis using CALIMA is shown in **Figure 9f – Figure 9h**. This analysis shows that, as seen in old BMDMs, the *Mcu*^{-/-} BMDMs exhibit many more oscillations per cell and the length of the oscillations is also increased. Together, these data establish that the increased cytosolic Ca^{2+} -signaling in the old BMDMs is a direct consequence of the reduced mitochondrial Ca^{2+} uptake.

Figure 9: Characterization of mitochondria in aged macrophages and cytosolic Ca^{2+} dynamics in *Mcu*^{-/-} macrophages.

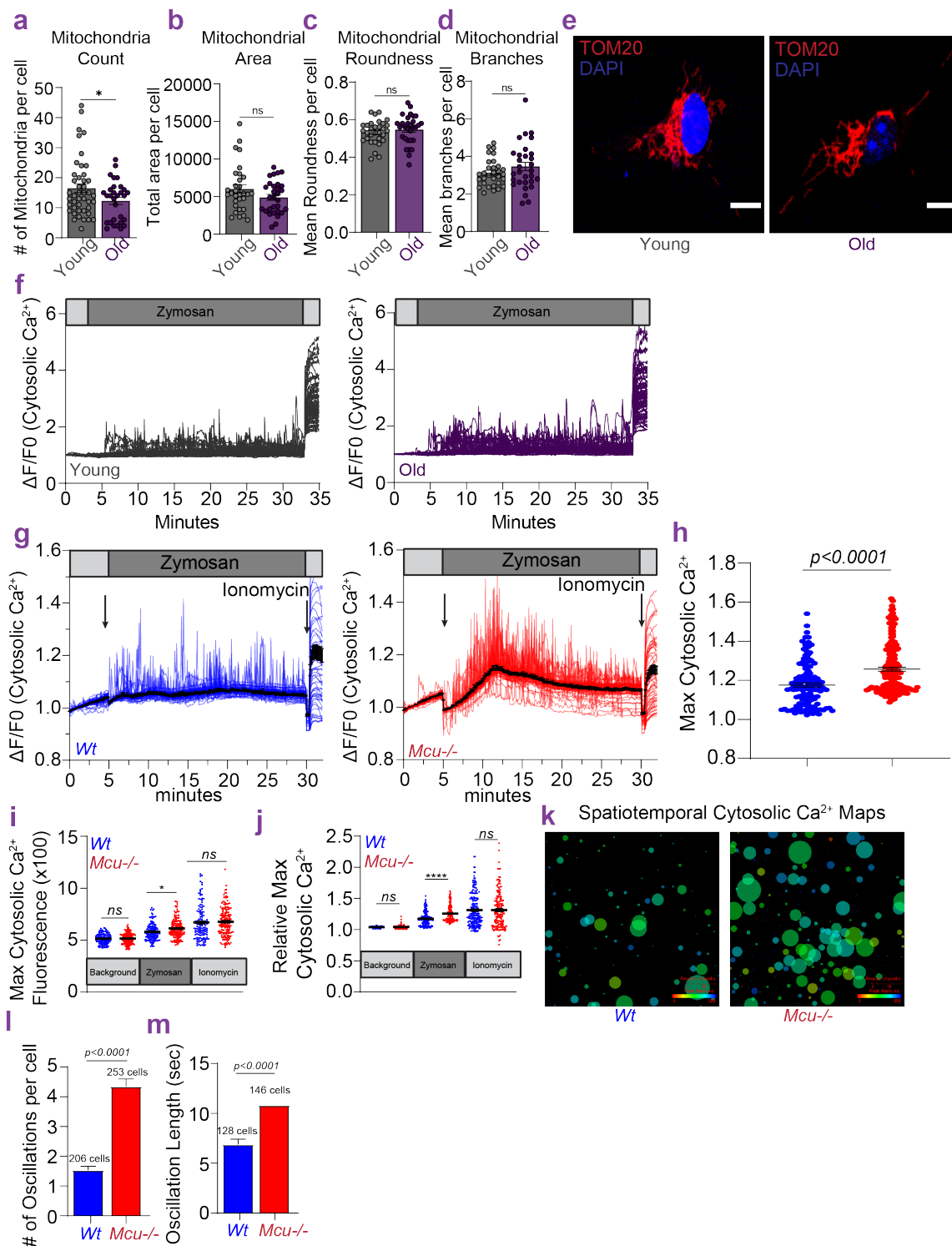


Figure 9: Characterization of mitochondria in aged macrophages and cytosolic Ca^{2+} dynamics in *Mcu*^{-/-} macrophages.

a. Mitochondrial count determined by MitoGenie from the same cells analyzed in panel a. Error bars reflect SEM; not statistically significant according to Welch's t test, two-tailed.

b. Mitochondrial area determined by MitoGenie from the same cells analyzed in panel a. Error bars reflect SEM; not statistically significant according to Welch's t test, two-tailed.

c. Mitochondrial roundness determined by MitoGenie from the same cells analyzed in panel a. Error bars reflect SEM; not statistically significant according to Welch's t test, two-tailed.

d. Mitochondrial branches determined by MitoGenie from the same cells analyzed in panel a. Error bars reflect SEM; not statistically significant according to Welch's t test, two-tailed.

e. Representative images of BMDMs immunostained for TOM20. Scale bar at 10 μm .

f. Cytosolic Ca^{2+} Oscillations in BMDMs derived from *young* (n = 88 cells) and *old* (n = 87 cells) mice using the ratiometric Ca^{2+} indicator FURA2-AM. Ionomycin (5 μM) was added at the end of the experiment.

g. Cytosolic Ca^{2+} Oscillations in *wt* and *Mcu*^{-/-} BMDMs from an imaging field are overlaid – these are representative and typical traces from two individual experiments. $\Delta\text{F}/\text{F}_0$ values for Fluo-4-AM loaded BMDMs are plotted. Images were taken every 5 secs. Ionomycin (5 μM) was added last to determine maximal signal for individual cells.

h. Maximum cytosolic Ca^{2+} amplitudes achieved in individual cells during zymosan stimulation, as determined by max $\Delta\text{F}/\text{F}_0$. Error bars represent SEM; $p < 0.0001$ according to Welch's t test, two-tailed.

i. Maximum cytosolic Ca^{2+} determined by maximum Fluo-4 intensity achieved in individual cells. Error bars represent SEM; $p < 0.0001$ (****), $p \leq 0.001$ (***), $p \leq 0.01$ (**), $p \leq 0.05$ (*) determined by the Brown-Forsythe and Welch ANOVA test.

j. Maximum cytosolic Ca^{2+} determined by max $\Delta F/F_0$ during zymosan stimulation for individual cells. Error bars represent SEM of two independent experiments; $p < 0.0001$ (****), $p \leq 0.001$ (***), $p \leq 0.01$ (**), $p \leq 0.05$ (*) determined by the Brown-Forsythe and Welch ANOVA test.

k. CALIMA maps depicting spatiotemporal aspects of cytosolic Ca^{2+} elevations. Circle size is proportional to number of Ca^{2+} spikes per given cellular location. Circle color, along the spectrum shown, reflects the relative time the first Ca^{2+} spike was recorded at that location.

l. Average number of oscillations per cell, seen during zymosan stimulation. Error bars represent SEM; $p < 0.0001$ according to Welch's t test, two-tailed.

m. Mean of oscillation lengths during zymosan stimulation. Error bars represent SEM; $p < 0.0001$ according to Welch's t test, two-tailed.

BMDMs-O and *Mcu*^{-/-} macrophages show signatures of senescence.

Aging is commonly associated with the presence of senescent cells and a long standing hallmark of senescent cells has been the senescence-associated β -galactosidase activity (SA- β -gal) attributed to the lysosomal β -galactosidase in mammals¹³⁵. To determine if aged macrophages had signs of cellular senescence we measured SA- β -gal from BMDMs-O and compared them to BMDMs-Y (**Figure 7r**). In this assay cells are stained with X-gal and imaged for the presence of blue precipitates formed from the activity of SA- β -gal. These precipitates can be observed under bright field on a light microscope and appears as dark aggregates. Measuring hundreds of cells across multiple mice we observed a robust senescent signature in BMDMs-O as measured by SA- β -gal staining area (**Figure 7r**). We reasoned that if loss of *Mcu* contributed to this senescent signature we would observe SA- β -gal activity in *Mcu*^{-/-} macrophages from young mice. Surprisingly, *Mcu*^{-/-} macrophages from young mice had robust SA- β -gal activity indicating macrophages lacking *Mcu* had signatures of premature aging (**Figure 7s**). If loss of *Mcu* in young mice was capable of driving macrophages to a senescent phenotype we wondered if other aging phenotypes are similar between BMDMs-O and young *Mcu*^{-/-} macrophages. An interesting link between inflammaging aging and senescence is the senescence-associated secretory phenotype (SASP) which results from dysregulated inflammatory gene expression in senescent cells¹³⁶.

Hyper-inflammatory responses in both *wt* BMDMs-O and *Mcu*^{-/-} BMDMs-Y.

We hypothesized that the abnormally increased cytosolic Ca²⁺-signaling in BMDMs-O would result in increased inflammation. Indeed, in response to zymosan, BMDMs-O expressed higher levels of proinflammatory cytokines IL-6 and IL-1 β when compared to BMDMs-Y (**Figure 10a**). NF κ B plays a crucial role in the transcription of these proinflammatory genes, and its activation is highly sensitive to Ca²⁺-signaling^{16,137}. We measured NF κ B translocation (p65) in BMDMs-Y and BMDMs-O stimulated with zymosan and found that in accord with

our model, the translocation of NF κ B was significantly enhanced in the BMDMs-O (**Figure 10b**, **Figure 11a**). The quantification of the ratio of nuclear to cytoplasmic NF κ B shows that significantly more NF κ B translocated to the nuclei of BMDMs-O (**Figure 10c**). These data show that macrophages from the older mice are hyper-inflammatory in response to zymosan. Consistently, we found that *Mcu*^{-/-} macrophages from young mice also exhibit a hyperinflammatory response to zymosan stimulation, establishing a model wherein reduction in mCa²⁺-uptake increases inflammatory output through amplified cCa²⁺-signaling (**Figure 10d**). Predictably, the *Mcu*^{-/-} BMDMs-Y show significantly increased expression of both IL-1 β and IL-6 (**Figure 10e**). Note that when ionomycin is added to artificially increase cytosolic Ca²⁺, even *wt* BMDMs-Y increase the expression of IL-1 β , highlighting the sensitivity of the macrophage inflammatory response to cytosolic Ca²⁺. A similar effect is observed in the case of IL-6 but there was a key difference that while ionomycin increased the expression of IL-6 in *wt* cells, it also decreased the expression of IL-6 in *Mcu*^{-/-} BMDMs. A possible reason for this is that unlike the oscillatory effects caused by reduced mCa²⁺ uptake, ionomycin causes a global and sustained elevation of Ca²⁺. In *Mcu*^{-/-} BMDMs, this elevation is unbuffered by mCa²⁺-uptake, and this may inhibit other regulatory elements of IL-6 transcription. Nevertheless, the upregulation of both IL-1 β and IL-6 is highly dependent on Ca²⁺-signaling. BAPTA-AM, a cell permeable, high-affinity Ca²⁺ chelator that prevents the elevation of cytosolic Ca²⁺ during zymosan-triggered inflammatory signaling completely abrogates the expression of IL-1 β and IL-6 (**Figure 10f**). NF κ B translocation was also found to be enhanced in *Mcu*^{-/-} BMDMs-Y (**Figure 10g**). Quantification on nuclear/cytoplasmic ratio revealed a striking increase in NF κ B activation in *Mcu*^{-/-} BMDMs-Y (**Figure 10h**). Representative line intensity plots across the nucleus and cytosol are shown (**Figure 10i**). The increased activation of NF κ B in *Mcu*^{-/-} macrophages was also seen when they were stimulated with the fungal pathogen *C. albicans* (**Figure 11b**), but the translocation kinetics were slower in comparison to zymosan stimulation (**Figure 11c**). Representative line intensity

plots are shown (**Figure 11d**). Overall, these data argue strongly that reduced mitochondrial Ca^{2+} uptake seen in BMDMs-O renders them hyper-inflammatory because of reduced mitochondrial Ca^{2+} -uptake and amplified cytosolic Ca^{2+} -signaling. Another aspect of macrophage biology related to NF κ B translocation is the polarization of macrophages into M1 and M2 phenotypes *ex vivo*. Previous reports on the role of m Ca^{2+} on macrophage polarization have shown links between m Ca^{2+} and macrophage polarization. *Mcu* inhibition has been linked to an impaired M2 polarization¹²⁴ while deletion of *McuB* has been linked to enhanced M1 polarization and impaired M2 polarization¹²³. To build on these studies we performed M1 and M2 polarization in *Mcu*^{-/-} macrophages (**Figure 11e – Figure 11f**). M1 polarization in *Mcu*^{-/-} macrophages showed enhanced expression of NF κ B target gene with unexpected expression of Arg1 in *Mcu*^{-/-} macrophages stimulated with LPS+IFN γ , suggesting a complexity in the dysregulation of NF κ B. Interestingly, M2 polarization also showed enhanced expression of M2 markers. However, these experiments are performed over the course of 24hrs in the context of IL-4 and IFN γ stimulation that can result in a host of secondary and tertiary signaling cascades in macrophages. The salient observation from these experiments is that m Ca^{2+} uptake plays a critical role in NF κ B mediated gene transcription and further mechanistic studies are necessary to resolve this complexity.

Figure 10: Both wt BMDMs-O and *Mcu*^{-/-} BMDMs-Y exhibit a hyper-inflammatory response to fungal stimulation.

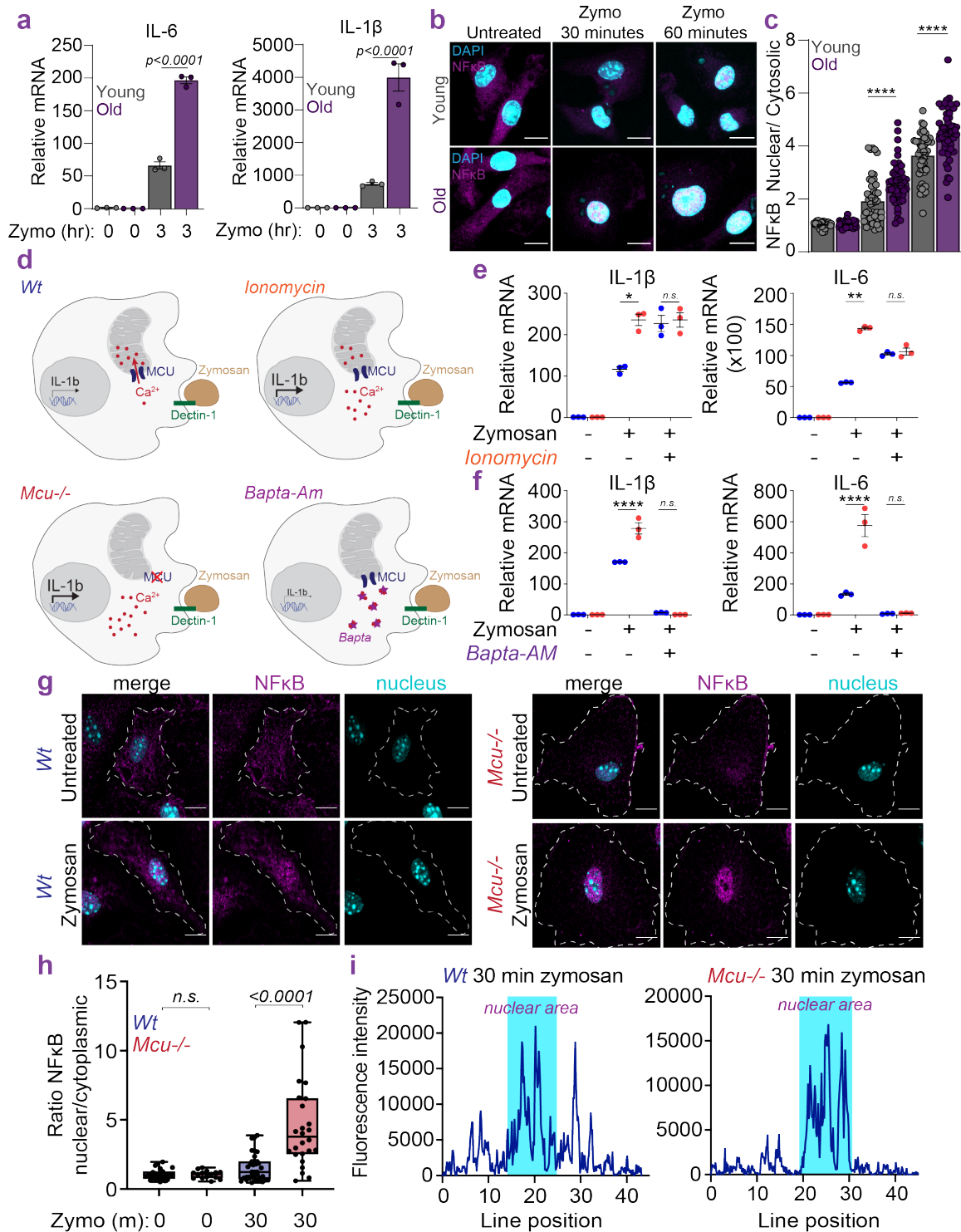


Figure 10: Both wt BMDMs-O and *Mcu*^{-/-} BMDMs-Y exhibit a hyper-inflammatory response to fungal stimulation.

a. IL-6 and IL-1 β mRNA expression from BMDMs derived from *young* and *old* mice, stimulated with Zymosan for 3 hours. Error shown as SEM; $p < 0.0001$ according to one-way ANOVA.

b. Representative images from indicated BMDMs stimulated with zymosan for 30 and 60 minutes. Magenta shows immunostaining of NF κ B p65 subunit and cyan shows DAPI staining of nuclei.

c. Nuclear to cytoplasmic ratios of the fluorescent intensity of NF κ B. Bars reflect means of ratios; $p < 0.0001$ (****) according to one-way ANOVA.

d. Model depicting how mCa²⁺ uptake affects cytosolic Ca²⁺ and inflammatory gene expression in response to zymosan.

e. IL-1 β and IL-6 mRNA expression in *wt* and *Mcu*^{-/-} macrophages. Error bars represent SEM; $p < 0.0001$ (****), $p \leq 0.001$ (***), $p \leq 0.01$ (**), $p \leq 0.05$ (*) determined by 2way ANOVA.

f. IL-1 β and IL-6 expression in *wt* and *Mcu*^{-/-} macrophages. Error bars represent SEM; $p < 0.0001$ (****), $p \leq 0.001$ (***), $p \leq 0.01$ (**), $p \leq 0.05$ (*) determined by 2way ANOVA.

g. Representative images from *wt* and *Mcu*^{-/-} macrophages, untreated or stimulated with zymosan for 30 minutes and immunostained for NF κ B p65 subunit and nuclei (DAPI).

h. Nuclear to cytoplasmic ratios of the fluorescent intensity of NF κ B. Box and whiskey plots represents the min to max values for each data set. Line is at the median; $p < 0.0001$ according to one-way ANOVA.

i. Representative analysis of fluorescent intensity of p65 staining along a line drawn across the cytoplasm and nucleus (DAPI staining) which is shaded blue.

Figure 11: NF κ B translocation in response to *C. albicans* and M1 vs M2 immune-profiling of *Mcu*^{-/-} macrophages.

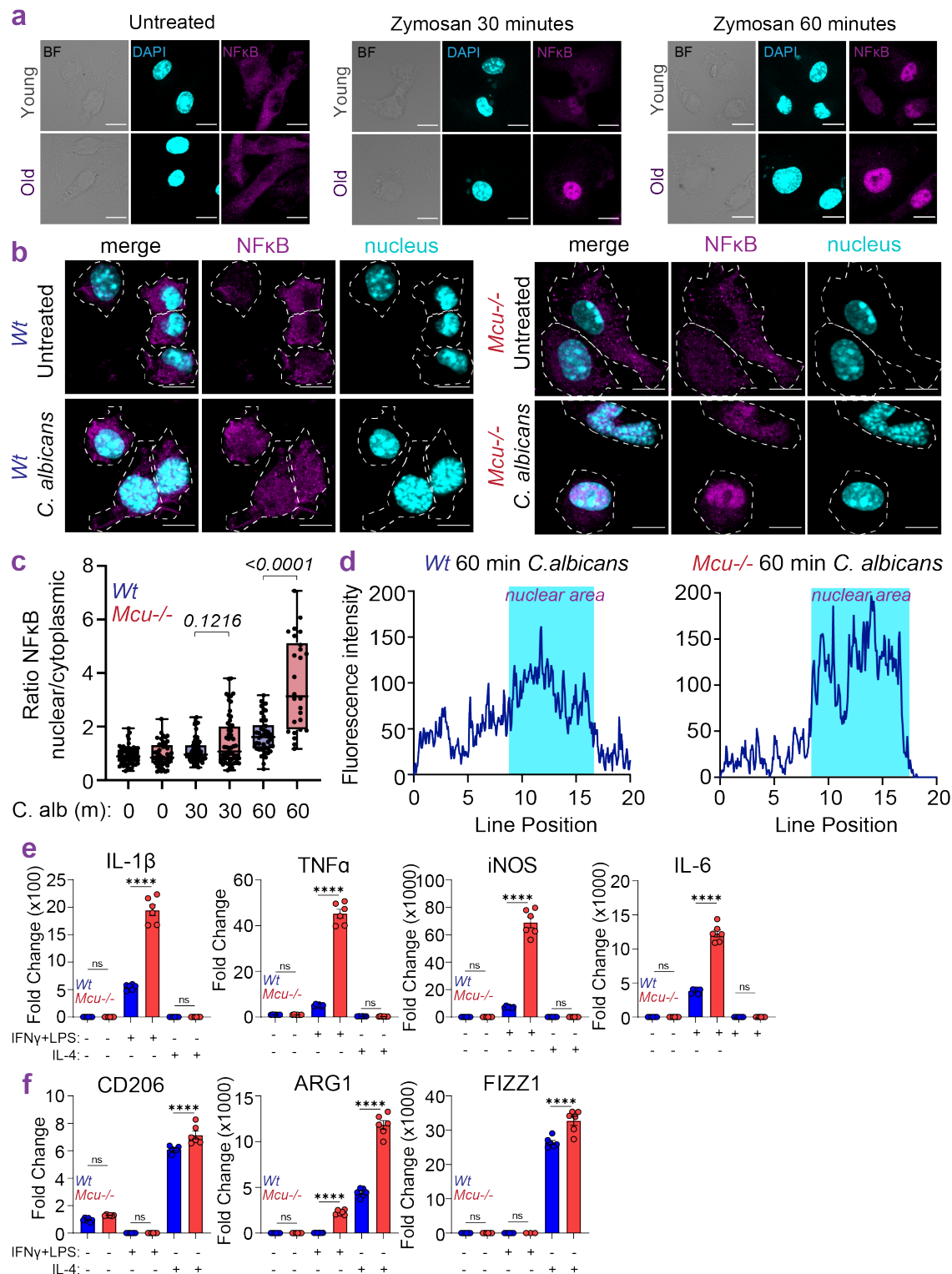


Figure 11: NFκB translocation in response to *C. albicans* and M1 vs M2 immune-profiling of *Mcu*^{-/-} macrophages.

- a.** Representative images from Figure 3g shown as single channels.
- b.** Representative images from *wt* and *Mcu*^{-/-} macrophages, untreated or stimulated with *C. albicans*, for 30 or 60 minutes and immunostained for NFκB p65 subunit and nuclei (DAPI). Outline of cells was determined by bright field images.
- c.** Nuclear to cytoplasmic ratios of the fluorescent intensity of NFκB for images shown in *panel b*. Box and whiskey plots represents the min to max values for each data set. Line is at the median; $p < 0.0001$ (****) according to one-way ANOVA.
- d.** Representative analysis of fluorescent intensity of p65 staining along a line drawn across the cytoplasm and nucleus, as determined by DAPI staining (shaded blue).
- e-f.** BMDMs from *wt* and *Mcu*^{-/-} mice were treated either with IFN-γ (100 ng/ml) and LPS (100 ng/ml; to induce polarization toward a M1 phenotype) or with IL-4 (20 ng/ml; to induce polarization toward a M2 phenotype). Twenty-four hours after polarization, total mRNA was extracted for qPCR. Proinflammatory cytokines (M1) *IL-1β*, *IL-6*, and *iNOS* (**e**) and anti-inflammatory (M2) *CD206*, *ARG1*, and *FIZZ1* (**f**) markers were assessed. Error bars represent SEM; $p < 0.0001$ (****), $p \leq 0.001$ (***), $p \leq 0.01$ (**), $p \leq 0.05$ (*) determined by one-way ANOVA.

Increased cytosolic Ca^{2+} is the driver of hyperinflammation in *Mcu*^{-/-} macrophages.

To address the complexity of mCa^{2+} signaling on the observed differences in inflammatory gene transcription from several groups^{123,124} and the immediate effects of mCa^{2+} signaling on inflammatory gene transcription we attempted to disconnect the effects of enhanced cCa^{2+} and loss of mCa^{2+} observed in *Mcu*^{-/-} macrophages. To do this we reasoned we could use pharmacological inhibition of calcium release-activated channels (CRAC) to dampen the enhanced cCa^{2+} in *Mcu*^{-/-} macrophages and reveal the contributions of enhanced cCa^{2+} . While inhibition of the pyruvate dehydrogenase kinase (PDK) in *Mcu*^{-/-} macrophages would restore metabolic defects from the loss of mCa^{2+} in *Mcu*^{-/-} macrophages reveal contributions from the loss of mCa^{2+} . In this scenario, if enhanced inflammatory phenotype was dependent on enhanced cCa^{2+} in *Mcu*^{-/-} macrophages and not loss of mCa^{2+} , inhibition of CRAC would dampen the hyperinflammation in *Mcu*^{-/-} macrophages while inhibition of PDK would have minimal to no effect. In these experiments we pretreated *Wt* and *Mcu*^{-/-} macrophages with BTP2 (10 μM) or zegocractin (1 μM), zegocractin has a much higher affinity and specificity for CRAC, for 30 minutes prior to treatment with zymosan (2 particles/cell) for 3 hrs. RNA was harvested for qPCR and inflammatory genes IL-1 β and IL-6 were measured as a fold change from untreated cells. Inhibition of CRAC with BTP2 (**Figure 12a**) and Zegocractin (**Figure 12c**) significantly decreased inflammatory gene expression in *Mcu*^{-/-} macrophages restoring them to levels of *Wt* with little effect on *Wt* macrophages. Inhibition of PDK with AZD7545 (1 μM) had little effect on inflammatory gene transcription in *Mcu*^{-/-} macrophages (**Figure 12d**). When we compare the hyperinflammation of *Mcu*^{-/-} macrophages to that of BMDMS-O we see the increase in inflammatory gene transcription is much greater in *Mcu*^{-/-} macrophages most likely due to a complete loss in mCa^{2+} uptake compared to partial loss in BMDMS-O (**Figure 12e**). Together these findings suggest the

major driver of hyper inflammation in *Mcu*^{-/-} macrophages is through its dysregulation of cCa²⁺.

Figure 12: Enhanced cytosolic Ca²⁺ drives hyper inflammatory phenotype in *Mcu*^{-/-} macrophages.

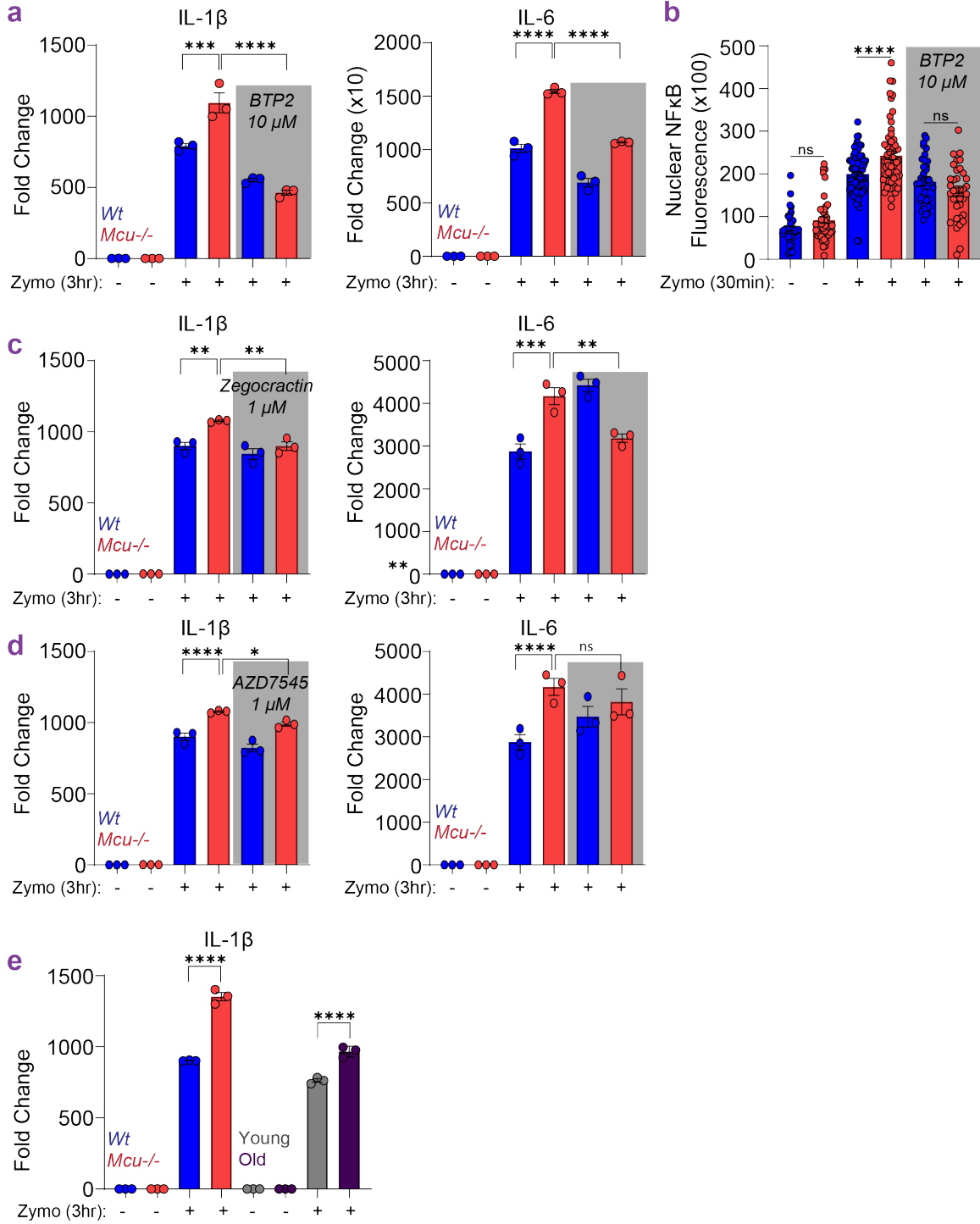


Figure 12: Enhanced cytosolic Ca^{2+} drives hyper inflammatory phenotype in *Mcu*^{-/-} macrophages.

a. BMDMs from *wt* and *Mcu*^{-/-} mice were treated with zymosan (2particles/cell) for 3 hours with or without the CRAC inhibitor BTP2 (10 μM). Total RNA was extracted for qPCR. *IL-1 β* and *IL-6* expression was determined as a fold change to untreated samples. Error bars represent SEM; $p < 0.0001$ (****), $p \leq 0.001$ (***), $p \leq 0.01$ (**), $p \leq 0.05$ (*) determined by one-way ANOVA.

b. BMDMs from *wt* and *Mcu*^{-/-} mice were treated with zymosan (2particles/cell) for 30 minutes with or without the CRAC inhibitor BTP2 (10 μM). Nuclear fluorescent intensity of NF κ B was quantified for individual cells. Error bars represent SEM; $p < 0.0001$ (****), $p \leq 0.001$ (***), $p \leq 0.01$ (**), $p \leq 0.05$ (*) determined by one-way ANOVA.

c. BMDMs from *wt* and *Mcu*^{-/-} mice were treated with zymosan (2particles/cell) for 3 hours with or without the CRAC inhibitor Zegocractin (1 μM). Total RNA was extracted for qPCR. *IL-1 β* and *IL-6* expression was determined as a fold change to untreated samples. Error bars represent SEM; $p < 0.0001$ (****), $p \leq 0.001$ (***), $p \leq 0.01$ (**), $p \leq 0.05$ (*) determined by one-way ANOVA.

d. BMDMs from *wt* and *Mcu*^{-/-} mice were treated with zymosan (2particles/cell) for 3 hours with or without the PDK inhibitor AZD7545 (1 μM). Total RNA was extracted for qPCR. *IL-1 β* and *IL-6* expression was determined as a fold change to untreated samples. Error bars represent SEM; $p < 0.0001$ (****), $p \leq 0.001$ (***), $p \leq 0.01$ (**), $p \leq 0.05$ (*) determined by one-way ANOVA.

e. BMDMs from *wt*, *Mcu*^{-/-}, *young* and *old* mice were treated with zymosan (2particles/cell) for 3 hours. RNA was extracted for qPCR. *IL-1 β* and *IL-6* expression was determined as a fold change to untreated samples. Error bars represent SEM; $p < 0.0001$ (****), $p \leq 0.001$ (***), $p \leq 0.01$ (**), $p \leq 0.05$ (*) determined by one-way ANOVA.

***Mcu*^{-/-} BMDMs also show increased pyroptosis and secretion of IL-1 β after NLRP3 inflammasome activation.**

Next, we evaluated if the increased inflammatory gene expression caused by decreased mitochondrial Ca²⁺ uptake also increases inflammasome activation. *Wt* and *Mcu*^{-/-} macrophages from young mice were stimulated with zymosan for 3 hours prior to the addition of Nigericin (5 μ M) for 1 hour to activate the NLRP3 inflammasome. *Mcu*^{-/-} macrophages released significantly more IL-1 β (**Figure 13a**) and LDH (**Figure 13b**) and this effect was also seen when the macrophages were first stimulated with LPS (**Figure 13c – Figure 13d**). We wondered if the assembly of the NLRP3 inflammasome is also accentuated in *Mcu*^{-/-} macrophages. Assembly of NLRP3 inflammasome can be visualized through immunofluorescence microscopy of ASC speck formation¹³⁸⁻¹⁴². We did not see any significant difference in ASC speck formation in *Mcu*^{-/-} BMDMs (**Figure 13e – Figure 13f**) indicating that decreased mitochondrial Ca²⁺ uptake, and concomitantly increased cytosolic Ca²⁺-signaling, does not have a major impact on the assembly of NLRP3 inflammasome. Activation of the NLRP3 inflammasome results in the proteolytic cleavage and activation of caspase-1 (CASP1). Activated CASP1 catalyzes the proteolytic processing of pro-IL-1 β to its secreted form IL-1 β . CASP1 also cleaves monomeric Gasdermin D (GSDMD), thus catalyzing their oligomerization into a large multimeric gasdermin pore in the plasma membrane. The release of many potent proinflammatory mediators, including IL-1 β and IL-18 is mediated through this large GSDMD pore. Overall, this process results in a highly inflammatory form of cell death called pyroptosis. We assessed the cleavage of CASP1 and GSDMD in NLRP3 activated macrophages. Notably, we found that the cleavage of both CASP1 and GSDMD is significantly increased in *Mcu*^{-/-} macrophages – in both cell pellets (**Figure 13g**) and in supernatants (**Figure 13h**). These findings indicate that while decreased mitochondrial Ca²⁺ uptake does not affect NLRP3 assembly, it does have a significant impact on the downstream processing of CASP1 and Gasdermin D. Finally, we evaluated whether deletion of *Mcu* in the myeloid cells

would manifest a hyperinflammatory response *in vivo*. Previous reports have shown that long exposures to fungal β -glucans can activate the NLRP3 inflammasome in macrophages¹⁴³. In a model of zymosan induced peritonitis, mice lacking *Mcu* in the myeloid cells exhibited significantly worse clinical scores, and increased levels of IL-1 β and TNF α in the peritoneal cavity (**Figure 14a – Figure 14d**). However, we did not see increased levels of other proinflammatory cytokines (IL-1 β , IL-6 and IFN α) that we measured in this model.

Figure 13: *Mcu*^{-/-} BMDMs-Y show increased pyroptosis and secretion of IL-1 β after NLRP3 inflammasome activation.

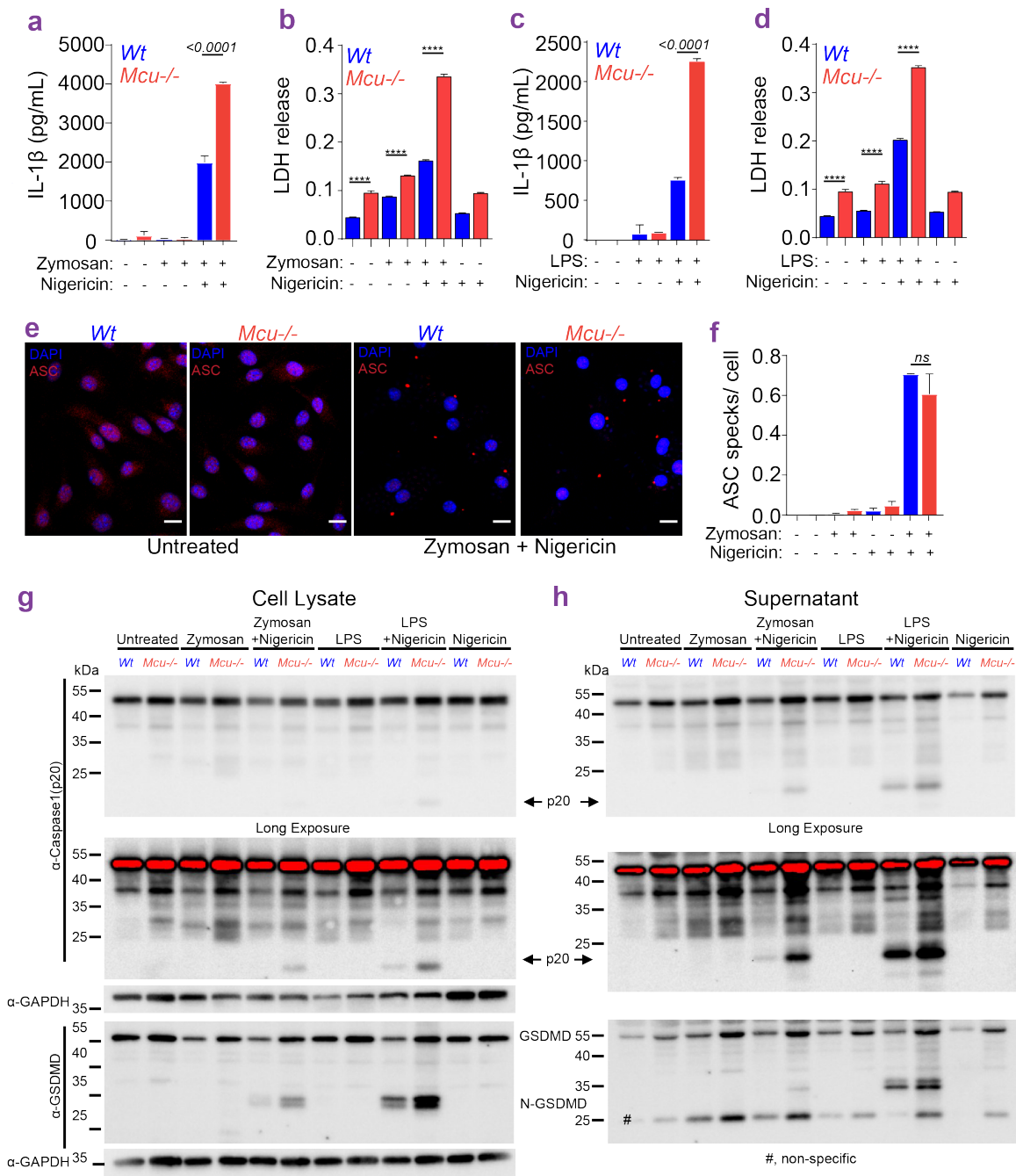


Figure 13: *Mcu*^{-/-} BMDMs-Y show increased pyroptosis and secretion of IL-1 β after NLRP3 inflammasome activation.

- a.** IL-1 β ELISA of cell supernatants collected from *wt* and *Mcu*^{-/-} macrophages. Cells were stimulated with zymosan for 3 hours followed by Nigericin (5 μ M) overnight. Error bars represent SEM; p values determined by one-way ANOVA.
- b.** LDH levels in cell supernatants collected from *wt* and *Mcu*^{-/-} macrophages. Error bars represent SEM; $p < 0.0001$ (****) determined by the one-way ANOVA.
- c.** IL-1 β ELISA of cell supernatants collected from *wt* and *Mcu*^{-/-} macrophages. Cells were stimulated with LPS for 3 hours followed by Nigericin (5 μ M) overnight. Error bars represent SEM; p values determined by one-way ANOVA.
- d.** LDH levels in cell supernatants collected from *wt* and *Mcu*^{-/-} macrophages. Error bars represent SEM; $p < 0.0001$ (****) determined by one-way ANOVA.
- e.** Representative images of *Mcu*^{-/-} and *wt* macrophages immunostained for ASC and nuclei (DAPI). Cells were stimulated with zymosan for 3 hours followed by Nigericin (5 μ M) for 1 hour.
- f.** Quantification of ASC specks, average number of specks counted per cell, for *wt* and *Mcu*^{-/-} macrophages. Error bars represent SEM; *no significance* was determined by the one-way ANOVA.
- g.** Western blot analysis of cell lysates from *wt* and *Mcu*^{-/-} macrophages stimulated with zymosan for 3 hours followed by Nigericin (5 μ M) for 1 hour. Cell lysates were immunoblotted for Caspase1 (p20), GSDMD, and GAPDH.
- h.** Western blot analysis of supernatants corresponding to samples shown in panel g. Cell supernatants were immunoblotted for Caspase1 (p20), GSDMD, and GAPDH.

Figure 14: A model of Zymosan-Induced Peritonitis in *Mcu(M)*^{-/-} mice.

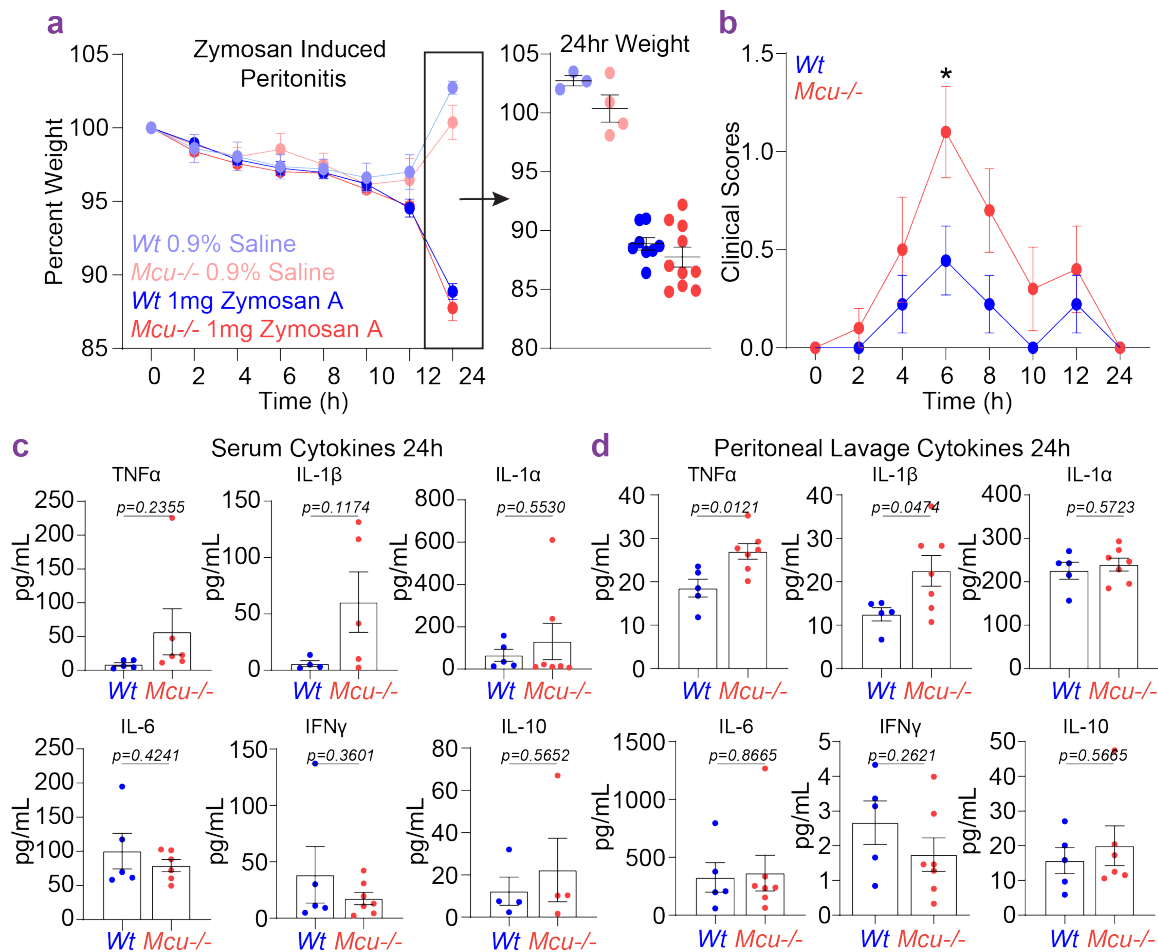


Figure 14: A model of Zymosan-Induced Peritonitis in *Mcu(M)*^{-/-} mice.

- a.** Percent weight change for *wt* and *Mcu*^{-/-} mice in a model of Zymosan Induced Peritonitis.
- b.** Clinical Scores for *wt* and *Mcu*^{-/-} mice in a model of Zymosan Induced Peritonitis. Error bars represent SEM; $p \leq 0.05$ (*) determined by the one-way ANOVA
- c.** ELISA determined serum cytokines in *wt* and *Mcu*^{-/-} mice, at 24 hours, in a model of Zymosan Induced Peritonitis. Error bars represent SEM; $p < 0.0001$ according to Welch's t test, two-tailed.
- d.** Peritoneal lavage cytokines at 24 hours. Error bars represent SEM of two independent experiments: *p-values* according to Welch's t test, two-tailed.

Diminished mCa²⁺-uptake increases inflammatory outputs in presence and absence of inflammatory stimuli.

To develop a systems level picture of how mitochondrial Ca²⁺-uptake affects the inflammatory response, we performed RNA-seq analysis on *wt*, *Mcu*^{-/-} and BAPTA-AM loaded macrophages (all derived from young mice), before and after zymosan stimulation. In brief, the experiment was designed to reveal the Ca²⁺-sensitive genes that are dysregulated when mCa²⁺ uptake is diminished. Note that BAPTA-AM loading will affect all Ca²⁺-sensitive genes by ‘clamping’ intracellular Ca²⁺-elevations to near resting levels (<100 nM). We were especially interested in groups of genes that are relatively upregulated in *Mcu*^{-/-} macrophages and downregulated in BAPTA-AM loaded cells. As expected, a volcano plot revealed that many inflammatory genes are significantly upregulated in zymosan-stimulated *Mcu*^{-/-} macrophages when compared to their *wt* counterparts (**Figure 15a**). Conversely, BAPTA-AM loading broadly decreased the expression of inflammatory gene transcription (**Figure 15b**). GSEA pathway analysis revealed the key pathways that follow this pattern of regulation in macrophages – upregulated when mCa²⁺ is diminished (cCa²⁺ signaling is enhanced) and downregulated when all Ca²⁺-signaling is prevented by BAPTA-AM (**Figure 15c**). Genes involved in inflammatory responses and those involved in the overlapping TNF α -NF κ B pathway showed this pattern most clearly. Using normalized counts, we show significantly increased expression of *IL-1 β* , *IL-1 α* , *IL-6*, *Nlrp3*, *Cxcl9* and *Clec5a* when mCa²⁺-uptake is diminished during an inflammatory response to zymosan (**Figure 15d**). In total, we identified 668 genes that are regulated by mCa²⁺ uptake in zymosan-stimulated macrophages (**Figure 16a**). The analysis so far has focused on gene expression changes in response to a potent inflammatory stimulus (zymosan). We checked if abrogation of mCa²⁺ uptake in *Mcu*^{-/-} macrophages upregulates inflammatory genes at baseline – without any overt exposure to an inflammatory stimulus. Surprisingly, although the expression levels were low in quiescent macrophages, we observed a clear upregulation of inflammatory response genes in unstimulated *Mcu*^{-/-}

macrophages (**Figure 15e – Figure 15g**). Similar to zymosan stimulation, GSEA pathway analysis revealed a significant enrichment of inflammatory pathways in *Mcu*^{-/-} macrophages at baseline when compared to *wt* controls (**Figure 16a – Figure 16b**). Within the inflammatory pathway genes, the chemokines *Cxcl10* and *Ccl5*, and proinflammatory cytokines *IL-6* and *IL-12 α* were significantly elevated (**Figure 15h**). Together these data show that diminished mitochondrial Ca^{2+} uptake drives low-grade inflammation in absence of overt inflammatory stimuli and promotes a hyper-inflammatory response when the macrophages are exposed to inflammatory stimuli.

Figure 15: Bulk RNA-seq on *Mcu*^{-/-} BMDMs-Y reveals hyper-inflammatory phenotype in response to fungal pathogens and under baseline conditions.

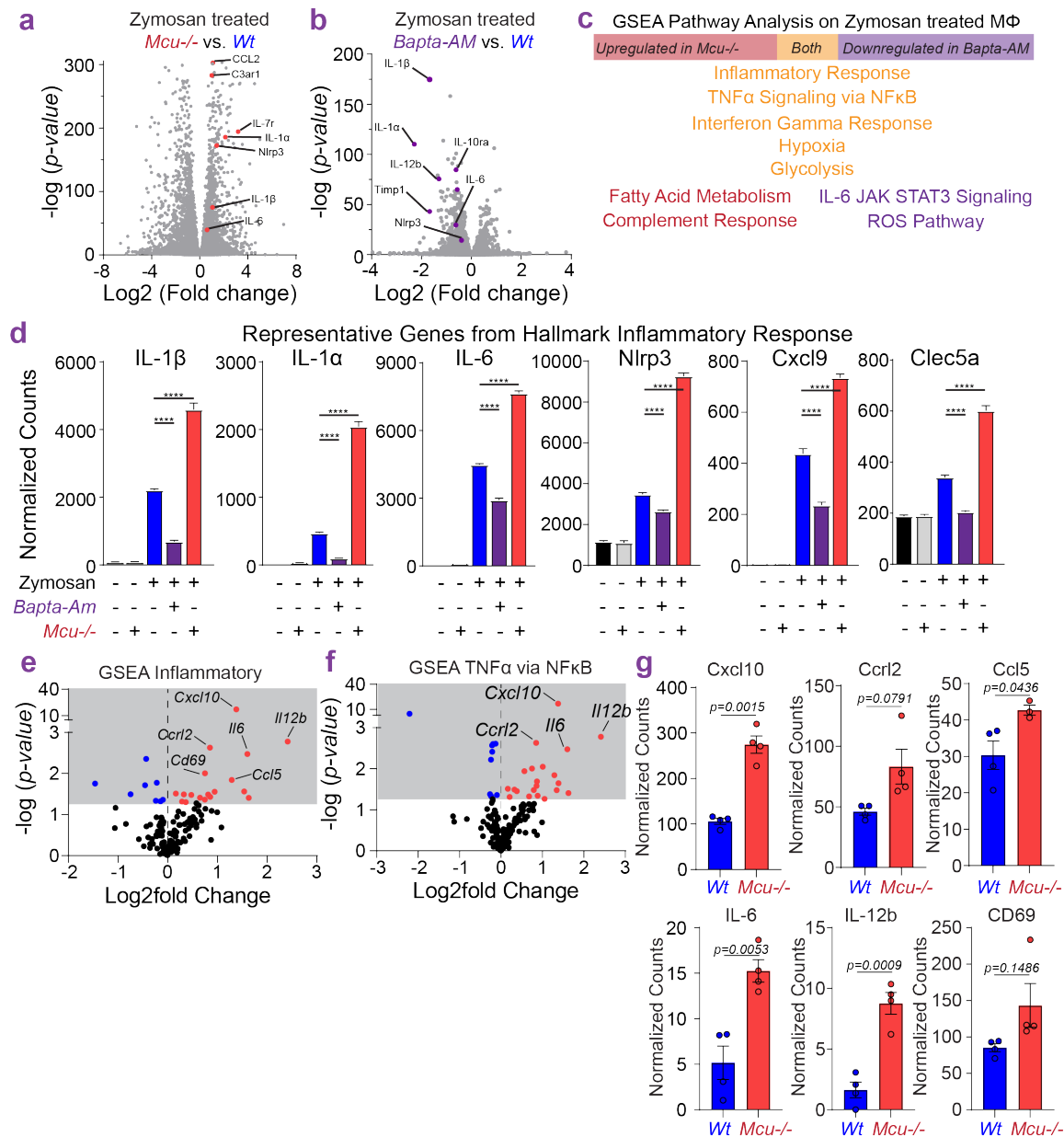


Figure 15: Bulk RNA-seq on *Mcu*^{-/-} BMDMs-Y reveals hyper-inflammatory phenotype in response to fungal pathogens and under baseline conditions.

- a.** Volcano plot showing increased expression of inflammatory genes in *Mcu*^{-/-} BMDMs, compared to *wt* BMDMs, treated with zymosan for 3 hours.
- b.** Volcano plot showing reduced expression of inflammatory genes in *BAPTA-AM* loaded BMDMs, when compared to unloaded BMDMs, treated with zymosan for 3 hours.
- c.** GSEA pathway analysis of *Mcu*^{-/-}, *BAPTA-AM* loaded (*wt*) and unloaded *wt* BMDMs stimulated with zymosan for 3 hours. Pathways upregulated in *Mcu*^{-/-} are shown in red, pathways downregulated in *BAPTA-AM*-loaded are shown in purple, and pathways upregulated in *Mcu*^{-/-} and also downregulated in *BAPTA-AM*-loaded are shown in yellow.
- d.** Normalized counts for representative genes in the GSEA hallmark inflammatory response pathway. Error bars represent SEM; $p < 0.0001$ (****), $p \leq 0.001$ (***), $p \leq 0.01$ (**), $p \leq 0.05$ (*) determined by the one-way ANOVA.
- e.** Volcano plot showing expression of genes of the GSEA inflammatory response pathway in unstimulated *Mcu*^{-/-} macrophages, compared to their *wt* counterparts.
- f.** Volcano plot showing expression of genes of the GSEA TNF α -NF κ B pathway in unstimulated *Mcu*^{-/-} macrophages, compared to their *wt* counterparts.
- g.** Normalized counts for representative genes in the GSEA hallmark inflammatory response pathway. Error bars represent SEM; *p-value* determined by Welch's T test.

Figure 16: Analysis of Ca^{2+} -sensitive inflammatory gene profiles point to a key role for RelA family of transcription factors.

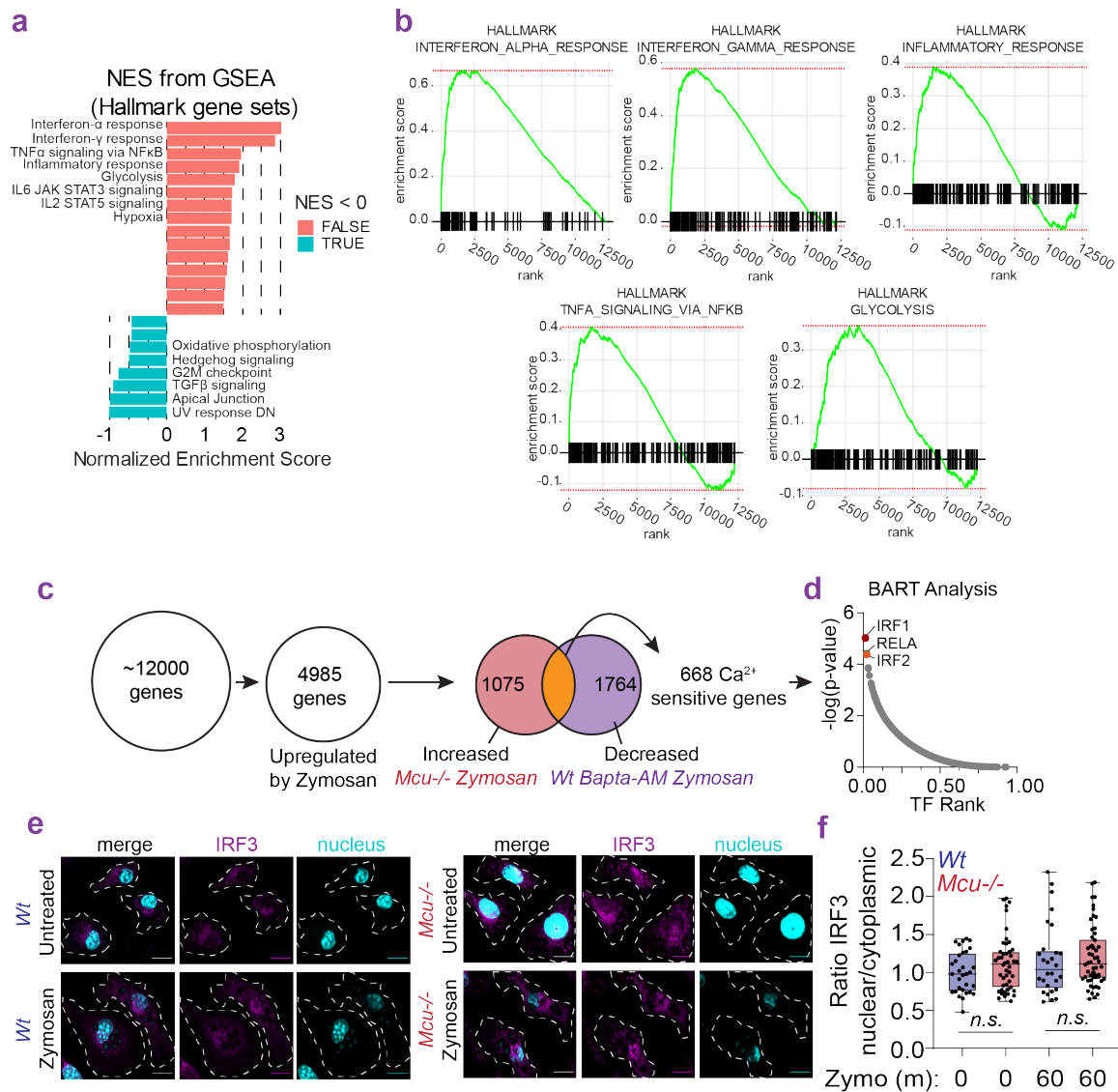


Figure 16: Analysis of Ca²⁺-sensitive inflammatory gene profiles point to a key role for RelA family of transcription factors.

- a.** GSEA hallmark gene set enrichment analysis based on DSeq2 analysis of *Mcu*^{-/-} versus *wt* BMDMs at baseline (untreated). Pathways are ranked by statistical significance (*p-value*) and plotted with normalized enrichment scores.
- b.** Gene set enrichment analysis of GSEA pathways that are differentially expressed in *Mcu*^{-/-} versus *wt* BMDMS at baseline (unstimulated). Enrichment scores (ES) are plotted on y-axis and genes ranked in ordered dataset are plotted in x-axis.
- c.** Schematic showing gene transcripts used for BART analysis.
- d.** Binding Analysis for Regulation of Transcription (BART) analysis of 668 mCa²⁺ sensitive genes identified in panel A. Transcription factor (TF) rank is plotted against the $-\log(p\text{-value})$ for each identified transcription factor.
- e.** Representative images from *wt* and *Mcu*^{-/-} macrophages, untreated or stimulated with zymosan, for 30 minutes and immunostained for IRF3 and nuclei (DAPI). Outline of cells was determined by bright field image.
- f.** Quantified nuclear to cytoplasmic ratios of IRF3 fluorescence intensities in *wt* and *Mcu*^{-/-} macrophages, unstimulated and zymosan-stimulated. Box and whiskey plots represent the min to max values for each data set. Line is at the median; *significance* was calculated by one-way ANOVA test and found insignificant.

Analysis of Ca²⁺-sensitive inflammatory gene expression points to a key role for RelA family of transcription factors.

We applied the Binding Analysis for Regulation of Transcription (BART) analysis¹⁴⁴ to predict transcriptional regulators of the 668 mCa²⁺-sensitive genes we identified (**Figure 16c – Figure 16d**). This analysis complemented our *ex vivo* experiments by implicating the RelA family, which includes NFκB, as being the responsible transcription factors. However, this analysis also suggested that transcription by interferon regulatory transcription factor (IRF) family proteins IRF1 and IRF3 is regulated by mCa²⁺-uptake. However, unlike NFκB, we did not find any enhancement of IRF3 translocation in *Mcu*^{-/-} cells (**Figure 16e – Figure 16f**). It is however possible that Ca²⁺-signaling regulates an ancillary process of IRF3-mediated gene transcription.

siRNA mediated *Mcu* knockdown in human blood born macrophages increases their inflammatory output.

As illustrated (**Figure 18a**), we differentiated Human Monocyte-derived Macrophages (HMDMs) by first enriching the human monocytes from donor buffy coats and then culturing them for 7 days in growth media supplemented with M-CSF. Flow cytometry analysis confirmed proper differentiation of the HMDMs. The HMDMs exhibited high density staining of the macrophage markers CXCL10 and CD86, which were absent on undifferentiated monocytes on day 0 (**Figure 18b – Figure 18c**). The siRNA-mediated knockdown of *MCU* successfully reduced the mRNA levels of *MCU*, as measured by the qRT-PCR analysis of *MCU Exon 3* as well as *Exon 6* (**Figure 18d**). Comparison of the mitochondrial Ca²⁺ uptake capacity clearly showed a robust uptake in HMDMs transfected with scrambled siRNA control (*siNT*-HMDMs) and a significantly diminished mCa²⁺ uptake in HMDMs transfected with *MCU* siRNA (*siMCU*-HMDMs) (**Figure 17a**). When stimulated with zymosan, the control *siNT*-HMDMs displayed Ca²⁺ oscillations throughout the 30 minutes of imaging. But similar to BMDMs-O and *Mcu*^{-/-} BMDMs, the *siMCU*-HMDMs showed a significant increase in both the

frequency and amplitude of the Ca^{2+} oscillations (**Figure 17b – Figure 17c**). The spatiotemporal analysis of the Ca^{2+} oscillations also revealed a similarity to mouse wt BMDMs-O and *Mcu*^{-/-} BMDMs-Y. The *siMCU*-HMDMs exhibited significantly more Ca^{2+} spikes on an individual basis (**Figure 17d – Figure 17f**). Then we checked the inflammatory response in *siMCU*-HMDMs and found that, as predicted, the expression levels of proinflammatory cytokines IL-1 β , IL-6 and TNF α were significantly higher when compared to *siNT*-HMDMs (**Figure 17g**). Similar results were seen with LPS stimulation (**Figure 18e**). These results show that the sensitivity of inflammatory response to mitochondrial Ca^{2+} uptake is conserved and can be demonstrated readily in human macrophages.

Figure 17: Mcu knockdown in human-monocyte derived macrophages recapitulates mouse phenotype.

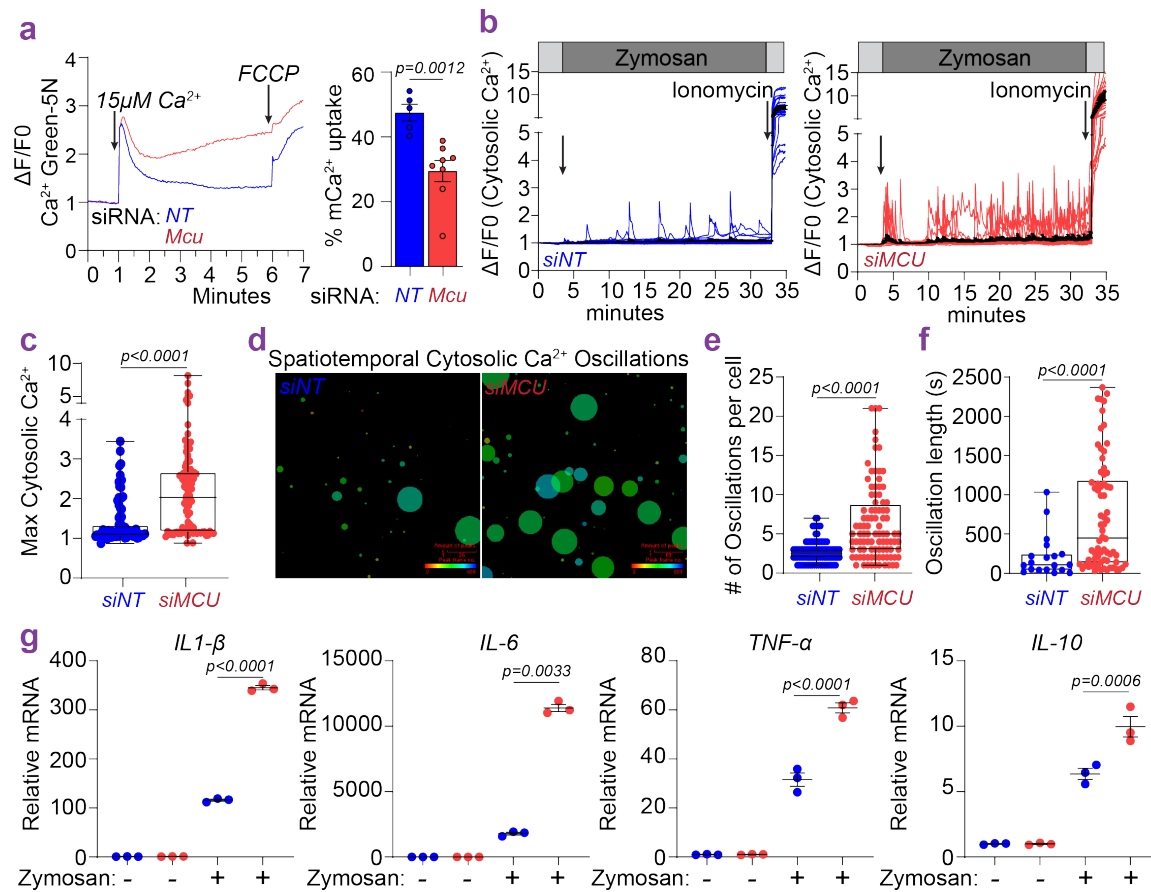


Figure 17: Mcu knockdown in human-monocyte derived macrophages recapitulates mouse phenotype.

- a.** Representative trace for a mitochondrial Ca^{2+} uptake in permeabilized *siNT* and *siMCU-transfected* HMDMs. *Right panel* shows quantification of mitochondrial Ca^{2+} uptake. Error bars represent SEM; $p=0.0012$ determined by t-test.
- b.** Cytosolic Ca^{2+} Oscillations in *siNT* and *siMCU-transfected* HMDMs. $\Delta F/F_0$ values for Fura-2-AM loaded macrophages are plotted. Images were taken every 3 secs.
- c.** Maximum cytosolic Ca^{2+} levels in individual cells determined by max $\Delta F/F_0$ values. Box and whiskey plots represent the min to max values for each data set. Line is at the median; $p<0.0001$ according to Welch's t test, two-tailed.
- d.** CALIMA maps depicting spatiotemporal aspects of cytosolic Ca^{2+} elevations. Circle size is proportional to number of Ca^{2+} spikes originating from that cellular location. Circle colors represent the time at which the first Ca^{2+} spike was detected at that point.
- e.** Oscillation frequency determined for individual cells. Box and whiskey plots represent the min to max values for each data set. Line is at the median; $p<0.0001$ according to Welch's t test, two-tailed.
- f.** Oscillation length determined for individual cells. Box and whiskey plots represents the min to max values for each data set. Line is at the median; $p<0.0001$ according to Welch's t test, two-tailed.
- g.** Increased gene expression of IL-1 β , IL-6, TNF α , and IL-10 mRNA in *siMCU-transfected* zymosan-stimulated HMDMs. Error bars represent SEM; *P-values* determined by the one-way ANOVA test.

Figure 18: Validation of *Mcu* knockdown in HMDMs.

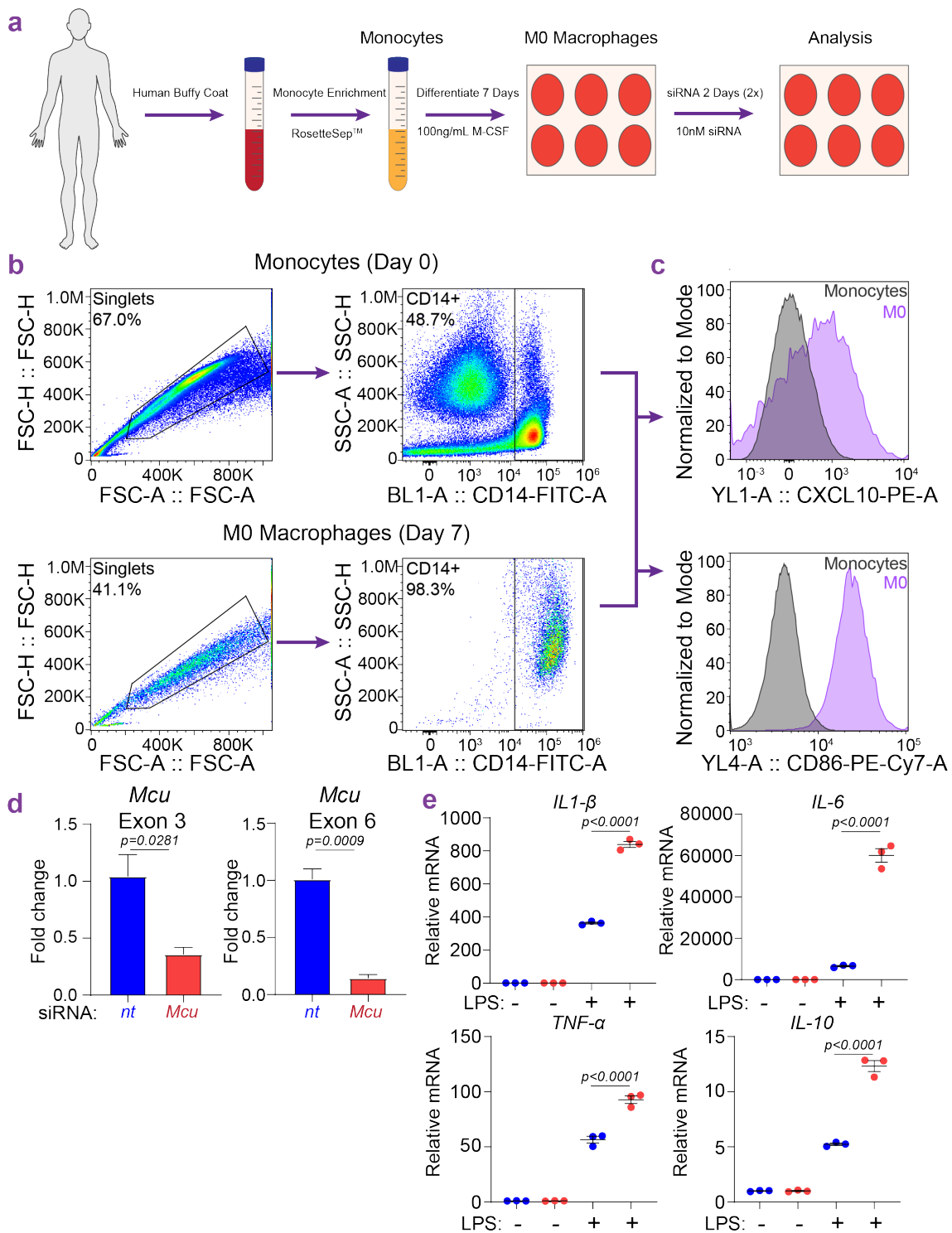


Figure 18: Validation of M_{cu} knockdown in HMDMs.

- a.** Schematic for isolation and differentiation of HMDMs from human buffy coats.
- b.** Flow cytometry-based validation of enriched human monocytes and differentiated HMDMs.
- c.** Upregulation of CXCL10 and CD86 in HMDMs after differentiation from monocytes
- d.** *MCU* mRNA levels in *siNT* and *siMCU-transfected* HMDMs. Error bars represent SEM; *p* values determined by unpaired t-test.
- e.** Fold changes in the gene expression of IL-1 β , IL-6, TNF α , and IL-10 mRNA in *siNT* and *siMCU* HMDMs. Cells were stimulated with vehicle or LPS (1 μ g/mL). Error bars represent SEM; *p*-values determined by the one-way ANOVA.

Discussion

In this study, we report a conceptually simple, but surprising discovery that mitochondrial Ca^{2+} uptake capacity in macrophages drops significantly with age. The ensuing amplification of cytosolic Ca^{2+} -signaling promotes NF κ B activation, renders the macrophages prone to chronic low-grade inflammatory output at baseline and hyper-inflammatory when stimulated. Although mitochondrial dysfunction has long been a suspected driver of aging, our study pinpoints the Mitochondrial Calcium Uniporter (MCU) complex as a keystone molecular apparatus that links age-related changes in mitochondrial physiology to macrophage-mediated inflammation.

Our hypothesis that reduced mitochondrial Ca^{2+} -uptake in macrophages drives inflammaging emerged from our analyses of age-related gene expression in different human tissues. Gene expression analyses of human blood revealed clear signs of chronic age-associated inflammation. These findings support the idea that gene-expression analysis of human blood can be used to monitor biomarkers of age-related low-grade inflammation. The genes associated with inflammatory responses were upregulated in the blood cells of older humans while the genes associated with oxidative phosphorylation, a mitochondrial process were downregulated. Both chronic low-grade inflammation and mitochondrial dysfunction are known hallmarks of aging but clear mechanistic links between these two processes have not been defined with clear links to human biology^{92,145}. For example, defective mitophagy in *Parkin*^{-/-} mice contributes to inflammaging by shedding mitochondrial DNA as an inflammatory stimulus¹⁴⁵. But a progressive age-associated decline in mitophagy is not evident in human myeloid cells and in any case, it would not explain the lowered activation threshold in the macrophages of aged humans. If one supposes that there is a steady age-associated shedding of inflammatory mediators from senescent cells, our findings predict that the decreased mitochondrial Ca^{2+} -uptake capacity will render the macrophages hyper-responsive to such age-associated inflammatory stimuli and thereby drive inflammaging. Although we

chose to focus on macrophage-mediated inflammation, the broad outlines of the mechanistic model are likely applicable to other myeloid cells such as neutrophils and mast cells too, and that is an important line for future investigations.

A major finding of this study is that macrophages derived from older mice exhibit a marked reduction in mitochondrial Ca^{2+} -uptake and increased cytosolic Ca^{2+} oscillations in response to inflammatory stimulus. We also demonstrate that *Mcu*^{-/-} BMDMs derived from young mice recapitulate the increased cytosolic Ca^{2+} signals seen in BMDMs derived from old mice. In this study, we used zymosan as a pathogen-derived inflammatory stimulus, but this general mechanism should also hold for endogenous tissue-damage associated inflammatory stimuli like ATP. Macrophages are constantly exposed to such purinergic signals¹⁴⁶ and our model predicts that in older mice and humans, the reduced Ca^{2+} -buffering capacity of mitochondria will render the myeloid cells hyper-responsive to chronic exposures to such purinergic signals. In *ex vivo* conditions, like macrophages derived from older mice, the *Mcu*^{-/-} macrophages show a hyper-inflammatory response when stimulated and even without any stimulation, RNAseq analysis shows clear signs of chronic low grade inflammatory output. Whether *Mcu*^{-/-} mice are hyper-inflammatory to all kinds of inflammatory stimuli is an outstanding question and a systematic survey of different inflammatory stimuli will help establish whether this phenomenon shows any dichotomies. In addition to increased inflammation, a reduction in mitochondrial Ca^{2+} uptake also affects the ability of macrophages to phagocytose and kill pathogens, an immunological deficit known to be age-related. Analysis of genes that are especially sensitive to mitochondrial Ca^{2+} -uptake points to RelA family as the key transcription factors involved in this process. Consistently, we show that the nuclear translocation of NF κ B, which is central to the inflammatory response, is greatly promoted when mitochondrial Ca^{2+} -uptake is diminished. Notably, in T-cells, the loss of m Ca^{2+} -uptake also results in hyperactivation of NFAT¹³², a transcription factor that is exquisitely sensitive to Ca^{2+} -signaling. But in contrast to NFAT regulation, where Ca^{2+} is known to regulate NFAT nuclear

translocation through the Ca^{2+} -activated phosphatase Calcineurin^{147,148}, the precise mechanisms through which Ca^{2+} regulates NF κ B translocation are not entirely clear. Along similar lines, we do not yet fully understand the regulation of the mitochondrial Ca^{2+} -uptake. In a landmark study, Kirichok and colleagues used direct patch clamp recordings of mitoplasts to demonstrate that MCU current density varies greatly between tissues⁵⁰. Remarkably, they found that MCU current densities in the cardiac mitoplasts from the newborn mice were nearly five times larger than those found in the adult counterparts. In accord with those findings, our analysis of the human gene expression data shows that the expression of *MCU* in the heart reduce progressively with age. In addition to age-related changes in gene expression, other ancillary mechanisms, such as post-translational modifications of the MCU complex are also going to be very relevant to the overall regulation of the mitochondrial Ca^{2+} -uptake. Future investigation may reveal novel molecular components that play an important role in inflammaging as upstream regulators of the MCU complex.

In contrast to immediate-early inflammatory signaling, the functional polarization programs are highly complex and far more difficult to understand using *ex vivo* approaches. The older and simplistic M1/M2 polarization framework depends on *ex vivo* culture in highly artificial conditions and the outcomes are very sensitive to minute changes in initial starting conditions. Another reason M1/M2 polarization study are steadily falling out of favor among innate immunologists is that they are not proving to be physiologically relevant. *In vivo*, macrophages integrate the plethora of signals in their microenvironment and acquire a much wider spectrum of functionally specializations and cellular heterogeneity. Nevertheless, we carried out these studies to evaluate the role of mCa^{2+} -uptake in shaping the functional plasticity of macrophages. Predictably, the results show that in the absence of MCU, the macrophages polarize abnormally but without a striking skew toward either of the artificial poles defined by this paradigm. A recent study showed that *McuB*, a negative regulator of

MCU, also influences inflammatory gene programs but this study concluded a clearer skew toward M1-like phenotype¹²³. Overall, mCa²⁺ uptake is emerging as a crucial regulator of innate immunity and inflammatory responses, with MCU function implicated in macrophage polarization^{123,124}, host defense^{122,125} and tissue homeostasis¹²⁶⁻¹²⁸. Our study takes a major step forward by revealing an exciting new role for mCa²⁺-uptake in age-associated inflammation and it defines an immediate-early mechanistic paradigm through which mCa²⁺ uptake regulates cytosolic Ca²⁺ dynamics and NFκB-mediated transcriptional programs in both human and mouse macrophages.

A major paradox in the field of mitochondrial Ca²⁺-signaling is that despite the fact that this machinery is highly conserved in invertebrates and vertebrates⁵³, and expressed ubiquitously in mammalian tissues, the deletion of *Mcu*, in the mixed background, yields smaller but viable mice⁵¹. These mice display moderate defects in skeletal muscle function⁵¹ but the overall phenotype is surprisingly mild for a process that is so well-conserved. The phenotype of global *Mcu*^{-/-} mice is likely confounding in this respect because when a gene is deleted during embryogenesis, there is often a developmental compensation (not necessarily in the same molecular function) around such deletion. More generally, it looks increasingly that the salience of MCU functions has been underestimated because of the relatively mild phenotypes in the global knockouts. It is now becoming increasingly clear that a major role for mitochondrial Ca²⁺-signaling is tied to innate immune responses, the salience of which is largely masked in unchallenging conditions of a mouse vivarium. Recent studies establish that far from being a redundant Ca²⁺-buffering system, this molecular apparatus, centered on MCU and its regulatory subunits, has a profound role in host defense and inflammatory processes. Ironically, a steady age-associated erosion of its activities not only retards the innate immune responses to fungal pathogens¹²², but also drives chronic low-grade inflammation. Interestingly, *Mcu*-mutant flies show reduced lifespan⁶⁶ but analyses of *Mcu*-null hemocytes, the cells that constitute the drosophila innate

immune system, were not carried out. In mammals, tissue-resident macrophages occupy specialized niches in all organ systems. Age-associated decrease in the mitochondrial Ca^{2+} -uptake capacity in these specialized tissue-resident macrophages may increase local inflammation and thereby have a major impact on organ physiology and homeostasis. An intriguing possibility is that resident macrophages of certain organ systems may be especially susceptible to such age-related changes. Our study sets the stage for many such research directions that may ultimately allow us to slow the onset and progression of many age-related diseases where chronic inflammation plays either a germinating or exacerbating role.

Acknowledgements

We thank the members of the Desai lab for their scientific insights and feedback. We thank Drs. Hervé Agaisse (UVA), Doug Bayliss (UVA), Michelle Bland (UVA), and Kevin Lynch (UVA) for helpful and timely advice as Thesis Committee advisors to PVS. We also thank the following core facilities for their technical resources and support: UVA Flow Cytometry Core, Carter Immunology Center Flow Cytometry Core, Advanced Microscopy Facility Core (UVA) and the UVA Research Histology Core.

Author Contributions

Conception: P.V.S., B.N.D.; **Research Design:** P.V.S., B.N.D.; **Investigation:** P.V.S., T.K.D., M.E.S., X.Z., S.V. L.H., R.O., S.E.E.; **Data analysis:** P.V.S., M.E.S., S.V., L.H., P.V.S; **Resource assistance:** J.K.; **Writing - Draft and Editing:** P.V.S., T.K.D., B.N.D.; **Project Administration:** B.N.D.

Declaration of Interests

The authors declare that they have no conflicts of interest to disclose

Resource Availability**Lead Contact**

Further information and requests for resources and reagents should be directed to and will be fulfilled by the Lead Contact, Bimal N. Desai: bdesai@virginia.edu

Materials Availability

All unique/stable reagents generated in this study are available from the Lead Contact with a completed Materials Transfer Agreement.

Experimental Model and Subject Details

Mouse Strains

Male and female mice aged 15 to 25 weeks (young) and 80-90 weeks (old) were used for all experiments. C57BL/6 mice were purchased from Jackson Laboratories (Stock: 000664) within indicated age ranges. For wt and *Mcu*^{-/-} experiments mice were used between ages 15-25 weeks for all experiments. *Mcu*(*M*)/*fl/fl* Cx3cr1 cre mice were generated by crossing B6;129S-Mcutm1.1Jmol/J (Jackson Laboratories; 029817) mice to B6J.B6N(Cg)-Cx3cr1tm1.1(cre)Jung/J (Jackson Laboratories; 025524). Genotyping of *Mcu*(*M*)/*fl/fl* was performed using Jax genotyping protocols for B6J.B6N(Cg)-Cx3cr1tm1.1(cre)Jung/J and B6;129S-Mcutm1.1Jmol/J strains. Mice were housed and bred in accordance with policies and procedures of the University of Virginia Institutional Animal Care and Use Committee (IACUC).

Cell culture

All cells were grown and maintained at 37°C, 5% CO₂. Bone marrow-derived macrophages (BMDMs) were isolated and cultured as previously described¹⁴⁹. In brief, bone marrow was extracted from mouse femur and tibia via centrifugation. The RBCs were lysed with ACK lysis buffer and the remaining cells were counted and plated on petri dishes at a density of 2-4x10⁶ cells/ plates in BMDM Media (RPMI 1640 + 10% FBS + 20% L929-conditioned media). Cells were differentiated for 7 days, and media was replaced every 3 days. For experiments BMDMs were used between days 9 - 14 post-harvest.

Methods

GTEx and differential gene expression analysis

GTEx Analysis V8, gene counts and metadata were downloaded from the GTEx portal (gtexportal.org)¹²⁹ and analyzed using RStudio. Expression profile data were obtained for different tissues, binned into age groups and then subjected to differential gene expression analysis using DESeq2¹⁵⁰ R package. PCA plots were generated using plotPCA function. The differentially expressed genes were ranked based on log2fold change and FDR corrected p-values. The ranked list was then used to perform pathway analysis using GSEA software¹⁵¹. For the analysis of genes associated with mitochondrial functions, the differentially expressed genes were uploaded to MitoXplorer1.0¹³⁰ for pathway analysis. Comparative plots were generated for specified pathways and Log2fold change was plotted for individual genes.

Mitochondrial Ca²⁺ uptake in permeabilized macrophages

Ca²⁺ uptake assay was adapted for macrophages from Wettmarshausen, et al¹⁵². Cells were washed two times in D-PBS (w/o Ca²⁺ and Mg²⁺) and resuspended in ICM buffer containing 125 mM KCl, 1 mM MgCl₂, 2 mM KH₂PO₄, 20 mM HEPES, 5 mM succinate, 5 mM malate, 5 mM glutamate and 0.1 μM calcium green-5N. Cells were immediately permeabilized with 35 μM digitonin for 5 minutes prior to recording on a FlexStation plate reader. Calcium green-5N fluorescent intensity was recorded every 2 seconds for 7 minutes with injections of 10 μM CaCl₂ and 10 μM FCCP at indicated times.

Cytosolic Ca²⁺-imaging using ratiometric Fura-2

For ratiometric Ca²⁺ imaging, macrophages were incubated for 30 min with gentle agitation at RT with 5 μM Fura-2-AM, 0.02% of pluronic acid and 500 μM probenecid in Ringer solution ([in mM] 155 NaCl, 4.5 KCl, 2 CaCl₂, 1 MgCl₂, 5 HEPES, 10 glucose, pH 7.4). Fura-2 emissions were collected at 510 nm and

with 340/380 nm excitation. Excitation was performed using a DG4 Illuminator (Sutter Instruments). Imaging was carried out on Zeiss Cell Observer microscope fitted with an ORCA-Flash 4.0 V2 CMOS camera (Hamamatsu). Image acquisition and analysis were carried out using the SlideBook 6 software. Analysis was performed using a background subtraction of 5 ROIs drawn evenly across the field of view for both 340nm and 380nm. The Fura-2 ratio of emission at 340 nm and 380 nm was calculated and treated as F value. $\Delta F/F_0$ values were calculated by taking the average of the first 1 minute of imaging as F_0 . Max cytosolic Ca^{2+} values are calculated as the max value achieved during stimulation from the $\Delta F/F_0$ calculations. Number of oscillations were determined by counting the number of times an individual cell reached >1.2 fold ($\Delta F/F_0$). Oscillation length was determined by measuring the number of frames where the Ca^{2+} -level sustained an elevation >1.2 fold ($\Delta F/F_0$). This value was calculated for each oscillation that occurred within a given cell.

CALIMA analysis

Images acquired from cytosolic Ca^{2+} imaging were uploaded into the CalciumImagingAnalyser from Radstake, et al¹³³. ROIs were drawn manually over cells and processed for recorded cell activity. Spike detection parameters were set to same values for each replicate and excel sheets were exported for analysis in PRISM.

Bulk RNAseq analysis

On average we received 30 million paired end sequences for each of the replicates. RNAseq libraries were checked for their quality using the fastqc program (<http://www.bioinformatics.babraham.ac.uk/projects/fastqc/>). The results from fastqc were aggregated using multiqc software¹⁵³. In-house developed program was used for adaptor identification, and any contamination of adaptor sequence was removed with cutadapt (<https://cutadapt.readthedocs.io/en/stable/>). Reads were then mapped with the

“splice aware” aligner ‘STAR’¹⁵⁴, to the transcriptome and genome of mm10 genome build. The HTseq software¹⁵⁵ was used to count aligned reads that map onto each gene. The count table was imported to R to perform differential gene expression analysis using the DESeq2 package¹⁵⁰. Low expressed genes (genes expressed only in a few replicates and had low counts) were excluded from the analysis before identifying differentially expressed genes. Data normalization, dispersion estimates, and model fitting (negative binomial) was carried out with the DESeq function. The differentially expressed genes were ranked based on the log2fold change and FDR corrected p-values. The ranked file was used to perform pathway analysis using GSEA software¹⁵¹. The enriched pathways were selected based on enrichment scores as well as normalized enrichment scores.

Binding Analysis for Regulation of Transcription (BART)

Gene list of 668 Ca²⁺ sensitive genes was uploaded into the BART web interface developed and maintained by the Chongzhi Zang lab at the University of Virginia¹⁴⁴. The software identified the most likely transcription factors regulating the input genes. Area under the curve and p-values were exported and plotted.

Immunoblotting

For analysis of Caspase-1 and GSDMD: After treatment, the plates were centrifuged at 400 x g for 4 min and cell free supernatants were collected. Cell lysates were prepared by directly adding 1x Laemmli sample buffer into the pellets and stored at -80°C. At the day of electrophoresis, cell lysates were transferred into a 1.5 ml tube, sonicated, and boiled at 95°C for 5 min. Collected supernatants were cleared again by centrifugation at 400xg for 5 min. Proteins in the supernatants were precipitated using 20% trichloroacetic acid (TCA), resuspended in 1x Laemmli sample buffer, and boiled at 95°C for 5 min. Cell lysates and concentrated supernatants were run on a 12% home-made SDS-PAGE gel and transferred on to a 0.45 µm PVDF membrane (Millipore) using Towbin wet transfer buffer. After transfer, Ponceau S staining was performed to

confirm equal loading of total proteins and the membrane was then blocked by 5% non-fat milk in TBST for 1 hour at room temperature. Primary antibodies were diluted in TBST and incubated at 4°C overnight. HRP conjugated secondary antibodies were diluted in TBST at 1:10,000 and incubated for 1 hour at room temperature. Membrane was developed by adding Luminata Forte Western HRP substrate (Millipore, WBLUF0100) and imaged on a Bio-Rad ChemiDoc Imager. Primary antibodies used: mouse anti-mCasp1(p20) (AdipoGen, Casper-1, 1:1000); rabbit anti-mGSDMD (Abcam, ab209845, 1:1000). Secondary antibodies used: anti-mouse, HRP (Jackson, 115-035-003); anti-rabbit, HRP (Jackson, 111-035-144).

Nuclear and cytoplasmic fractions

The ThermoScientific NE-PER Nuclear Cytoplasmic Extraction Reagent kit was used to generate nuclear and cytosolic fractions from cells following zymosan stimulation. Briefly, cells underwent reagent-based lysis using cytoplasmic extraction reagents I & II followed by centrifugation for 5 min at 16,000 g to separate nuclei from cytosolic fractions. The nuclei were then lysed using the nuclear extraction reagent and centrifuged for 5 min at 16,000 g. The resulting supernatant contained the nuclear extract and was used for subsequent western blotting.

qPCR

For all qPCR experiments macrophages cell were plated at ~80% confluency into tissue culture treated plates and rested overnight. For inflammatory gene expression, the following day BMDMs were stimulated with Zymosan A BioParticles, ThermoFisher (Cat#Z2849) at 2particles/cell. For pharmacological pretreatments, on day of experiment BMDMs were treated with inhibitors for 30 minutes prior to addition of Zymosan, as described above. Inhibitor information and concentration used: BAPTA-AM, ThermoFisher (Cat# B6769) (10 μ M), Ionomycin, Cayman Chemicals (Cat# 10004974) (1 μ M), BTP2, Sigma (Cat#

203890-M) (10 μ M), Zegocractin, MedChemExpress (Cat# HY-101942) (1 μ M), AZD7545, MedChemExpress (Cat# HY-16082) (1 μ M). For M1 vs M2 polarization, BMDMs were treated either with IFN- γ , R&D Systems (Cat# 485-MI-100/CF) (100 ng/ml) and LPS, Invivogen (Cat# tlrl-eb1ps) (100 ng/ml; to induce polarization toward a M1 phenotype) or with IL-4, R&D Systems (Cat# 404-ML-010) (20 ng/ml; to induce polarization toward a M2 phenotype). Total RNA was isolated from treated cells using RNeasy Plus Mini Kit. Following isolation, RNA concentration was determined using a NanoDrop 2000c spectrophotometer. RNA was converted to cDNA in a two-step reverse transcriptase process using the Promega Reverse Transcription Master Mix. Following cDNA synthesis, a Bio-Rad CFX Connect Real-Time system was used to perform quantitative PCR reactions with SYBR Select Master Mix and 1 to 5 ng cDNA per well in a 96-well plate.

Primers for qPCR

Arg1 Ms Forward (5' – CTGACAACCAGCTCTGGGAA – 3'), Arg1 Ms Reverse (5' – TCCTGGTACATCTGGGAACTTT – 3'), Fizz1 Ms Forward (5' – ACTTCTTGCCAATCCAGCTAAC – 3'), Fizz1 Ms Reverse (5' – CACCCAGTAGCAGTCATCCC – 3'), CD206 Ms Forward (5' – TTCAGCTATTGGACGCGAGG – 3'), CD206 Ms Reverse (5' – GAATCTGACACCCAGCGGAA – 3'), McuB Ms Forward (5' – GCCTTCCCTTGGTAACCCTC – 3'), McuB Ms Reverse (5' – ATTTCACTGCCATCTGCCGT – 3'), EMRE Ms Forward (5' – AGAACTTCGCTGCTCTGCTT – 3'), EMRE Ms Reverse (5' – GCTCCCTGTGCCCTGTTAAT – 3'), Micu2 Ms Forward (5' – AAGGTAGCGACTGGACAGGA – 3'), Micu2 Ms Reverse (5' – TGTGACACCCATAAGCCTCG – 3'), Micu1 Ms Forward (5' – AATTGCCAGGAACGAGAAA – 3'), Micu1 Ms Reverse (5' – GAGGACTGTTGTGAGGAAGATG – 3'), Mcu Ms Forward 1 (5' – TGAACGACGTGAAGACCCTG – 3'), Mcu Ms Reverse 1 (5' –

TTCGTACCTTCTCCAGGGGG – 3'), Mcu Ms Forward 2 (5' –
 CCCCCTGGAGAAGGTACGAA – 3'), Mcu Ms Reverse 2 (5' –
 AACTGGGTGGCCATGTAGG – 3'), IL-1 β Ms Forward (5' –
 GCAACTGTTCTGAACTCAACT – 3'), IL-1 β Ms Reverse (5' –
 ATCTTTTGGGGTCCGTCAACT – 3'), iNOS Ms Forward (5' –
 GTTCTCAGCCAACAATACAAGA – 3'), iNOS Ms Reverse (5' –
 GTGGACGGGTTCGATGTCAC – 3'), IL-6 Ms Forward (5' –
 TAGTCCTTCCTACCCAATTTCC – 3'), IL-6 Ms Reverse (5' –
 TTGGTCCTTAGCCACTCCTTC – 3'), TNF α Ms Forward (5' –
 CCCTCACACTCAGATCATCTTCT – 3'), TNF α Ms Reverse (5' –
 GCTACGACGTGGGCTACAG – 3'), IL-1 β Human Forward (5' –
 TCGCCAGTGAAATGATGGCT – 3'), IL-1 β Human Reverse (5' –
 TGGAAGGAGCACTTCATCTGTT – 3'), IL-6 Human Forward (5' –
 TTCTCCACAAGCGCCTTC – 3'), IL-6 Human Reverse (5' –
 GGCGGCTACATCTTTGGAAT – 3'), TNF α Human Forward (5' –
 CCTGCTGCACTTTGGAGTGA – 3'), TNF α
 Human Reverse (5' – CAGCTTGAGGGTTTGCTACAAC – 3'), IL-10 Human
 Forward (5' – TACGGCGCTGTCATCGATTT – 3'), IL-10 Human Reverse (5' –
 TAGAGTCGCCACCCTGATGT – 3').

Immunofluorescence

Cells were plated overnight on coverslips prior to experiments. BMDMs were stimulated with Zymosan A BioParticles, Thermofisher (Cat#Z2849) at 2particles/cell for indicated times. Following treatments, coverslips were washed 3x in PBS to remove loose/non-adherent cells. Coverslips were fixed in 4% PFA, 4% sucrose (30 min, RT). Coverslips were washed 3X in wash buffer (PBS with 0.05% Tween-20), blocked and permeabilized at RT for 1 hour in B/P buffer (1% BSA, 0.1% Triton X-100, and 0.05% Tween-20 in PBS), and then incubated with primary antibody diluted in B/P buffer overnight at 4°C. Coverslips were washed 3X in wash buffer and incubated at RT with the appropriate secondary antibody

in B/P buffer for 2 h, followed by 3X washes in wash buffer. Coverslips were mounted on glass slides (ProLong Gold Antifade; ThermoFisher #P36930), stored in a desiccated box at 4°C until imaged. Confocal microscopy was performed on Zeiss LSM880. Data was acquired with Zen Black and analyzed using ImageJ. Antibodies used for Immunofluorescence: Anti-ASC/TMS1/PYCARD Antibody (F-9): sc-271054, Santa Cruz; Anti-NFκB p65 (D14E12) XP® Rabbit mAb #8242, Cell Signaling; Anti-IRF-3 (D83B9) Rabbit mAb #4302, Cell Signaling.

MitoGenie

To analyze mitochondrial morphology and other characteristics, images were cropped into individual cells and processed using a mitochondrial analysis workflow developed by the Kashatus lab¹³¹. Images were first input into the MitoCatcher application on the MitoGenie platform, generating binarized images of segmented mitochondrial networks. The MiA application on MitoGenie was used to analyze the images of the mitochondrial networks and produce quantitative measurements describing mitochondrial morphology.

LDH assay

BMDM cells were incubated for 3 hours with LPS, Invivogen (Cat# tlr1-eb1ps) (100 ng/ml) or Zymosan A BioParticles, ThermoFisher (Cat#Z2849) (2particles/cell) at 37°C, 5% CO₂. After 3h, cells were washed 3X with HBSS, resuspended in Ringer solution ([in mM] 155 NaCl, 4.5 KCl, 2 CaCl₂, 1 MgCl₂, 5 HEPES, 10 glucose, pH 7.4) with or without Nigericin, Invivogen (Cat# tlr1-nig) (5 μM). After 24 hours, LDH was measured in the supernatants using Pierce™ LDH Cytotoxicity Assay Kit (ThermoScientific) according to manufacturer instructions.

IL-1β ELISA

BMDM cells were incubated for 3 hours with LPS, Invivogen (Cat# tlr1-eb1ps) (100 ng/ml) or Zymosan A BioParticles, ThermoFisher (Cat#Z2849)

(2particles/cell) at 37°C, 5% CO₂. After 3h, cells were washed 3X with HBSS, resuspended in Ringer solution ([in mM] 155 NaCl, 4.5 KCl, 2 CaCl₂, 1 MgCl₂, 5 HEPES, 10 glucose, pH 7.4) with or without Nigericin, Invivogen (Cat# tlrl-nig) (5 µM). After 24 hours, IL-1β was measured in the supernatants using ELISA MAX™ Standard Mouse IL-1β (Biolegend) according to manufacturer instructions.

Zymosan-Induced Peritonitis

Mcu(M)^{-/-} and *wt* mice were subjected to a model of zymosan-induced peritonitis¹⁵⁶. In brief, mice were IP injected with 55 mg/kg Zymosan-A and monitored for 24hrs for clinical scores of conjunctivitis, lethargy, changes in hair coat and grimace pain to indicate symptoms of illness. Weight was monitored every 2 hours and scoring was performed by a blinded member of the lab. Following 24 hours, mice were euthanized. Blood and peritoneal lavage fluid was collected for Luminex Analysis and cytokine detection.

Differentiation of Human Monocyte Derived Macrophages (HMDMs)

Human buffy coats from healthy donors were procured from the American Red Cross for the isolation of human monocytes. Differentiation of HMDMs was performed using PromoCell, Serum-free and Zeno-free cell culture method. In brief, buffy coats were enriched for monocytes using RosetteSep™ Human Monocyte Enrichment Cocktail. Enriched monocytes were plated on 6-well plates in monocyte attachment medium for 1 hour in a 5% CO₂, 37°C incubator. Cells were washed three times with vigorous swirling in warm monocyte attachment media to remove non-adherent cells. Cells were cultured for 7 days in Macrophage Generation Medium DXF with supplement Mix to generate HMDMs. The siRNA knockdown of *MCU* was performed two times over 48 hours using Lipofectamine 3000 with 10 nM siRNA. Antibodies used for flow cytometry: FITC anti-human CD14 Antibody, Biolegend Cat# 325603; PE/Cyanine7 anti-human CD86 Antibody, Biolegend Cat# 305421; PE anti-human CXCL10 (IP-10)

Antibody, Biolegend Cat# 519503. siRNA used for Mcu knockdown: Dharmacon Cat# L-015519-0-0005, ON-TARGETplus Human MCU (90550) siRNA – SMARTpool, 5nmol. ON-TARGETplus SMARTpool siRNA J-015519-17, MCU Target Sequence: GAUCAGGCAUUGUGGAAUA; ON-TARGETplus SMARTpool siRNA J-015519-18, MCU Target Sequence: GUUUUGACCUAGAGAAAUA; ON-TARGETplus SMARTpool siRNA J-015519-19, MCU Target Sequence: ACUGAGAGACCCAUUACAA; ON-TARGETplus SMARTpool siRNA J-015519-20, MCU Target Sequence: GUAAUGACACGCCAGGAAU.

Quantification and Statistical Analysis

Statistics

All data were analyzed using Excel (Microsoft) and GraphPad Prism 8 (GraphPad) software. All datasets were subjected to ROUT outlier test and the data points with $Q < 1\%$ were considered outliers and removed. In bar graphs, data are presented as means with error bars reflecting standard error of the mean (SEM) or as indicated in figure legends. Statistical significance ($p < 0.05$) was computed using one-way ANOVA, 2-way ANOVA, and Welch's t test (two-tailed), as indicated in figure legends. The sample size and representation of 'n' (mice, experimental repeats, or cells) is indicated in figure legends. In Box Plots, the whiskers represent min and max values, the box represents 75th and 25th percentile and the horizontal line is the median.

Chapter Three: Mitochondrial Ca²⁺-signaling is an Electrometabolic Switch to Fuel Phagosome Killing

Authors:

Philip V. Seegren^{1,2}, Taylor K. Downs^{1, 2}, Marta E. Stremaska^{2, 3}, Logan R. Harper¹, Ruofan Cao^{4, 5}, Rachel J. Olson¹, Clint M. Upchurch^{1,2}, Catherine A. Doyle^{1, 2}, Joel Kennedy¹, Eric L. Stipes¹, Norbert Leitinger^{1, 2}, Ammasi Periasamy^{4, 5}, Bimal N. Desai^{1, 2*}

Affiliations:

¹Pharmacology Department, University of Virginia, Pinn Hall, 1340 Jefferson Park Avenue, Charlottesville, VA 22908

²Carter Immunology Center, University of Virginia, 345 Crispell r. MR-6, Charlottesville, VA 22908

³Microbiology, Immunology, and Cancer Biology Department, University of Virginia, Pinn Hall, 1340 Jefferson Park Avenue, Charlottesville, VA 22908

⁴The W.M. Keck Center for Cellular Imaging, University of Virginia, Physical and Life Sciences Building (PLSB), 90 Geldard Drive, Charlottesville, VA 22904

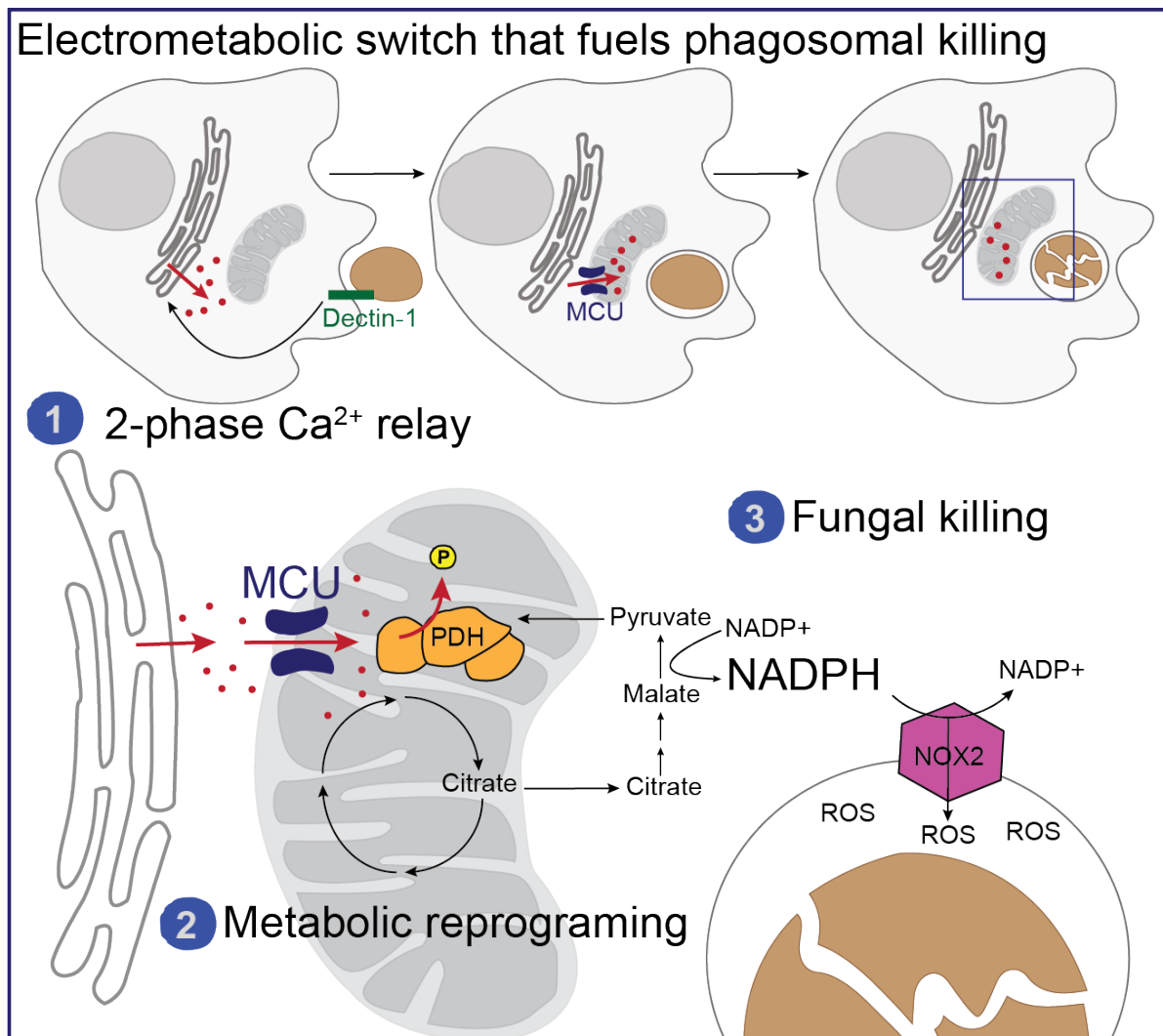
⁵Departments of Biology, University of Virginia, Physical and Life Sciences Building (PLSB), 90 Geldard Drive, Charlottesville, VA 22904

*Correspondence and Lead Contact: bdesai@virginia.edu

Note

The contents of this chapter appear as published in Cell reports. 2020 Nov 24;33(8):108411.

Graphic Abstract



Highlights

- Identification of MCU as a major regulator of phagosomal killing by macrophages
- Mice lacking *Mcu* in myeloid cells are highly susceptible to in vivo candidiasis
- Fungal pathogens elicit mitochondrial Ca^{2+} elevations using a fast 2-phase Ca^{2+} relay
- Mitochondrial Ca^{2+} signaling activates Pyruvate dehydrogenase during phagocytosis

Abstract

Phagocytes reallocate metabolic resources to kill engulfed pathogens but the intracellular signals that rapidly switch the immunometabolic program necessary to fuel microbial killing are not understood. We report that macrophages use a fast two-step Ca^{2+} -relay to meet the bioenergetic demands of phagosomal killing. Upon detection of a fungal pathogen, macrophages rapidly elevate cytosolic Ca^{2+} (phase 1) and by concurrently activating the Mitochondrial Ca^{2+} Uniporter (MCU), they trigger a rapid influx of Ca^{2+} into the mitochondria (phase 2). The mitochondrial Ca^{2+} -signaling reprograms mitochondrial metabolism, at least in part, through the activation of Pyruvate dehydrogenase (PDH). Deprived of mitochondrial Ca^{2+} signaling, the *Mcu*^{-/-} macrophages are deficient in phagosomal ROS production and defective at killing fungi. Mice lacking MCU in their myeloid cells are highly susceptible to disseminated candidiasis. In essence, this study reveals an elegant design principle that MCU-dependent Ca^{2+} -signaling is an electrometabolic switch to fuel phagosome killing.

Introduction

Sentinel cells such as macrophages and dendritic cells detect, engulf and digest invading pathogens. A precisely choreographed cell-intrinsic immune response marshals a befitting adaptive immune response through the secretion of inflammatory mediators and presentation of antigenic peptides to the T-cells¹⁵⁷. Efficient killing of the engulfed pathogen by macrophages is therefore a transformative cell-intrinsic defense process in host defense. During phagosome maturation, endosomal fusion events recruit the vacuolar ATPase (V-ATPase) and NADPH oxidase (NOX) complex to the nascent phagosome¹⁵⁸. The V-ATPase complex hydrolyzes ATP to pump protons into the phagosomal lumen, acidifying it and promoting the digestion of pathogens by acid-optimized proteases, lipases and endonucleases. The NOX complexes oxidize NADPH to inject super oxide (O_2^-) into the phagosome¹⁵⁹ and this oxidative pressure is crucial for the destruction of fungal pathogens. Sustained NOX activity is essential for fungal defense and patients with mutations in NOX present with frequent fungal infections^{160,161}. The overall process of phagosomal killing therefore requires a bioenergetic burst and macrophages are adept at rapidly reprogramming their metabolism to fuel phagosomal killing¹⁶². At the same time, within the deadly environment of the phagosome, pathogens fight for survival by adapting their own transcriptional and metabolic programs that subvert the cell-intrinsic defenses and evade destruction^{163,164}. Our understanding of the metabolic changes that fuel the anti-microbial machineries in sentinel cells such as macrophages and dendritic is mostly limited to transcriptional changes occurring 24 hours after pathogen recognition^{165,166}. While these responses are critical for inflammation and resolution⁸⁵ they don't account for the immediate and early bioenergetic demands of pathogen destruction. Our study identifies a fast two-step Ca^{2+} -relay culminating in mitochondrial Ca^{2+} signaling that is required for pathogen killing in macrophages.

In screening for ion channels that regulate the cell-intrinsic immunity, we made a serendipitous discovery that the Mitochondrial Ca^{2+} Uniporter (MCU) plays a crucial role in the killing of *C. albicans*. MCU is a Ca^{2+} -selective ion channel located in the inner membrane of mitochondria^{5,39,94}. In conjunction with its regulatory subunits MICU1 and MICU2, the MCU complex can mediate a rapid influx of cytosolic Ca^{2+} into the mitochondrial matrix^{43,44,167}. The inner mitochondrial membrane has a resting membrane potential between -160 mV to -200 mV relative to the cytosol, and the enormous driving force for cationic influx into the mitochondrial matrix can be leveraged to convert cytosolic Ca^{2+} -signaling into rapid metabolic responses. We report that in response to a fungal pathogen, macrophages rapidly elevate cytosolic Ca^{2+} and by concurrently gating open the Mitochondrial Ca^{2+} Uniporter⁹⁵ (MCU), they trigger a near instantaneous influx of Ca^{2+} into the electrically charged mitochondria. This fast two-step Ca^{2+} -relay reprograms the mitochondrial metabolism, at least in part, by activating Pyruvate Dehydrogenase, a key enzyme in the TCA cycle.

Pyruvate is the end-product of glycolysis that lies at the vital intersection of cellular metabolic network. Since its catalytic fate can govern the flux of multiple pathways, it is a keystone metabolite for metabolic reprogramming. When transported into the mitochondrial matrix, Pyruvate can either be directed toward gluconeogenesis by Pyruvate Decarboxylase or toward the TCA cycle by the Pyruvate Dehydrogenase Complex¹⁶⁸. We show that the rapid mitochondrial Ca^{2+} -signaling promotes metabolic reprogramming by activating the PDH complex in macrophages. In response to fungal pathogens, mitochondrial Ca^{2+} signaling activates the PDH and increases intracellular citrate, an intermediate of the TCA cycle. Citrate is known to be exported from the mitochondrial matrix to the cytosol for generation of NADPH through the activity of Malic Enzyme¹⁶⁹. Thus, mitochondrial Ca^{2+} signaling drives the production of NADPH necessary for phagosomal ROS production. The MCU^{-/-} macrophages are deficient in the generation of phagosomal ROS and this impairs the killing of phagocytosed *C. albicans*. The higher order immunological significance is that mice lacking MCU

in their myeloid cells and thus deficient in mitochondrial Ca^{2+} signaling are highly susceptible to disseminated candidiasis. In essence, the study reveals a design principle that MCU-dependent Ca^{2+} -signaling relay is a fast electrometabolic switch to fuel phagosomal killing. This design principle is likely significant for many other processes of cell intrinsic immunity, but this study focuses exclusively on phagosomal killing of *C. albicans*.

Results

MCU has a crucial function in cell autonomous killing of fungal pathogens.

To identify the Ca^{2+} channels necessary for macrophage fungal killing, we developed an siRNA screen in RAW264.7 cells, a murine macrophage cell line. The siRNAs used in the screen were validated to knockdown the Ca^{2+} -conducting channels expressed in macrophages (Figure 19A). After siRNA transfection, RAW264.7 macrophages were fed *C. albicans* (MOI=1) and assessed as described for pathogen killing (Figure 19B). The z-scores, which reflect a change in the capacity to kill relative to macrophages transfected with control siRNA (scrambled siRNA), are plotted against the normalized expression of the targeted ion channels in macrophages (Figure 19C). In this screen, we identified MCU as a regulator of *C. albicans* killing in macrophages (Figure 19D). A significant defect in *C. albicans* killing at MOI1 was observed with an approximately 50% reduction in *Mcu* transcript levels (Figure 20A). We substantiated this screen with additional tests using siRNA-mediated knockdown of MCU in bone marrow-derived macrophages (BMDMs) and again observed a significant defect in killing *C. albicans* (Figure 20B). To further define the function of MCU in pathogen killing by macrophages, we generated a mouse line with a *CX3CR1-Cre* driven deletion of *Mcu* in myeloid cells (herein *Mcu(M)*^{-/-} mice) (Figure 19E). The bone marrow of *Mcu(M)*^{-/-} mice differentiated normally into macrophages (data not shown) and both mRNA (Figure 19F) and protein levels (Figure 19G and Figure 20I) of MCU were depleted in *Mcu*^{-/-} macrophages. In an *in vitro* assay of mitochondrial Ca^{2+} uptake, the mitochondria isolated from

Mcu^{-/-} macrophages were deficient in their ability to rapidly take up Ca²⁺ added to the *in vitro* preparation (Figure 19H and Figure 19I). Additionally, using a permeabilized cell assay *Mcu*^{-/-} macrophages showed a striking inability to take up Ca²⁺ when compared to *wt* macrophages (Figure 19J). Surprisingly, *Mcu*^{-/-} macrophages showed no significant defect in basal ATP levels or oxygen consumption rate (OCR) (Figure 20C and Figure 20D). Analysis of mitochondrial membrane potential using JC-1 dye showed that *Mcu*^{-/-} macrophages show normal mitochondrial membrane potential (Figure 20E and Figure 20F). This was further substantiated by measuring the membrane potential using the dye TMRM. Both baseline membrane potential and FCCP-induced depolarization were nearly identical in both *wt* and *Mcu*^{-/-} macrophages (Figure 20G and Figure 20H). These analyses show that in absence of a pathogenic challenge, *Mcu*^{-/-} macrophages do not show any obvious mitochondrial dysfunction. However, when exposed to *C. albicans* in killing assays (MOI1), the *Mcu*^{-/-} macrophages exhibited a clear defect in the killing of *C. albicans* (Figure 19K) and *Saccharomyces cerevisiae* (Figure 19L). Since macrophages have been reported to undergo pyroptosis during *C. albicans* phagocytosis¹⁷⁰, we tested whether *Mcu*^{-/-} macrophages are more susceptible to *C. albicans* induced pyroptosis. We found no significant release of LDH at 6h of exposure to *C. albicans* and no difference between *wt* and *Mcu*^{-/-} macrophages (Figure 19M and Figure 19N). Together, these results reveal a role for MCU and mitochondrial Ca²⁺-signaling in the cell autonomous killing of *C. albicans*.

Figure 19: MCU has a crucial function in cell autonomous killing of fungal pathogens.

A. Schematic depicting the selection of siRNA targets for Ca^{2+} channel screen in myeloid cells.

B. Schematic depicting the *C. albicans* killing experiment in RAW264.7 cells.

C. Scatter plot showing Z-scores of *C. albicans* killing in relationship to relative gene expression. Ion channel genes that were screened are shown as individual points. Z-score calculations are described in *Methods*. Normalized expression value is the average expression level across four macrophage populations (ImmGen database). Knockdown of *Mcu* (marked) resulted in a significant deficit in *C. albicans* killing relative control.

D. Killing of *C. albicans* by macrophages transfected with control siRNA and *Mcu*-targeting siRNA. Individual replicates from the siRNA screen are shown (n=4). Error bars represent standard error of mean (SEM); $p < 0.0001$ according to Welch's t test, two-tailed.

E. Schematic showing the breeding strategy used to generate *Mcu(M)*^{-/-} mice.

F. Gene expression analysis (qPCR) of *Mcu* mRNA in *wt* (n=6, mice) and *Mcu*^{-/-} (n=6, mice) bone-marrow derived macrophages. Error bars represent SEM; $p < 0.0001$ according to Welch's t test, two-tailed.

G. Protein quantification from immunoblots of whole cell lysates from *wt* (n=7, mice) and *Mcu*^{-/-} (n=7, mice) bone-marrow derived macrophages. Error bars represent SEM; $p = 0.0014$ according to Welch's t test, two-tailed. See Figure S11 for immunoblots.

H. Mitochondrial Ca^{2+} uptake assay using mitochondria isolated from *wt* and *Mcu*^{-/-} bone-marrow derived macrophages as reported by the reduction in extramitochondrial Ca^{2+} signal, after addition of 45 μM Ca^{2+} to the isolated mitochondria.

I. Quantification of Ca^{2+} uptake in mitochondria isolated from *wt* (n=4) and *Mcu*^{-/-} (n=4) BMDMs. mCa^{2+} uptake is calculated as percent of max. Error bars represent SEM; $p < 0.0001$ according to Welch's t test, two-tailed.

J. Mitochondrial Ca^{2+} uptake assay using digitonin permeabilized BMDMs. 15 μM Ca^{2+} was added to 500,000 digitonin-permeabilized BMDMs in a 96-well plate and Ca^{2+} Green-5N fluorescence was monitored Ex/Em: 505/535 every 2 seconds for 6 minutes. 5 μM FCCP was added as positive control to uncouple mitochondria and release Ca^{2+} at the end of each run.

K. *C. albicans* killing by *wt* (n=10) and *Mcu*^{-/-} (n=10) BMDMs. Error bars represent SEM; $p=0.0015$ according to Welch's t test, two-tailed.

L. Killing of *S. cerevisiae* by *wt* (n=10) and *Mcu*^{-/-} (n=10) BMDMs. Error bars represent SEM; $p<0.0001$ according to Welch's t test, two-tailed.

M. LDH release by *wt* and *Mcu*^{-/-} BMDMs in response to *C. albicans* MOI1. LDH release is reported as a percent of maximum release (black). Error bars represent SEM; *no significant difference* was detected between *wt* and *Mcu*^{-/-} at baseline (n=4, each group) or 6 h (n=6, each group) according to Ordinary one-way ANOVA with multiple comparisons.

N. LDH release by *wt* and *Mcu*^{-/-} BMDMs in response to zymosan. LDH release is reported as a percent of maximum release (black). Error bars represent SEM; *no significant difference* was detected between *wt* and *Mcu*^{-/-} at baseline (n=4, each group) or 6h (n=6, each group) according to Ordinary one-way ANOVA with multiple comparisons.

Figure 20: Characterization of *Mcu*^{-/-} macrophages at baseline

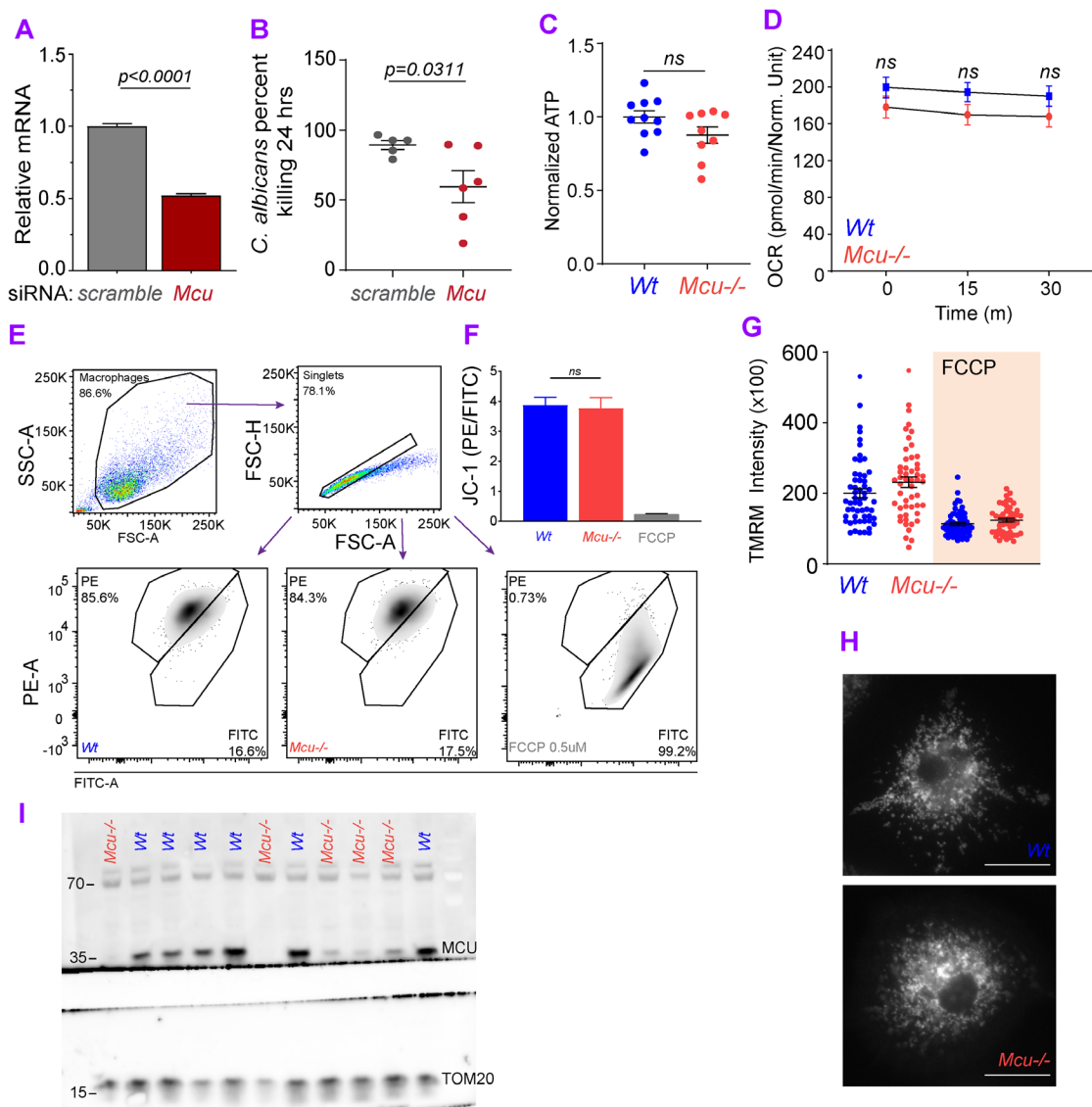


Figure 20: Characterization of *Mcu*^{-/-} macrophages at baseline

A. Gene expression analysis (qPCR) of *Mcu* mRNA in *scrambled* (n=3) and *Mcu* knockdown (n=3) RAW264.7 cells. Error bars represent SEM; $p < 0.0001$ according to Welch's t test, two-tailed

B. *C. albicans* killing by BMDMs transfected with *scrambled* (n=5) and *Mcu* siRNA (n=6). Error bars represent SEM; $p = 0.0311$ according to Welch's t test, two-tailed.

C. Normalized ATP levels in *wt* (n=10) and *Mcu*^{-/-} (n=10) BMDMs. Error bars represent SEM of six independent experiments. No significant difference detected between *wt* and *Mcu*^{-/-} according to Welch's t test, two-tailed.

D. Oxygen consumption rates (OCR) measured by Seahorse Analyzer across 30 min in *wt* (n=5) and *Mcu*^{-/-} (n=5) BMDMs. Error bars represent SEM; no significant difference detected between *wt* and *Mcu*^{-/-} according to Ordinary one-way ANOVA with multiple comparisons.

E. Gating strategy for flow cytometry of JC-1 dye. Viable Singlet BMDMs were gated prior to quantification of JC1 fluorescence in FITC and PE channels. Maximum mitochondrial depolarization was achieved by pretreating the BMDMs with FCCP (1 μ M) for 15 min prior to analysis.

F. JC-1 PE:FITC ratio calculated for *wt* (n=4) and *Mcu*^{-/-} (n=4) BMDMs. Error bars represent SEM; no significant difference was detected between *wt* and *Mcu*^{-/-} according to Welch's t test, two-tailed.

G. Quantification of TMRM (mitochondrial membrane potential dye) intensity in *wt* and *Mcu*^{-/-} macrophages at baseline. FCCP (1 μ M) was added to show maximum depolarization. No significant difference detected between *wt* and *Mcu*^{-/-} according to Welch's t test, two-tailed.

H. Representative images from *wt* and *Mcu*^{-/-} macrophages stained with TMRM (mitochondrial membrane potential dye). Cells were imaged every 10s. Baseline fluorescence was measured for 1 min followed by the addition of FCCP (1 μ M). Scale bar is 6 μ m.

I. Western blot of MCU and TOM20 in *wt* and *Mcu*^{-/-} BMDMs.

***Mcu(M)*^{-/-} mice are highly susceptible to disseminated candidiasis**

To determine if the deletion of MCU in myeloid cells increased susceptibility to fungal infections, we tested *Mcu(M)*^{-/-} mice in a model of disseminated candidiasis. Mice were tail vein injected with 1×10^6 viable blastospores of *C. albicans* and monitored for disease progression for 4-days post-infection. The clinical scores for the infected mice were recorded over time in a blinded protocol. *Mcu(M)*^{-/-} mice showed increased morbidity and lethargy compared to *wt* mice (**Figure 21A**). *Mcu(M)*^{-/-} mice also had a strikingly lower survival rate with only 9% of mice surviving until day 4, compared to 46% in the *wt* control group (**Figure 21B**). The *Mcu(M)*^{-/-} mice succumbed to disease at a faster rate (median survival 48 h) than *wt* (median survival 72 h) (**Figure 21B**). We excised the livers and kidneys of the infected mice to analyze them for fungal burden. The organ homogenates were plated on YPD agar plates to derive CFUs/gram of tissue. *Mcu(M)*^{-/-} mice had increased fungal burden in both kidney and liver (**Figure 21C and Figure 21D**). To assess fungal burden using tissue histology we stained kidney sections with Periodic Acid Schiff (PAS), which stains mucopolysaccharides and can thereby detect fungal burden in the stained tissue. Histology of the kidney sections 2 days post infection (dpi) showed severe fungal burden in *Mcu(M)*^{-/-} mice (**Figure 21E**). The H&E tissue sections (**Figure 21F**) of *wt* and *Mcu(M)*^{-/-} kidneys showed comparable number of immune cells (**Figure 21G**) indicating that the *Mcu*^{-/-} macrophages are not deficient in the recruitment of immune cells. In fact, in comparison to *wt* mice, the *Mcu(M)*^{-/-} mice exhibited substantially increased pro-inflammatory cytokines in their serum (**Figure 21H**). Vehicle controls had no detectable cytokine levels or any discernible changes in H&E and PAS staining (data not shown). These results indicate that the striking susceptibility of *Mcu(M)*^{-/-} mice to *C. albicans* is not a result of defective detection of *C. albicans* or of reduced output of inflammatory cytokines. It is predominantly due to defective cell autonomous killing mechanisms. Since MCU mediates mitochondrial Ca^{2+} -influx, these results suggest that mitochondrial Ca^{2+} -signaling is a crucial component of fungal killing.

Figure 21: *Mcu(M)*^{-/-} mice are highly susceptible to disseminated candidiasis

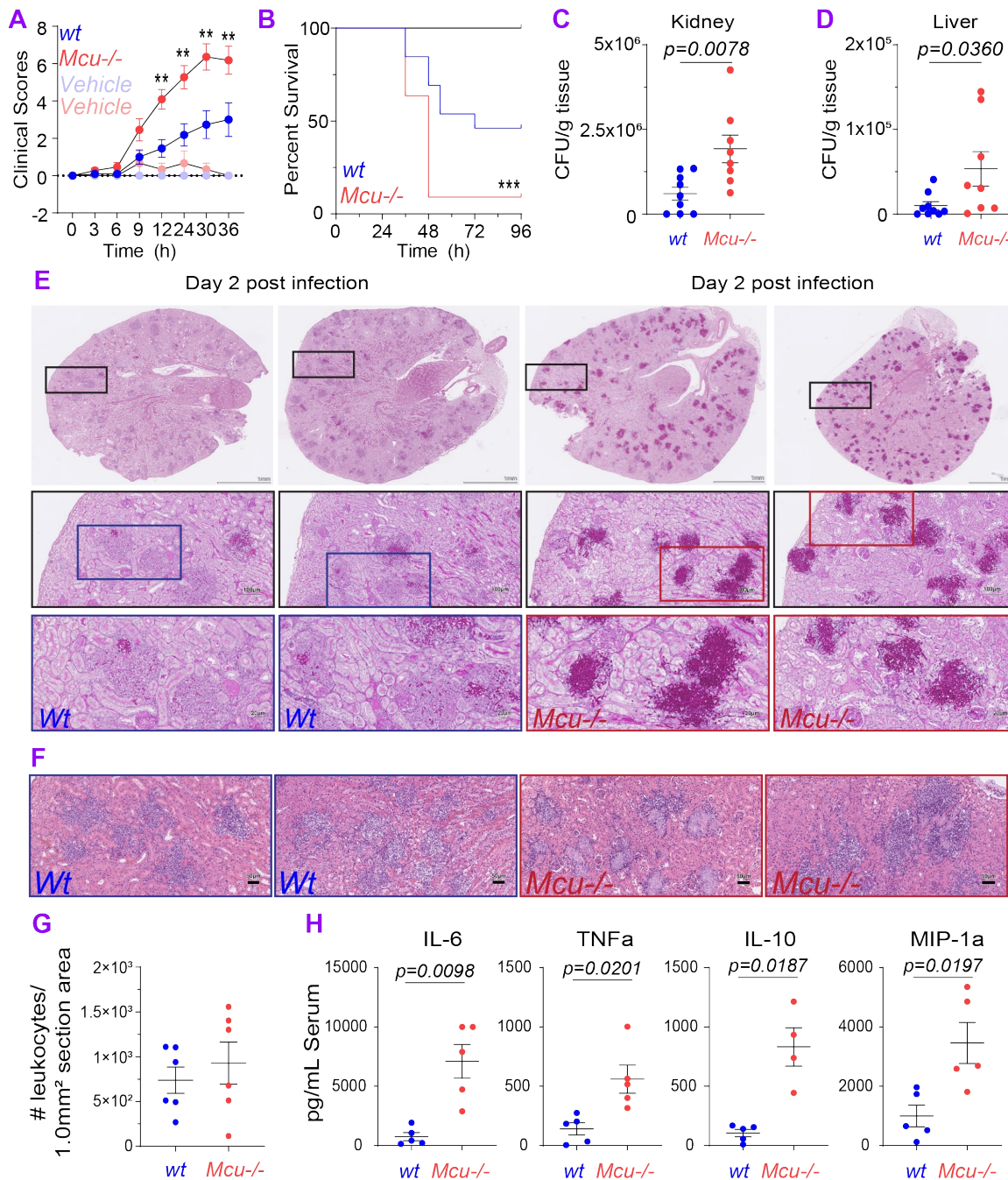


Figure 21: *Mcu(M)*^{-/-} mice are highly susceptible to disseminated candidiasis.

A. Clinical scores in *wt* and *Mcu(M)*^{-/-} mice injected in the tail vein with 100 μ L 1×10^6 *C. albicans* or vehicle control (100 μ L 0.9% saline). Infected *Mcu(M)*^{-/-} mice (n=11, mice) trace is shown in red and *wt* (n=13, mice) in blue. Vehicle controls for *Mcu(M)*^{-/-} (n=3, mice) are shown in light red and *wt* (n=6, mice) in light blue. Error bars represent SEM for individual timepoints across three individual experiments; *significance* [$p < 0.0500$ (*), < 0.005 (**)] is reported for each time point according to 2-way ANOVA with multiple comparisons.

B. Kaplan-Meier survival curves for *wt* and *Mcu(M)*^{-/-} mice infected with tail vein injections of (100 μ L) 1×10^6 *C. albicans* or vehicle control (100 μ L 0.9% saline). Infected *Mcu(M)*^{-/-} (n=11, mice) trace is shown in red and *wt* (n=13, mice) in blue. Vehicle controls for *Mcu(M)*^{-/-} (n=3, mice) and *wt* (n=6, mice) are shown in black (no mice died). At 48 h timepoint 69.2% of *wt* mice are alive compared to 9.1% of *Mcu(M)*^{-/-}. Curve comparison was made using a Log-rank (Mantel-Cox) test. Data was collected from three individual experiments; $p=0.0008$ (***).

C. Colony forming units (CFU) of *C. albicans* counted per gram of kidney at time of sacrifice in *wt* (n=9, mice) and *Mcu(M)*^{-/-} (n=8, mice) mice infected with tail vein injection of 100 μ L 1×10^6 *C. albicans*. Vehicle control (100 μ L 0.9% saline) for both groups had no CFUs. Error bars represent SEM from three individual experiments; $p=0.0078$ according to Mann-Whitney test, two-tailed

D. CFU of *C. albicans* counted per gram of liver at time of sacrifice in *wt* (n=9, mice) and *Mcu(M)*^{-/-} (n=8, mice) mice infected with tail vein injection of *C. albicans* (100 μ L, 1×10^6). Vehicle control (100 μ L 0.9% saline) for both groups had no CFUs. Error bars represent SEM from three individual experiments; $p=0.0360$ according to Mann-Whitney test, two-tailed

E. Representative periodic acid-Schiff (PAS) staining on kidney sections from *wt* and *Mcu(M)*^{-/-} mice, 2-days post tail vein injection of (100 μ L, 1×10^6) *C. albicans*. Sections were mounted on slides and entire slides were imaged at 20X. Boxes represent the region of each subsequent magnification. Scale is 1 mm for whole kidney section. Scale is 100 μ M and 20 μ M for subsequent zooms.

F. Representative Hematoxylin and Eosin (H&E) sections from *wt* and *Mcu*^{-/-} kidneys. Scale bar is 50 μ M

G. Hematoxylin and Eosin (H&E) stained kidneys were blindly scored for recruitment of leukocytes at time of sacrifice in infected mice (tail vein injection of 100 μ L 1×10^6 *C. albicans*). Control mice (100 μ L of 0.9% saline) did not show any immune cell recruitment and are not shown. Error bars represent SEM; no significant difference was detected between *wt* (n=6, mice) and *Mcu(M)*^{-/-} (n=6, mice) according to Mann-Whitney test, two-tailed.

H. Measurement of serum cytokines using Luminex Multiplex assay. Serum samples were collected from *wt* (n=5, mice) and *Mcu(M)*^{-/-} mice (n=4-5, mice) at the time of sacrifice and the indicated cytokines were measured. Vehicle controls had no detectable levels of serum cytokines. Error bars represent SEM; indicated *p values* calculated according to Welch's t test, two-tailed.

Fungal pathogens trigger store operated Ca^{2+} entry, the phase 1 of mitochondrial Ca^{2+} signaling.

The first phase of the two step Ca^{2+} relay in response to fungal pathogens is the elevation of cytosolic Ca^{2+} . The crucial requirement of cytosolic Ca^{2+} elevation is revealed by the drastically reduced killing of fungi by macrophages loaded with a fast Ca^{2+} chelator BAPTA-AM (**Figure 22A**). To record cytosolic Ca^{2+} we loaded bone-marrow derived macrophages with the ratiometric Ca^{2+} indicator Fura-2 AM. Aqueous extracts of heat-killed *S. cerevisiae* were obtained in 0 mM and 2 mM Ca^{2+} solutions. Macrophages stimulated with both fungal extracts elicited a robust cytosolic Ca^{2+} response (**Figure 22B**). The elevation of cytosolic Ca^{2+} in macrophages stimulated in 0 mM extracellular Ca^{2+} indicates that the Ca^{2+} is released from an intracellular store such as endoplasmic reticulum (ER). To measure store operated Ca^{2+} entry (SOCE), 10 mM Ca^{2+} was added to the bath once the intracellular release of Ca^{2+} returned to baseline. This resulted in a robust uptake of extracellular Ca^{2+} , presumably through the store operated Orai channels. Similar results were observed when macrophages were stimulated with the fungal cell wall component, β -glucan, a potent agonist of Dectin-1 (**Figure 22C**). Fungal stimulation of Dectin-1 has been proposed to facilitate Ca^{2+} elevations through Syk mediated activation of PLC^{171,172}. Indeed, the Ca^{2+} elevations were completely arrested in the presence of GSK143 and U73122, potent inhibitors of Syk and PLC, respectively (**Figure 22D**). We measured cytosolic Ca^{2+} in *wt* and *Mcu*^{-/-} macrophages in response to zymosan (**Figure 22E and Figure 22F**) and *C. albicans* extracts (**Figure 22G and Figure 22H**). These results show that cytosolic Ca^{2+} was modestly higher in *Mcu*^{-/-} macrophages as the rapid MCU-dependent m Ca^{2+} uptake was absent. Overall, these results show that the fungal PAMPs trigger an immediate store operated Ca^{2+} entry (SOCE, phase 1) as a prelude to mitochondrial Ca^{2+} signaling (phase 2, see below).

Figure 22: Fungal pathogens trigger store operated Ca^{2+} entry, the phase 1 of mitochondrial Ca^{2+} signaling

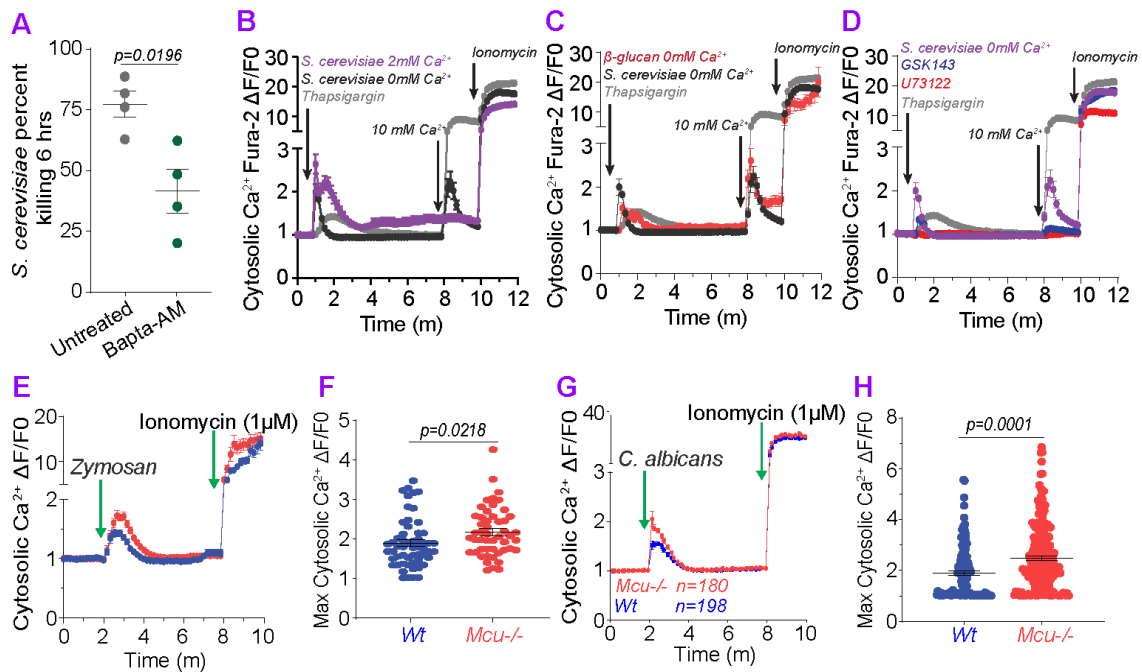


Figure 22: Fungal pathogens trigger store operated Ca^{2+} entry, the phase 1 of mitochondrial Ca^{2+} signaling.

A. Killing of *S. cerevisiae* by BMDMs preloaded with vehicle (n=4) or 5 μM BAPTA-AM (n=4). Error bars represent SEM; $p=0.0196$ according to Welch's t test, two-tailed.

B. Cytosolic Ca^{2+} elevations in BMDMs stimulated with *S. cerevisiae* extracts in 0 mM (n=78, cells) or 2 mM Ca^{2+} (n=44, cells) or in response to thapsigargin (w/ extracellular 0 mM Ca^{2+}) (n=44, cells) (positive control). The plotted values were calculated as a change in fluorescence/initial fluorescence ($\Delta\text{F}/\text{F}_0$). Error bars represent SEM.

C. Cytosolic Ca^{2+} elevations in BMDMs stimulated with *S. cerevisiae* extracts in 0 mM Ca^{2+} (n=78, cells), β -glucan in 0 mM Ca^{2+} (n=68, cells) and thapsigargin (positive control). Error bars represent SEM.

D. Cytosolic Ca^{2+} elevations in BMDMs stimulated with *S. cerevisiae* extracts in 0 mM Ca^{2+} and thapsigargin (positive control). BMDMs were stimulated in the presence of either GSK143 (2 μM , n=92, cells) or U73122 (1 μM , n=22, cells). Error bars represent SEM.

E. Cytosolic Ca^{2+} elevations in response to zymosan in *wt* (n=56, cells) and *Mcu*^{-/-} (n=50, cells) loaded with Fura-2 AM. These values are calculated as a change in fluorescence/ initial fluorescence ($\Delta\text{F}/\text{F}_0$). Error bars represent SEM.

F. Peak cytosolic Ca^{2+} elevations in response to zymosan in *wt* (n=56, cells) and *Mcu*^{-/-} (n=50, cells) loaded with Fura-2 AM. Error bars represent SD; *p* values were calculated according to Welch's t test, two-tailed.

G. Cytosolic Ca^{2+} elevations in response to *C. albicans* extracts in *wt* (n=198, cells) and *Mcu*^{-/-} (n=180, cells) loaded with Fura-2 AM. These values are calculated as a change in fluorescence/ initial fluorescence ($\Delta\text{F}/\text{F}_0$). Error bars represent SEM.

H. Peak cytosolic Ca^{2+} elevations in response to *C. albicans* supernatant in *wt* (n=180, cells) and *Mcu*^{-/-} (n=198, cells) loaded with Fura-2 AM. Error bars represent SD; *p* values were calculated according to Welch's t test, two-tailed.

Rapid elevations in mitochondrial Ca^{2+} (phase 2) are detected immediately after the recognition of *C. albicans*.

To license the activation of MCU, cytosolic Ca^{2+} must be sufficiently elevated to allow the gatekeeper MICU1 to promote mitochondrial Ca^{2+} uptake¹⁶⁷. In response to fungal pathogens, the cytosolic Ca^{2+} is elevated through SOCE. The close juxtaposition of mitochondria to the ER then allows the second phase of the Ca^{2+} relay into the mitochondria. To measure mitochondrial Ca^{2+} (m Ca^{2+}) elevations in macrophages, we established a RAW264.7 stable cell line expressing the genetically encoded mitochondrial Ca^{2+} sensor, CEPIA3mt¹⁷³ (herein RAW-3mt). In these cells, CEPIA3mt colocalized with the mitochondrial marker dye MitoTracker-Red (**Figure 24A**) and reported sharp m Ca^{2+} transients when the cells were treated with the Ca^{2+} ionophore ionomycin (**Figure 24B and Figure 24C**). Recognition and phagocytosis of fungal pathogens is commonly simulated by zymosan particles, a sterile cell wall preparation from *S. cerevisiae* that stimulates cell surface receptors TLR2 and Dectin-1. When RAW-3mt cells are exposed to fluorescent zymosan, they readily phagocytose the particles and trigger the elevation of m Ca^{2+} . As reported previously¹⁷⁴, a concurrent movement of the mitochondria to the phagosome is also seen. m Ca^{2+} elevations were recorded by drawing regions of interest (ROIs) around the mitochondrial network in macrophages actively engulfing zymosan particles (**Figure 23A**). Zymosan-triggered m Ca^{2+} elevations were significantly reduced in RAW-3mt cells wherein MCU was knocked down with siRNA (**Figure 23B**). Similarly, *C. albicans* supernatant elicited robust mitochondrial Ca^{2+} -elevations (**Figure 23C**) but with faster kinetics. The mitochondrial Ca^{2+} elevations in response to *C. albicans* are also MCU-dependent (**Figure 23D**). The movement of the mitochondria to the *C. albicans*-containing phagosome led us to investigate the membrane proximity through Transmission Electron Microscopy (TEM). We observed intimate mitochondrial juxtaposition to *C. albicans*-containing phagosomes with a distance of ~50 nm separating the phagosomal membrane from the mitochondrial outer membrane (**Figure 23E**). Similar association was observed in response to

zymosan (**Figure 23F**). The close juxtaposition is therefore similar to that observed in ER-mitochondrial contact sites and such repositioning can facilitate mCa^{2+} uptake from the Ca^{2+} released from the phagosome or from the adjoining ER^{175,176}. To analyze the mCa^{2+} elevations in the mitochondria juxtaposed with the phagosome, we analyzed the ROIs around the phagosome for changes in periphagosomal mitochondrial Ca²⁺ (PPMiCa). The PPMiCa elevations were then normalized to the mCa^{2+} across the mitochondrial network in that cell (**Figure 24D**) to reveal the PPMiCa dynamics during phagocytosis. Despite the heterogeneity of mCa^{2+} elevations in terms of amplitude and kinetics, the analysis showed that PPMiCa was significantly higher relative to the mCa^{2+} across the mitochondrial network and in comparison to control cells, the PPMiCa elevations were suppressed in cells wherein MCU was knocked down using siRNA (**Figure 23G and Figure 23H**). Time courses of PPMiCa responses are shown in (**Figure 24E**). These analyses reveal that detection and phagocytosis of fungal particles elicits the activation of MCU and robust mCa^{2+} elevations throughout the mitochondrial network. The mitochondria that are in close proximity to the phagosome show especially increased mCa^{2+} signaling. The precise regulatory mechanism underlying the gating of MCU channel during phagosomal killing is not a focus of this study. However, since it was recently reported that *Mcu* is activated by AMPK during cell division¹⁷⁷, we tested the role of AMPK inhibition during fungal killing. Macrophages treated with the AMPK inhibitor, dorsomorphin dihydrochloride, did not show an impairment in fungal killing (**Figure 23I**) indicating that MCU is not regulated by AMPK during phagosomal killing.

Figure 23: Rapid elevations in mitochondrial Ca^{2+} (phase 2) are detected after fungal recognition

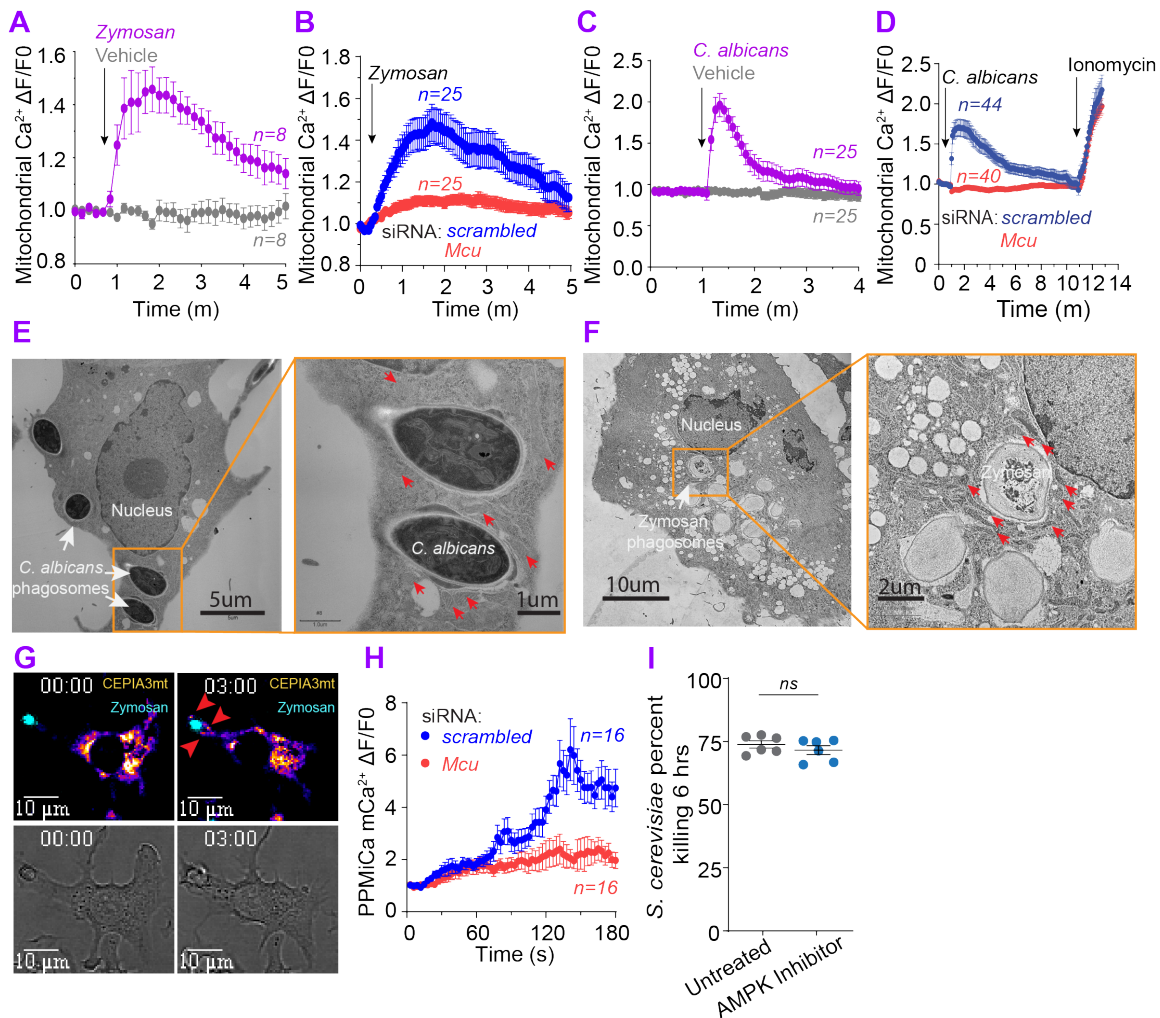


Figure 23: Rapid elevations in mitochondrial Ca^{2+} (phase 2) are detected after fungal recognition

A. Whole cell mCa^{2+} elevations in zymosan stimulated (n=8 cells) and untreated (n=8 cells) RAW3mt macrophages. Cells were sampled every 10 seconds. Error bars represent SEM.

B. Whole cell mCa^{2+} elevations in zymosan stimulated RAW3mt macrophages. *Scrambled* siRNA (n=25, cells) or *Mcu siRNA* (n=25, cells) treated RAW3mt cells were imaged every 3 seconds. Error bars represent SEM.

C. Whole cell mCa^{2+} elevations in RAW3mt macrophages stimulated with *C. albicans* extract (n=25 cells) and vehicle (n=25 cells). Cells were sampled every 5s. Error bars represent SEM.

D. Whole cell mCa^{2+} elevations in RAW3mt macrophages stimulated with *C. albicans* extract. *Scrambled* siRNA (n=40, cells) or *Mcu siRNA* (n=44, cells) treated RAW3mt cells were imaged every 3 seconds. Error bars represent SEM.

E. Representative TEM image of BMDMs infected with *C. albicans* for 6 h. Magnification of *C. albicans* phagosomes shows peri-phagosomal juxtaposition of mitochondria indicated by *red* arrows.

F. Representative TEM image of BMDMs exposed to zymosan for 6 h. Magnification of zymosan phagosomes shows peri-phagosomal juxtaposition of mitochondria indicated by *red* arrows.

G. Representative PPMiCa responses in RAW3mt cells. Merged images of CEPIA3mt (Fire LUT) and Zymosan (cyan LUT) are shown (top). Brightfield images (bottom). Red arrows indicate PPMiCa signals.

H. PPMiCa traces from zymosan stimulated RAW3mt macrophages. The values are calculated as a change in fluorescence/ initial fluorescence ($\Delta F/F_0$). *Scrambled* siRNA (n=16 cells) or *Mcu siRNA* (n=16 cells) treated RAW3mt cells were imaged every 3 seconds. Error bars represent SEM.

I. Killing of *S. cerevisiae* by macrophages treated with vehicle (n=5) or 1 μM AMPK inhibitor Dorsomorphin dihydrochloride (n=5). Error bars represent SEM; $p < 0.0001$ according to Welch's t test, two-tailed.

Figure 24: RAW3mt validation and analysis of PPMiCa responses

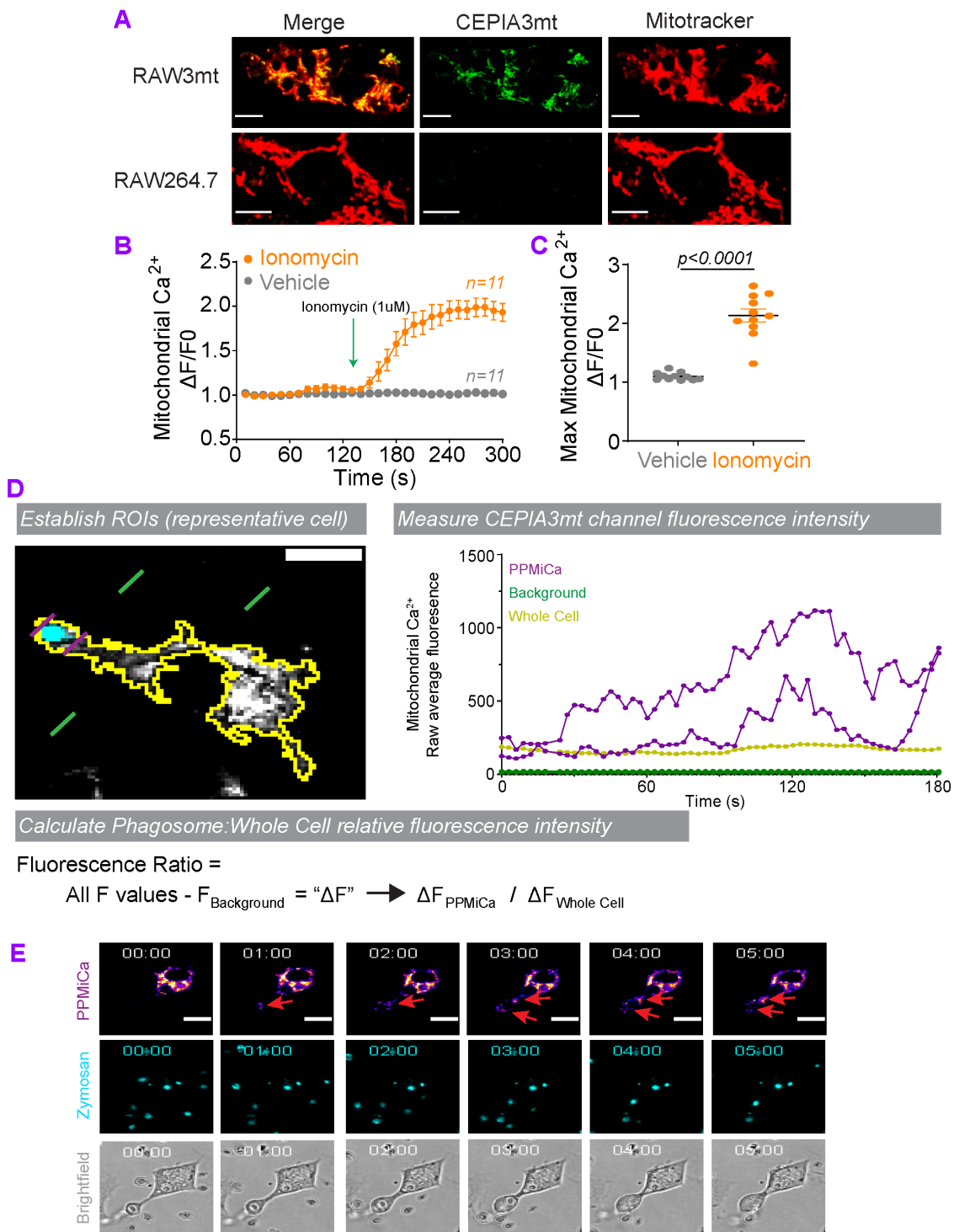


Figure 24: RAW3mt validation and analysis of PPMiCa responses

- A.** RAW3mt and RAW264.7 macrophages stained with MitoTracker Red (200 nM) and analyzed on confocal microscopy. Scale bar is 5 μm .
- B.** Whole cell mCa^{2+} elevations from ionomycin (1 μM) stimulated RAW3mt macrophages. Whole cell mCa^{2+} is taken from the average fluorescence intensity of ROIs drawn over entire mitochondrial network (See extended Figure 5). These values are calculated as a change in fluorescence/initial fluorescence ($\Delta F/F_0$). RAW3mt cells were imaged every 10 seconds; error bars represent SEM.
- C.** Quantification of peak whole cell mCa^{2+} elevations from FigureS2B Error bars represent SEM; $p < 0.0001$ according to Welch's t test, two-tailed.
- D.** Representative analysis for PPMiCa and whole cell mCa^{2+} responses in RAW3mt. Note the entire mitochondrial network in the ROI. Scale bar is 10 μm .
- E.** Representative time course of PPMiCa responses in RAW3mt. *Red* arrows indicated PPMiCa responses near phagosome. CEPIA3mt (top images; Fire LUT), Zymosan (middle; cyan LUT), and brightfield (bottom image; grey LUT) were acquired using confocal microscopy (sampling rate: 1 frame/10s). Scale bar is 10 μm .

Mitochondrial Ca²⁺ signaling controls phagosomal ROS production.

The acidification of the nascent phagosome is carried out by V-ATPase complex, and we reasoned that the process may put an unusually high demand on ATP. We hypothesized that mCa²⁺-signaling during phagocytosis drives the acidification of phagosome through a burst of ATP generation in the proximity of the phagosome. To assess the engulfment of *C. albicans* and the subsequent acidification of the phagosome, we labeled *C. albicans* with two dyes – CellTrace Violet (CTV) which is relatively insensitive to acidic pH and CypHer-5E (fluoresces brightly with low pH). The dually labeled *C. albicans* was then offered to *wt* and *Mcu*^{-/-} macrophages and the cells were analyzed by flow cytometry to assess engulfment (CTV fluorescence) and phagosome acidification (CypHer-5E fluorescence). Surprisingly, these experiments revealed that *Mcu*^{-/-} macrophages were not defective in engulfment (**Figure 25A and Figure 25B**) or phagosome acidification (**Figure 25C - Figure 25E**). The gating strategy and representative flow cytometry plots are shown (**Figure 26A – Figure 26C**). The ATP levels during phagocytosis of *C. albicans* were also normal in *Mcu*^{-/-} macrophages (**Figure 25F**). In both *wt* and *Mcu*^{-/-} macrophages, cellular ATP levels decreased only modestly at 1h and returned to baseline at 6h post-stimulation. Recent reports have shown a role for mitochondrial ROS (mROS) in pathogen destruction^{174,178}. Using MitoSox, a fluorescent sensor of mROS, we did not see an impairment in the acute production of mROS in *Mcu*^{-/-} macrophages during their response to the pathogenic stimuli (**Figure 27A and Figure 27B**). Only after 18 h of zymosan stimulation, *Mcu*^{-/-} macrophages begin to show a modest defect in mROS production (**Figure 27C- Figure 27D**). The phagosomal destruction of pathogens is also mediated by injection of ROS in the phagosome by NADPH oxidase complex (NOX). The activity of NOX requires substantial bioenergetic expenditure in the form of NADPH. To assess phagosomal ROS generation by the NOX complex, we developed a flow cytometry-based assay. We labeled *C. albicans* with CellRox (a dye that fluoresces when oxidized by ROS) and CTV. This assay reports the NOX-

mediated generation of ROS with high fidelity, and this is demonstrated by the validation control wherein the macrophages are pre-treated with Diphenyleneiodonium (DPI), a potent inhibitor of NOX¹⁷⁹, prior to pathogen exposure. Macrophages treated with DPI displayed a significant decrease in CellRox fluorescence (**Figure 27E – Figure 27H**). We found that production of phagosomal ROS in *Mcu*^{-/-} macrophages engulfing *C. albicans* was also significantly reduced 3h post-engulfment – reduced to ~50% relative to *wt* cells (**Figure 25G - Figure 25I**). These results indicate that during phagocytosis, V-ATPase activity is not influenced by mCa²⁺ signaling but phagosomal ROS production is highly dependent on MCU-dependent mCa²⁺ signaling.

Figure 25: Mitochondrial Ca^{2+} signaling controls phagosomal ROS production

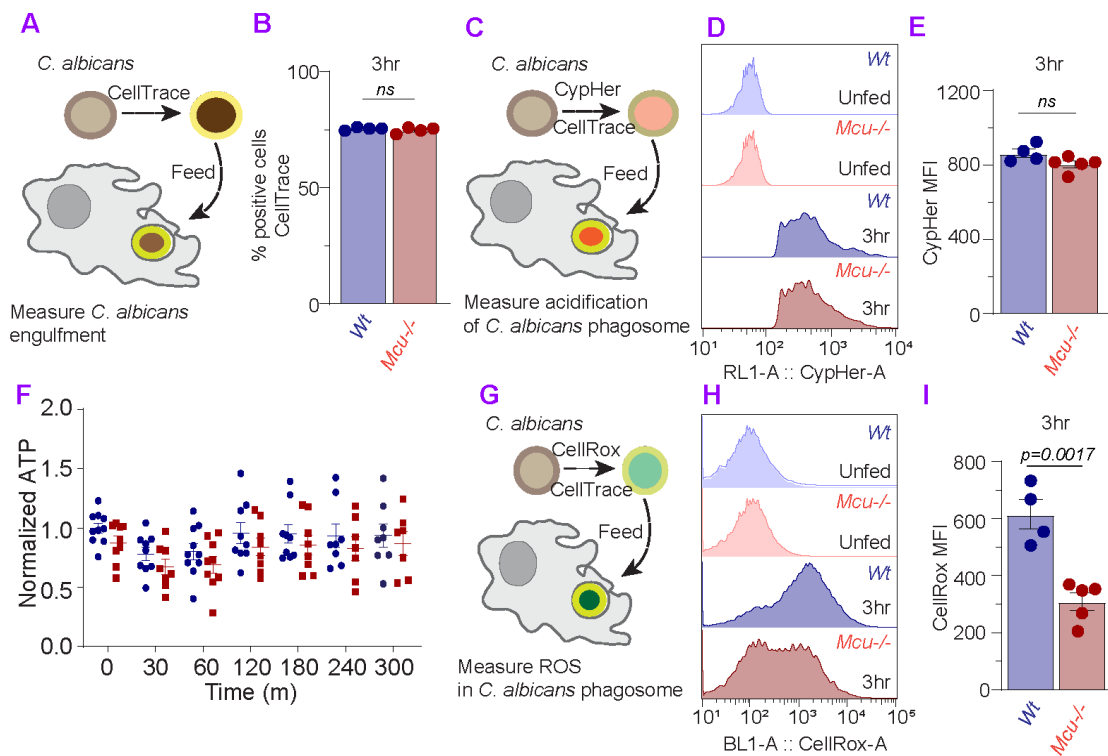


Figure 25: Mitochondrial Ca²⁺ signaling controls phagosomal ROS production

A. Schematized experimental design to measure *C. albicans* engulfment in macrophages using flow cytometry. *C. albicans* were labeled with CellTrace Violet (CTV) prior to phagocytosis.

B. Quantification of CTV-positive cells at 3h post phagocytosis for *wt* (n=4) and *Mcu*^{-/-} (n=4) BMDMs. Error bars represent SEM; no significance was detected according to Welch's t test, two-tailed.

C. Schematized experimental design to measure phagosome acidification in macrophages using flow cytometry. *C. albicans* were labeled with CypHer5E (fluoresces with acidic pH) and CTV (to confirm engulfment) prior to phagocytosis.

D. Flow cytometry histograms of CypHer5E fluorescence intensity in *wt* and *Mcu*^{-/-} BMDMs after 3h of phagocytosis.

E. Quantification CypHer5E MFI in *wt* (n=4) and *Mcu*^{-/-} (n=5) BMDMs after 3h of phagocytosis. Error bars represent SEM; no significance was detected according to Welch's t test, two-tailed.

F. Quantification of relative ATP levels in *wt* (n=8-10 for each time point) and *Mcu*^{-/-} (n=8-10 for each time point) BMDMs. Cells were stimulated with zymosan, and ATP levels were measured at each time point. Error bars represent SEM; no significance was detected according to 2-way ANOVA, two-tailed.

G. Schematized experimental design to measure phagosomal ROS in BMDMs. *C. albicans* were labeled with CellRox (reports oxidative stress) and CTV (to confirm engulfment) prior to phagocytosis.

H. Flow cytometry histograms of CellRox fluorescence intensity in *wt* and *Mcu*^{-/-} BMDMs after 3h of phagocytosis.

I. Quantification CellRox MFI in *wt* (n=4) and *Mcu*^{-/-} (n=5) BMDMs after 3h of phagocytosis. Error bars represent SEM; $p=0.0017$ according to Welch's t test, two-tailed.

Figure 26: Gating strategy for flow cytometry

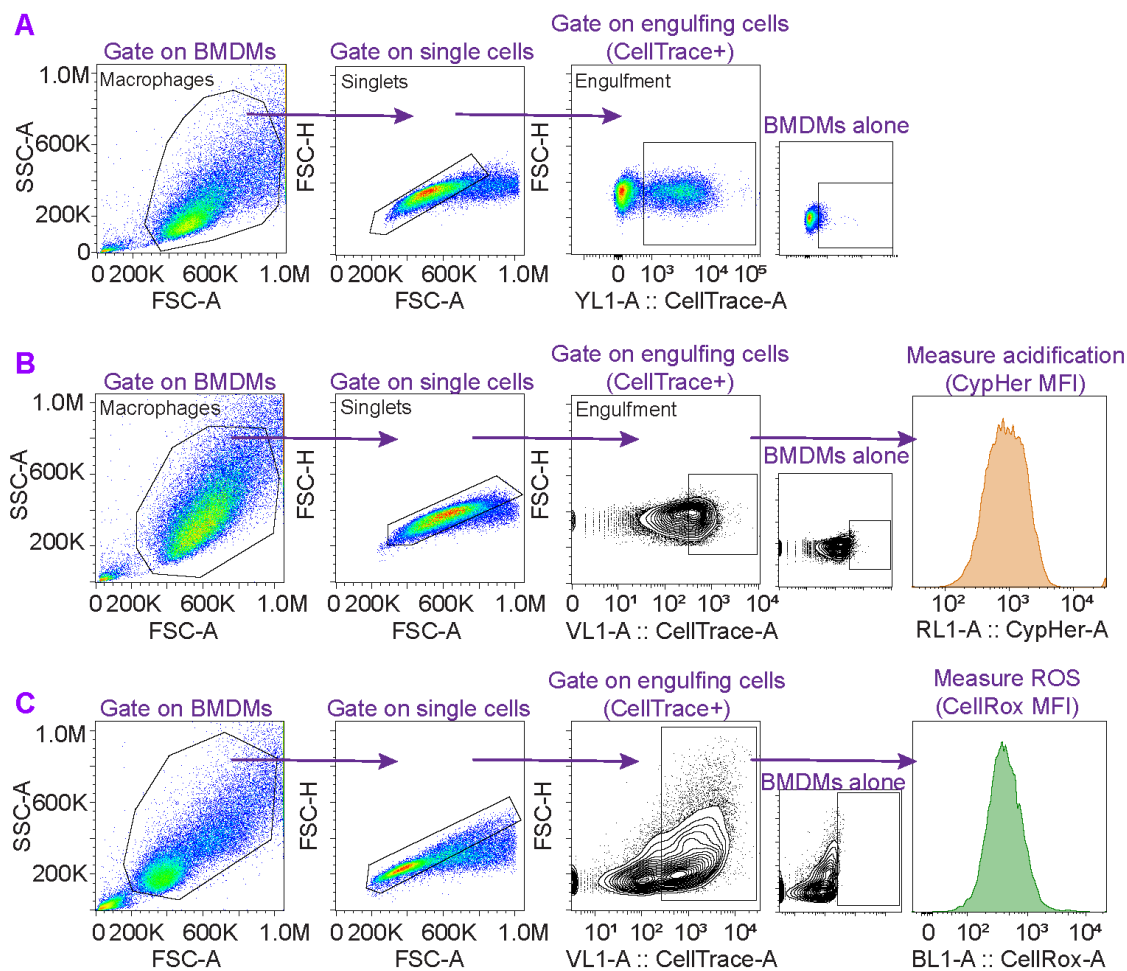


Figure 26: Gating strategy for flow cytometry

- A.** Gating strategy for measuring engulfment of *C. albicans* in BMDMs.
- B.** Gating strategy for measuring phagosome acidification of *C. albicans* in BMDMs.
- C.** Gating strategy for measure phagosomal ROS in BMDMs.

Figure 27: Mitochondrial ROS and validation of phagosomal ROS by flow cytometry

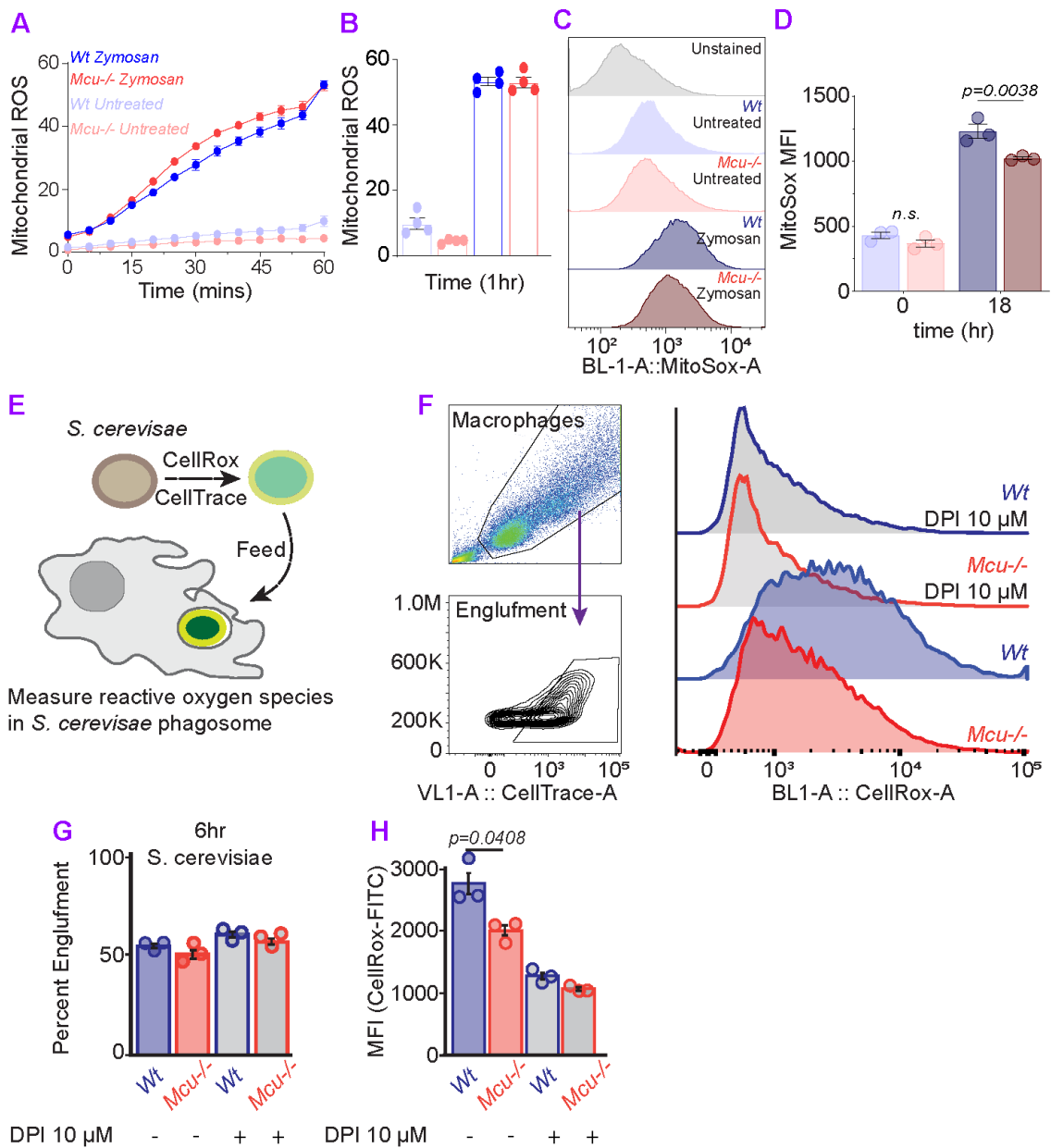


Figure 27: Mitochondrial ROS and validation of phagosomal ROS by flow cytometry

A. Change in MitoSox fluorescence in *wt* (n=4) and *Mcu*^{-/-} (n=4) macrophages stimulated with zymosan. Fluorescence was recorded every 5 min (Ex: 510, Em: 580). Zymosan was added at 2 particles per cell prior to recording. Error bars represent SEM.

B. Quantification of MitoSox fluorescence at 60 min post zymosan stimulation. No significant difference was found between *wt* (n=4) and *Mcu*^{-/-} (n=4) BMDMs. Error bars represent SEM; no significance was detected according to Welch's t test, two-tailed.

C. Representative histograms from *wt* and *Mcu*^{-/-} BMDMs.

D. Quantification of MitoSox flow cytometry from *wt* (n=3) and *Mcu*^{-/-} (n=3) bone-marrow derived macrophages. Cells were treated for 18 h with Zymosan 2:1, particles per cell. Error bars represent SEM; $p=0.0038$ according to 2-way ANOVA, two-tailed.

E. Schematized experimental design to measure phagosomal ROS in BMDMs. *S. cerevisiae* were labeled with CellRox (reports oxidative stress) and CTV (to confirm engulfment) prior to phagocytosis.

F. Flow cytometry gating strategy for measuring phagosomal ROS in BMDMs engulfing *S. cerevisiae*.

G. Quantification of CTV⁺ cells (measures engulfment) at 6 h post phagocytosis for *wt* (n=3), *Mcu*^{-/-} (n=3) BMDMs. Macrophages were treated with DPI (10 μ M, inhibitor of NADPH oxidase) or vehicle control (DMSO) for the duration of the experiment. Error bars represent SEM; no significant difference was detected between *wt* and *Mcu*(M)^{-/-} in either condition according to Welch's, two-tailed test.

H. Quantification of phagosomal ROS (CellRox fluorescence) in *wt* (n=3) and *Mcu*^{-/-} (n=3) BMDMs, after 6h of phagocytosis. Macrophages were treated with DPI (10 μ M) or vehicle control (DMSO) for the duration of the experiment. Error bars represent SEM; $p=0.0408$ according to Welch's, two-tailed test.

***Mcu*^{-/-} macrophages are unable to meet the NADPH demand of phagosomal killing.**

Since NOX activity is NADPH-dependent, we reasoned that mCa²⁺ signaling controls the metabolic shift needed to increase cellular NADPH metabolism required for phagocytosis. To measure this metabolic shift, we took advantage of the native fluorescent properties of NAD(P)H and used fluorescent lifetime imaging microscopy (FLIM) for a quantitative analysis of cellular NAD(P)H levels. The NAD⁺/NADH and NADP⁺/NADPH redox couples are critical determinants of the cellular redox^{180,181}. FLIM enables the study of NAD(P)H photochemistry in living cells by measuring the rates of fluorescence decay (fluorescence lifetime). The lifetime of NAD(P)H fluorescence is sensitive to its microenvironment and metabolic bursts that increase NAD(P)H levels register a sharp increase in enzyme bound NAD(P)H with increased fluorescence lifetimes. Since the enzyme-bound fraction of NAD(P)H (fraction a2%) can be calculated based on FLIM, we explored the technique in measuring the metabolic shifts that alter NAD(P)H synthesis and utilization in macrophages engulfing and killing *C. albicans*. The *wt* macrophages engulfing *C. albicans* exhibit a steady increase in bound NAD(P)H fraction reflecting the increased a2% fraction (**Figure 28A**). Strikingly, the *Mcu*^{-/-} macrophages show a severe deficit in a2% fraction during phagocytosis (**Figure 28A and Figure 28B**). These results indicate that mitochondrial Ca²⁺-signaling controls the NAD(P)H metabolism during response to fungal pathogens. To substantiate these findings further, we measured NADP⁺ and NADPH levels using biochemical assays (**Figure 29A – Figure 29C**). We found no significant change in the NADPH/NADP⁺ ratio at baseline but the ratio was significantly reduced in *Mcu*^{-/-} macrophages after 3h of exposure to zymosan. This difference is largely accounted by a significantly reduced levels of NADPH (~30% reduction) in *Mcu*^{-/-} macrophages (**Figure 29B**). The difference in NADP⁺ is relatively modest (**Figure 29C**).

***Mcu*^{-/-} macrophages exhibit an abnormal immunometabolic shift in response to fungal pathogens.**

To further characterize the defects in metabolic reprogramming, we used the Seahorse analyzer, an instrument for measuring key cellular bioenergetic parameters such as Oxygen Consumption Rate (OCR), which reflects oxidative phosphorylation in the mitochondria and Extracellular Acidification Rate (ECAR), which reflects the glycolytic activity. After 30 min of baseline measurement, we injected zymosan particles directly onto the macrophages and monitored the change in OCR and ECAR over 6h. At baseline, *wt* and *Mcu*^{-/-} macrophages showed no significant differences in OCR but after zymosan stimulation, the *Mcu*^{-/-} macrophages were unable to maintain the OCR (**Figure 28C**). Maximal OCR that the mitochondria are capable of is revealed by addition of BAM15, a mitochondrial uncoupler. Interestingly, absence of MCU modestly reduced the maximal OCR that the mitochondria are capable of during phagosomal killing (**Figure 29E**). Exposure to zymosan significantly increased the ECAR in both *wt* and *Mcu*^{-/-} macrophages but when compared to *wt* macrophages, the increase in ECAR was significantly lower in the *Mcu*^{-/-} macrophages (**Figure 28D**) The difference was especially evident at 5h post-engulfment (**Figure 29F**). To observe the combined bioenergetics profile revealed by seahorse analysis we plotted OCR by ECAR during the course of zymosan stimulation (**Figure 28E**). This reveals that *Mcu*^{-/-} macrophages had an impaired metabolic response to fungal stimulation. *Wild type* macrophages increase their bioenergetic output as measured by OCR and ECAR, while *Mcu*^{-/-} macrophages do not.

Figure 28: *Mcu*^{-/-} macrophages exhibit an abnormal immunometabolic shift in response to fungal pathogens

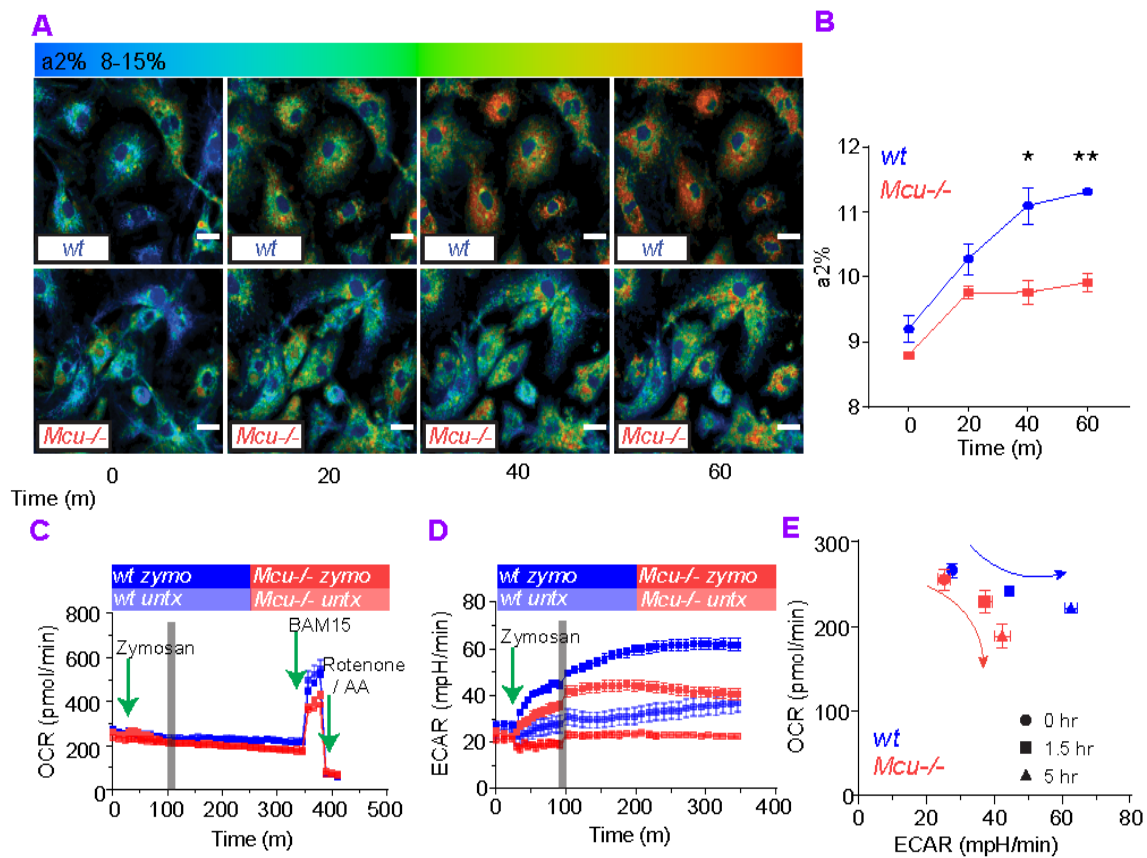


Figure 28: *Mcu*^{-/-} macrophages exhibit an abnormal immunometabolic shift in response to fungal pathogens

A. Representative FLIM images from before and after *C. albicans* engulfment. $a_2\%$ is shown as a shift from blue to red. Scale bar is 10 μm .

B. Assessment of $a_2\%$ (reflects NADPH levels) in *wt* (n=4) and *Mcu*^{-/-} (n=3) BMDMs. Error bars represent SEM; $p=0.0123$ at 40 min and $p=0.0038$ at 60 min according to Welch's, two-tailed test.

C. Mitochondrial oxygen consumption rate (OCR) in *wt* (n=4) and *Mcu*^{-/-} (n=4) macrophages in response to zymosan. Cells were measured at baseline for 30 min followed by the injection of zymosan. BAM15 (mitochondrial uncoupler) and Rotenone and antimycin A injected at indicated times (green arrows).

D. Extracellular acidification rate (ECAR) of *wt* (n=4) and *Mcu*^{-/-} (n=4) macrophages in response to zymosan. Cells were measured at baseline for 30 min followed by the injection of zymosan (green arrow). The gray bar denotes a change in sampling rate from a measurement every 5 min to a measurement every 10 min.

E. Seahorse bioenergetics profile, shown as relationship of OCR and ECAR, in *wt* (n=4) and *Mcu*^{-/-} (n=4) BMDMs responding to zymosan.

Figure 29: NADPH/NADP+ biochemical analysis and Seahorse quantification

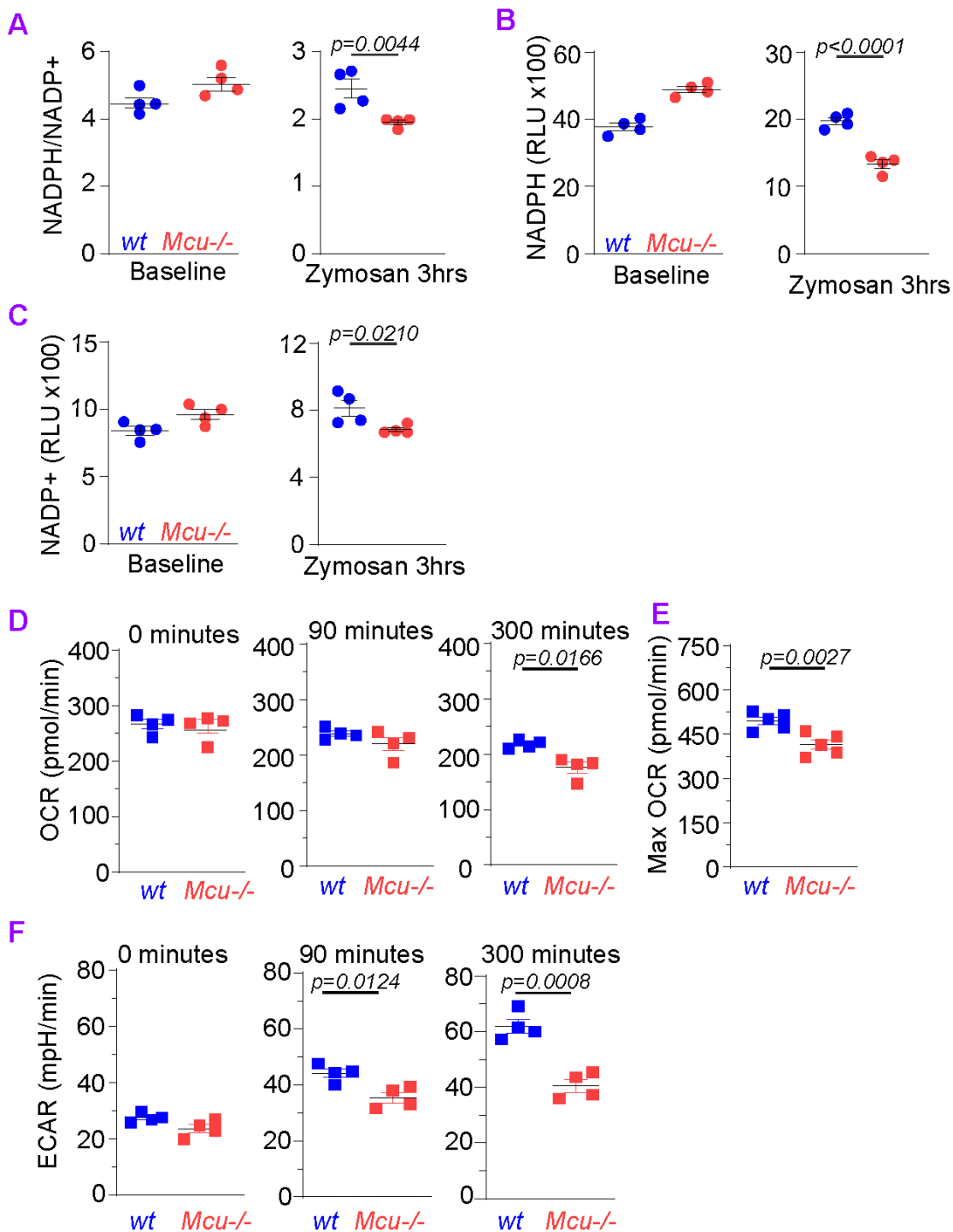


Figure 29: NADPH/NADP+ biochemical analysis and Seahorse quantification

A. NADPH/NADP+ ratios in *wt* and *Mcu*^{-/-} BMDMs at baseline (left panel) and after zymosan stimulation (3h, right panel). Error bars represent SEM; $p=0.0044$ between zymosan treated *wt* (n=4) and *Mcu*^{-/-} (n=4) according to Welch's, two-tailed test.

B. NADPH luminescence in *wt* and *Mcu*^{-/-} macrophages (same experiment as panel A). Error bars represent SEM; $p<0.0001$ between zymosan treated *wt* (n=4) and *Mcu*^{-/-} (n=4) according to Welch's, two-tailed test.

C. NADP+ luminescence in *wt* and *Mcu*^{-/-} macrophages. Error bars represent SEM; $p=0.0210$ between zymosan treated *wt* (n=4) and *Mcu*^{-/-} (n=4) according to Welch's, two-tailed test.

D. Quantification of OCR at baseline, 90 min and 300 min from Figure 6C. Error bars represent SEM; No significant differences were detected between zymosan treated *wt* (n=4) and *Mcu*^{-/-} (n=4) according to Welch's, two-tailed test.

E. Quantification of maximal OCR following the addition of BAM15 (mitochondrial uncoupler) from Figure 6C. Error bars represent SEM; $p=0.0059$ between zymosan treated *wt* (n=4) and *Mcu*^{-/-} (n=4) according to Welch's, two-tailed test.

F. Quantification of ECAR at baseline, 90 min and 300 min from Figure 6D. Error bars represent SEM; $p=0.0351$ at 90 min and $p=0.0003$ at 300 min between zymosan treated *wt* (n=4) and *Mcu*^{-/-} (n=4) according to Welch's, two-tailed test.

Metabolomic analysis of *Mcu*^{-/-} macrophages responding to zymosan.

Metabolomic analysis of *Mcu*^{-/-} and *wt* macrophages before and after zymosan stimulation revealed considerable differences in the levels of glycolytic metabolites but the levels of pyruvate and lactate, the final products of glycolysis were not significantly different at 6h (**Figure 31B**). There was no significant difference in the glycolytic capacity of *Mcu*^{-/-} macrophages, measured as the glycolytic stress test (GST) using Seahorse Analyzer (**Figure 31C – Figure 31D**). The intermediates of the pentose phosphate pathway (PPP) were also altered in *Mcu*^{-/-} macrophages (**Figure 31E**). We observed decreased glucose-6-phosphate and increased phosphoribosyl pyrophosphate (PRPP) in *Mcu*^{-/-} macrophages at both 3h and 6h zymosan exposure. Interestingly, we saw no significant difference in G6PGDH activity following zymosan stimulation in *Mcu*^{-/-} macrophages (**Figure 31F**). Nevertheless, we tested the possibility that the PPP is a key contributor of NADPH necessary for efficient fungal killing in macrophages. To test the role of the PPP in fungal killing, we inhibited G6PGDH with 6-aminonicotinamide (6-AN) but did not observe significant defects in fungal killing (**Figure 31G**). These findings therefore indicate that although mitochondrial Ca²⁺ dynamics influence the PPP pathway, NADPH production by the PPP pathway is dispensable for fungal killing.

Dysregulated TCA cycle underlies defective killing by *Mcu*^{-/-} macrophages.

Small Molecule Pathway Database (SMPDB) analysis of metabolites revealed significant dysregulation of TCA cycle metabolites (**Figure 30A and Figure 30B**). Citrate and Aconitate, the TCA metabolites immediately downstream of PDH were significantly reduced in zymosan-stimulated *Mcu*^{-/-} macrophages at 6h (**Figure 30C and Figure 30D**). We observed similar decreases in citrate at 3h (**Figure 32B**). Previously, it has been suggested that the TCA cycle intermediate citrate is essential for metabolic reprogramming of macrophages during inflammatory stimulations¹⁶⁹. Our analysis supports these findings as the relative abundance of citrate and aconitate increased in response

to zymosan stimulation (**Figure 32B**). However, *Mcu*^{-/-} macrophages do not increase the relative abundance of citrate and aconitate after zymosan stimulation indicating that mitochondrial Ca²⁺-signaling is essential for this metabolic response. These data indicate that mCa²⁺-signaling has a direct impact on TCA cycle in general and more specifically on the accumulation of citrate and aconitate, during phagosomal killing. We hypothesized that mCa²⁺-dependent accumulation of citrate is necessary for the cytosolic NADPH generation because citrate can be exported into the cytosol and then utilized by Malic Enzymes to generate NADPH. To test this hypothesis, we tested the prediction that supplementation of citrate will rescue the defective killing in *Mcu*^{-/-} macrophages. We ascertained the ability of *wt* and *Mcu*^{-/-} macrophages to kill *C. albicans* in media supplemented with 2 mM citrate. The citrate supplementation completely rescued the killing defect of *Mcu*^{-/-} macrophages (**Figure 30E and Figure 30F**). Together these data reveal a vital role for mitochondrial Ca²⁺ signaling in the regulation of TCA cycle and citrate-dependent NADPH generation necessary for fungal killing.

Mitochondrial Ca²⁺ triggers dephosphorylation and activation of pyruvate dehydrogenase.

As shown above, a major abnormality of the TCA cycle in *Mcu*^{-/-} macrophages is that Citrate and Aconitate, the TCA metabolites immediately downstream of PDH are significantly reduced during phagocytosis (**Figure 30C and Figure 30D**). To further substantiate the metabolic salience of TCA cycle in phagosomal killing, we tested the inhibitors of Pyruvate dehydrogenase (PDH) and Succinate dehydrogenase (SDH) two key enzymes in the TCA cycle. Inhibition of PDH and α -ketoglutarate dehydrogenase using CPI 613 and SDH with 3-nitropropionic acid (3-NPA) reduced the killing of *S. cerevisiae* (**Figure 30G and Figure 30H**). These results show that the TCA cycle is critical for efficient fungal killing in macrophages. Pyruvate Dehydrogenase Complex (PDC) is a tightly regulated multi-component enzymatic complex that catalyzes the

conversion of pyruvate into acetyl CoA. Pyruvate dehydrogenase (PDH), the catalytic subunit of the PDC complex, is phospho-regulated by PDH kinases (PDKs) and PDH phosphatases (PDPs)¹⁶⁸. Phosphorylation of PDH is inhibitory whereas dephosphorylation at S293 activates the enzyme, increasing the flux of pyruvate into the TCA cycle. The PDPs are Ca^{2+} -activated phosphatases, and we hypothesized that mCa^{2+} signaling during phagocytosis can activate PDC through PDH dephosphorylation. Using antibodies specific for phospho-PDH, we monitored the activation state of PDH during phagocytosis of *C. albicans*. Macrophages engulfing *C. albicans* were stained with antibodies against PDH and phospho-PDH (pPDH). Confocal immunofluorescence microscopy was used to visualize and quantify total PDH and phospho-PDH at multiple time points. These results show striking dephosphorylation of PDH in *wt* macrophages but not in *Mcu*^{-/-} macrophages (**Figure 30I**). Representative images are shown for *wt* and *Mcu*^{-/-} macrophages at 30, 60, and 180 minutes after exposure to *C. albicans* (**Figure 32C – Figure 32F**). Quantification of images enabled the derivation of pPDH/PDH ratio (**Figure 30J**) and the results clearly demonstrate that dephosphorylation of PDH, a pivotal regulatory event in cellular metabolism is highly dependent on MCU-mediated mCa^{2+} -signaling initiated for cell-intrinsic response to *C. albicans*.

Figure 30: Dysregulated TCA cycle underlies defective killing by *Mcu*^{-/-} macrophages

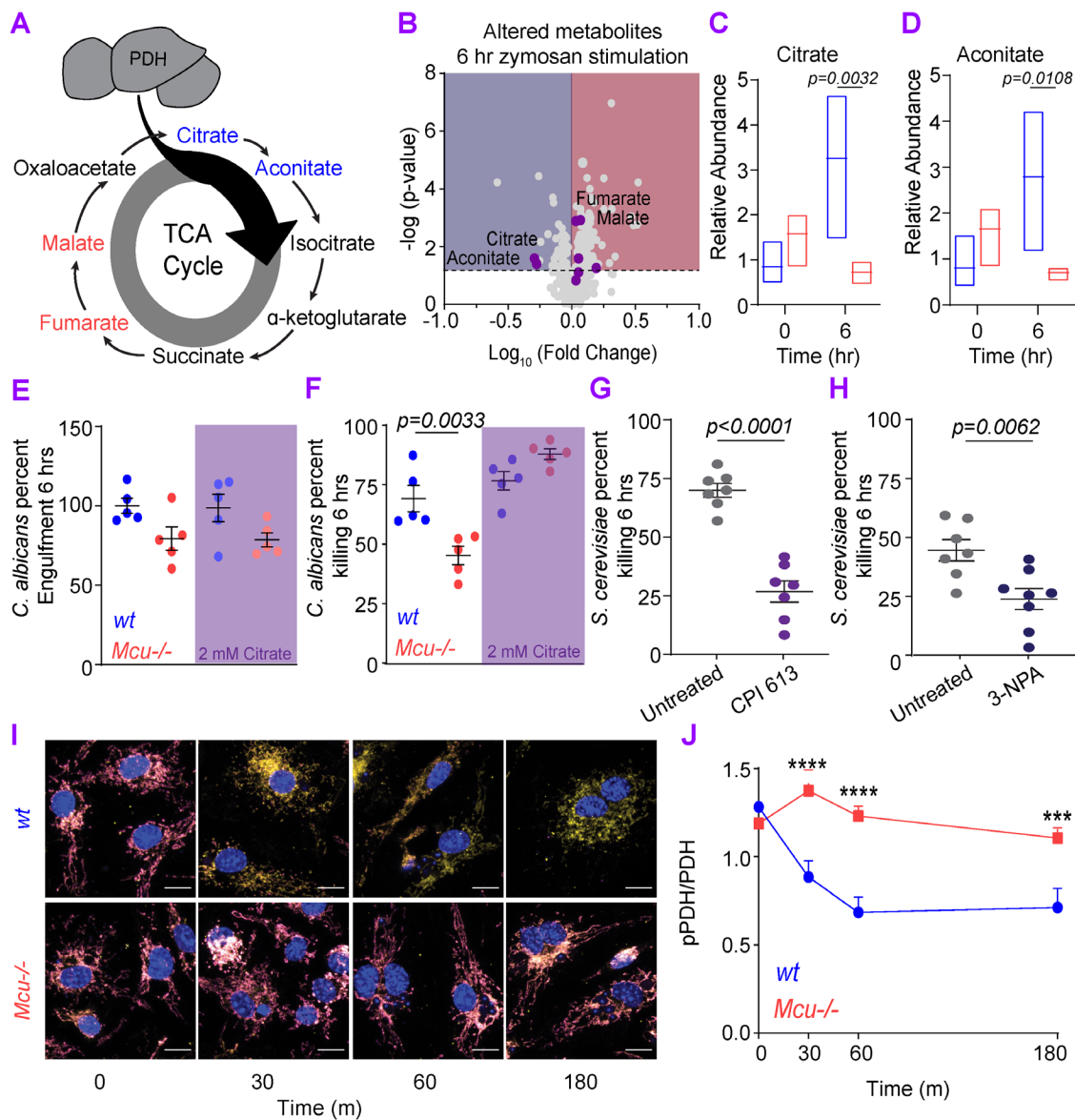


Figure 30: Dysregulated TCA cycle underlies defective killing by *Mcu*^{-/-} macrophages

A. Schematic of TCA cycle. Metabolites reduced in *Mcu*^{-/-} BMDMs responding to zymosan (6h) are blue. Metabolites that increased in *Mcu*^{-/-} BMDMs are red.

B. Volcano plot of significantly altered metabolites in *Mcu*^{-/-} macrophages compared to *wt* following 6 hours of zymosan stimulation. The dotted horizontal line represents the 75 percentile for $-\log(p\text{-values})$. TCA cycle metabolites are shown as purple dots.

C. Relative abundance of citrate measured in *wt* (blue) and *Mcu*^{-/-} (red) BMDMs at baseline and 6 hours following zymosan stimulation. Floating bars represent the min to max, and the line is at the mean for each data set; $p=0.0032$ was detected according to 2-way ANOVA, two-tailed.

D. Relative abundance of aconitate measured in *wt* (blue) and *Mcu*^{-/-} (red) BMDMs at baseline and 6 hours following zymosan stimulation. Floating bars represent the min to max, and the line is at the mean for each data set; $p=0.0108$ was detected according to 2-way ANOVA, two-tailed.

E. *C. albicans* engulfment in *wt* (n=5) and *Mcu*^{-/-} (n=5) BMDMs in the absence and presence of 2 mM citrate. Error bars represent SEM; $p=0.0033$ according to one-way ANOVA.

F. *C. albicans* killing by *wt* (n=5) and *Mcu*^{-/-} (n=5) BMDMs in the absence and presence of 2 mM citrate. Error bars represent SEM; $p=0.0033$ according to one-way ANOVA.

G. Killing of *S. cerevisiae* by BMDMs treated with vehicle (n=7) or 100 μ M CPI 613 (n=7). Error bars represent SEM; $p<0.0001$ according to Welch's t test, two-tailed.

H. Killing of *S. cerevisiae* by BMDMs treated with vehicle (n=7) or 100 μ M 3-Nitropropionic Acid (n=8). Error bars represent SEM; $p<0.0001$ according to Welch's t test, two-tailed.

I. Representative IF images from *wt* and *Mcu*^{-/-} BMDMs in response to *C. albicans*. pPDH (magenta LUT), PDH (yellow LUT), and nucleus (DAPI; blue LUT) were acquired using LSM880 confocal microscope. Scale bar is 10 μ m.

J. Quantification of pPDH/PDH from *wt* and *Mcu*^{-/-} macrophages in response to *C. albicans*. Cells quantified for each time point are 0 min (n=31), 30 min (n=23), 60 min (n=31), and 180 min (n=22) for *wt*. For *Mcu*^{-/-} all time points n=40 cells were quantified. Error bars represent SEM; $p < 0.001$ denoted as *** and $p < 0.0001$ as ****. *P* values calculated according to 2-way ANOVA, two-tailed.

Figure 31: Metabolomic analysis of glycolysis and pentose phosphate pathway

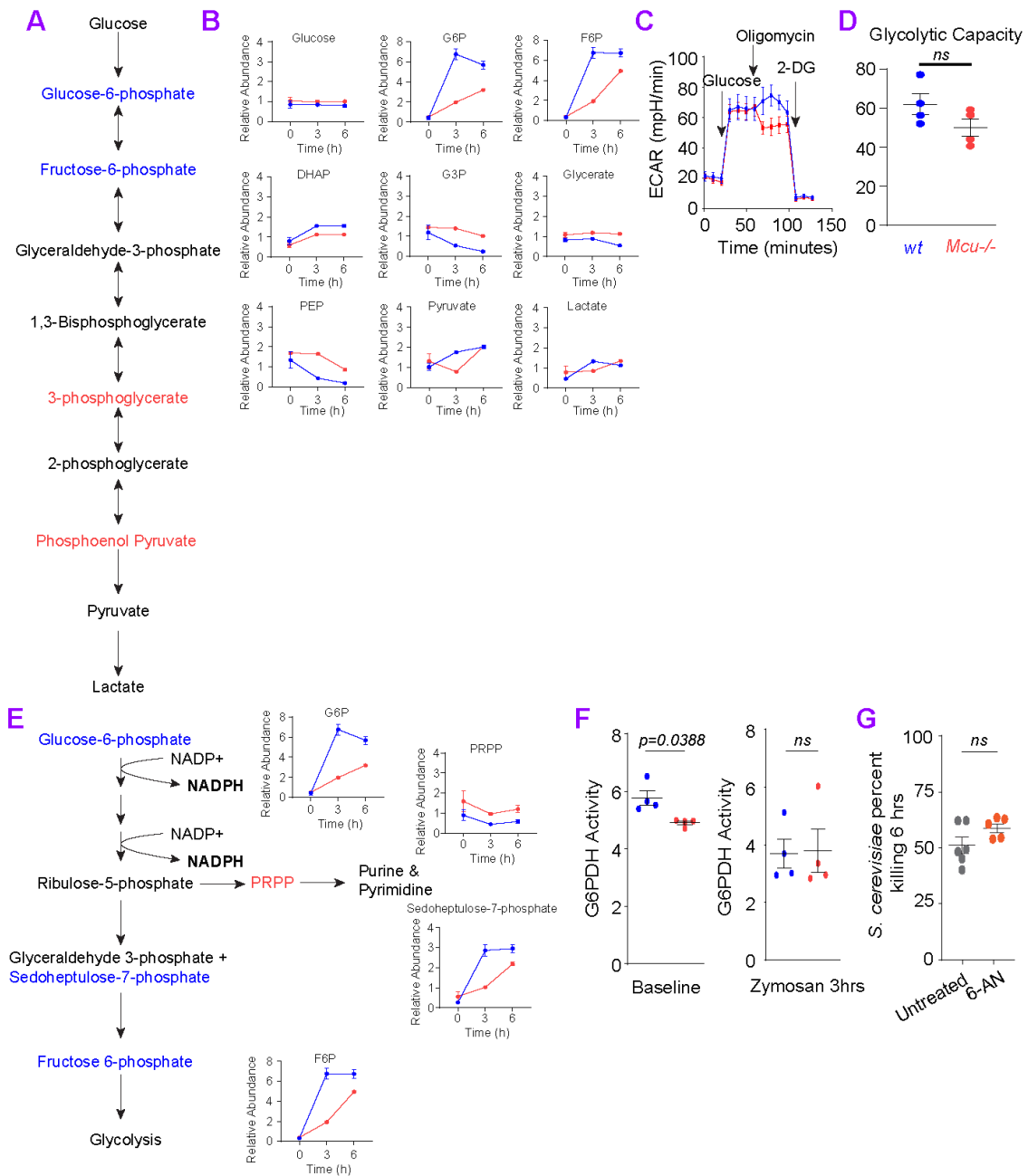


Figure 31: Metabolomic analysis of glycolysis and pentose phosphate pathway

A. Schematic of glycolysis. Metabolites reduced in *Mcu*^{-/-} BMDMs responding to zymosan (6h) are blue. Metabolites that increased in *Mcu*^{-/-} BMDMs are red.

B. Glycolytic metabolites measured at 0, 3 and 6 h after zymosan stimulation in *Mcu*^{-/-} (n=3) and *Wt* (n=3) macrophages. Error bars represent SEM.

C. Glycolytic Stress Test (GST) on *wt* (n=4) and *Mcu*^{-/-} (n=4) macrophages following 6 h of zymosan stimulation. Injections are indicated with arrows.

D. Glycolytic capacity of *wt* and *Mcu*^{-/-} macrophages following 6 h of zymosan stimulation Error bars are representing SEM, and significance was determined by Welch's, two-tailed t test.

E. Schematic of pentose phosphate pathway. Metabolites reduced in *Mcu*^{-/-} BMDMs responding to zymosan (6h) are blue. Metabolites that increased in *Mcu*^{-/-} BMDMs are red. Pentose phosphate pathway metabolites measured at 0, 3 and 6 h after zymosan stimulation in *Mcu*^{-/-} (n=3) and *Wt* (n=3) macrophages. Error bars represent SEM.

F. G6PDH activity was assessed using a colorimetric assay. *Mcu*^{-/-} macrophages showed a modest reduction in G6PDH activity at baseline but not after 3 h of zymosan stimulation. Error bars represent SEM (n=4); $p=0.0196$ according to 2-way ANOVA, two-tailed

G. Killing of *S. Cerevisiae* by BMDMs treated with vehicle (n=6) or 100 μ M 6-Aminonicotinamide (n=5). Error bars represent SEM from five independent experiments. No significant difference was detected by Welch's t test, two tailed.

Figure 32: Metabolomic analysis of TCA cycle and quantification of pPDH immunofluorescence

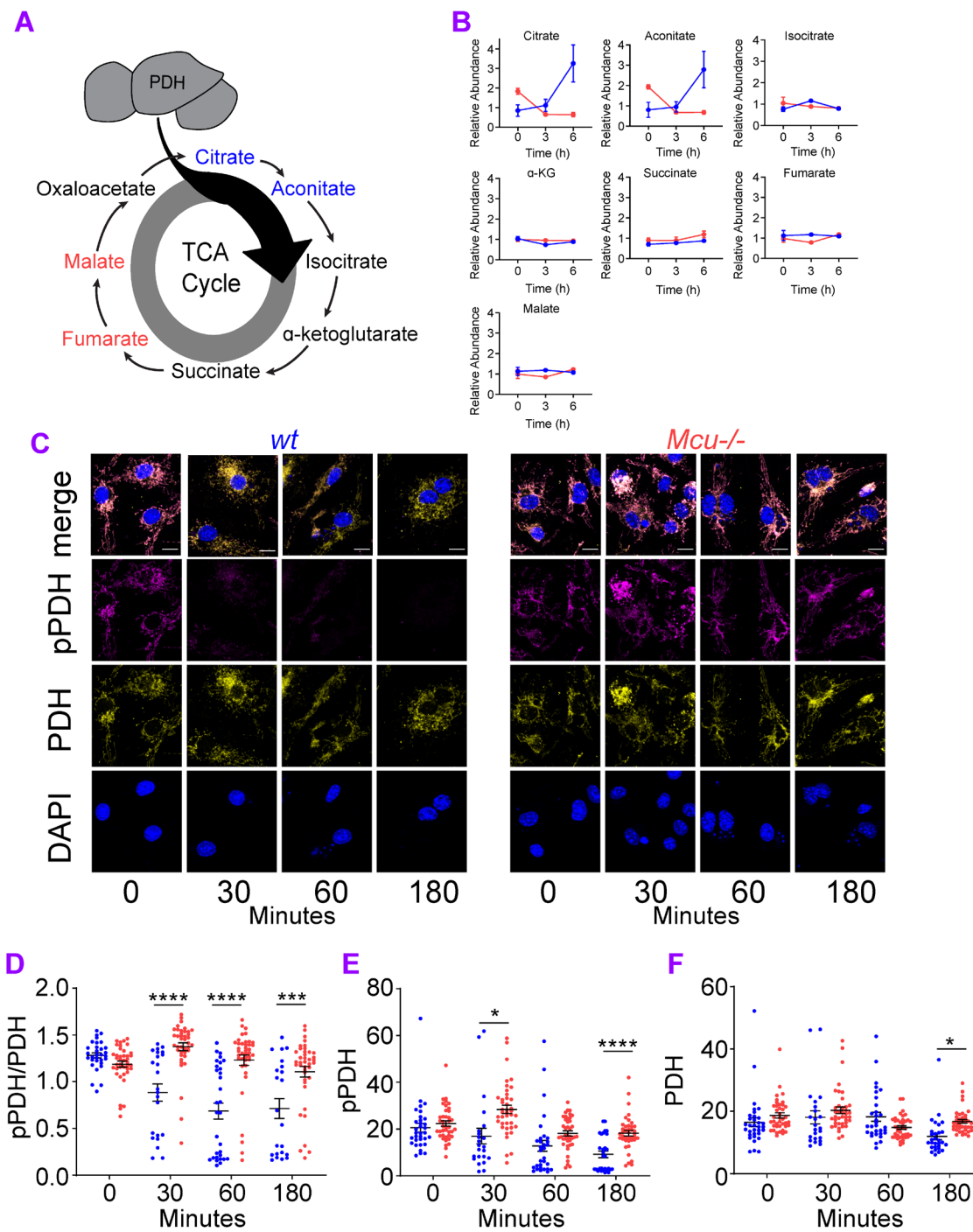


Figure 32: Metabolomic analysis of TCA cycle and quantification of pPDH immunofluorescence

A. Schematic of TCA cycle. Significantly decreased metabolites are blue and significantly increased metabolites are red. Significance was determined by Welch's, two-tailed t test.

B. TCA cycle metabolites measured at 0, 3 and 6 hours after zymosan stimulation in *Mcu*^{-/-} (n=3) and *Wt* (n=3) macrophages. Error bars represent SEM.

C. Representative IF images from *wt* and *Mcu*^{-/-} BMDMs responding to *C. albicans*. pPDH (magenta LUT), PDH (yellow LUT), and nucleus (DAPI; blue LUT) were acquired using LSM880 confocal microscope. Scale bar is 10 μ m.

D. Quantification of pPDH/PDH from *wt* and *Mcu*^{-/-} macrophages in response to *C. albicans*. Cells quantified for each time point are 0 h (n=31), 30 min (n=23), 60 min (n=31), and 180 min (n=22) for *wt*. For *Mcu*^{-/-} all time points n=40 cells were quantified. Error bars represent SEM; *p*-values (***p*=0.0001, *****p*<0.0001) was detected according to 2-way ANOVA, two-tailed.

E. Quantification of pPDH from *wt* and *Mcu*^{-/-} macrophages in response to *C. albicans*. Cells quantified for each time point are 0 h (n=31), 30 min (n=23), 60 min (n=31), and 180 min (n=22) for *wt*. For *Mcu*^{-/-} all time points n=40 cells were quantified. Error bars represent SEM; *p*-values (***p*<0.001, *****p*<0.0001) according to 2-way ANOVA, two-tailed.

F. Quantification of PDH from *wt* and *Mcu*^{-/-} macrophages in response to *C. albicans*. Cells were combined from three independent experiments. Error bars represent SEM; **p*=0.0109 was detected according to 2-way ANOVA, two-tailed.

Discussion

Our current understanding of immunometabolic reprogramming relies heavily on transcriptional changes initiated during macrophage activation. Such reprogramming undoubtedly plays an important role during an immune response, but transcriptional changes are too slow to mediate the metabolic burst required by the sentinel phagocytes when they first encounter and engulf a pathogen. How do the phagocytes rapidly switch the primary gears of their cellular metabolism during phagocytosis? Our study provides an important insight into this fundamental question. Although our study focuses on the killing of *C. albicans* by macrophages, the underlying design-principle may be of relevance to fast immunometabolic reprogramming in a variety of scenarios. In essence, we propose that the MCU-dependent mitochondrial Ca^{2+} -signaling is an electrometabolic switch to fuel cell-intrinsic immune responses.

Macrophages recognize *C. albicans* through the pattern-recognition receptors TLR2 and Dectin-1¹⁷¹. We show that recognition of *C. albicans* elicits a sharp elevation in cytosolic Ca^{2+} through store-operated Ca^{2+} -entry (SOCE). The phagocytes use this sharp but transient increase in cytosolic Ca^{2+} to mediate an MCU-dependent influx of Ca^{2+} into the mitochondrial matrix. The outer membrane of the mitochondria is not a barrier to this process because it is freely permeable to cations and once MCU is gated open, the membrane potential (-180 mV) across the inner membrane serves as a strong driving force for Ca^{2+} -entry into the matrix⁴³. The mechanisms that activate MCU are not fully understood yet but it is clear that MICU1 and MICU2, the two Ca^{2+} -sensing subunits of the MCU complex, play a key role in gating MCU. A recent study reported the direct gating of the MCU pore by AMPK-mediated phosphorylation¹⁷⁷ but we observed that AMPK inhibition has no impact on m Ca^{2+} signaling triggered by fungal pathogens. Whether the MCU complex is regulated through rapid post-translational modifications during cell-intrinsic immune responses remains an outstanding question that we plan to address in an independent line of investigation. In any case, when macrophages encounter

C. albicans, the sharp increases in cytosolic Ca^{2+} and concurrent gating of MCU mediate a rapid influx of Ca^{2+} into the matrix of the charged mitochondria.

Inside the mitochondrial matrix, Ca^{2+} can activate multiple enzyme complexes to stimulate the TCA cycle. These include the Pyruvate dehydrogenase (PDH), Isocitrate dehydrogenase (IDH) and Oxoglutarate dehydrogenase (OGDH)²⁸. As a major determinant of the metabolic fate of pyruvate, the PDH complex is central node in metabolism, and it is especially sensitive to Ca^{2+} -mediated phosphoregulation. We have shown that in macrophages engulfing *C. albicans*, the dephosphorylation (activation) of PDH is highly dependent on mCa^{2+} signaling. These findings are also supported by metabolomics analysis of the TCA cycle. Concomitant regulation of IDH and OGDH is also likely, but this was not investigated in our study. Together the effect of mitochondrial Ca^{2+} -signaling is rapid and profound. Interestingly, the *Mcu*^{-/-} macrophages can sustain the ATP levels necessary for the immune response but mCa^{2+} -signaling is critical for increasing cellular NAD(P)H levels. In macrophages phagocytosing *C. albicans*, there is increased NADPH production to drive NOX2-dependent phagosomal ROS production. The generation of NADPH is largely dependent on the pentose phosphate pathways (PPP) and the TCA cycle. During phagosomal killing, we show that inhibition of the PPP pathway has little or no effect on killing but inhibition of TCA enzymes drastically reduces killing. This suggests that mCa^{2+} signaling initiated during phagosomal killing drives the production of NADPH through the TCA cycle. Indeed, the defective killing by the *Mcu*^{-/-} macrophages can be rescued by supplementation of citrate, the key TCA intermediate that accumulates in an *Mcu* dependent manner. Citrate is known to be exported out of the mitochondria and serve as a substrate for Malic Enzyme-mediated NADPH production. The major sources of NADPH in the cell are the pentose phosphate pathway (PPP), folate metabolism, and malic enzyme (ME). We show that the PPP pathway is dispensable for early pathogen killing but instead, the TCA cycle and specifically citrate is necessary for fungal killing. We have shown that mCa^{2+} signaling is a key regulator of TCA

cycle and in absence of mCa^{2+} -signaling, there is a reduction in citrate levels. Citrate is also of long-term importance to immunometabolism because it is a necessary intermediate for fatty acid synthesis¹⁶⁹. It is therefore highly likely that over a more extended period, mCa^{2+} -signaling also controls the citrate shuttle necessary for fatty acid synthesis and membrane biogenesis. In addition to the direct regulation of PDH and NADPH levels, mitochondrial Ca^{2+} signaling may also govern other important anaplerotic demands of phagosomal killing. However, since this study relied on snapshots of metabolite levels and did not evaluate metabolic flux using radioisotope labeling studies, a comprehensive understanding of the metabolic deficits in *Mcu*^{-/-} macrophages is still pending.

Previous studies have proposed a crucial role for mitochondrial ROS (mROS) in phagosomal killing of bacteria¹⁷⁴. This study reported that ECSIT depleted macrophages were deficient in bacterial killing over 12-24h period because of a deficit in the production of mROS. A more recent study from the same lab¹⁸² indicates that ECSIT^{-/-} macrophages constitutively generate high levels of mROS but remain deficient in additional production of mROS during TLR-stimulation. In our study, both *wt* and *Mcu*^{-/-} macrophages increased mROS production comparably in response to zymosan. *Mcu*^{-/-} macrophages showed no significant difference in the immediate production of mROS production but when we measured mROS production 18h after zymosan stimulation, we detected a modest deficit in *Mcu*^{-/-} macrophages. While it is possible that these modest deficits in mROS production contribute to phagosomal ROS in case of bacterial killing, our findings support a model wherein mCa^{2+} signaling is a key determinant of NOX-mediated phagosomal ROS production. We propose a simple and elegant design principle that mCa^{2+} signaling is an electrometabolic switch to fuel phagosomal killing and other cell-intrinsic defense mechanisms.

Acknowledgements

We thank the members of the Desai and Leitinger laboratories for scientific insights and technical help. We also thank Drs. Hervé Agaisse (UVA), Doug Bayliss (UVA), Michelle Bland (UVA), Sarah Ewald (UVA) and Kevin Lynch (UVA) for helpful and timely advice. We thank the lab of Dr. Sarah Ewald (UVA) for the use of an LSM880 microscope and W.M. Keck Center for Cellular Imaging (UVA) for the use of Zeiss 780 multiphoton FLIM microscope and Leica SP5X confocal – these instruments are supported by NIH Instrumentation grants (OD016446 and RR025616, respectively) to A.P. We also thank the following core facilities for their technical resources and support: UVA Flow Cytometry Core, Carter Immunology Center Flow Cytometry Core, Advanced Microscopy Facility Core (UVA) and the UVA Research Histology Core. The work was predominantly funded with following NIH research grants: GM108989 (B.N.D), T32 GM007055-46 (P.V.S), AG067048 (A.P.).

Author Contributions

Conception: P.V.S., B.N.D.; **Research Design:** P.V.S., B.N.D.; **Investigation:** P.V.S., T.K.D., M.E.S., C.A.D., L.H., R.O., R.C.; **Data analysis:** P.V.S., T.K.D., R.C.; **Resource assistance:** N.L., C.M.U., E.J.S., J.K. A.P.; **Writing -- Draft and Editing:** P.V.S., T.K.D., B.N.D.; **Project Administration:** B.N.D.

Declaration of Interests

The authors declare that they have no conflicts of interest to disclose.

Resource Availability

Lead Contact:

Further information and requests for resources and reagents should be directed to and will be fulfilled by the Lead Contact, Bimal N. Desai: bdesai@virginia.edu

Materials Availability

All unique/stable reagents generated in this study are available from the Lead Contact with a completed Materials Transfer Agreement.

Data and Code Availability

Requests for data should be directed to Lead Contact, Bimal Desai. Data will be made available upon request.

Experimental Model and Subject Details

Mouse Strains

Male and female mice aged 7 to 14 weeks were used for all experiments. *Mcu(M)fl/fl* Cx3cr1 cre mice were generated by crossing B6;129S-Mcutm1.1Jmol/J (Jackson Laboratories; 029817) mice to B6J.B6N(Cg)-Cx3cr1tm1.1(cre)Jung/J (Jackson Laboratories; 025524). Genotyping of *Mcu(M)fl/fl* was performed using Jax genotyping protocols for B6J.B6N(Cg)-Cx3cr1tm1.1(cre)Jung/J and B6;129S-Mcutm1.1Jmol/J strains. Genetic deletion was confirmed using quantitative real-time PCR analysis, western blot analysis, and mitochondrial Ca²⁺ uptake assays on isolated mitochondria. Mice were housed and bred in accordance with policies and procedures of the University of Virginia Institutional Animal Care and Use Committee (IACUC).

Cell lines and cell culture

The complete list of cell lines used in this study are given in the Key Resources Table. All cell lines were grown at 37°C 5% CO₂ and maintained according to ATCC guidelines. Bone marrow-derived macrophages (BMDMs) were isolated and cultured as previously described¹⁴⁹. In brief, bone marrow was extracted from mouse femur and tibia via centrifugation. The RBCs were lysed with ACK lysis buffer and the remaining cells were counted and plated on petri dishes at a density of 2-4x10⁶ cells/ plates in BMDM Media (RPMI 1640 + 10% FBS + 20% L929-conditioned media). Cells were differentiated for 7 days, and media was replaced every 3 days. For experiments BMDMs were used between days 9 - 14 post-harvest. RAW264.7 cell line (ATCC TIB-71) was maintained according to ATCC guidelines.

Methods

Ca²⁺ channel siRNA screen

RAW264.7 cells were collected and aliquoted into individual cell suspension for each siRNA target. RAW264.7 cells were resuspended in OptiMem (ThermoFisher; 31985062) with 10 nM siRNA (Dharmacon) and Lipofectamine 3000 (ThermoFisher; L3000015), according to manufacturer's instructions. Cells were plated at 0.5×10^6 cells/mL in 6-well tissue culture treated plates for 48 h. After 48 h, cells were washed 3X with HBSS and detached by gentle scraping. Cells were then counted and 0.5×10^6 cells were aliquoted into individual tubes for each siRNA target and resuspended in siRNA mix as described above. Cells were plated at 0.1×10^6 cells/well in 24-well tissue culture treated plate for another 48h. A single colony of *C. albicans* was grown overnight at 30°C in 5 mL YPD broth. On the day of the experiment, *C. albicans* were washed 3X in complete media and counted using OD600. *C. albicans* were resuspended in complete media at desired multiplicity of infection (MOI=1). RAW264.7 cells were washed 3X with HBSS and *C. albicans* were added to each well at MOI1 in 100uL complete media. RAW cells were incubated with *C. albicans* for 30 minutes at 37°C 5% CO₂. After 30 minutes, cells were washed 3X with HBSS to remove non-engulfed *C. albicans* and resuspended in complete media. One plate of cells was harvested at this 30-minute time point and lysed in sterile diH₂O for 30 minutes before being serial diluted and plated on YPD agar plates for T0 colony forming units (CFUs). Remaining cells were grown for 8h (T2). Cells were harvested as described above. Percent killing was calculated by the formula $(T0 - T2)/(T0) * 100$. Gene knockdown was confirmed via quantitative real-time PCR. Z-scores were calculated as the difference in percent killing between siRNA and siScramble-treated cells for a given siRNA target, divided by the standard deviation of the data set; z-scores across the experiment were then averaged and plotted as shown.

***In vivo* (mouse) disseminated candidiasis model**

In vivo candidiasis was performed as described¹⁸³. In brief, *wt* and *Mcu(M)*^{-/-} mice (ages between 7-12 weeks) were tail vein injected with 100 μ L of 1×10^6 viable *C. albicans*. Mice were monitored every 3 h for first 24 h and every 6 h for remainder of the study for disease symptoms using a blinded clinical score system (see *Supplemental Information* for scoring parameters). Mice were euthanized at humane endpoints: >25% loss in body weight or >7 clinical score for two consecutive time points. Mice kidneys and livers were harvested for CFU analysis and histology. Serum was analyzed by Flow Cytometry for LuminexTM analysis.

Isolation of mitochondria

Bone-marrow derived macrophages from *wt* and *Mcu*^{-/-} mice were lysed in IB++ buffer (100 mM KCl, 50 mM Tris-HCl pH 7.4, 2 mM EDTA-KOH pH 7.4, 0.5% fatty acid-free BSA, 1X protease inhibitors (Roche)). Lysates were homogenized at 4°C using a Dounce homogenizer. Whole cell fraction was spun at 600xg for 10 min at 4°C. Supernatant was transferred to prechilled Eppendorf tubes and centrifuged at 8000xg for 10 min at 4°C. Mitochondria were resuspended in IB++ w/o BSA for BCA.

Killing assays

RAW264.7 and BMDM cells were incubated with *C. albicans* or *S. cerevisiae* for 30 min (37°C, 5% CO₂). After 30 min, cells were washed 3X with HBSS to remove non-engulfed fungus and resuspended in complete media. One plate of cells was harvested at this 30 min time point and lysed in sterile distilled H₂O for 30 min before being serially diluted and plated on YPD agar plates for T₀ colony forming units (CFUs). Remaining cells were co-incubated with *C. albicans* for indicated times (T₂). *C. albicans* percent survival was calculated by the formula (T₂/T₀)*100.

***In vitro* mitochondrial Ca²⁺ uptake assay**

Crude mitochondria from *wt* and *Mcu*^{-/-} macrophages were diluted to 1 mg/mL in RB++ (137 mM KCl, 10 mM HEPES-KOH, 2.5 mM MgCl₂, 3 mM KH₂PO₄, 25 μM EDTA, 5 mM Succinate, 5 mM glutamate, 5 mM malate and 0.4 nM Ca²⁺ Green-5N (pH = 7.4) and added to a 96-well glass bottom black wall plate (CellVis, Cat#P96-1-N). Mitochondrial Ca²⁺ uptake was recorded on a FlexStation 3 with excitation/emission 515/530nm. 45 μM CaCl₂ was injected at indicated timepoint. Fluorescence was recorded every 2 seconds for the duration of experiment.

Preparation of fungal aqueous extracts

Single colonies of *C. albicans* or *S. cerevisiae* were grown overnight in 5mL of YPD at 30°C. Cells were washed 3x in BMDM Media (RPMI 1640 + 10% FBS + 20% L929-conditioned media). Cells were counted using OD600 and normalized to 4x10⁷ cells/mL and incubated at 4°C overnight. The following day cells were heat-killed at 95°C for 30 min and centrifuged at 10000xg for 10 min to pellet cell debris. The resulting supernatants (*C. albicans* extracts) was at 5X concentration for experiments and used to stimulated macrophages for indicated experiments.

LDH release assay

BMDM cells were incubated with *C. albicans* for 30 min at 37°C, 5% CO₂. After 30 min, cells were washed 3X with HBSS to remove un-engulfed *C. albicans* and resuspended in complete media. After 6 h, LDH was measured in the supernatants and Triton-X-treated positive controls. For zymosan treatment, cells were stimulated with zymosan (2:1, particles:cell) for 6 h before measuring LDH in the resulting supernatant. LDH was measured with Pierce™ LDH Cytotoxicity Assay Kit (ThermoScientific) according to manufacturer instructions using a Flexstation 3 plate reader.

Generation of RAW3mt stable cell line

RAW264.7 macrophages were transduced with CEPIA3mt lentivirus and seeded on 6-well tissue culture treated plates. Transduced cells were replenished with Selection Media (DMEM + 10% FBS + 1mg/mL puromycin) every 24h for 10 days. Surviving cells were counted and single cell cloned on 96 well plates. Single colonies were selected for validation of CEPIA3mt protein and Ca²⁺ sensitivity.

Live cell mitochondrial Ca²⁺ imaging during zymosan phagocytosis

RAW3mt cells were plated overnight on coverslips prior to imaging. Coverslips were washed 1x in Ringer Solution (155 mM NaCl, 4.5 mM KCl, 2 mM CaCl₂, 1 mM MgCl₂, 5 mM HEPES, 10 mM D-glucose) and placed in the imaging chamber. Coverslips were imaged at 37°C +/- 1°C. Microscopy was performed with an open pinhole on the Leica SP5 microscope with excitation from 'white light' and 488 nm argon lasers using Leica Applicate Suite Software (Leica). The images were processed using ImageJ software. Texas Red-conjugated zymosan *A. S. cerevisiae* Bioparticles (ThermoFisher; Z2843) were fed to macrophages on coverslips and imaged for phagocytosis. "Whole cell mCa²⁺" was analyzed by drawing ROIs around individual cells during zymosan phagocytosis. For measurements of PPMiCa response, data analysis was performed as described in **Figure 27**.

Transmission Electron Microscopy (TEM)

BMDMs were seeded onto 13 mm diameter Thermanox plastic coverslips (EMS; #72280) at 0.1x10⁶ cell per well in a 24-well plate. *C. albicans* and Zymosan were fed for 30 min (37°C, 5% CO₂). After 30 min, cells were washed 3X with HBSS to remove un-engulfed *C. albicans* and resuspended in complete media. Cells were then cultured for indicated times before fixation (4% PFA and 2.5% EM-grade glutaraldehyde). Samples were submitted to the Advanced Microscopy

Facility Core (UVA), where they were stained and cut for imaging on JOEL 1230 TEM.

Cytosolic Ca²⁺ imaging using ratiometric Fura-2

For ratiometric Ca²⁺ imaging, macrophages were incubated for 30 min with gentle agitation at RT with 5 μ M Fura-2-AM, 0.02% of pluronic acid and 500 μ M probenecid in Ringer solution ([in mM] 155 NaCl, 4.5 KCl, 2 CaCl₂, 1 MgCl₂, 5 HEPES, 10 glucose, pH 7.4). Fura-2 emissions were collected at 510 nm and with 340/380 nm excitation. Excitation was performed using a DG4 Illuminator (Sutter Instruments) and fluorescence was detected using an ORCA-Flash 4.0 V2 CMOS camera (Hamamatsu) using SlideBook 6 software. Cells were imaged every 10 secs for the duration of the experiment. *C. albicans* extracts and ionomycin were perfused at indicated times.

ATP measurements

BMDM cells were plated at 2×10^5 cells per well in a 96-well plate overnight (~16 h). On the day of the experiment, the wells were treated in triplicated for indicated times with zymosan (2:1, particles:cell). Cells were lysed and ATP was measured using the CellTiter-Glo® Luminescent cell viability assay (Promega) according to manufacturer's instruction.

Flow cytometry

BMDMs were plated at 4×10^5 cells per well in a 12-well non-tissue culture treated plate overnight (~16 h). A single colony of *C. albicans* was grown overnight at 30°C in 5mL YPD broth. On the day of the experiment, *C. albicans* were washed 3X in complete media and counted using OD600. *C. albicans* were resuspended in complete media at desired multiplicity of infection (MOI=1). *C. albicans* were washed in 3X in HBSS (w/ Mg²⁺ and Ca²⁺) and stained with 10 μ M CellTrace dye and/or 10 μ M CellRox dye, 2 μ M CypHer5E dye for 45 min at 37°C and 5% CO₂. Labeled *C. albicans* were washed 3X in complete media and added to macrophages. Cells with centrifuged for 5 min at 500 xg to facilitate macrophage

phagocytosis. Macrophages were incubated with labeled *C. albicans* for 30 min (37°C, 5% CO₂). After 30 min, cells were washed 3X with HBSS to remove unengulfed *C. albicans* and resuspended in complete media. Macrophages were then incubated for indicated times. Prior to flow cytometry, cells were detached from wells using 0.25% trypsin + EDTA, washed 2X with HBSS and analyzed using Attune NxT flow cytometer. CellTrace violet was detected using the 405nm laser with bandpass filter 440/50. CellRox was detected using 488nm laser with bandpass filter 530/30. CypHer was detected using 640nm laser with bandpass filter 670/14. Macrophages exposed to unlabeled yeast were used for gating controls. Gating strategies are shown in the extended figures.

Mitochondrial ROS measurements

BMDMs were plated into a 96-well plate at 200,000 cells per well. Cells were stained with MitoSox according to manufacturer's protocol and imaged using the FlexStation 3 (Molecular Devices). Zymosan or vehicle control was added to the wells prior to imaging. MitoSox fluorescence intensity was measured every 5 min (Ex/ Em 510/580) for 1 hour.

Fluorescence Lifetime Imaging (FLIM) microscopy

For imaging BMDMs, cells were plated on 25 mm round #1.5 glass coverslips (overnight) to obtain 70-90% confluence. Cells were washed 1X in Ringer Solution (155 mM NaCl, 4.5 mM KCl, 2 mM CaCl₂, 1 mM MgCl₂, 5 mM HEPES, 10 mM D-glucose) and placed in imaging chamber at 37°C +/- 1°C for imaging. Baseline NAD(P)H was monitored followed by the addition of *C. albicans* extract. NAD(P)H lifetime was monitored for indicated times. Cells were imaged on a Zeiss LSM-780 NLO confocal/multiphoton microscopy system with Chameleon Vission-II (Coherent Inc.) ultrafast Ti:sapphire laser with dispersion compensation (W.M. Keck Center UVA). Channel 2 460-500nm was used to collect NAD(P)H signal. Time-resolved fluorescence is recorded in TCSPC mode using SPCM (9.74) acquisition software.

Seahorse assays

Extracellular flux assays were performed on the XF24 Extracellular Flux Analyzer (Agilent Technologies). Cells were plated at a density of 1×10^5 cells per well overnight (~16h, 37°C, 5% CO₂). At beginning of the experiment, assay media was changed to DMEM containing pyruvate (Thermo-Fisher Cat#12800017; pH = 7.35 at 37°C) and cells were equilibrated for 30 min. OCR (pmol O₂/min) was measured every 5 min for the first hour of recording and then changed to 15 min intervals for the remainder of experiment (indicated by gray bar on figure). Zymosan (2:1 particles:cell) particles were injected following 3 baseline measurements of OCR. To measure maximal OCR, 2 μM BAM15 was injected at the indicated timepoint. Antimycin A (1 μM) and Rotenone (100 nM) were injected at the end of experiment. Respiration was calculated by subtracting the average of the post-Antimycin A and Rotenone measurements from the recorded measurements.

Immunofluorescence

Cells were plated overnight on coverslips prior to experiments. Following treatments, coverslips were washed 3x in PBS to remove media and loose/non-adherent cells. Coverslips were fixed in 4% PFA (30 min, RT). Coverslips were washed 3X in wash buffer (PBS with 0.05% Tween-20), blocked and permeabilized at RT for 1 h in B/P buffer (2.5% donkey serum, 2.5% goat serum, 1% BSA, 0.1% fish gelatin, 0.1% Triton X-100, and 0.05% Tween-20 in PBS), and then incubated with primary antibody diluted in B/P buffer overnight at 4°C. Coverslips were washed 3X in wash buffer and incubated at RT with the appropriate secondary antibody in B/P buffer for 2 h, followed by 3X washes in wash buffer. Coverslips were mounted on glass slides (ProLong Gold Antifade; ThermoFisher #P36930), stored in a desiccated box at 4°C and imaged within 48h. Confocal microscopy was performed on Zeiss LSM880. Data were acquired with Zen Black and analyzed using ImageJ.

Metabolomics

Confluent 12-cm plates of bone-marrow derived macrophages were used for each condition with 3-5 replicates per condition. Cells were plated overnight prior to experiment. On the day of the experiment, plates were stimulated with zymosan (2:1 particles:cell) or vehicle control for indicated time points (3 hours or 6 hours). Following stimulation, cells were washed 3X in HBSS and packed into 50-100uL pellets by centrifugation at 1000 xg for 5 min. Cells were resuspended in HBSS and transferred to pre-labeled 2.0 mL polypropylene tubes. Cells were centrifuged at 1000 xg for 5 min. Supernatant was removed and pellets were flash frozen in liquid nitrogen and stored at -80°C until shipped to Metabolon Inc. for analysis. MetaboAnalyst was used for data processing and visualization. Volcano plots were generated in Graphpad Prism by plotting the $-\log(p\text{-value})$ relative to the Log_{10} (fold change) for individual metabolites.

Key Resources Table

Table 3: Key Resources Table Cell Reports Paper

REAGENT or RESOURCE	SOURCE	IDENTIFIER
Antibodies		
Anti-Pyruvate Dehydrogenase E1-alpha subunit antibody [9H9AF5]	Abcam	Abcam Cat# ab110330, RRID:AB_10858459
Recombinant Anti-Pyruvate Dehydrogenase E1-alpha subunit (phospho S293) antibody [EPR12200]	Abcam	Abcam Cat# ab177461, RRID:AB_2756339
Anti-MCU antibody	Abcam	Cat#ab121499
Tom20 (D8T4N) Rabbit mAb	Cell Signaling Technology	Cell Signaling Technology Cat# 42406, RRID:AB_2687663
Pyruvate Dehydrogenase (C54G1) Rabbit mAb	Cell Signaling Technology	Cell Signaling Technology Cat# 3205, RRID:AB_2162926
Bacterial and Virus Strains		
pCMV-CEPIA3mt	Suzuki et al	Addgene Cat#58219, RRID: addgene_58219
Lenti-X™ Packaging Single Shots (VSV-G)	Takara	Cat#631275
Chemicals, Peptides, and Recombinant Proteins		
Carbonyl cyanide 4-(trifluoromethoxy)phenylhydrazone (FCCP)	Sigma	Cat# C2920-10MG
JC-1 Dye (Mitochondrial Membrane Potential Probe)	ThermoFisher Scientific	Cat#T3168
Calcium Green™-5N, Hexapotassium Salt, cell impermeant	ThermoFisher Scientific	Cat#C3737
Fura-2, AM, cell permeant	ThermoFisher Scientific	Cat#F1221
Probenecid	Enzo	Cat# ALX-430-113-G005
Pluronic F-127 (20% solution in DMSO)	ThermoFisher Scientific	Cat#P3000MP
Ionomycin	Cayman Chemical	Cat#10004974
MitoTracker Red	ThermoFisher Scientific	Cat#M22425
CypHer5E NHS Ester	GE healthcare	Cat#PA15401
BAM15	Cayman Chemical	Cat#17811

Antimycin A	Sigma	Cat# A8674-25MG
Rotenone	Sigma	Cat#R8875-1G
Zymosan A <i>S. cerevisiae</i> BioParticles™, Texas Red™ conjugate	ThermoFisher Scientific	Cat#Z2843
Zymosan A <i>S. cerevisiae</i> BioParticles™, unlabeled	ThermoFisher Scientific	Cat#Z2849
Dorsomorphin dihydrochloride	Tocris	Cat#3093
6-Aminonicotinamide	Cayman Chemical	Cat#10009315
6,8-Bid(benzylthio)octanoic acid	Tocris	Cat#5348
BAPTA-AM, cell permeant chelator	ThermoFisher Scientific	Cat#B6769
Beta-glucan peptide	Invivogen	Cat#tlrl-bgp
Thapsigargin	ThermoFisher Scientific	Cat#T7458
Critical Commercial Assays		
CellTiter-Glo® 2.0 Cell Viability Assay	Promega	Cat#G9241
CellTrace™ Violet Cell Proliferation Kit, for flow cytometry	ThermoFisher Scientific	Cat#C34557
CellTrace™ Yellow Cell Proliferation Kit, for flow cytometry	ThermoFisher Scientific	Cat#C34567
CellROX™ Green Reagent, for oxidative stress detection	ThermoFisher Scientific	Cat#C10444
Pierce LDH Cytotoxicity Assay Kit	ThermoFisher Scientific	Cat#88953
Experimental Models: Cell Lines		
RAW264.7 ATCC TIB-71	ATCC	ATCC Cat# TIB-71, RRID:CVCL_0493
Experimental Models: Organisms/Strains		
<i>S. cerevisiae sy1022 fy5</i>	This paper	Gift: Jeff Smith (UVA)
Culti-Loops <i>Candida albicans</i> ATCC 10231	ThermoFisher Scientific	Cat#R4601503
Mouse: B6;129S- <i>Mcu</i> ^{tm1.1Jmol/J}	The Jackson Laboratory	IMSR Cat# JAX:029817, RRID:IMSR_JAX:029817
Mouse: B6J.B6N(Cg)- <i>Cx3cr1</i> ^{tm1.1(cre)/Jung/J}	The Jackson Laboratory	IMSR Cat# JAX:025524, RRID:IMSR_JAX:025524
Oligonucleotides		

MCU Exon 5 Forward Primer 5'-TGAACGACGTGAAGACCCTG-3'	This Paper	N/A
MCU Exon 5 Reverse Primer 5'-TTCGTACCTTCTCCAGGGGG-3'	This Paper	N/A
Software and Algorithms		
ImageJ		https://imagej.nih.gov/ij/
SPCM	Wallrabe et al	https://www.becker-hickl.com/products/spcm/
Graphpad Prism	GraphPad Prism	https://www.graphpad.com/scientific-software/prism/
Seahorse Wave	Agilent	https://www.agilent.com/en/products/cell-analysis/software-download-for-wave-desktop
Other		
CFX Connect Real-Time system (Bio-Rad)	qPCR	N/A
XF24 Extracellular Flux Analyzer (Agilent Technologies)	Seahorse	N/A
FlexStation 3	In vitro mitochondrial Ca ²⁺ uptake, LDH assay, ATP assay	N/A
Leica SP5 X Confocal/Spectral Imaging Microscopy System with White Light Laser	Live mCa ²⁺ imaging for RAW-3mt	N/A
Zeiss Axio Observer with DG4 Illuminator and ORCA-Flash 4.0 V2 CMOS camera	Fura-2 Ca ²⁺ imaging	N/A
LSM880 confocal and a Chameleon multiphoton light source	Immunofluorescence	N/A
Attune NxT equipped with four lasers (488nm, 640nm, 405nm, and 561nm)	Flow Cytometry	N/A
JEOL 1230 Transmission Electron Microscope	TEM	N/A
FUIJ Film LAS-4000	Western Blotting	N/A

Quantification and Statistical Analysis

Statistics

All data were analyzed using Excel (Microsoft) and GraphPad Prism 8 (GraphPad) software. Data are presented as means with error bars which reflect standard error of the mean (SEM) as indicated in figure legends. Statistical significance ($p < 0.05$) was computed using one-way ANOVA, 2-way ANOVA, and Welch's t test (two-tailed) as indicated in figure legends. Survival curves were analyzed using Kaplan-Meier method and statistical significance ($p < 0.05$) was computed using Log-rank (Mantel-Cox) test. The sample size and representation of 'n' (mice, experimental repeats, or cells) is indicated in figure legends.

Chapter Four: Discussion and Future Directions

In previous chapters, we have discussed the implications of our findings and how they relate to a greater body of work pertaining to mCa^{2+} and MCU. In this final chapter, I take the liberty to step back to synthesize a bigger picture and speculate.

Every organ system has tissue-resident macrophages that integrate environmental signals to regulate tissue homeostasis and host defense. Within each macrophage, there are hundreds of mitochondria that sense and adapt to fuel the engines of immune responses. The flux of Ca^{2+} through MCU is a key signal to regulate this system. MCU was discovered 5 years before the start of these projects. When we began, we found ourselves serendipitously positioned to define a function for MCU in innate immunity. This thesis has shown us that mCa^{2+} uptake restrains excessive inflammatory response (Chapter 2) and fuels the bioenergetic demands of pathogen killing (Chapter 3). These concrete and definite findings have significant implications for broader physiological processes such as aging, systemic inflammation and acute infections discussed previously. In this section, I discuss the many outstanding questions that arise from my research.

Aging and mCa^{2+} uptake

Aging is a complex biological process that succeeds innumerable biological inputs. At the core of the phenomenology is the observation that chronic-low grade inflammation underlies the end physiology and pathologies associated with aging. This is the basis for the growing theory of *inflammaging* (a term coined by those who made the seminal observation – I did not make it up!!) (**Figure 33**). However, the underlying mechanisms of inflammaging are murky. We broke the problem down to two vital questions: (1) which cells contribute to

inflammaging within specific tissues and (2) what are the molecular, genetic, and environmental factors that drive inflammatory signaling in these cells.

Our studies indicate that diminished mitochondrial Ca^{2+} uptake in macrophages drives this process. This is not the sole mechanism of age-associated inflammation, and we concede that other environmental and genetic changes contribute to this complex phenomenon. In fact, our study clearly demonstrates that loss of m Ca^{2+} uptake is not universal with age, but rather a tissue-specific process of aging.

At this point, it is reasonable to assume that long-lived cells of the myeloid system – hematopoietic stem cells, myeloid progenitors and tissue-resident macrophages are likely major contributors to inflammaging. We show that *Mcu* expression is indeed downregulated in the bone-marrow progenitors that were the cellular precursors for the differentiation of our “aged” macrophages. The loss of *Mcu* expression does not grossly affect differentiation of macrophages but rather, predisposes them to a hyper-responsive phenotype. This leads to the as yet untested hypothesis that, *in vivo*, aged hematopoietic cells generate mature myeloid cells with a deficiency in m Ca^{2+} uptake. Additionally, as humans age, hematopoietic stem cells are biased towards increased myeloid differentiation¹⁸⁴. It is therefore possible that the chronic low grade inflammatory tone is set by increased abundance of myeloid cells, especially macrophages, with impaired m Ca^{2+} uptake. We also have preliminary evidence that peripheral blood mononuclear cells (PBMCs) isolated from aged mice have impaired m Ca^{2+} uptake (data not shown). This suggests that the defect in m Ca^{2+} uptake is present in aged hematopoietic cells and is carried over into the differentiated immune cells. Notably, we also find that the young *Mcu*^{-/-} mice have similar circulating immune composition to that of an 80-week-old mouse (**Figure 34A-B**). This suggests that inflammaging itself may exacerbate the process further in a feed-forward loop. The most obvious experiment to perform next is a bone-marrow replacement of young mice into old to see if we can rescue the defect in

Mcu expression and mCa^{2+} uptake observed from circulating immune cells. This future direction will establish mCa^{2+} uptake as a measure of age-associated immunological fitness and modulation of mCa^{2+} uptake could have therapeutic implications for many age-associated diseases where inflammation is involved in the etiology or pathology.

Tissue resident macrophages (TRM) are another potential source of organ-specific inflammaging. Understanding the diversity and heterogeneity of mCa^{2+} uptake across this wide spectrum of specialized macrophages may be beneficial to our understanding of age-related diseases. For example, do microglia increase their inflammatory output because of decreased mCa^{2+} uptake? If so, would this affect the onset and progression of neurodegenerative diseases. Do alveolar macrophages from older individuals have a predisposition for increased inflammation during respiratory infections? Is mCa^{2+} uptake impaired in Kupffer cells of older patients and thereby promotes non-alcoholic fatty-liver disease? All these systems and diseases have clear inflammatory and age associations to patient prognosis. It would therefore be prudent to extend this line of investigation into high resolution histological studies and determine which, if any, TRM depend on mCa^{2+} uptake to restrain them in a non-inflammatory state that is fine-tuned for that organ's physiology and homeostasis. For further mechanistic analysis on the loss of mCa^{2+} with age, our studies have two logical follow-ups: (1) what are the signals that promote mCa^{2+} uptake in aged tissues and (2) how is mCa^{2+} uptake reduced in cells?

Figure 33: Inflammaging

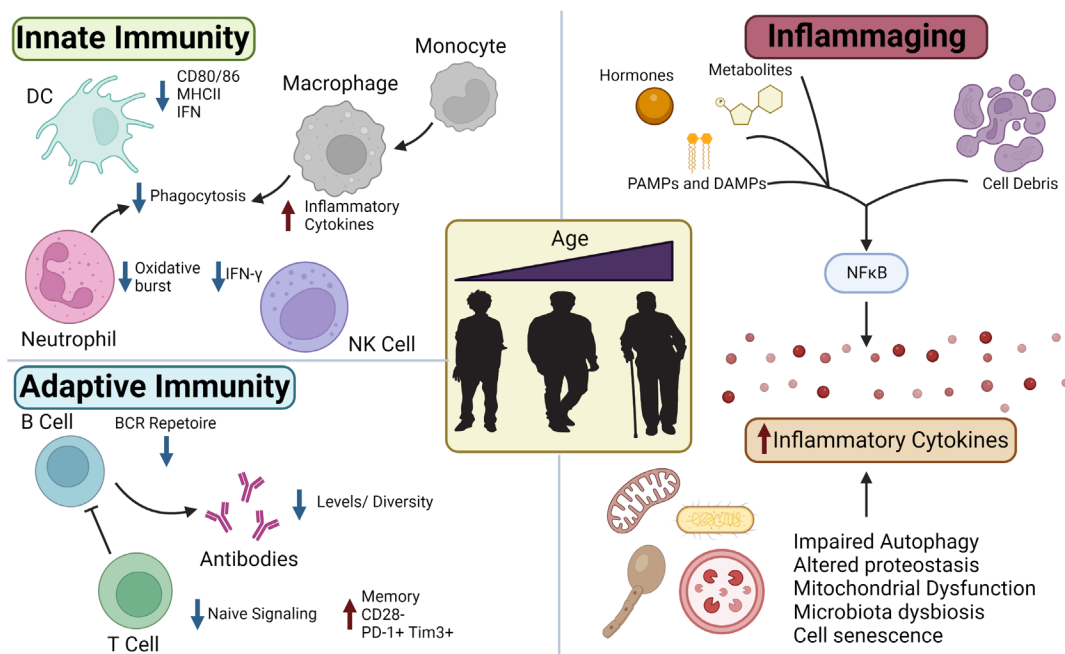


Figure 33: Inflammaging

A. Schematic of immunological changes during aging. Image is adapted from Pietrobon et al, 2020¹⁹¹.

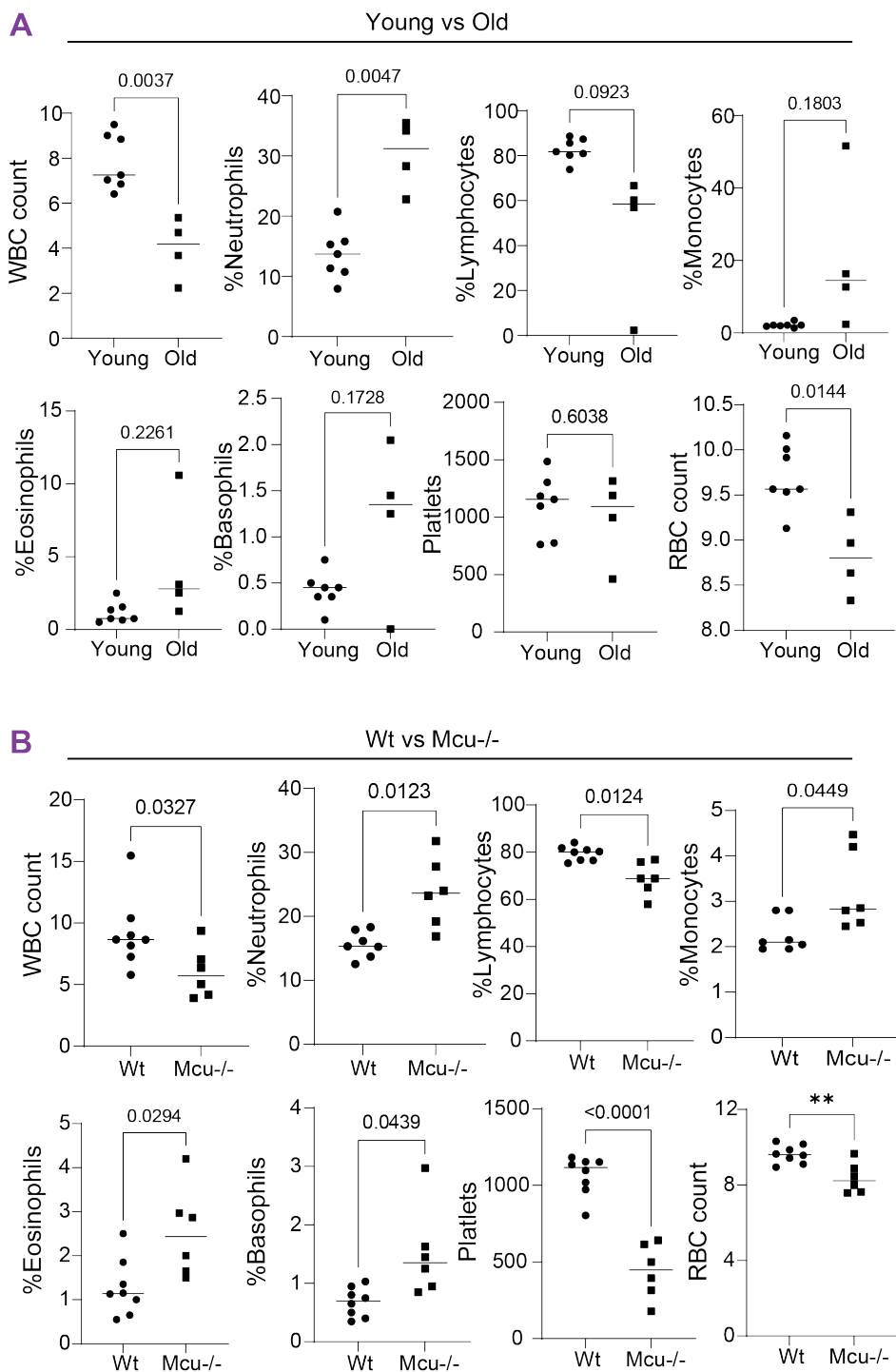
Figure 34: Immunophenotyping young vs old, *Mcu*^{-/-} vs wt

Figure 34: Immunophenotyping young vs old, M_{cu}^{-/-} vs wt

A. Young (>25wks) and old (>80wks) complete blood counts on whole blood.

B. Young wt (>25wks) and young M_{cu}^{-/-} (>25wks) complete blood counts on whole blood.

Relationship between SOCE and mCa²⁺ uptake

Earlier, I discussed the cytosolic Ca²⁺ (cCa²⁺) elevations in BMDMs-O and BMDMs-Y, in response to ATP and OxPAPC (**Figure 7J-Q**). ATP released from dead and dying cells is a normal process that occurs every day in our bodies. Under healthy conditions, this process is non-inflammatory. However, in aged macrophages, the increased cCa²⁺ elevations in response to ATP suggest that such purinergic signaling promote inflammation and, in that case, the TRM may promote inflammation in organs where purinergic signaling is especially more pronounced. Similarly, we showed that cells lacking MCU have enhanced inflammatory output in response to fungal pathogens. The relevance of this finding in age-related inflammation is obvious in the case of acute infection, but even in normal circumstances, a major component of age-related inflammation is dysbiosis and “leaky gut”¹⁸⁵. This dysregulation in the microbiome allows commensal gut microbes and microbial molecules to “leak” into the periphery causing chronic low-grade inflammation. *Candida albicans* is an abundant microbe found in the microflora of a variety of organs: intestines, lungs, and skin¹⁸⁶. It is therefore likely that fungal antigens play a major role in age-associated dysbiosis and inflammation.

Interestingly, when we investigated OxPAPC as yet another chronic mediator of inflammation, we did not see amplified cCa²⁺ responses in BMDMs-O. Unlike OxPAPC, zymosan triggers store-operated Ca²⁺ entry (SOCE) and perhaps mCa²⁺ uptake is only relevant for inflammatory stimuli that trigger SOCE. For OxPAPC, the upstream Ca²⁺ signaling, in terms of Ca²⁺ activated channels, are unknown and perhaps unaffected by mCa²⁺ buffering. This analysis revealed an interesting dichotomy in the regulation of cCa²⁺ by diminished mCa²⁺ uptake. This observation will need a more thorough investigation. If we focus our attention on inflammatory stimuli that promote SOCE, we can limit our search to Gq-coupled G-protein coupled receptors (GPCRs) and receptor-tyrosine kinases (RTKs) that are known to activate phospholipase C (PLC). For example, do molecules such as histamine, leukotriene, complement, lysophosphatidic acid,

and β -hydroxybutyric acid give SOCE in macrophages? If so, these will emerge as additional signals that promote age-associated inflammation.

Transcriptional regulation of *Mcu*

In our investigations, we found that diminished mCa^{2+} uptake promoted inflammation and then in turn, inflammation reduced the gene expression of *Mcu* (**Figure 35A**) – a feed forward inflammatory loop. But mechanistically, it is also a causality dilemma – what comes first? To make meaningful progress, it will be important to take a closer look at the transcriptional regulation of *Mcu*. We have shown that *Mcu* expression is dynamic but there has only been one study that has looked at its transcriptional regulation¹⁸⁷. Their model proposed a Ca^{2+} -dependent activation of cyclic adenosine monophosphate response element-binding protein (CREB) that controls *Mcu* expression and mCa^{2+} uptake capacity in lymphocytes. However, the authors fell short of demonstrating CREB binding to the *Mcu* promoter, and the study lacked detailed analyses of the many regulatory factors that are likely involved in *Mcu* expression. Our analysis of *Mcu* expression in aged immune cells revitalizes the need to understand the transcriptional elements responsible for *Mcu* expression.

Figure 35: *Mcu* expression in response to zymosan

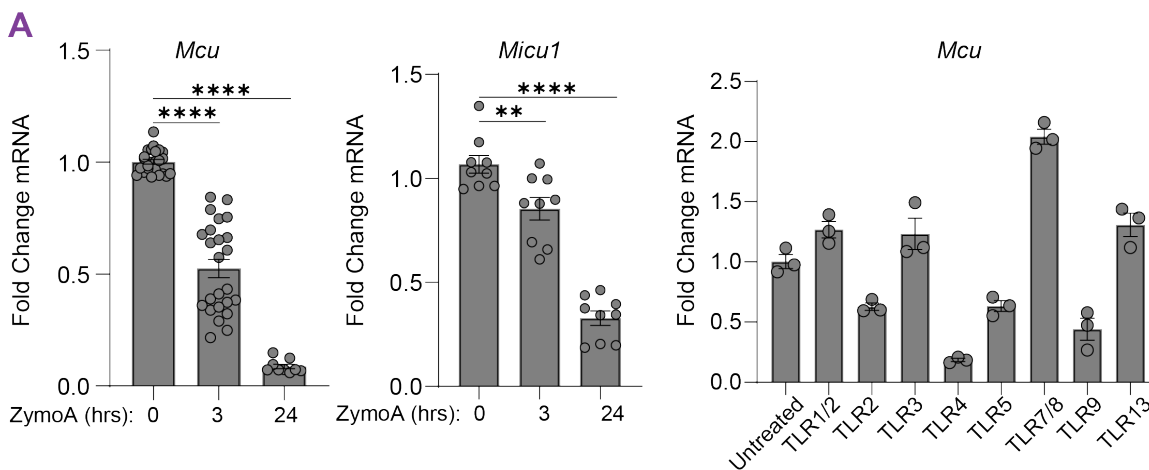
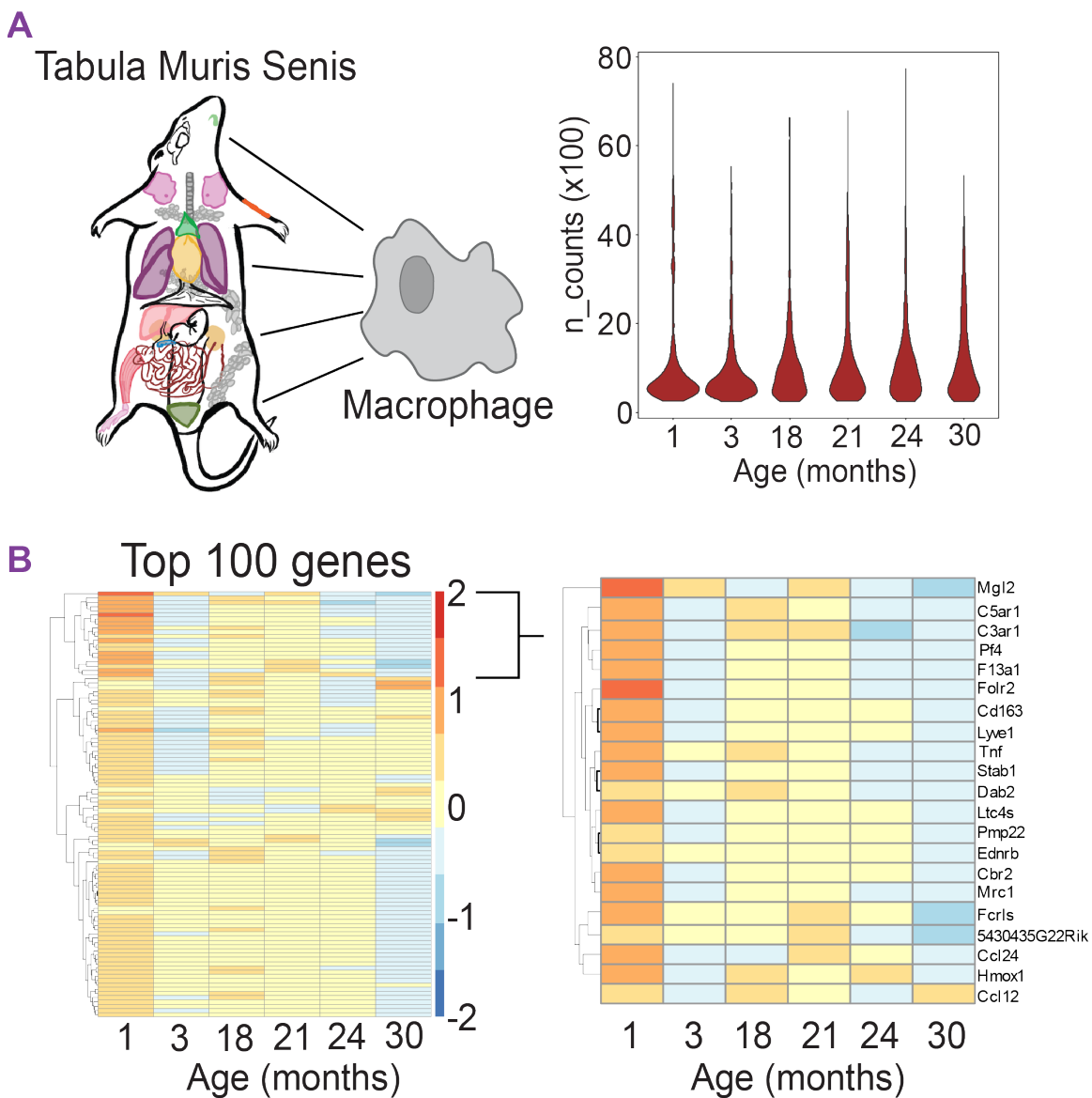


Figure 35: *Mcu* expression in response to zymosan

A. BMDMs from *wt* mice were treated with zymosan (2particles/cell) for indicated times. Total RNA was extracted for qPCR. *Mcu* expression was determined as a fold change to untreated samples. Error bars represent SEM; $p < 0.0001$ (****), $p \leq 0.001$ (***), $p \leq 0.01$ (**), $p \leq 0.05$ (*) determined by one-way ANOVA.

Cellular Aging

We have identified loss of mCa^{2+} uptake as a cellular process that underlies age-associated inflammatory state of macrophages. Aging is a complex physiological process with many known and unknown drivers. We have identified one key driver which might be amenable to pharmacological manipulation, but our study ignored the heterogeneity in macrophage populations. Using scRNAseq analyses of macrophages populations in various organs and tissues, it may be possible to identify niche populations that play an especially salient role in age-associated inflammation. In mice, we have used *Tabula Muris Senis*, or 'Mouse Aging Cell Atlas' for pilot studies¹⁸⁸ and I analyzed this dataset for insights on macrophage aging (**Figure 36A**). Preliminary studies point to key transcriptional changes associated with long lived tissue-resident macrophages, but the dataset is limited in cell numbers and read-depth (**Figure 36B**).

Figure 36: Aging Macrophages from *Tabula Muris Senis*Figure 36: Aging Macrophages from *Tabula Muris Senis*

A. Model from *Tabula Muris Senis* with n-counts plotted for each age group.

B. Macrophage populations were pooled from all peripheral organs analyzed in *Tabula Muris Senis*. Differential gene expression analysis was performed across all age groups to determine significant decreased genes.

Phagocytosis requires a rapid switch in metabolism

In Chapter 3, we showed that loss of mCa^{2+} increases pathogen burden in a model of fungal infection and renders macrophages incapable of efficient killing of fungal pathogens. An extensive body of highly cited publications have demonstrated the metabolic requirements for pathogen recognition but have largely ignored the process of phagocytosis^{85,165,169,189}. This framework relies heavily on transcriptional changes to the metabolic machinery and slow accumulation of metabolites of hours and days. The persistent and mystifying question in immunometabolism remains: How do cells switch their metabolism to meet the needs of pathogen killing? The slow nature of the responses described thus far does not resonate with the key observation that macrophages and neutrophils can kill within minutes of pathogen recognition.

Ca^{2+} -signaling provides a perfect switch for rapid change. We reported that during fungal infection, macrophages use a fast two-phase Ca^{2+} -relay to switch mitochondrial metabolism into overdrive. Within the mitochondria, Ca^{2+} rapidly changes the metabolic output of key metabolites by increasing the activity of PDH. This switch occurs within minutes and would precede transcriptional and metabolic changes occurring hours later. Macrophages lacking MCU fail to switch metabolism and have difficulty killing pathogens. In this analysis, we identified citrate as a key metabolite for NADPH production within the cytosol. We hypothesized citrate can produce NADPH by shuttling through the malic enzyme pathway. To confirm this hypothesis, it will be important to study the contributions of malic enzyme to pathogen killing and NADPH production during fungal infection. Additionally, steady state metabolite analysis has its shortcomings. The ideal experiment to prove flux through this pathway would be to perform metabolic flux assays on pyruvate.

Metabolic requirements for pathogen killing

As we discussed in Chapter 1, Ca^{2+} can have many effects on metabolic processes and mitochondrial proteins. In our study, we focused our analysis on

PDH, but it is likely that we missed many other metabolic pathways influenced by mCa^{2+} . For example, in our metabolomics studies one of the most significantly down-regulated pathways in *Mcu*^{-/-} macrophages was the Urea Cycle. The Urea Cycle is an important metabolic pathway which converts toxic ammonia into urea for excretion from the cell. It is important to note that luminal alkalinization occurs during *Candida albicans* phagocytosis and can contribute to pathogen escape¹⁹⁰. It is therefore possible that the Urea Cycle plays an important role in macrophage survival during fungal killing. Furthermore, the Urea Cycle is responsible for the generation of arginine prior to its conversion into Urea by arginase enzymes. Arginine is the substrate for the nitric oxidase synthase responsible for generating nitric oxide in response to phagocytosis. We do not understand how mCa^{2+} plays a role in this pathway, but our data would suggest that the metabolic state of *Mcu*^{-/-} macrophages influences the Urea Cycle and nitric oxide production. We must evaluate the metabolic contributions of the Urea cycle to phagosomal killing.

Despite the numerous papers on immunometabolism, there are very few papers that look at the role of metabolism in pathogen killing. Our work has yielded a framework to understand the contributions of specific metabolic pathways to pathogen killing. In an unpublished screen of metabolic inhibitors, I found that the TCA cycle is required for both fungal and pathogen killing while glycolytic pathways are more important for bacterial killing (**Figure 37A-B**). This screen is not comprehensive because specific metabolic inhibitors are not available for most metabolic pathways. Nevertheless, our work provides a starting point for a comprehensive analysis on the metabolic requirements for pathogen killing.

Summary

MCU is at the heart of innate immunity and macrophage aging. My thesis has shown us that (1) loss of mCa^{2+} buffering disrupts cCa^{2+} dynamics promoting inflammatory gene transcription and (2) mitochondrial Ca^{2+} provides a rapid

signal that can shift macrophage metabolism within minutes. Considering the future directions I outlined, it is possible that we will see MCU emerge as a molecular target for immunomodulation and to treat the many age-related diseases where inflammation contributes to pathology.

Figure 37: Metabolic regulation of pathogen killing

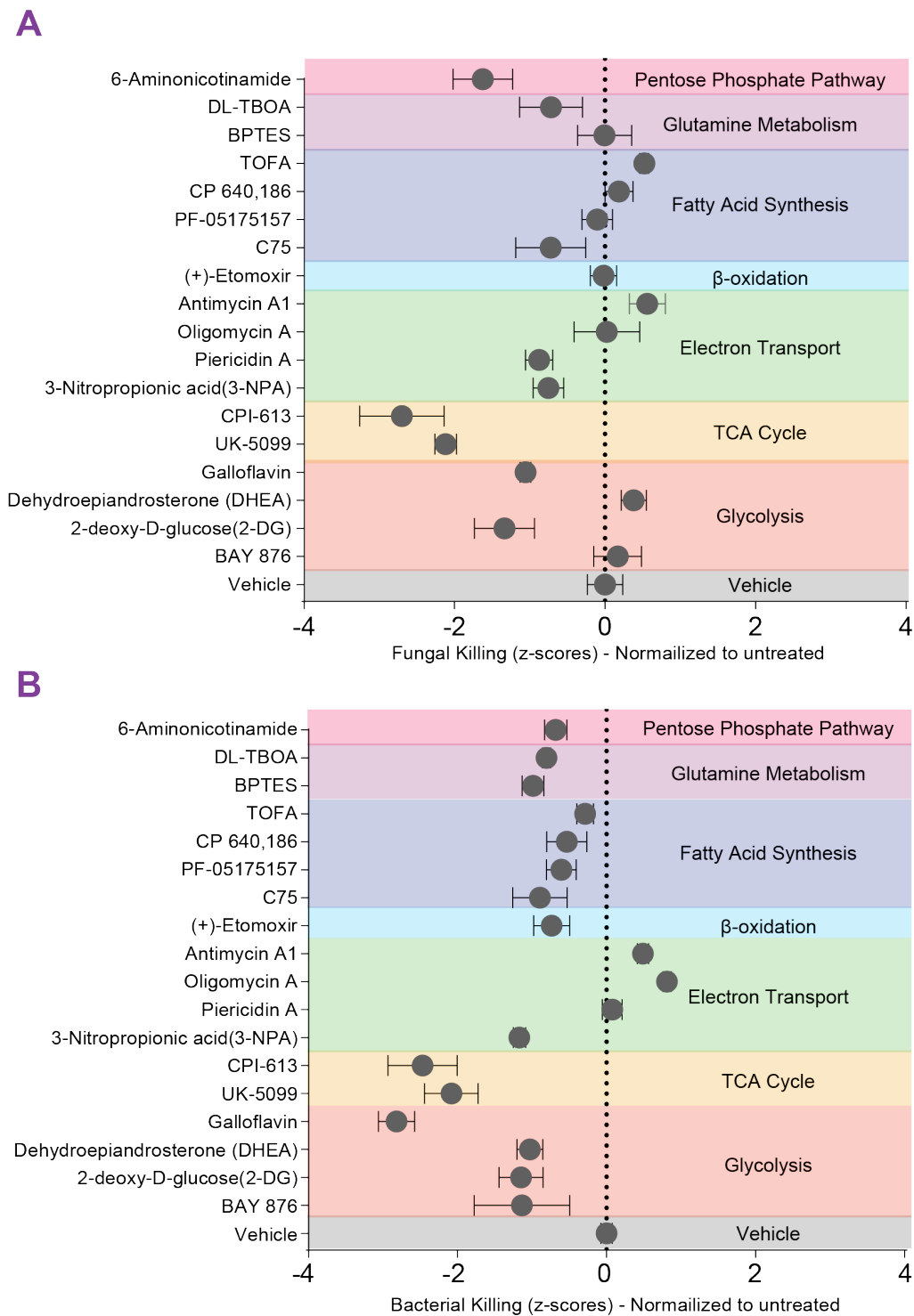


Figure 37: Metabolic regulation of pathogen killing

A. Killing of *S. cerevisiae* by macrophages transfected with pretreated with metabolic inhibitors as indicated. All inhibitors were used between 1 and 10 μM and cells were treated 30 minutes prior to infection. Plots are indicative of 4 replicates for each treatment. Error bars represent standard error of mean (SEM); $p < 0.0001$ according to one-way ANOVA.

B. Killing of *E. coli* by macrophages transfected with pretreated with metabolic inhibitors as indicated. All inhibitors were used between 1 and 10 μM and cells were treated 30 minutes prior to infection. Plots are indicative of 4 replicates for each treatment. Error bars represent standard error of mean (SEM); $p < 0.0001$ according to one-way ANOVA.

References

- 1 Carafoli, E. Historical review: Mitochondria and calcium: ups and downs of an unusual relationship. *Trends in Biochemical Sciences* **28**, 175-181, doi:10.1016/s0968-0004(03)00053-7 (2003).
- 2 Carafoli, E. The fateful encounter of mitochondria with calcium: how did it happen? *Biochim Biophys Acta* **1797**, 595-606, doi:10.1016/j.bbabi.2010.03.024 (2010).
- 3 Carafoli, E. The interplay of mitochondria with calcium: an historical appraisal. *Cell Calcium* **52**, 1-8, doi:10.1016/j.ceca.2012.02.007 (2012).
- 4 Baughman, J. M. *et al.* Integrative genomics identifies MCU as an essential component of the mitochondrial calcium uniporter. *Nature* **476**, 341-345, doi:10.1038/nature10234 (2011).
- 5 De Stefani, D., Raffaello, A., Teardo, E., Szabo, I. & Rizzuto, R. A forty-kilodalton protein of the inner membrane is the mitochondrial calcium uniporter. *Nature* **476**, 336-340, doi:10.1038/nature10230 (2011).
- 6 Vasington, F. D. & Murphy, J. V. Ca ion uptake by rat kidney mitochondria and its dependence on respiration and phosphorylation. *J Biol Chem* **237**, 2670-2677 (1962).
- 7 Deluca., H. F. & Engstrom., G. W. Calcium uptake by rat kidney mitochondria. *Biochemistry* **47** (1961).
- 8 Lehninger, A. L., Rossi, C. S. & Greenawalt, J. W. Respiration-dependent accumulation of inorganic phosphate and Ca ions by rat liver mitochondria. *Biochem Biophys Res Commun* **10**, 444-448, doi:10.1016/0006-291x(63)90377-2 (1963).
- 9 Rossi, C. S. & Lehninger, A. L. Stoichiometric Relationships between Accumulation of Ions by Mitochondria and the Energy-Coupling Sites in the Respiratory Chain. *Biochem Z* **338**, 698-713 (1963).
- 10 Carafoli, E. & Lehninger, A. L. Binding of adenine nucleotides by mitochondria during active uptake of Ca^{++} . *Biochem Biophys Res Commun* **16**, 66-70, doi:10.1016/0006-291x(64)90212-8 (1964).
- 11 Carafoli, E., Gamble, R. L. & Lehninger, A. L. On the maximum stoichiometry of energy-linked Ca^{++} accumulation during electron transport in rat liver

- mitochondria. *Biochem Biophys Res Commun* **21**, 215-220, doi:10.1016/0006-291x(65)90274-3 (1965).
- 12 Perocchi, F. *et al.* MICU1 encodes a mitochondrial EF hand protein required for Ca²⁺ uptake. *Nature* **467**, 291-296, doi:10.1038/nature09358 (2010).
- 13 Clapham, D. E. Calcium signaling. *Cell* **131**, 1047-1058, doi:10.1016/j.cell.2007.11.028 (2007).
- 14 Nalefski, E. A. & Falke, J. J. The C2 domain calcium-binding motif: structural and functional diversity. *Protein Sci* **5**, 2375-2390, doi:10.1002/pro.5560051201 (1996).
- 15 Kulkarni, S., Das, S., Funk, C. D., Murray, D. & Cho, W. Molecular basis of the specific subcellular localization of the C2-like domain of 5-lipoxygenase. *J Biol Chem* **277**, 13167-13174, doi:10.1074/jbc.M112393200 (2002).
- 16 Dolmetsch, R. E., Lewis, R. S., Goodnow, C. C. & Healy, J. I. Differential activation of transcription factors induced by Ca²⁺ response amplitude and duration. *Nature* **386**, 855-858, doi:10.1038/386855a0 (1997).
- 17 Dolmetsch, R. E., Xu, K. & Lewis, R. S. Calcium oscillations increase the efficiency and specificity of gene expression. *Nature* **392**, 933-936, doi:10.1038/31960 (1998).
- 18 Lane, N. & Martin, W. The energetics of genome complexity. *Nature* **467**, 929-934, doi:10.1038/nature09486 (2010).
- 19 Hansford, R. G. & Chappell, J. B. The effect of Ca²⁺ on the oxidation of glycerol phosphate by blowfly flight-muscle mitochondria. *Biochem Biophys Res Commun* **27**, 686-692, doi:10.1016/s0006-291x(67)80090-1 (1967).
- 20 MacDonald, M. J. & Brown, L. J. Calcium activation of mitochondrial glycerol phosphate dehydrogenase restudied. *Arch Biochem Biophys* **326**, 79-84, doi:10.1006/abbi.1996.0049 (1996).
- 21 Denton, R. M. *et al.* The hormonal regulation of pyruvate dehydrogenase complex. *Adv Enzyme Regul* **36**, 183-198, doi:10.1016/0065-2571(95)00020-8 (1996).
- 22 Denton, R. M., McCormack, J. G. & Edgell, N. J. Role of calcium ions in the regulation of intramitochondrial metabolism. Effects of Na⁺, Mg²⁺ and ruthenium red on the Ca²⁺-stimulated oxidation of oxoglutarate and on pyruvate dehydrogenase activity in intact rat heart mitochondria. *Biochem J* **190**, 107-117, doi:10.1042/bj1900107 (1980).

- 23 Marshall, S. E., McCormack, J. G. & Denton, R. M. Role of Ca²⁺ ions in the regulation of intramitochondrial metabolism in rat epididymal adipose tissue. Evidence against a role for Ca²⁺ in the activation of pyruvate dehydrogenase by insulin. *Biochem J* **218**, 249-260, doi:10.1042/bj2180249 (1984).
- 24 McCormack, J. G. & Denton, R. M. Role of Ca²⁺ ions in the regulation of intramitochondrial metabolism in rat heart. Evidence from studies with isolated mitochondria that adrenaline activates the pyruvate dehydrogenase and 2-oxoglutarate dehydrogenase complexes by increasing the intramitochondrial concentration of Ca²⁺. *Biochem J* **218**, 235-247, doi:10.1042/bj2180235 (1984).
- 25 Denton, R. M. & McCormack, J. G. Physiological role of Ca²⁺ transport by mitochondria. *Nature* **315**, 635, doi:10.1038/315635a0 (1985).
- 26 McCormack, J. G. Characterization of the effects of Ca²⁺ on the intramitochondrial Ca²⁺-sensitive enzymes from rat liver and within intact rat liver mitochondria. *Biochem J* **231**, 581-595, doi:10.1042/bj2310581 (1985).
- 27 Turkan, A., Hiromasa, Y. & Roche, T. E. Formation of a complex of the catalytic subunit of pyruvate dehydrogenase phosphatase isoform 1 (PDP1c) and the L2 domain forms a Ca²⁺ binding site and captures PDP1c as a monomer. *Biochemistry* **43**, 15073-15085, doi:10.1021/bi048901y (2004).
- 28 Denton, R. M. Regulation of mitochondrial dehydrogenases by calcium ions. *Biochim Biophys Acta* **1787**, 1309-1316, doi:10.1016/j.bbabi.2009.01.005 (2009).
- 29 Teague, W. M., Pettit, F. H., Wu, T. L., Silberman, S. R. & Reed, L. J. Purification and properties of pyruvate dehydrogenase phosphatase from bovine heart and kidney. *Biochemistry* **21**, 5585-5592, doi:10.1021/bi00265a031 (1982).
- 30 Vassilyev, D. G. & Symersky, J. Crystal structure of pyruvate dehydrogenase phosphatase 1 and its functional implications. *J Mol Biol* **370**, 417-426, doi:10.1016/j.jmb.2007.05.002 (2007).

- 31 McCormack, J. G. & Denton, R. M. The effects of calcium ions and adenine nucleotides on the activity of pig heart 2-oxoglutarate dehydrogenase complex. *Biochem J* **180**, 533-544, doi:10.1042/bj1800533 (1979).
- 32 Rutter, G. A. & Denton, R. M. The binding of Ca²⁺ ions to pig heart NAD⁺-isocitrate dehydrogenase and the 2-oxoglutarate dehydrogenase complex. *Biochem J* **263**, 453-462, doi:10.1042/bj2630453 (1989).
- 33 Denton, R. M., Richards, D. A. & Chin, J. G. Calcium ions and the regulation of NAD⁺-linked isocitrate dehydrogenase from the mitochondria of rat heart and other tissues. *Biochem J* **176**, 899-906, doi:10.1042/bj1760899 (1978).
- 34 Rutter, G. A. & Denton, R. M. Regulation of NAD⁺-linked isocitrate dehydrogenase and 2-oxoglutarate dehydrogenase by Ca²⁺ ions within toluene-permeabilized rat heart mitochondria. Interactions with regulation by adenine nucleotides and NADH/NAD⁺ ratios. *Biochem J* **252**, 181-189, doi:10.1042/bj2520181 (1988).
- 35 Saotome, M. *et al.* Bidirectional Ca²⁺-dependent control of mitochondrial dynamics by the Miro GTPase. *Proc Natl Acad Sci U S A* **105**, 20728-20733, doi:10.1073/pnas.0808953105 (2008).
- 36 Liu, X. & Hajnoczky, G. Ca²⁺-dependent regulation of mitochondrial dynamics by the Miro-Milton complex. *Int J Biochem Cell Biol* **41**, 1972-1976, doi:10.1016/j.biocel.2009.05.013 (2009).
- 37 Wang, X. & Schwarz, T. L. The mechanism of Ca²⁺ -dependent regulation of kinesin-mediated mitochondrial motility. *Cell* **136**, 163-174, doi:10.1016/j.cell.2008.11.046 (2009).
- 38 Rizzuto, R., Simpson, A. W., Brini, M. & Pozzan, T. Rapid changes of mitochondrial Ca²⁺ revealed by specifically targeted recombinant aequorin. *Nature* **358**, 325-327, doi:10.1038/358325a0 (1992).
- 39 Kirichok, Y., Krapivinsky, G. & Clapham, D. E. The mitochondrial calcium uniporter is a highly selective ion channel. *Nature* **427**, 360-364, doi:10.1038/nature02246 (2004).
- 40 Sancak, Y. *et al.* EMRE is an essential component of the mitochondrial calcium uniporter complex. *Science* **342**, 1379-1382, doi:10.1126/science.1242993 (2013).

- 41 Csordas, G. *et al.* MICU1 controls both the threshold and cooperative activation of the mitochondrial Ca²⁺(+) uniporter. *Cell Metab* **17**, 976-987, doi:10.1016/j.cmet.2013.04.020 (2013).
- 42 Plovanich, M. *et al.* MICU2, a paralog of MICU1, resides within the mitochondrial uniporter complex to regulate calcium handling. *PLoS One* **8**, e55785, doi:10.1371/journal.pone.0055785 (2013).
- 43 Kamer, K. J. & Mootha, V. K. MICU1 and MICU2 play nonredundant roles in the regulation of the mitochondrial calcium uniporter. *EMBO Rep* **15**, 299-307, doi:10.1002/embr.201337946 (2014).
- 44 Patron, M. *et al.* MICU1 and MICU2 finely tune the mitochondrial Ca²⁺ uniporter by exerting opposite effects on MCU activity. *Molecular cell* **53**, 726-737, doi:10.1016/j.molcel.2014.01.013 (2014).
- 45 Patron, M., Granatiero, V., Espino, J., Rizzuto, R. & De Stefani, D. MICU3 is a tissue-specific enhancer of mitochondrial calcium uptake. *Cell Death Differ* **26**, 179-195, doi:10.1038/s41418-018-0113-8 (2019).
- 46 Garg, V. *et al.* The mechanism of MICU-dependent gating of the mitochondrial Ca²⁺uniporter. *Elife* **10**, doi:10.7554/eLife.69312 (2021).
- 47 Raffaello, A. *et al.* The mitochondrial calcium uniporter is a multimer that can include a dominant-negative pore-forming subunit. *EMBO J* **32**, 2362-2376, doi:10.1038/emboj.2013.157 (2013).
- 48 Fan, M. *et al.* Structure and mechanism of the mitochondrial Ca²⁺ uniporter holocomplex. *Nature* **582**, 129-133, doi:10.1038/s41586-020-2309-6 (2020).
- 49 Wang, Y. *et al.* Structural insights into the Ca²⁺-dependent gating of the human mitochondrial calcium uniporter. *Elife* **9**, doi:10.7554/eLife.60513 (2020).
- 50 Fieni, F., Lee, S. B., Jan, Y. N. & Kirichok, Y. Activity of the mitochondrial calcium uniporter varies greatly between tissues. *Nat Commun* **3**, 1317, doi:10.1038/ncomms2325 (2012).
- 51 Pan, X. *et al.* The physiological role of mitochondrial calcium revealed by mice lacking the mitochondrial calcium uniporter. *Nat Cell Biol* **15**, 1464-1472, doi:10.1038/ncb2868 (2013).

- 52 Murphy, E. *et al.* Unresolved questions from the analysis of mice lacking MCU expression. *Biochem Biophys Res Commun* **449**, 384-385, doi:10.1016/j.bbrc.2014.04.144 (2014).
- 53 Bick, A. G., Calvo, S. E. & Mootha, V. K. Evolutionary diversity of the mitochondrial calcium uniporter. *Science* **336**, 886, doi:10.1126/science.1214977 (2012).
- 54 Kamer, K. J., Grabarek, Z. & Mootha, V. K. High-affinity cooperative Ca(2+) binding by MICU1-MICU2 serves as an on-off switch for the uniporter. *EMBO Rep* **18**, 1397-1411, doi:10.15252/embr.201643748 (2017).
- 55 Logan, C. V. *et al.* Loss-of-function mutations in MICU1 cause a brain and muscle disorder linked to primary alterations in mitochondrial calcium signaling. *Nat Genet* **46**, 188-193, doi:10.1038/ng.2851 (2014).
- 56 MacEwen, M. J. S. *et al.* Molecular basis of EMRE-dependence of the human mitochondrial calcium uniporter. doi:10.1101/637918 (2019).
- 57 Wang, Y. *et al.* Structural Mechanism of EMRE-Dependent Gating of the Human Mitochondrial Calcium Uniporter. *Cell* **177**, 1252-1261 e1213, doi:10.1016/j.cell.2019.03.050 (2019).
- 58 Garbincius, J. F. & Elrod, J. W. Mitochondrial calcium exchange in physiology and disease. *Physiol Rev* **102**, 893-992, doi:10.1152/physrev.00041.2020 (2022).
- 59 Holmstrom, K. M. *et al.* Assessment of cardiac function in mice lacking the mitochondrial calcium uniporter. *J Mol Cell Cardiol* **85**, 178-182, doi:10.1016/j.yjmcc.2015.05.022 (2015).
- 60 Luongo, T. S. *et al.* The Mitochondrial Calcium Uniporter Matches Energetic Supply with Cardiac Workload during Stress and Modulates Permeability Transition. *Cell Rep* **12**, 23-34, doi:10.1016/j.celrep.2015.06.017 (2015).
- 61 Kwong, J. Q. *et al.* The Mitochondrial Calcium Uniporter Selectively Matches Metabolic Output to Acute Contractile Stress in the Heart. *Cell Rep* **12**, 15-22, doi:10.1016/j.celrep.2015.06.002 (2015).
- 62 Mammucari, C. *et al.* The mitochondrial calcium uniporter controls skeletal muscle trophism in vivo. *Cell Rep* **10**, 1269-1279, doi:10.1016/j.celrep.2015.01.056 (2015).

- 63 Kwong, J. Q. *et al.* The mitochondrial calcium uniporter underlies metabolic fuel preference in skeletal muscle. *JCI Insight* **3**, doi:10.1172/jci.insight.121689 (2018).
- 64 Flicker, D., Sancak, Y., Mick, E., Goldberger, O. & Mootha, V. K. Exploring the In Vivo Role of the Mitochondrial Calcium Uniporter in Brown Fat Bioenergetics. *Cell Rep* **27**, 1364-1375 e1365, doi:10.1016/j.celrep.2019.04.013 (2019).
- 65 Drago, I. & Davis, R. L. Inhibiting the Mitochondrial Calcium Uniporter during Development Impairs Memory in Adult *Drosophila*. *Cell Rep* **16**, 2763-2776, doi:10.1016/j.celrep.2016.08.017 (2016).
- 66 Tufi, R. *et al.* Comprehensive Genetic Characterization of Mitochondrial Ca(2+) Uniporter Components Reveals Their Different Physiological Requirements In Vivo. *Cell Rep* **27**, 1541-1550 e1545, doi:10.1016/j.celrep.2019.04.033 (2019).
- 67 Liu, J. C. *et al.* EMRE is essential for mitochondrial calcium uniporter activity in a mouse model. *JCI Insight* **5**, doi:10.1172/jci.insight.134063 (2020).
- 68 Antony, A. N. *et al.* MICU1 regulation of mitochondrial Ca(2+) uptake dictates survival and tissue regeneration. *Nat Commun* **7**, 10955, doi:10.1038/ncomms10955 (2016).
- 69 Debattisti, V. *et al.* Dysregulation of Mitochondrial Ca(2+) Uptake and Sarcolemma Repair Underlie Muscle Weakness and Wasting in Patients and Mice Lacking MICU1. *Cell Rep* **29**, 1274-1286 e1276, doi:10.1016/j.celrep.2019.09.063 (2019).
- 70 Bick, A. G. *et al.* Cardiovascular homeostasis dependence on MICU2, a regulatory subunit of the mitochondrial calcium uniporter. *Proc Natl Acad Sci U S A* **114**, E9096-E9104, doi:10.1073/pnas.1711303114 (2017).
- 71 Puente, B. N. *et al.* MICU3 Plays an Important Role in Cardiovascular Function. *Circ Res* **127**, 1571-1573, doi:10.1161/CIRCRESAHA.120.317177 (2020).
- 72 Huo, J. *et al.* MCUB Induction Protects the Heart From Postischemic Remodeling. *Circ Res* **127**, 379-390, doi:10.1161/CIRCRESAHA.119.316369 (2020).

- 73 Lewis-Smith, D. *et al.* Homozygous deletion in MICU1 presenting with fatigue and lethargy in childhood. *Neurol Genet* **2**, e59, doi:10.1212/NXG.0000000000000059 (2016).
- 74 O'Grady, G. L. *et al.* Diagnosis and etiology of congenital muscular dystrophy: We are halfway there. *Ann Neurol* **80**, 101-111, doi:10.1002/ana.24687 (2016).
- 75 Musa, S. *et al.* A Middle Eastern Founder Mutation Expands the Genotypic and Phenotypic Spectrum of Mitochondrial MICU1 Deficiency: A Report of 13 Patients. *JIMD Rep* **43**, 79-83, doi:10.1007/8904_2018_107 (2019).
- 76 Mojibafan, M. *et al.* Reporting a rare form of myopathy, myopathy with extrapyramidal signs, in an Iranian family using next generation sequencing: a case report. *BMC Med Genet* **21**, 77, doi:10.1186/s12881-020-01016-y (2020).
- 77 Wilton, K. M. *et al.* Developmental brain abnormalities and acute encephalopathy in a patient with myopathy with extrapyramidal signs secondary to pathogenic variants in MICU1. *JIMD Rep* **53**, 22-28, doi:10.1002/jmd2.12114 (2020).
- 78 Shamseldin, H. E. *et al.* A null mutation in MICU2 causes abnormal mitochondrial calcium homeostasis and a severe neurodevelopmental disorder. *Brain* **140**, 2806-2813, doi:10.1093/brain/awx237 (2017).
- 79 Mills, E. L. *et al.* Succinate Dehydrogenase Supports Metabolic Repurposing of Mitochondria to Drive Inflammatory Macrophages. *Cell* **167**, 457-470 e413, doi:10.1016/j.cell.2016.08.064 (2016).
- 80 Everts, B. *et al.* TLR-driven early glycolytic reprogramming via the kinases TBK1-IKKvarepsilon supports the anabolic demands of dendritic cell activation. *Nat Immunol* **15**, 323-332, doi:10.1038/ni.2833 (2014).
- 81 Infantino, V. *et al.* The mitochondrial citrate carrier: a new player in inflammation. *Biochem J* **438**, 433-436, doi:10.1042/BJ20111275 (2011).
- 82 Infantino, V., Iacobazzi, V., Palmieri, F. & Menga, A. ATP-citrate lyase is essential for macrophage inflammatory response. *Biochem Bioph Res Co* **440**, 105-111, doi:10.1016/j.bbrc.2013.09.037 (2013).
- 83 Cordes, T. *et al.* Immunoresponsive Gene 1 and Itaconate Inhibit Succinate Dehydrogenase to Modulate Intracellular Succinate Levels. *J Biol Chem* **291**, 14274-14284, doi:10.1074/jbc.M115.685792 (2016).

- 84 Lampropoulou, V. *et al.* Itaconate Links Inhibition of Succinate Dehydrogenase with Macrophage Metabolic Remodeling and Regulation of Inflammation. *Cell Metab* **24**, 158-166, doi:10.1016/j.cmet.2016.06.004 (2016).
- 85 Mills, E. L. *et al.* Itaconate is an anti-inflammatory metabolite that activates Nrf2 via alkylation of KEAP1. *Nature* **556**, 113-117, doi:10.1038/nature25986 (2018).
- 86 Lopez-Otin, C., Blasco, M. A., Partridge, L., Serrano, M. & Kroemer, G. The hallmarks of aging. *Cell* **153**, 1194-1217, doi:10.1016/j.cell.2013.05.039 (2013).
- 87 Franceschi, C. *et al.* Inflammaging and anti-inflammaging: a systemic perspective on aging and longevity emerged from studies in humans. *Mech Ageing Dev* **128**, 92-105, doi:10.1016/j.mad.2006.11.016 (2007).
- 88 Franceschi, C., Garagnani, P., Parini, P., Giuliani, C. & Santoro, A. Inflammaging: a new immune-metabolic viewpoint for age-related diseases. *Nat Rev Endocrinol* **14**, 576-590, doi:10.1038/s41574-018-0059-4 (2018).
- 89 van Beek, A. A., Van den Bossche, J., Mastroberardino, P. G., de Winther, M. P. J. & Leenen, P. J. M. Metabolic Alterations in Aging Macrophages: Ingredients for Inflammaging? *Trends Immunol* **40**, 113-127, doi:10.1016/j.it.2018.12.007 (2019).
- 90 Crunkhorn, S. Reversing inflammaging. *Nat Rev Drug Discov* **19**, 168, doi:10.1038/d41573-020-00019-x (2020).
- 91 Fulop, T. *et al.* Immunology of Aging: the Birth of Inflammaging. *Clin Rev Allergy Immunol*, doi:10.1007/s12016-021-08899-6 (2021).
- 92 Zhang, H., Menzies, K. J. & Auwerx, J. The role of mitochondria in stem cell fate and aging. *Development* **145**, doi:10.1242/dev.143420 (2018).
- 93 Sun, N., Youle, R. J. & Finkel, T. The Mitochondrial Basis of Aging. *Mol Cell* **61**, 654-666, doi:10.1016/j.molcel.2016.01.028 (2016).
- 94 Chaudhuri, D., Sancak, Y., Mootha, V. K. & Clapham, D. E. MCU encodes the pore conducting mitochondrial calcium currents. *Elife* **2**, e00704, doi:10.7554/eLife.00704 (2013).
- 95 Kamer, K. J. & Mootha, V. K. The molecular era of the mitochondrial calcium uniporter. *Nat Rev Mol Cell Biol* **16**, 545-553, doi:10.1038/nrm4039 (2015).

- 96 Oxenoid, K. *et al.* Architecture of the mitochondrial calcium uniporter. *Nature* **533**, 269-273, doi:10.1038/nature17656 (2016).
- 97 Ghosh, S. & Hayden, M. S. New regulators of NF-kappaB in inflammation. *Nat Rev Immunol* **8**, 837-848, doi:10.1038/nri2423 (2008).
- 98 Hayden, M. S. & Ghosh, S. Shared principles in NF-kappaB signaling. *Cell* **132**, 344-362, doi:10.1016/j.cell.2008.01.020 (2008).
- 99 Hayden, M. S. & Ghosh, S. NF-kappaB, the first quarter-century: remarkable progress and outstanding questions. *Genes Dev* **26**, 203-234, doi:10.1101/gad.183434.111 (2012).
- 100 Zhang, Q., Lenardo, M. J. & Baltimore, D. 30 Years of NF-kappaB: A Blossoming of Relevance to Human Pathobiology. *Cell* **168**, 37-57, doi:10.1016/j.cell.2016.12.012 (2017).
- 101 Franceschi, C. Inflammaging as a major characteristic of old people: can it be prevented or cured? *Nutr Rev* **65**, S173-176, doi:10.1111/j.1753-4887.2007.tb00358.x (2007).
- 102 Matacchione, G. *et al.* Senescent macrophages in the human adipose tissue as a source of inflammaging. *Geroscience*, doi:10.1007/s11357-022-00536-0 (2022).
- 103 Leng, S., Chaves, P., Koenig, K. & Walston, J. Serum interleukin-6 and hemoglobin as physiological correlates in the geriatric syndrome of frailty: a pilot study. *J Am Geriatr Soc* **50**, 1268-1271, doi:10.1046/j.1532-5415.2002.50315.x (2002).
- 104 Bruunsgaard, H. & Pedersen, B. K. Age-related inflammatory cytokines and disease. *Immunol Allergy Clin North Am* **23**, 15-39, doi:10.1016/s0889-8561(02)00056-5 (2003).
- 105 Ferrucci, L. *et al.* The origins of age-related proinflammatory state. *Blood* **105**, 2294-2299, doi:10.1182/blood-2004-07-2599 (2005).
- 106 Dinarello, C. A. Interleukin 1 and interleukin 18 as mediators of inflammation and the aging process. *Am J Clin Nutr* **83**, 447S-455S, doi:10.1093/ajcn/83.2.447S (2006).
- 107 van Deursen, J. M. The role of senescent cells in ageing. *Nature* **509**, 439-446, doi:10.1038/nature13193 (2014).

- 108 Kuilman, T. *et al.* Oncogene-induced senescence relayed by an interleukin-dependent inflammatory network. *Cell* **133**, 1019-1031, doi:10.1016/j.cell.2008.03.039 (2008).
- 109 Kuilman, T. & Peeper, D. S. Senescence-messaging secretome: SMS-ing cellular stress. *Nat Rev Cancer* **9**, 81-94, doi:10.1038/nrc2560 (2009).
- 110 Okabe, Y. & Medzhitov, R. Tissue biology perspective on macrophages. *Nat Immunol* **17**, 9-17, doi:10.1038/ni.3320 (2016).
- 111 Nobs, S. P. & Kopf, M. Tissue-resident macrophages: guardians of organ homeostasis. *Trends Immunol* **42**, 495-507, doi:10.1016/j.it.2021.04.007 (2021).
- 112 Adler, A. S. *et al.* Motif module map reveals enforcement of aging by continual NF-kappaB activity. *Genes Dev* **21**, 3244-3257, doi:10.1101/gad.1588507 (2007).
- 113 Donato, A. J., Black, A. D., Jablonski, K. L., Gano, L. B. & Seals, D. R. Aging is associated with greater nuclear NF kappa B, reduced I kappa B alpha, and increased expression of proinflammatory cytokines in vascular endothelial cells of healthy humans. *Aging Cell* **7**, 805-812, doi:10.1111/j.1474-9726.2008.00438.x (2008).
- 114 Osorio, F. G. *et al.* Nuclear lamina defects cause ATM-dependent NF-kappaB activation and link accelerated aging to a systemic inflammatory response. *Genes Dev* **26**, 2311-2324, doi:10.1101/gad.197954.112 (2012).
- 115 Wang, Y. *et al.* NF-kappaB signaling in skin aging. *Mech Ageing Dev* **184**, 111160, doi:10.1016/j.mad.2019.111160 (2019).
- 116 Garg, V. & Kirichok, Y. Y. Patch-Clamp Analysis of the Mitochondrial Calcium Uniporter. *Methods Mol Biol* **1925**, 75-86, doi:10.1007/978-1-4939-9018-4_7 (2019).
- 117 Wang, C., Jacewicz, A., Delgado, B. D., Baradaran, R. & Long, S. B. Structures reveal gatekeeping of the mitochondrial Ca(2+) uniporter by MICU1-MICU2. *Elife* **9**, doi:10.7554/eLife.59991 (2020).
- 118 Wu, W. *et al.* The structure of the MICU1-MICU2 complex unveils the regulation of the mitochondrial calcium uniporter. *EMBO J* **39**, e104285, doi:10.15252/embj.2019104285 (2020).
- 119 Duchon, M. R. Mitochondria and calcium: from cell signalling to cell death. *J Physiol* **529 Pt 1**, 57-68, doi:10.1111/j.1469-7793.2000.00057.x (2000).

- 120 Rizzuto, R., De Stefani, D., Raffaello, A. & Mammucari, C. Mitochondria as sensors and regulators of calcium signalling. *Nat Rev Mol Cell Biol* **13**, 566-578, doi:10.1038/nrm3412 (2012).
- 121 Feske, S., Wulff, H. & Skolnik, E. Y. Ion channels in innate and adaptive immunity. *Annu Rev Immunol* **33**, 291-353, doi:10.1146/annurev-immunol-032414-112212 (2015).
- 122 Seegren, P. V. *et al.* Mitochondrial Ca(2+) Signaling Is an Electrometabolic Switch to Fuel Phagosome Killing. *Cell Rep* **33**, 108411, doi:10.1016/j.celrep.2020.108411 (2020).
- 123 Feno, S. *et al.* The dominant-negative mitochondrial calcium uniporter subunit MCUB drives macrophage polarization during skeletal muscle regeneration. *Sci Signal* **14**, eabf3838, doi:10.1126/scisignal.abf3838 (2021).
- 124 Tedesco, S. *et al.* Mitochondrial Calcium Uptake Is Instrumental to Alternative Macrophage Polarization and Phagocytic Activity. *International Journal of Molecular Sciences* **20**, doi:ARTN 4966 10.3390/ijms20194966 (2019).
- 125 Li, T. *et al.* *Listeria monocytogenes* upregulates mitochondrial calcium signalling to inhibit LC3-associated phagocytosis as a survival strategy. *Nat Microbiol* **6**, 366-379, doi:10.1038/s41564-020-00843-2 (2021).
- 126 Sebag, S. C. *et al.* Inhibition of the mitochondrial calcium uniporter prevents IL-13 and allergen-mediated airway epithelial apoptosis and loss of barrier function. *Exp Cell Res* **362**, 400-411, doi:10.1016/j.yexcr.2017.12.003 (2018).
- 127 Gu, L. *et al.* Mitochondrial calcium uniporter regulates PGC-1alpha expression to mediate metabolic reprogramming in pulmonary fibrosis. *Redox Biol* **26**, 101307, doi:10.1016/j.redox.2019.101307 (2019).
- 128 Rimessi, A. *et al.* Pharmacological modulation of mitochondrial calcium uniporter controls lung inflammation in cystic fibrosis. *Sci Adv* **6**, eaax9093, doi:10.1126/sciadv.aax9093 (2020).
- 129 Consortium, G. T. The Genotype-Tissue Expression (GTEx) project. *Nat Genet* **45**, 580-585, doi:10.1038/ng.2653 (2013).

- 130 Yim, A. *et al.* mitoXplorer, a visual data mining platform to systematically analyze and visualize mitochondrial expression dynamics and mutations. *Nucleic Acids Res* **48**, 605-632, doi:10.1093/nar/gkz1128 (2020).
- 131 Rohani, A., Kashatus, J. A., Sessions, D. T., Sharmin, S. & Kashatus, D. F. Mito Hacker: a set of tools to enable high-throughput analysis of mitochondrial network morphology. *Sci Rep* **10**, 18941, doi:10.1038/s41598-020-75899-5 (2020).
- 132 Yoast, R. E. *et al.* The Mitochondrial Ca(2+) uniporter is a central regulator of interorganellar Ca(2+) transfer and NFAT activation. *J Biol Chem* **297**, 101174, doi:10.1016/j.jbc.2021.101174 (2021).
- 133 Radstake, F. D. W., Raaijmakers, E. A. L., Luttge, R., Zinger, S. & Frimat, J. P. CALIMA: The semi-automated open-source calcium imaging analyzer. *Comput Methods Programs Biomed* **179**, 104991, doi:10.1016/j.cmpb.2019.104991 (2019).
- 134 Spychala, M. S. *et al.* Age-related changes in the gut microbiota influence systemic inflammation and stroke outcome. *Ann Neurol* **84**, 23-36, doi:10.1002/ana.25250 (2018).
- 135 Lee, B. Y. *et al.* Senescence-associated beta-galactosidase is lysosomal beta-galactosidase. *Aging Cell* **5**, 187-195, doi:10.1111/j.1474-9726.2006.00199.x (2006).
- 136 Coppe, J. P., Desprez, P. Y., Krtolica, A. & Campisi, J. The senescence-associated secretory phenotype: the dark side of tumor suppression. *Annu Rev Pathol* **5**, 99-118, doi:10.1146/annurev-pathol-121808-102144 (2010).
- 137 Brough, D. *et al.* Ca²⁺ stores and Ca²⁺ entry differentially contribute to the release of IL-1 beta and IL-1 alpha from murine macrophages. *J Immunol* **170**, 3029-3036, doi:10.4049/jimmunol.170.6.3029 (2003).
- 138 Srimathi, T. *et al.* Mapping of POP1-binding site on pyrin domain of ASC. *J Biol Chem* **283**, 15390-15398, doi:10.1074/jbc.M801589200 (2008).
- 139 Hara, H. *et al.* Phosphorylation of the adaptor ASC acts as a molecular switch that controls the formation of speck-like aggregates and inflammasome activity. *Nat Immunol* **14**, 1247-1255, doi:10.1038/ni.2749 (2013).

- 140 Shi, J. *et al.* Cleavage of GSDMD by inflammatory caspases determines pyroptotic cell death. *Nature* **526**, 660-665, doi:10.1038/nature15514 (2015).
- 141 Kofoed, E. M. & Vance, R. E. Innate immune recognition of bacterial ligands by NALPs determines inflammasome specificity. *Nature* **477**, 592-595, doi:10.1038/nature10394 (2011).
- 142 Fink, S. L. & Cookson, B. T. Caspase-1-dependent pore formation during pyroptosis leads to osmotic lysis of infected host macrophages. *Cell Microbiol* **8**, 1812-1825, doi:10.1111/j.1462-5822.2006.00751.x (2006).
- 143 Kankkunen, P. *et al.* (1,3)-beta-glucans activate both dectin-1 and NLRP3 inflammasome in human macrophages. *J Immunol* **184**, 6335-6342, doi:10.4049/jimmunol.0903019 (2010).
- 144 Wang, Z. *et al.* BART: a transcription factor prediction tool with query gene sets or epigenomic profiles. *Bioinformatics* **34**, 2867-2869, doi:10.1093/bioinformatics/bty194 (2018).
- 145 Sliter, D. A. *et al.* Parkin and PINK1 mitigate STING-induced inflammation. *Nature* **561**, 258-262, doi:10.1038/s41586-018-0448-9 (2018).
- 146 Desai, B. N. & Leitinger, N. Purinergic and calcium signaling in macrophage function and plasticity. *Front Immunol* **5**, 580, doi:10.3389/fimmu.2014.00580 (2014).
- 147 Muller, M. R. & Rao, A. NFAT, immunity and cancer: a transcription factor comes of age. *Nat Rev Immunol* **10**, 645-656, doi:10.1038/nri2818 (2010).
- 148 Li, H., Rao, A. & Hogan, P. G. Interaction of calcineurin with substrates and targeting proteins. *Trends Cell Biol* **21**, 91-103, doi:10.1016/j.tcb.2010.09.011 (2011).
- 149 Schappe, M. S. *et al.* Chanzyme TRPM7 Mediates the Ca(2+) Influx Essential for Lipopolysaccharide-Induced Toll-Like Receptor 4 Endocytosis and Macrophage Activation. *Immunity* **48**, 59-74 e55, doi:10.1016/j.immuni.2017.11.026 (2018).
- 150 Love, M. I., Huber, W. & Anders, S. Moderated estimation of fold change and dispersion for RNA-seq data with DESeq2. *Genome Biol* **15**, 550, doi:10.1186/s13059-014-0550-8 (2014).

- 151 Subramanian, A. *et al.* Gene set enrichment analysis: a knowledge-based approach for interpreting genome-wide expression profiles. *Proc Natl Acad Sci U S A* **102**, 15545-15550, doi:10.1073/pnas.0506580102 (2005).
- 152 Wettmarshausen, J. *et al.* MICU1 Confers Protection from MCU-Dependent Manganese Toxicity. *Cell Rep* **25**, 1425-1435 e1427, doi:10.1016/j.celrep.2018.10.037 (2018).
- 153 Ewels, P., Magnusson, M., Lundin, S. & Kaller, M. MultiQC: summarize analysis results for multiple tools and samples in a single report. *Bioinformatics* **32**, 3047-3048, doi:10.1093/bioinformatics/btw354 (2016).
- 154 Dobin, A. *et al.* STAR: ultrafast universal RNA-seq aligner. *Bioinformatics* **29**, 15-21, doi:10.1093/bioinformatics/bts635 (2013).
- 155 Anders, S., Pyl, P. T. & Huber, W. HTSeq--a Python framework to work with high-throughput sequencing data. *Bioinformatics* **31**, 166-169, doi:10.1093/bioinformatics/btu638 (2015).
- 156 Cash, J. L., White, G. E. & Greaves, D. R. Zymosan-Induced Peritonitis as a Simple Experimental System for the Study of Inflammation. *Method Enzymol* **461**, 379-396, doi:10.1016/S0076-6879(09)05417-2 (2009).
- 157 Wang, A., Luan, H. H. & Medzhitov, R. An evolutionary perspective on immunometabolism. *Science* **363**, doi:10.1126/science.aar3932 (2019).
- 158 Kinchen, J. M. & Ravichandran, K. S. Phagosome maturation: going through the acid test. *Nat Rev Mol Cell Biol* **9**, 781-795, doi:10.1038/nrm2515 (2008).
- 159 Nauseef, W. M. The phagocyte NOX2 NADPH oxidase in microbial killing and cell signaling. *Current opinion in immunology* **60**, 130-140, doi:10.1016/j.coi.2019.05.006 (2019).
- 160 Gazendam, R. P. *et al.* Two independent killing mechanisms of *Candida albicans* by human neutrophils: evidence from innate immunity defects. *Blood* **124**, 590-597, doi:10.1182/blood-2014-01-551473 (2014).
- 161 Davies, L. C., Rice, C. M., McVicar, D. W. & Weiss, J. M. Diversity and environmental adaptation of phagocytic cell metabolism. *J Leukocyte Biol* **105**, 37-48, doi:10.1002/Jlb.4ri0518-195r (2019).
- 162 Buck, M. D., Sowell, R. T., Kaech, S. M. & Pearce, E. L. Metabolic Instruction of Immunity. *Cell* **169**, 570-586, doi:10.1016/j.cell.2017.04.004 (2017).

- 163 Jimenez-Lopez, C. & Lorenz, M. C. Fungal immune evasion in a model host-pathogen interaction: *Candida albicans* versus macrophages. *PLoS Pathog* **9**, e1003741, doi:10.1371/journal.ppat.1003741 (2013).
- 164 Brown, G. D. Innate Antifungal Immunity: The Key Role of Phagocytes. *Annual Review of Immunology, Vol 29* **29**, 1-21, doi:10.1146/annurev-immunol-030409-101229 (2011).
- 165 O'Neill, L. A., Kishton, R. J. & Rathmell, J. A guide to immunometabolism for immunologists. *Nat Rev Immunol* **16**, 553-565, doi:10.1038/nri.2016.70 (2016).
- 166 Palsson-McDermott, E. M. *et al.* Pyruvate Kinase M2 Regulates Hif-1a Activity and IL-1b Induction and Is a Critical Determinant of the Warburg Effect in LPS-Activated Macrophages. *Cell Metabolism* **21**, 65-80 (2015).
- 167 Mallilankaraman, K. *et al.* MICU1 is an essential gatekeeper for MCU-mediated mitochondrial Ca²⁺ uptake that regulates cell survival. *Cell* **151**, 630-644, doi:10.1016/j.cell.2012.10.011 (2012).
- 168 Gray, L. R., Tompkins, S. C. & Taylor, E. B. Regulation of pyruvate metabolism and human disease. *Cell Mol Life Sci* **71**, 2577-2604, doi:10.1007/s00018-013-1539-2 (2014).
- 169 Williams, N. C. & O'Neill, L. A. J. A Role for the Krebs Cycle Intermediate Citrate in Metabolic Reprogramming in Innate Immunity and Inflammation. *Front Immunol* **9**, 141, doi:10.3389/fimmu.2018.00141 (2018).
- 170 Uwamahoro, N. *et al.* The pathogen *Candida albicans* hijacks pyroptosis for escape from macrophages. *mBio* **5**, e00003-00014, doi:10.1128/mBio.00003-14 (2014).
- 171 Goodridge, S. H., Simmons, R. M. & Underhill, D. M. Dectin-1 Stimulation by *Candida albicans* Yeast or Zymosan Triggers NFAT Activation in Macrophages and Dendritic Cells. *Journal of Immunology* (2006).
- 172 Strijbis, K. *et al.* Bruton's Tyrosine Kinase (BTK) and Vav1 contribute to Dectin1-dependent phagocytosis of *Candida albicans* in macrophages. *PLoS Pathog* **9**, e1003446, doi:10.1371/journal.ppat.1003446 (2013).
- 173 Suzuki, J. *et al.* Imaging intraorganellar Ca²⁺ at subcellular resolution using CEPIA. *Nat Commun* **5**, 4153, doi:10.1038/ncomms5153 (2014).

- 174 West, A. P. *et al.* TLR signalling augments macrophage bactericidal activity through mitochondrial ROS. *Nature* **472**, 476-480, doi:10.1038/nature09973 (2011).
- 175 Csordas, G. *et al.* Structural and functional features and significance of the physical linkage between ER and mitochondria. *Journal of Neurochemistry* **104**, 6-6 (2008).
- 176 Csordas, G. *et al.* Imaging Interorganelle Contacts and Local Calcium Dynamics at the ER-Mitochondrial Interface. *Biophys J* **98**, 380a-380a (2010).
- 177 Zhao, H. *et al.* AMPK-mediated activation of MCU stimulates mitochondrial Ca(2+) entry to promote mitotic progression. *Nat Cell Biol* **21**, 476-486, doi:10.1038/s41556-019-0296-3 (2019).
- 178 Geng, J. *et al.* Kinases Mst1 and Mst2 positively regulate phagocytic induction of reactive oxygen species and bactericidal activity. *Nat Immunol* **16**, 1142-1152, doi:10.1038/ni.3268 (2015).
- 179 Altenhofer, S., Radermacher, K. A., Kleikers, P. W., Wingler, K. & Schmidt, H. H. Evolution of NADPH Oxidase Inhibitors: Selectivity and Mechanisms for Target Engagement. *Antioxid Redox Signal* **23**, 406-427, doi:10.1089/ars.2013.5814 (2015).
- 180 Blacker, T. S. *et al.* Separating NADH and NADPH fluorescence in live cells and tissues using FLIM. *Nat Commun* **5**, 3936, doi:10.1038/ncomms4936 (2014).
- 181 Wallrabe, H. *et al.* Segmented cell analyses to measure redox states of autofluorescent NAD(P)H, FAD & Trp in cancer cells by FLIM. *Sci Rep* **8**, 79, doi:10.1038/s41598-017-18634-x (2018).
- 182 Carneiro, F. R. G., Lepelley, A., Seeley, J. J., Hayden, M. S. & Ghosh, S. An Essential Role for ECSIT in Mitochondrial Complex I Assembly and Mitophagy in Macrophages. *Cell Rep* **22**, 2654-2666, doi:10.1016/j.celrep.2018.02.051 (2018).
- 183 Conti, H. R., Huppler, A. R., Whibley, N. & Gaffen, S. L. Animal models for candidiasis. *Curr Protoc Immunol* **105**, 19 16 11-19 16 17, doi:10.1002/0471142735.im1906s105 (2014).

- 184 Pang, W. W. *et al.* Human bone marrow hematopoietic stem cells are increased in frequency and myeloid-biased with age. *Proc Natl Acad Sci U S A* **108**, 20012-20017, doi:10.1073/pnas.1116110108 (2011).
- 185 Martel, J. *et al.* Gut barrier disruption and chronic disease. *Trends Endocrinol Metab* **33**, 247-265, doi:10.1016/j.tem.2022.01.002 (2022).
- 186 Limon, J. J., Skalski, J. H. & Underhill, D. M. Commensal Fungi in Health and Disease. *Cell Host Microbe* **22**, 156-165, doi:10.1016/j.chom.2017.07.002 (2017).
- 187 Shanmughapriya, S. *et al.* Ca²⁺ signals regulate mitochondrial metabolism by stimulating CREB-mediated expression of the mitochondrial Ca²⁺ uniporter gene MCU. *Sci Signal* **8**, ra23, doi:10.1126/scisignal.2005673 (2015).
- 188 Tabula Muris, C. A single-cell transcriptomic atlas characterizes ageing tissues in the mouse. *Nature* **583**, 590-595, doi:10.1038/s41586-020-2496-1 (2020).
- 189 Jade, D. B. *et al.* Nitric Oxide Modulates Metabolic Remodeling in Inflammatory Macrophages through TCA Cycle Regulation and Itaconate Accumulation. *Cell Reports* **28**, 218-230 (2019).
- 190 Westman, J., Moran, G., Mogavero, S., Hube, B. & Grinstein, S. *Candida albicans* Hyphal Expansion Causes Phagosomal Membrane Damage and Luminal Alkalinization. *mBio* **9**, doi:10.1128/mBio.01226-18 (2018).
- 191 Pietrobon, A. J., Teixeira, F. M. E. & Sato, M. N. Immunosenescence and Inflammaging: Risk Factors of Severe COVID-19 in Older People. *Front Immunol* **11**, 579220, doi:10.3389/fimmu.2020.579220 (2020).